ORNL/HTSPC-14

ORNL Superconducting Technology Program for Electric Power Systems

Annual Report for FY 2002

SUPERCONDUCTIVITY FOR ELECTRIC SYSTEMS

DOCUMENT AVAILABILITY

Reports produced after January 1, 1996, are generally available free via the U.S. Department of Energy (DOE) Information Bridge:

Web site: http://www.osti.gov/bridge

Reports produced before January 1, 1996, may be purchased by members of the public from the following source.

National Technical Information Service
5285 Port Royal Road
Springfield, VA 22161
Telephone 703-605-6000 (1-800-553-6847)
TDD 703-487-4639
Fax 703-605-6900
E-mail info@ntis.fedworld.gov
Web site http://www.ntis.gov/support/ordernowabout.htm

Reports are available to DOE employees, DOE contractors, Energy Technology Data Exchange (ETDE) representatives, and International Nuclear Information System (INIS) representatives from the following source.

Office of Scientific and Technical Information
P.O. Box 62
Oak Ridge, TN 37831
Telephone 865-576-8401
Fax 865-576-5728
E-mail reports@adonis.osti.gov
Web site http://www.osti.gov/contact.html

This report was prepared as an account of work sponsored by an agency of the United States Government. Neither the United States Government nor any agency thereof, nor any of their employees, makes any warranty, express or implied, or assumes any legal liability or responsibility for the accuracy, completeness, or usefulness of any information, apparatus, product, or process disclosed, or represents that its use would not infringe privately owned rights. Reference herein to any specific commercial product, process, or service by trade name, trademark, manufacturer, or otherwise, does not necessarily constitute or imply its endorsement, recommendation, or favoring by the United States Government or any agency thereof. The views and opinions of authors expressed herein do not necessarily state or reflect those of the United States Government or any agency thereof.

ORNL/HTSPC-14

ORNL SUPERCONDUCTING TECHNOLOGY PROGRAM FOR ELECTRIC POWER SYSTEMS

ANNUAL REPORT FOR FY 2002

Compiled by
R. A. Hawsey
A. W. Murphy

Edited by
W. S. Koncinski

Manuscript Completed: February 2003
Date Published: May 2003

Prepared for the
Office of Distributed Energy and Electricity Reliability
Office of Energy Efficiency and Renewable Energy
U.S. DEPARTMENT OF ENERGY
(EB 50 01 00 0)

Prepared by
OAK RIDGE NATIONAL LABORATORY
P.O. Box 2008
Oak Ridge, TN 37831-6285
Managed by
UT-Battelle, LLC
for the
U.S. DEPARTMENT OF ENERGY
under contract DE-AC05-00OR22725

Front row (left to right): Hans M. Christen, Michael J. Gouge, Patrick M. Martin, Claudia Cantoni, Ron Feenstra, J. Winston Lue, Keith J. Leonard, and Yifei Zhang.

Second row (left to right): Noel Rutter, Lee Heatherly, Jr., Dominic F. Lee, Cookie Murphy, M. Parans Paranthaman, John P. Stovall, David K. Christen, Tolga Aytug, Michelle V. Buchanan, and Marilyn A. Brown.

Third row (left to right): Hong-Ying Zhai, Joseph A. Marasco, Jonathan A. Demko, Ben W. McConnell, Robert C. Duckworth, John F. Cooke, H. Richard Kerchner, Robert A. Hawsey, Srivatsan Sathyamurthy, Eliot D. Specht, Amit Goyal, Donald M. Kroeger, Albert A. Gapud, and James B. Roberto.

Not pictured: David B. Beach, Everett E. Bloom, John D. Budai, Sylvester W. Cook, Larry M. Dickens, Alvin R. Ellis, Huey S. Hsu, D. Randy James, Sukill Kang, Fred A. List III, Stanley L. Milora, Isidor Sauers, S. William Schwenterly, James R. Thompson, Robert K. Williams, Yong Li Xu, and Jaeun Yoo.

Contents

List of Figures

List of Tables

Abbreviated Terms

NOMENCLATURE

$\Delta\phi$	in-plane texture
$\Delta\omega$	out-of-plane texture
ρ	normal-state resistivity
B_{irr}	irreversibility field
$c\ (2 \times 2)$	centered (2×2) superstructure
I_c	critical current
I_p	peak current
I_{mp}	propagation current
I_{rms}	root mean square cable current
J_c	critical current density
J_E	engineering critical current density (K_c/t)
K_c	critical current per unit width of conductor (I_c/w)
langmuir	10^{-6} Torr/s
ML	surface adsorbate atoms per surface substrate atoms
M_{sat}	saturation magnetization
P_{base}	base pressure
$P(H_2O)$	water vapor partial pressure
$P(O_2)$	oxygen partial pressure
T	tesla
T_c	critical temperature/transition temperature
t	thickness

ACRONYMS AND INITIALISMS

ac	alternating current
ACCI	Accelerated Coated Conductor Initiative
ACCL	Accelerated Coated Conductor Laboratory
AES	Auger electron spectroscopy
AFM	atomic force microscopy
AMSC	American Superconductor Corporation
ANL	Argonne National Laboratory
BSCCO	Bi-Sr-Ca-Cu-O
CCC	coated conductor composite
CCVD	combustion chemical vapor deposition
CRADA	cooperative research and development agreement
dc	direct current
DOE	U.S. Department of Energy
DOE-HQ	DOE Headquarters

e-beam	electron beam
EDS	energy-dispersive spectroscopy
EDX	energy-dispersive X-ray diffraction
fcc	face-centered cubic lattice
FWHM	full width at half maximum
GBMD	grain-boundary misorientation distribution
GE	General Electric
HRSEM	high-resolution scanning electron microscope
HTS	high-temperature superconductivity/superconductor/superconducting
HV	high vacuum
IBAD	ion-beam-assisted deposition
IEEE	Institute of Electrical and Electronics Engineers, Inc.
IGC	Intermagnetics General Corporation
ISD	inclined substrate deposition
ISTEC	International Superconductivity Technology Center
LANL	Los Alamos National Laboratory
LMO	$LaMnO_3$
LN_2	liquid nitrogen
LSMO	$La_{0.7}Sr_{0.3}MnO_3$
LZO	lanthanum zirconium oxide ($La_2Zr_2O_7$)
MBE	molecular beam epitaxy
MCT	MicroCoatings Technology, Inc.
MLI	multiple-layer superinsulation
MOCVD	metal-organic chemical vapor deposition
MOD	metal organic decomposition
MRS	Materials Research Society
ORNL	Oak Ridge National Laboratory
PD	partial discharge
PED	pulsed-electron deposition
PLD	pulsed-laser deposition
R&D	research and development
RABiTS™	Rolling-Assisted Biaxially Textured Substrate
RBS	Rutherford backscattering spectroscopy/spectrum
rf	radio frequency
RFP	request for proposal
RHEED	reflection high-energy electron diffraction
rms	root mean square
SAIC	Science Applications International Corporation
SD	standard deviation

SEM	scanning electron microscopy
SIMS	secondary ion mass spectrometer
SPI	Superconductivity Partnership Initiative
STO	$SrTiO_3$
TEM	transmission electron microscopy
TFA	trifluoroacetate
XRD	X-ray diffraction
XPS	X-ray photoelectron spectroscopy
WES	Waukesha Electric Systems
YBCO	yttrium barium copper oxide ($YBa_2Cu_3O_{7-d}$)
YSZ	yttria-stabilized zirconia

Executive Summary

The Oak Ridge National Laboratory (ORNL) Superconductivity Program for Electric Power Systems is conducted as part of a national effort by the U.S. Department of Energy's Office of Distributed Energy and Electricity Reliability, Office of Energy Efficiency and Renewable Energy. The purpose of the program is to jointly develop with industry the science and technology base needed for U.S. industry to proceed to commercial development of electric power applications. Major tasks include the following three project areas: (1) Strategic Research, (2) Second-Generation Wire Research, and (3) Superconductivity Partnerships with Industry.

This document describes the major research and development activities for ORNL together with related accomplishments, including those of the cooperative agreement partners in the private sector. The technical progress reported here was summarized from recent open literature publications, presentations, and information prepared for the FY 2002 Annual Program Peer Review held July 17–19, 2002. At that meeting, ORNL received the top rating in two of the three project areas. Aspects of ORNL's work that were presented at the Applied Superconductivity Conference in August 2002 are included in this report as well.

The Superconductivity Program for Electric Power Systems is highly leveraged by the staff and other resources of U.S. industry and universities. In fact, a major success story for FY 2002 was seeing ORNL science and technology adapted, improved upon, and implemented for the first time for meter-length, reel-to-reel processes by U.S. industry. In addition, the world's longest running high-temperature superconducting (HTS) cable system continues to break performance and reliability records at Southwire's facility in Carrollton, Georgia.

Interlaboratory teams are also in place on several strategic research projects. Working-group meetings, staff exchanges, and joint publications and presentations along with web postings of ORNL reports and peer review talks help to ensure that there *is* technology transfer with U.S. industry. Working together, the collaborative teams are making rapid progress in solving the scientific and technical issues necessary for the introduction of HTS-based devices in the nation's generation, transmission, and distribution systems.

Highlights

SECOND-GENERATION WIRE RESEARCH

- The "ex situ" barium fluoride process was used to produce a yttrium barium copper oxide (YBCO) coating on the Rolling-Assisted Biaxially Textured Substrate (RABiTS™) template in lengths greater than 1 m and with critical currents in excess of 90 amperes. Oak Ridge National Laboratory (ORNL) was the only national laboratory to report meter-length results at the 2002 U.S. Department of Energy (DOE) peer review. In addition, several ORNL cooperative research and development agreement (CRADA) partners reported, for the first time, meter lengths of YBCO on RABiTS™ .

- ORNL technology was adopted, improved upon, and implemented for meter-length, reel-to-reel processes by U.S. industry. For this, American Superconductor Corporation successfully adapted ORNL's RABiTS™ template, including the important sulfurization step, to produce ten tapes, each longer than 1 m, with an average critical current exceeding 100 amperes. American Superconductor used a nonvacuum "metal organic decomposition" (MOD) process to produce the superconducting films. This U.S.-leading performance has been accompanied by unprecedented uniformity along the tape length by using a reproducible process that American Superconductor believes is industrially scalable. In FY 2002, no other company or national laboratory demonstrated the uniformity, number of lengths, or current levels achieved by the ORNL–American Superconductor CRADA team.

- MicroCoating Technologies (Chamblee, Georgia), an industrial licensee of RABiTS™, has successfully scaled up the ORNL RABiTS™ template to reproducible long lengths and is now offering "RABiTS™ for sale," a first in the United States.

- Industrial users, including MicroCoating Technologies, American Superconductor, and 3M, began using the ORNL Accelerated Coated Conductor Laboratory.

STRATEGIC RESEARCH

- ORNL has demonstrated that YBCO can be formed by precursor conversion processes with a wide range of conversion pressures, all the way down to near-vacuum, offering manufacturers added flexibility in their reel-to-reel manufacturing processes. 3M Company reported 2-m lengths with critical currents exceeding 40 amperes end-to-end, the longest YBCO tapes reported by industry at the DOE Peer Review.

- Single buffer layers put down by solution processing on alloy tapes have yielded greater than 1 million amperes per square centimeter.

- Interlaboratory partnerships have been important this year.
  - — A strong collaboration with Los Alamos National Laboratory (LANL) has produced samples having high critical currents by LANL's pulsed-laser deposition (PLD) on an ORNL buffer layer deposited on the LANL ion-beam-assisted deposition (IBAD) MgO substrate.
  - — A similar collaboration with Argonne National Laboratory (ANL) has led to high critical current densities on the ANL "inclined substrate deposition" (ISD) substrate.
  - — PLD coatings more than 6 microns thick yielded high currents (300 amperes per centimeter width) on RABiTS™ ; collaborations with LANL and ANL, along with our own transmission electron microscope studies, helped reveal important microstructural and chemical information.

SUPERCONDUCTIVITY PARTNERSHIPS WITH INDUSTRY (SPI)

- The world's longest running high-temperature superconductivity (HTS) cable system is continuing to break performance and reliability records at Southwire Company, with more than 15,000 hours of providing full power to three manufacturing plants in Carrollton, Georgia. The terminations for this system were designed by ORNL, and the technology was transferred to U.S. industry. The system has been running unattended, carrying up to 20 MVA, since June 2001.

- With Southwire, ORNL completed the detailed design of a 5-m-long "triaxial" HTS cable system, including terminations. Southwire built the cable, and industry is building the new terminations, which are mechanically and electrically quite complex. Testing of the cable began at ORNL in the fall of 2002.

- A cooling system for the 5-MVA HTS transformer being built by Waukesha and Intermagnetics General Corp. (IGC) has been designed by ORNL, built by U.S. industry, and tested by the team to twice the normal operating thermal load expected of the transformer. The testing was 100% successful. Using a unique test facility, ORNL measured the alternating-current losses of an early prototype transformer coil built with the 5-MVA conductor by IGC.

- ORNL has one of the largest cryogenic dielectric research projects in the United States. Electrical insulation materials for operation at cryogenic temperatures were studied, and new materials were characterized for both Southwire and Waukesha. A method for obtaining cable aging data was demonstrated in FY 2002 as a promising alternative to the time-consuming methods currently used.

PROGRAMMATIC

- A new CRADA was executed with General Electric Company for joint research on the 100-MVA SPI project.

- The facilities and equipment in ORNL's Coated Conductor Research Laboratory were used by several companies in FY 2002. A key industrial partner visited ORNL to use a reel-to-reel X-ray diffraction diagnostic tool for superconducting wire research. MicroCoating Technologies brought four samples of one-meter lengths of coated conductor template to ORNL to gain first-hand experience with a new reel-to-reel X-ray diffraction system recently brought on line at the Coated Conductor Research Laboratory. The template was made with MicroCoating Technologies' proprietary combustion chemical vapor deposition process. The X-ray diffraction measurements showed that MicroCoating Technologies's templates are of excellent quality and exhibit a high degree of in-plane grain alignment, a necessary condition for high-performance superconductor deposition. In addition, American Superconductor visited ORNL during the year to use the new four-high rolling mill and the ex situ conversion system with an in situ X-ray source to monitor the conversion of their proprietary MOD films on various substrates.

- The International Workshop on Processing and Applications of Superconductors, sponsored by the Materials Research Society, was held in Gatlinburg, Tennessee, July 31–August 2, 2002. Organized by M. Parans Paranthaman (Chair), Amit Goyal, and Ron Feenstra of ORNL; Teruo Izumi of the International Superconductivity Technology Center (ISTEC), Japan; and Venkat Selvamanickam of IGC-SuperPower, the workshop presented work from an international group of 50 scientists from industry, national laboratories, and academia who are key players in the HTS field. Among the 100 workshop attendees were academics, researchers, and engineers from countries all over the world, including Japan, Germany, France, Korea, and Spain. This workshop also provided overviews of the

status of the second-generation YBCO coated conductors in the United States, Japan, and Europe. A pre-workshop tour of ORNL's Coated Conductor Research Laboratory was a highlight for the visitors.

- ORNL's superconductivity project hosted a record six summer undergraduate interns during June and August 2002. The six students worked on DOE Office of Energy Efficiency and Renewable Energy superconductivity projects in four ORNL research divisions. The internship program is managed by the Oak Ridge Institute for Science and Education. These students came from universities located across the United States: the University of Tennessee, California State University-Fresno, Indiana University of Pennsylvania, University of Wisconsin-Madison, Albion College (Michigan), and Tennessee Technological University.

- John Scudiere, general manager, Advanced Conductors at American Superconductor Corporation, visited ORNL on September 27, 2002. During the visit, Mr. Scudiere presented recognition awards to the three ORNL principal investigators in three different ORNL divisions with whom American Superconductor has worked over the past few years. He thanked the entire ORNL "coated-conductor team" for helping American Superconductor achieve world-record performance of next-generation HTS wire based in part on ORNL's patented RABiTS™ technology. Scudiere also announced that, in partnership with American Superconductor, the performance of the YBCO wires had increased by 15% since July to more than 140 amperes over a one-meter length, with outstanding uniformity along the length.

1. Technical Progress in Wire Development

1.1 PROGRESS IN CONTINUOUS REEL-TO-REEL EX SITU CONVERSION OF HIGH CURRENT CAPACITY YBCO COATED CONDUCTORS

D. F. Lee, K. J. Leonard, L. Heatherly Jr., J. Yoo, P. M. Martin, S. W. Cook, D. M. Kroeger, M. Paranthaman (ORNL); M. W. Rupich, D. T. Verebelyi (American Superconductor Corporation)

1.1.1 Introduction

For the past several years, there has been an increasing amount of worldwide attention focused on the ex situ conversion of $YBa_2Cu_3O_{7-\delta}$ (YBCO) films on textured substrates. Significant effort is being expended on various ex situ techniques [e.g., vapor-deposited BaF_2 precursor and the metal organic decomposition (MOD) trifluoroacetate (TFA) method] in the United States, Europe, and Japan.[1–7] The interest is, in large part, due to the nature of the process, in which the precursor deposition step is separated from YBCO formation. Hence, compositional control is separated from epitaxial YBCO growth, which lends the technique to simpler scale-up as well as potentially more economical and diverse instrumentation, such as batch processing.

ORNL has taken on the simultaneous challenge of proving the suitability of the Rolling-Assisted Biaxially Textured Substrate (RABiTS™) as a long-length substrate and the viability of the ex situ processing for YBCO deposition. Several factors that contributed to the lower-than-expected end-to-end critical current densities as well as highly nonuniform critical current densities our meter-length samples have been identified. Among these are RABiTS™-related issues, such as flaws in buffer texture and tape dimension, and precursor-related issues, such as nonstoichiometry due to discharge during precursor deposition. The vast majority of these issues have been resolved. The solutions include modification of the buffer architecture to a more repeatable one, imposition of a careful tape-handling protocol, and preconditioning of source metals for electron-beam (e-beam) precursor deposition. The result is long-length precursors on RABiTS™ with a high degree of textural and compositional uniformity that enabled us to obtain the excellent tape performances presented in the following sections.

1.1.2 Long-Length Tapes of YBCO on a 0.3-μm Precursor

Long-length, 1-cm-wide Ni-RABiTS™ with the architecture 150Å CeO_2 (rf sputtered)/1500Å yttria-stabilized zirconia (YSZ) (rf sputtered)/150Å Y_2O_3 (e-beam)/50 μm Ni was fabricated by using reel-to-reel systems. In the present RABiTS™ architecture, Y_2O_3 has replaced CeO_2 as seed material because it is less susceptible to cracking.[8] The full width at half maximum (FWHM) out-of-plane texture ($\Delta\omega$) and in-plane texture ($\Delta\phi$)of the metal and buffers are ~8° and ~10°, respectively, which is typical of our commercial Ni. A 2.3-m-long section of this Ni-RABiTS™ was loaded into our bench-top three-gun e-beam deposition chamber, and a 0.3-μm-thick BaF_2 precursor was deposited on the entire sample in a single pass.

Reel-to-reel ex situ conversion of the vapor-deposited precursor was performed in our 7-flow-module, 22-hot-zone chamber.[1,9] A simple pull-through approach was used to evaluate the tape's performance and uniformity. In this approach, various processing parameters in the flow modules were preset to desired values, and the sample was translated through the entire chamber at a fixed speed so that every location of the sample was subjected to the same treatment through the entire conversion process. To convert the

0.3-μm precursor (sample A, see Table 1.1), the conversion temperature was set at 740°C, the gas flow rate was 5.5 L/min per module, and the oxygen partial pressure [$P(O_2)$] was 160 mTorr. The water vapor partial pressure [$P(H_2O)$] of modules 1 to 5 were set at 67.5 Torr (module 1 is located at the entrance of the chamber) and modules 6 and 7 were dry. The total conversion time in the humidified zones (modules 1 to 5) was 120 min. These processing conditions were selected based on previous experiments of samples with identical precursor thickness, the best result of which was an 80-cm-long sample with an end-to-end critical current density (J_c) of 625 kA/cm^2 [critical current (I_c)/cm = 17.5 A]. The averaged 1-cm sectional J_c density was of 750 kA/cm^2 (I_c/cm = 21 A) with a standard deviation of 10.5%.[10]

Table 1.1. Processing parameters utilized in the reel-to-reel conversion of ex situ YBCO on RABiTS™

Sample	YBCO thickness (μm)[a]	Length (m)	RABiTS™ type	Conversion time (min)	Flow module water vapor partial pressure (Torr)				
					1	2	3	4	5
A	0.30	2.30	Ni	120	67.5	67.5	67.5	67.5	67.5
B	0.30	1.50	Ni-3%W[b]	120	67.5	67.5	67.5	67.5	67.5
C	0.58	0.50	Ni	Variable	27	67.5	67.5	67.5	67.5
D	0.58	0.50	Ni	Variable	20	36	36	67.5	67.5
E	0.58	0.50	Ni	Variable	3.5	20	20	36	36
F	0.58	1.15	Ni-3%W[b]	160	3.5	20	20	30	30
G	0.82	1.15	Ni-3%W	200	3.5	20	20	30	30

[a]Film thickness determined by Rutherford backscattering spectroscopy.
[b]Buffer layers deposited by American Superconductor Corp.

After conversion, a 1-μm-thick Ag stabilization layer was deposited onto the YBCO surface by radio-frequency (rf) sputtering followed by an oxygen annealing step. To perform critical-current measurements at 77 K and self-field, the sample was wound helically around a drum with sectional voltage taps located every 16 cm along the tape, together with end-taps 224 cm apart. The end-to-end current-voltage curve of this conductor is shown in Fig. 1.1; the end-to-end critical current was determined to be 18.9 A (J_c = 630 kA/cm^2) according to the 1-μV/cm criterion. Figure 1.2 shows the 16-cm sectional critical-current and critical-current-density results of the entire 2.3-m tape. It can be seen from this figure that the mean I_c = 19.1 A (J_c = 637 kA/cm^2) with a maximum I_c of 21.1 A (J_c = 703 kA/cm^2) and minimum I_c of 17.2 A (J_c = 573 kA/cm^2). The critical current density values are only slightly lower than those obtained in short samples with pulsed laser deposition (PLD) YBCO and are consistent with the texture of the underlying RABiTS™. More importantly, the current-carrying characteristics of this conductor are highly uniform, with a standard deviation of 5.4%. Since previous experience has shown that defects can occur in a length scale of less than 1 cm, the 2.3-m conductor was cut into two halves, and the halves were individually tested in a 1-cm sectional critical-current apparatus, which is capable of measuring tapes up to 1 m long. One-cm sectional critical-current tests revealed that one of the halves possesses a mean I_c = 20.1 A (J_c = 670 kA/cm^2) with

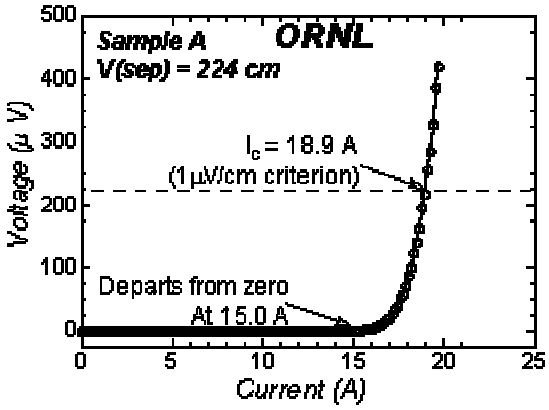

Fig. 1.1. End-to-end current-voltage curve for sample A (0.3-μm YBCO layer on a 2.3-m-long Ni-RABiTS™ tape).

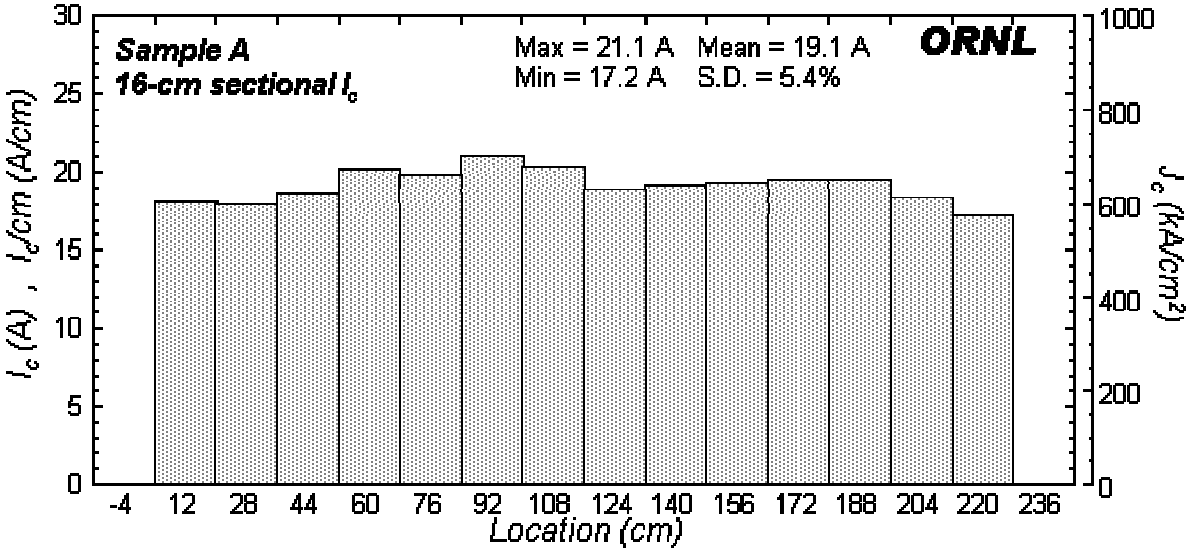

Fig. 1.2. Critical current and critical current density results for the 16-cm sectional measurements of the entire length of sample A (0.3-μm YBCO layer on a 2.3-m-long Ni-RABiTS™ tape).

a maximum I_c of 23.3 A (J_c = 777 kA/cm^2), minimum I_c of 16.8 A (J_c = 560 kA/cm^2), and a standard deviation of 7.7%. Values of the other half are mean I_c = 20.1 A (J_c = 670 kA/cm^2), maximum I_c = 23.0 A (J_c = 767 kA/cm^2), minimum I_c = 17.8 A (J_c = 593 kA/cm^2), and a standard deviation of 5.7%, respectively. These results, in totality, signified that no region with gross defects exists along the entire conductor length. Thus, with consistent texture as well as structural integrity provided by the Y_2O_3 seed, combined with improved tape-handling protocol, RABiTS™ is a suitable substrate for long-length coated conductors with uniform properties.

To further improve the critical current density, metal substrates with sharper textures need to be utilized. ORNL, working with its commercial vendors, has developed a series of strengthened alloy tapes with sharp textures, one of which is Ni-3at.%W. In collaboration with American Superconductor Corp. (AMSC), a 2.65-m-long Ni-3%W tape was texture annealed at ORNL and was sent to AMSC for buffer(s) deposition. Texture of the strengthened alloy RABiTS™ is considerably sharper than that of annealed nickel, with FWHM of $\Delta\omega$ ~5° and FWHM $\Delta\phi$ ~7°. Upon receiving the fully buffered Ni-3%W RABiTS™ from AMSC, a 0.3 μm-thick BaF_2 precursor was e-beam deposited onto a 1.5-m section of the substrate in a single pass. Reel-to-reel ex situ conversion of the tape (sample B) was performed in an identical manner as that of the Ni-RABiTS™ (Table 1.1). Following Ag deposition and oxygen annealing, the conductor was evaluated at 77 K and self-field as previously described. Figure 1.3 shows the end-to-end transport measurement with voltage separation of 138 cm. The result revealed that the coated conductor possesses a high end-to-end I_c of 44.2 A

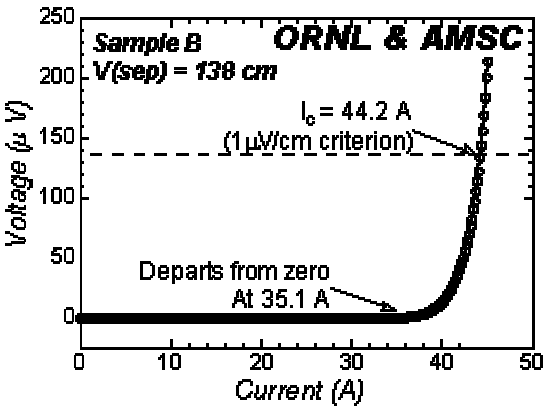

Fig. 1.3. End-to-end current-voltage curve for sample B (0.3-μm YBCO layer on a 1.5-m-long Ni-3%W RABiTS™ tape).

(J_c = 1.47 MA/cm^2) according to the 1-μV/cm criterion. In addition, 16-cm sectional measurements (Fig. 1.4) show that the mean I_c = 44.5 A (J_c = 1.48 MA/cm^2), maximum I_c = 46.7 A (J_c = 1.56 MA/cm^2), minimum I_c = 41.7 A (J_c = 1.39 MA/cm^2) with a standard deviation of only 4.0%. To better characterize the critical-current uniformity, 1.15 m-long section at the front of the tape was cut, and 1-cm sectional measurements were performed in our meter-long apparatus. It can be seen in Fig. 1.5 that the 1-cm sectional behavior closely resembles that of the 16-cm sectional counterpart, and the mean I_c = 46.1 A (J_c = 1.54 MA/cm^2), maximum I_c = 52.7 A (J_c = 1.76 MA/cm^2), minimum I_c = 38.2 A (J_c = 1.27 MA/cm^2), and a standard deviation of only 6.2%. Thus, with improvement in substrate texture, RABiTS™ with high critical current density can be obtained in lengths.

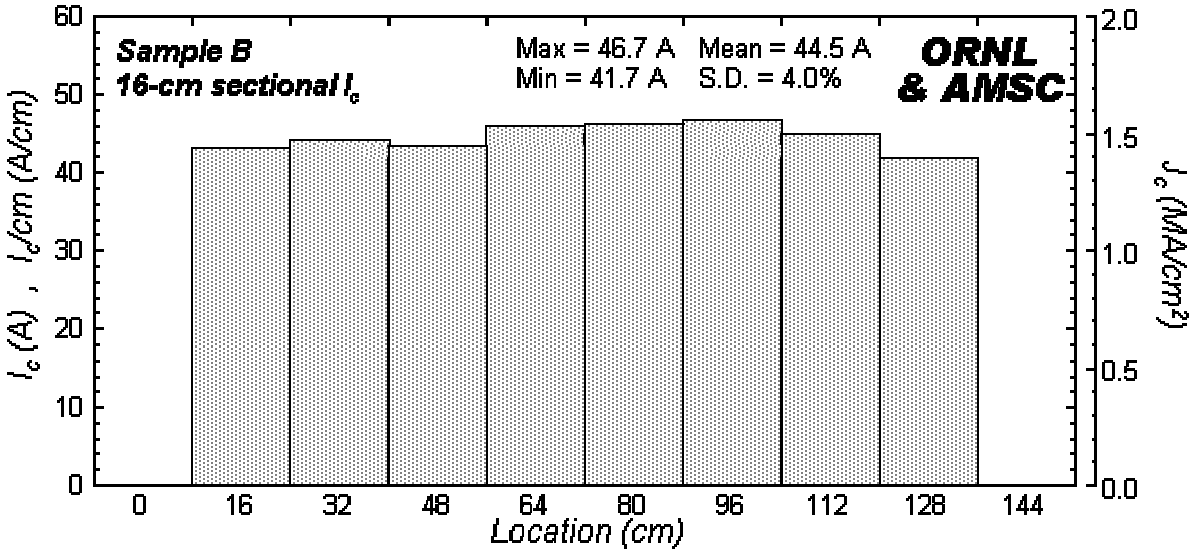

Fig. 1.4. Critical current and critical current density results for the 16-cm sectional measurements of the entire length of sample B (0.3-μm YBCO layer on a 1.5-m-long Ni-3%W RABiTS™ tape).

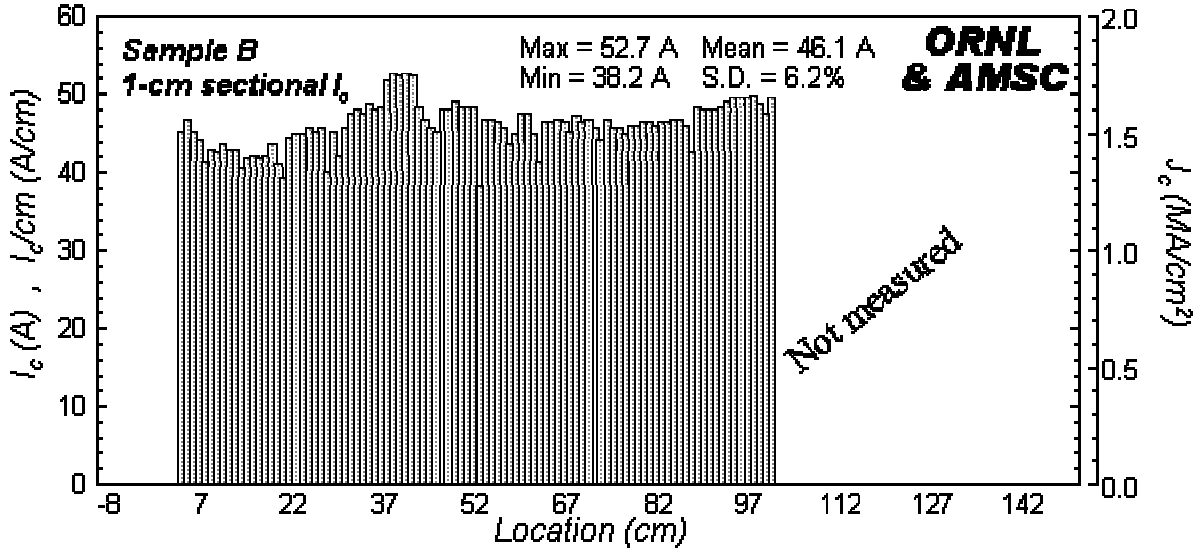

Fig. 1.5. Critical current and critical current density results for the 1-cm sectional measurements of the front 1.15 m of sample B.

1.1.3 Long-Length Tapes of YBCO on a 0.58-μm Precursor

While the suitability of RABiTS™ as a high-critical-current density long-length substrate for coated conductors has been demonstrated, the viability of the BaF_2 precursor to produce a high critical current YBCO tape has not been verified. To accomplish this, thick-film YBCO needs to be processed. This task was approached incrementally by depositing a 0.58-μm-thick precursor on a 1.7-m-long Ni-RABiTS™ in two passes. For preliminary testing, a 10-cm-long section was cut and pulled through the reel-to-reel chamber such that the conversion time was 200 min; other parameters were identical to those for samples A and B. The tape converted in such a manner was gray, contained a significant fraction of random YBCO, and exhibited a critical current near zero.

Next, a 50-cm-long section (sample C) was converted by using a variable conversion approach. In this approach, conversion parameters in the various flow modules are preset to desired values. Once these conditions have stabilized, the sample is translated into the reaction chamber at a prescribed speed. Tape motion is interrupted when the front of the sample has reached a desired location, and therefore, the desired conversion time ($t1$). Depending on sample length, the remaining portion of the tape would have undergone conversion for a time $t2$, where $t1 > t2$. Then, flowing gas in the modules is switched to dry, and the sample is cooled to room temperature. By using this approach, a sample for which the extent of conversion varies linearly along the length between $t1$ and $t2$ can be obtained all at once. Sample C was converted in such a fashion; the conversion parameters are listed in Table 1.1. The conversion parameters are nearly identical to those of samples A and B; however, it can be seen in Table 1.1 and Fig. 1.6 that $P(H_2O)$ in module 1 (i.e., the initial conversion condition) was set at a lower value. A lower $P(H_2O)$ was selected based on past experience; a smaller $P(H_2O)$ tends to favor nucleation of *c*-axis YBCO. Following conversion, X-ray diffraction (XRD) was performed at various locations on sample C. The θ-2θ scans showed that the YBCO film is mostly cube textured with a small amount of random YBCO component. Visually, however, the sample appears grayish along its entire length, a section of which is shown in Fig. 1.7. Sectional critical current measurements were performed on this sample, and the result is shown in Fig. 1.8 as function of conversion time that was calculated based on location and tape speed. During measurements, sections with conversion time of less than about 180 min possessed such low critical currents that local over-current resulted in the sections being burnt. Nevertheless, the critical current values of the remaining sections are disappointingly small, with a maximum located around 220 min for these conversion parameters. This lower-than-expected critical current over a wide range of conversion time is no larger than that of the best 0.3-μm tape and indicates that the conversion conditions are inappropriate for thicker films.

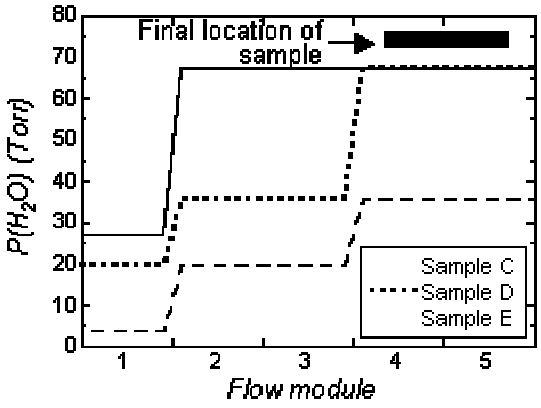

Fig. 1.6. Water vapor partial pressures in the different flow modules utilized during the variable conversion of samples C, D, and E (0.58-μm YBCO precursor on Ni-RABiTS™).

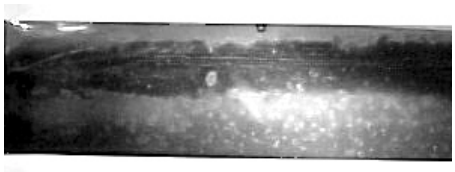

Fig. 1.7. Optical photograph of a section of sample C, showing the grayish appearance of the sample, especially along the edges.

To elucidate information about the grayish film as well as the phase assemblage of the precursor, a 1-μm-thick precursor was deposited onto a meter-long Ni-RABiTS™. This tape was

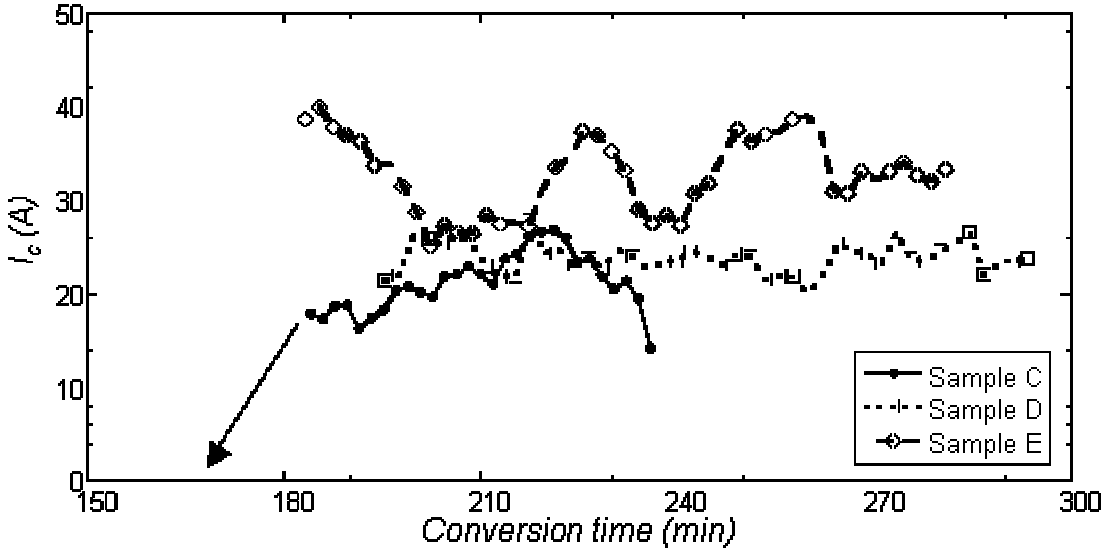

Fig. 1.8. Changes in critical current with processing time for sample C (variably converted 0.58-µm precursor on Ni-RABiTS™).

subjected to variable conversion conditions identical to those of sample C, with the front conversion time set at 120 min while the back of the sample was just entering the reaction chamber. Optical examination of the variably converted tape revealed that the entire sample surface, from the point where conversion temperature of 740°C had just been reached to the end where the sample was converted for 120 min, contained grayish particles. A section where the precursor had been converted for about 30 min was cut from the length, and depth profile Auger electron spectroscopy (AES), scanning electron microscopy (SEM), and cross-sectional transmission electron microscopy (TEM) were performed. Results from the depth profile AES are shown in Fig. 1.9, where it can be seen that the precursor is Cu-rich at the sample surface. This phase segregation has been confirmed by SEM as well as TEM (Fig. 1.10), where the grayish particles were identified as CuO by energy-dispersive spectroscopy (EDS). The depth profile AES also revealed that the middle of the precursor thickness was Ba-rich, and that the film contained a mixture of YBCO and precursor near the substrate/film interface. This inhomogeneous YBCO growth has also been seen in cross-sectional TEM [Fig. 1.10(b)], where a discontinuous block of *c*-axis YBCO is found at the substrate surface, surrounded by unreacted precursor. These results suggest that, under certain conditions, phase segregation and particle coarsening can occur, even at the initial stage of conversion, the consequences of which are retardation and incomplete YBCO conversion.

With indications that $P(H_2O)$ may affect phase segregation in our vapor-deposited BaF_2 precursor, a series of short sample conversions was performed on 0.58-µm precursor samples where $P(H_2O)$ was varied by nearly two orders of magnitude. Quick optical examinations revealed that the grayish film and accompanying surface CuO particles decreased with reducing $P(H_2O)$ below certain $P(H_2O)$ value, where few CuO particles were seen.

Based on these indicators, the remaining 1 m of 0.58-µm-precursor Ni-RABiTS™ was cut half (samples D and E); both samples were variably converted in reducing schedules of $P(H_2O)$, as shown in Table 1.1 and Fig. 1.6. It can be seen in Fig. 1.8 that with a relatively small reduction in initial $P(H_2O)$, sample D exhibited a uniform critical current over a wide range of conversion time. Even though the critical currents were still low, the average value was equal to the best section of sample C. In addition, the grayish appearance is greatly reduced compared with that of sample C. Sample E, with further

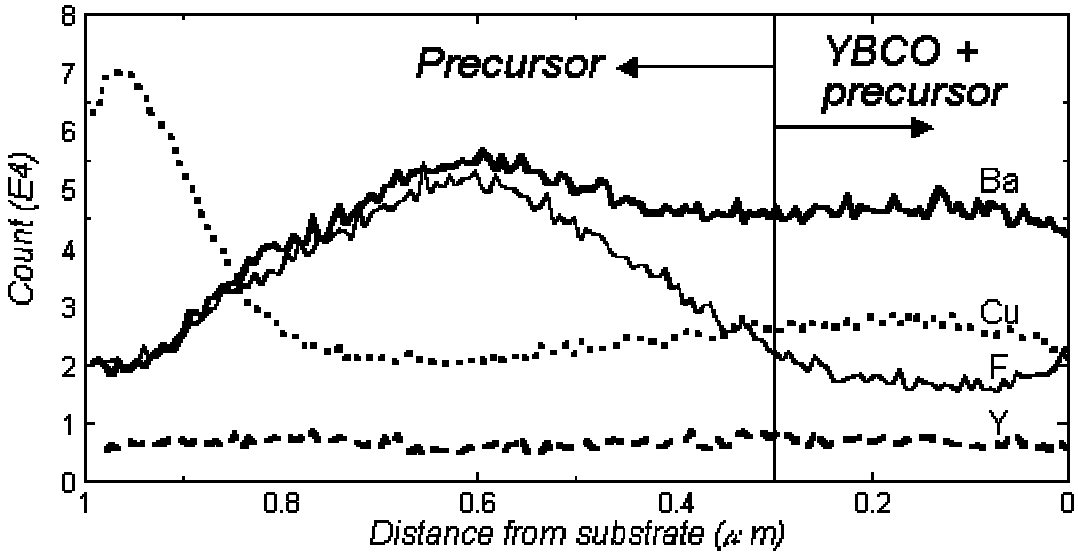

Fig. 1.9. Depth profile Auger results of a section of sample C (1-μm precursor on Ni-RABiTS™ converted under "high" water vapor partial pressure). Conversion time approximately 30 min.

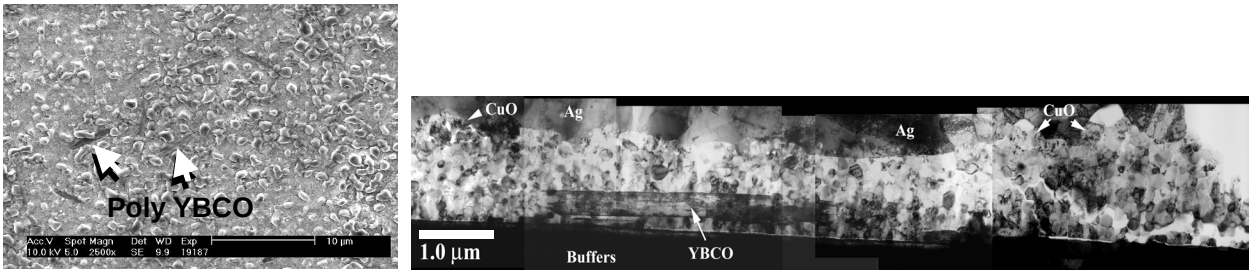

(a) (b)

Fig. 1.10. Images of a section of sample C (1-μm precursor on Ni-RABiTS™ converted under "high" water vapor partial pressure). (a) Surface SEM image, showing large CuO particles and a few randomly oriented YBCO areas. (b) Cross-sectional TEM image, showing CuO particles at the film surface and discontinuous *c*-axis YBCO growing from the substrate-film interface.

reduction in $P(H_2O)$ throughout the entire conversion process, was found to be black, with very few CuO particles visible on the film surface. Sectional critical currents of this sample are shown in Fig. 1.8, where it can be seen that portions of this tape attained a critical current value of 40 A (expected for a film on Ni-RABiTS™). In addition to the improved critical current, the high value seen at 180 min indicates that conversion time can be further reduced, even though the $P(H_2O)$ has been decreased. The significantly nonuniform critical current of the tape has been traced to small local texture variations in the buffer during deposition, a finding that emphasizes the advantage of further enhancement in substrate texture.

With a good handling of thicker precursor films, a 0.58-μm precursor was deposited on the remaining 1.15-m-long ORNL/AMSC Ni-3%W RABiTS™ in two passes (sample F). The sample was converted for 160 min by using the pull-through approach with various parameters listed in Table 1.1. It can be seen that $P(H_2O)$ in the final stages of conversion was lowered, the purpose of which was to reduce the extent of possible YBCO decomposition due to over-conversion. Following conversion, Ag deposition, and

oxygen annealing, the sample was placed in the 1-cm sectional apparatus for end-to-end and sectional critical-current measurements. The end-to-end current-voltage curve of sample F is shown in Fig. 1.11. It can be seen from this figure that with a voltage separation of 103 cm, a high end-to-end I_c of 85.6 A (J_c = 1.48 MA/cm^2) was obtained according to the 1-μV/cm criterion. Just as impressive are the 1-cm sectional measurements shown in Fig. 1.12, where the meter-long conductor is found to possess a mean I_c of 87.9 A (J_c = 1.52 MA/cm^2), maximum I_c of 96.9 A (J_c = 1.67 MA/cm^2), minimum I_c of 77.0 A (J_c = 1.33 MA/cm^2), and an SD of only 4.6%. The occurrence of two lower critical-current sections (marked by asterisks in Fig. 1.12) can be directly traced to scuffing of the buffer surface due to repeated winding and unwinding of the tape before precursor deposition. This high critical current and high critical current density result serves in establishing the basis that high current capacity YBCO can be fabricated by ex situ means in lengths.

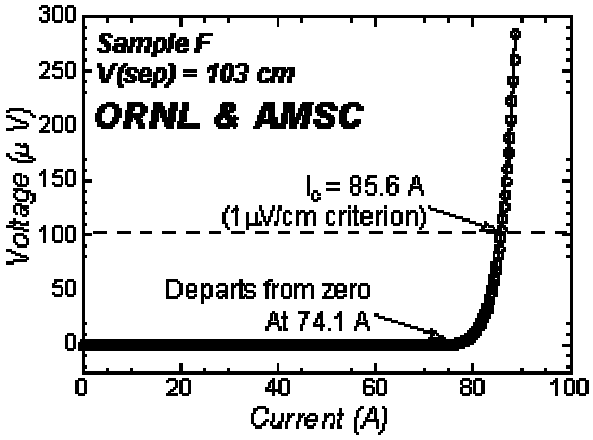

Fig. 1.11. End-to-end current-voltage curve of sample F (0.58-μm YBCO layer on a 1.15-m-long Ni-3%W RABiTS™ tape).

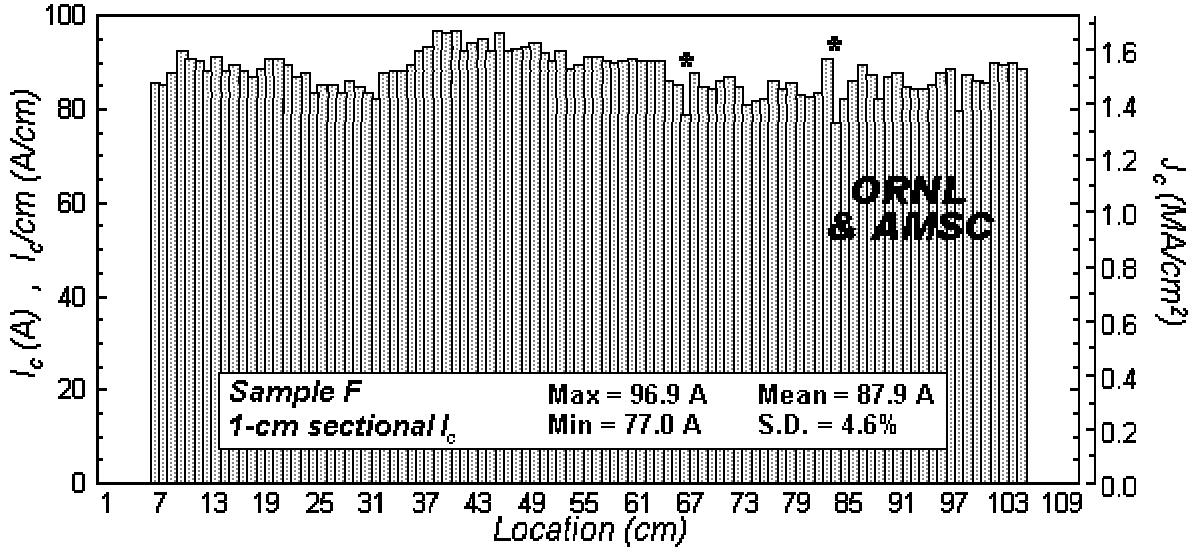

Fig. 1.12. Critical current and critical current density results for 1-cm sectional measurements of sample F. The asterisks mark two sections where the buffer surface was scuffed by repeated winding and unwinding of the tape before precursor deposition.

1.1.4 Long-Length Tapes of YBCO on a 0.82-μm Precursor

While exploring the processing details of thicker precursors, ORNL also developed the buffer deposition procedure for newly acquired commercial Ni-3%W tapes. The Ni-3%W RABiTS™ used in the next series of ex situ conversion experiments has the architecture 150Å CeO_2 (rf sputtered)/1500Å YSZ (rf sputtered)/150Å Y_2O_3 (e-beam)/1 μm Ni (dc sputtered)/50 μm Ni-3%W. Although a Y_2O_3 seed layer

can be epitaxially deposited directly on Ni-W alloys, the introduction of a Ni protective layer greatly reduces the possibility of local delamination of the buffers and therefore improves the consistency of the RABiTS™ (unpublished results). Also, this particular Ni-3%W RABiTS™ contains up to a few percent of randomly oriented components, the amount of which varies along the length of the tape. The origin of the random components had been traced to hardware issues during deposition of the protective nickel layer. This problem has since been resolved, and Ni-3%W RABiTS™ free of random components (according to XRD) is now being routinely fabricated at ORNL.

For the ex situ conversion of even thicker films, a 1.15-m-long section was cut from the Ni-3%W RABiTS™ containing random components, and BaF_2 precursor was deposited by e-beam in three passes. Averaged precursor thickness of this tape (sample G) was determined to be 0.82 mm by Rutherford backscattering spectroscopy (RBS). Sample G was converted in 200 min by using the pull-through approach with the following parameters: conversion temperature = 740°C, gas flow rate = 5.5 L/min per module, $P(O_2)$ = 160 mTorr, and $P(H_2O)$ of various modules are identical to those of sample F, and are listed in Table 1.1. Transport end-to-end and 1-cm sectional critical current measurements were performed on this sample following Ag deposition and oxygen annealing. The end-to-end current-voltage curve for sample G with voltage separation distance of 103 cm is shown in Fig. 1.13. As seen in the figure, this sample possesses a high end-to-end I_c of 92.0 A (J_c = 1.12 MA/cm^2) according to the 1-μV/cm criterion. Figure 1.14 shows the 1-cm sectional critical current of the entire tape, which has a mean I_c of 94.4 A (J_c = 1.15 MA/cm^2), maximum I_c of 102.2 A (J_c = 1.25 MA/cm^2), minimum I_c of 81.5 A (J_c = 0.99 MA/cm^2), and a very low standard deviation of 4.3%. Even with small amount of random components in the substrate, these current capacity values are considerable and further confirm that high-critical-current ex situ YBCO thick films can be processed in lengths.

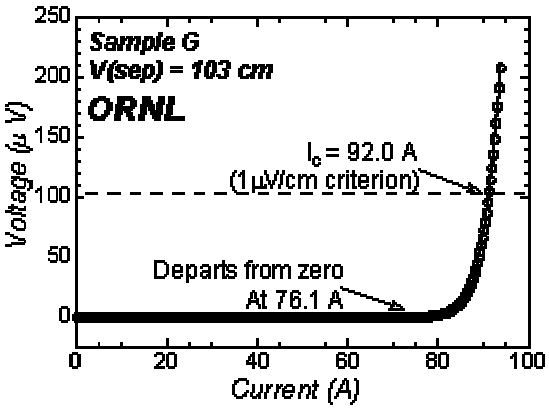

Fig. 1.13. End-to-end current-voltage curve for sample G (0.82-μm YBCO layer on a 1.15-m-long Ni-3%W RABiTS™ tape).

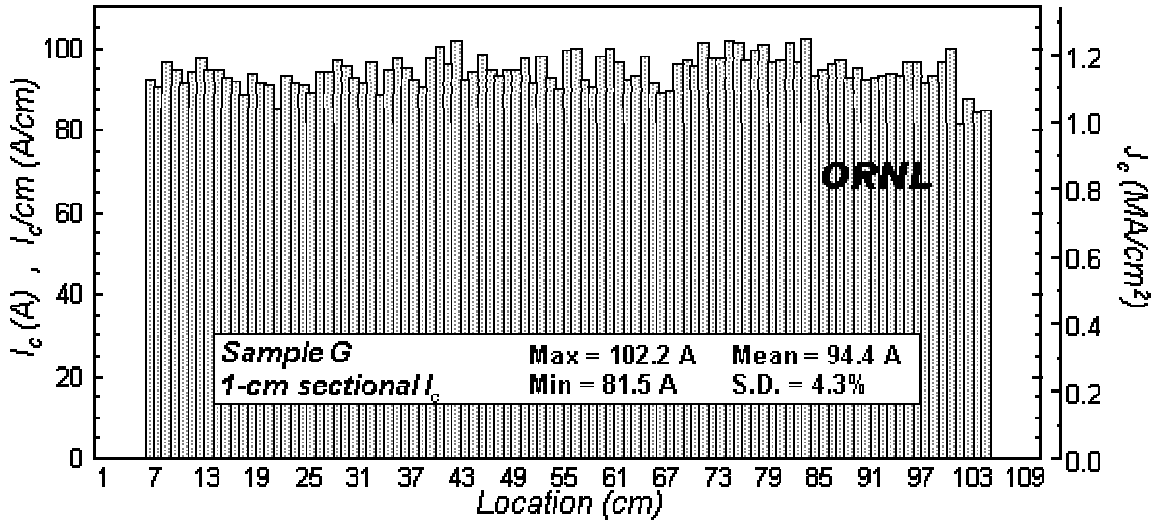

Fig. 1.14. Critical current and critical current density results of 1-cm sectional measurements along the entire length of sample G.

1.1.5 Summary

In this fiscal year, significant progress has been achieved in continuous reel-to-reel ex situ conversion of meter-length YBCO on RABiTS™. Uniform, high critical current density films of 0.3-μm thickness were obtained on commercial Ni as well as on new Ni-3%W RABiTS™. When the thickness of the BaF_2 precursor was increased, it was necessary to lower the $P(H_2O)$ to obtain thick YBCO films with high critical currents and critical current densities. In collaboration with industrial partner at AMSC, high-current-capacity tape was obtained with excellent transport uniformity on 0.58-μm-thick YBCO in meter lengths. Even higher critical current was obtained in a meter-long 0.82-μm-thick YBCO film on all-ORNL Ni-3%W RABiTS™ despite the presence of a small amount of randomly oriented components in the substrate. These results are summarized together with past performance in Fig. 1.15. It can be seen from the figure that with improved texture provided by the Ni-3%W template, a drastic enhancement of critical current density has been achieved. Concomitant with this enhancement is the improved critical current without significant degradation in critical current density, provided by thicker YBCO films. With further improvement in RABiTS™ texture and quality, and with refinements in conversion procedures and thicker YBCO films, significant contributions are expected to the realization of second-generation coated conductors in the coming years.

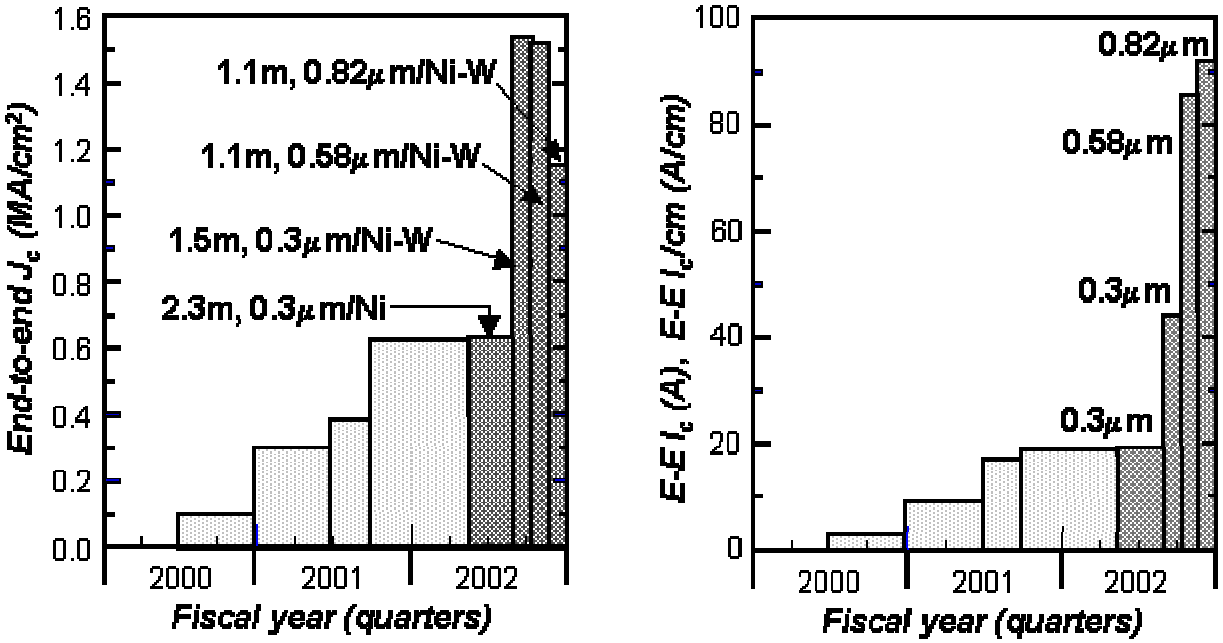

Fig. 1.15. Progress in the fabrication of meter-length YBCO-coated RABiTS™ tapes by the ex situ process.

1.1.6 References

1. D. F. Lee et al., "Issues and Progress Related to the Continuous ex situ BaF_2 Processing of Long-Length YBCO Coated Conductors, " in *Next Generation HTS Conductors*, A. Goyal, ed. (Plenum Publishing Corp., N.Y., 2003) to be published.
2. M. W. Rupich et al., "Low Cost Y-Ba-Cu-O Coated Conductors," *IEEE Trans. Appl. Supercond*. **11**(1) (2001) 2927.

3. V. F. Solovyov et al., "Kinetics of $YBa_2Cu_3O_7$ Film Growth by Postdeposition Processing," *App. Phys. Lett.* **76** (2000) 1911.
4. S. Annavarapu et al., "Progress Towards A Low-Cost Coated Conductor Technology," *Physica C* **341** (2000) 2319.
5. M. P. Siegal et al., "All Solution-Chemistry Approach for $YBa_2Cu_3O_{7-\delta}$ Coated Conductors," *App. Phys. Lett*. **80**(15) (2002) 2710.
6. O. Castano et al., "Epitaxial Nucleation and Growth of Buffer Layers and Y123 Coated Conductors Deposited by Metal-Organic Decomposition," *Physica C* **372** (2002) 806.
7. T. Araki et al., "Dip-Coated $YBa_2Cu_3O_{7-x}$ Film by Metalorganic Deposition using Trifluoroacetate," *Physica C* **372** (2002) 821.
8. D. F. Lee et al., "Alternative Buffer Architectures High Critical Current Density YBCO Superconducting Deposits on Rolling Assisted Biaxially-Textured Substrates," *Jpn. J. Appl. Phys. Lett Part II.* **38** (1999) L178.
9. D. F. Lee et al., "Long Length Conversion of Barium-Fluoride Precursor Films on RABiTS™," in Extended Abstract of the *2001 Int. Workshop on Superconductivity: Joint ISTEC/MRS Workshop,* June 2001, Honolulu, Hawaii.
10. D. F. Lee, "Continuous Processing of Coated Conductors," Presented at the 2001 DOE Superconductivity Program for Electric Systems Annual Peer Review, August 2001, Washington D.C.

1.2 STRENGTHENED Ni-W SUBSTRATES PRODUCED IN 35-M LENGTHS WITH SMOOTH SURFACES AND GOOD TEXTURE

M. Paranthaman, F. A. List, S. Sathyamurthy, T. Aytug, S. Cook, A. Goyal, and D. M. Kroeger

In an effort to produce long lengths of textured Ni-alloy substrates, a reel-to-reel annealing furnace was used to anneal Ni-W substrates. The 50-μm-thick, 1-cm-wide as-rolled Ni-W (3 at. %) tapes were cleaned in a recently developed reel-to-reel steam cleaner. After cleaning, about 35-m-long Ni-W substrates were loaded into a reel-to-reel continuous annealing furnace. (Fig. 1.16). Both ends of the Ni-W tape were electrically spot-welded to nickel leaders mounted on the two reels. The take-up reel was driven continuously by a stepper motor, and the pay-out reel was tensioned by a variable torque motor. The tapes were then annealed in the furnace, which had been preheated to 1200°C, in the presence of Ar/H_2 (4%). The flow rate of the Ar/H_2 (4%) gas purging the furnace was 2–4 L/min. The length of the hot zone was about 6 in. The travel speed of the tape was 60 cm/h. After the heat treatment, the tapes were spooled on the take-up reel.

The roughness measurements on the annealed Ni-W tape were done in a reel-to-reel laser reflectance and scattering unit. The unit and data are shown in Fig. 1.17. The average roughness is about 9.57 nm, typical for a very good textured substrate produced at ORNL. A reel-to-reel X-ray four-circle diffractometer was used to measure the texture of the tape at one position (1770 cm). The

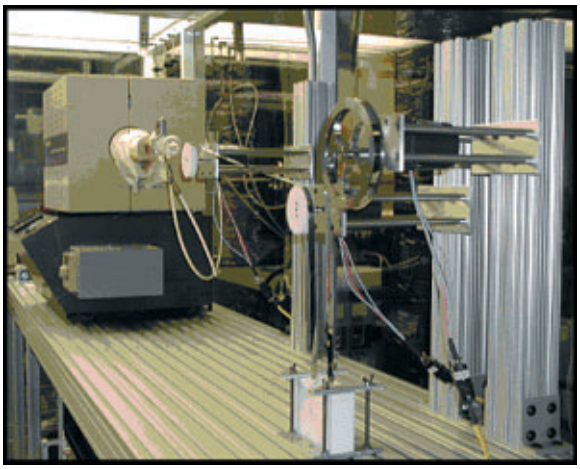

Fig. 1. 16. The ORNL reel-to-reel continuous annealing unit.

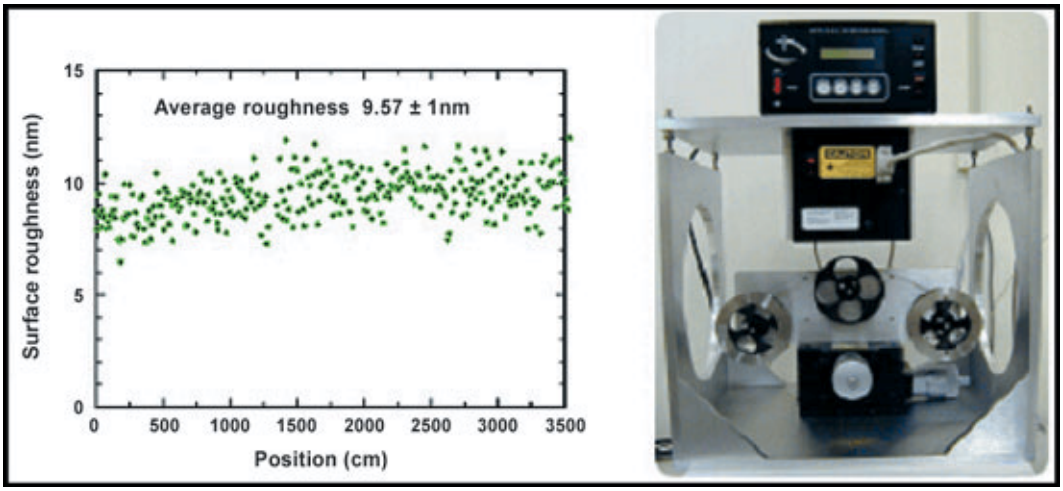

Fig. 1.17. Surface roughness data on the 35-m annealed Ni-W tape. Also shown is the reel-to-reel laser reflectance and scattering unit that was used to perform the measurements.

FWHM values for the Ni (002) omega scan was about 5.83° and for the Ni (111) phi scan was about 6.86°. The Ni (111) phi scan is shown in Fig. 1.18. To conclude, the capability was established to anneal substrates with fairly good texture in long lengths.

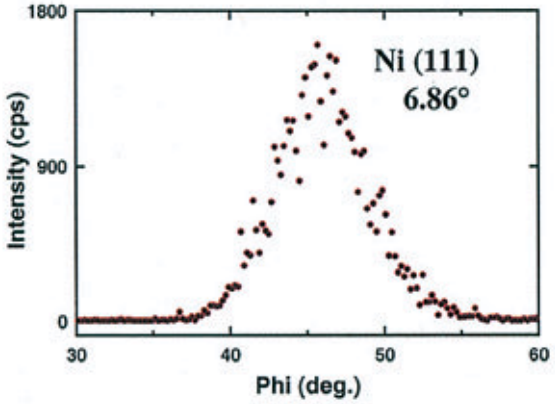

Fig. 1.18. Ni(111) phi scan for the annealed Ni-W tape at position 1770 cm.

1.3 SINGLE BUFFER LAYER TECHNOLOGY FOR YBCO COATED CONDUCTORS

M. Paranthaman, T. Aytug, H.-Y. Zhai, H. M. Christen, S. Sathyamurthy, P. M. Martin, and D. K. Christen (ORNL); R. E. Erickson and C. L. Thomas (3M)

In continuation of an effort to develop a single buffer technology, ORNL recently investigated the viability of lanthanum strontium manganate, $La_{0.7}Sr_{0.3}MnO_3$ (LSMO), buffer layer due to its electrical conductivity, good thermal stability, and structural compatibility with YBCO. A critical current density of 5×10^5 A/cm^2 at 77 K was obtained on YBCO films epitaxially grown on LSMO-buffered Ni substrates. The transition temperature, T_c, was also suppressed to 87 K. Secondary ion mass spectrometer (SIMS) depth-profile analyses on the YBCO/LSMO/Ni indicated the contamination of YBCO layers with Sr from LSMO layers. The diffusion of Ni through LSMO was contained at the LSMO/Ni interface. Hence, LSMO films can be used as a good diffusion barrier layer. The above observation suggests that an undoped $LaMnO_3$ (LMO) film should act as a good buffer layer if it can be made. Hence, LMO was chosen as a potential single buffer layer for this study.

The structure of LMO is shown in Fig. 1.19. The ideal perovskite structure has the cubic unit cell of Fig. 1.19 with space group Pm3m. Figure 1.19 shows the corner-sharing octahedral units (MnO_3 array in

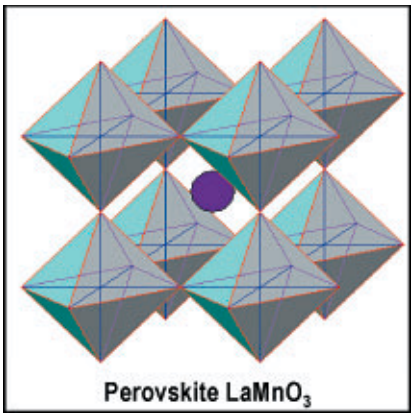

Fig. 1.19. The structure of LMO.

LMO) that form the stable skeleton of the structure. The La cation occupies the body-center position. The geometric tolerance factor $t \equiv$ (La-O)/$\sqrt{2}$ (Mn-O) is a measure of the mismatch between the equilibrium (La-O) and (Mn-O) bond lengths of an LMO perovskite. The ideal cubic structure should have $t = 1$. The perovskite structure occurs only within the range $0.75 < t < 1.00$. Accommodation to a $t < 1$ is accomplished by a cooperative rotation of the corner-shared $MnO_{6/2}$ octahedra, which bend the Mn-O-Mn bond angles to (180°-ϕ). Rotations about the cubic [111] axis give rhombohedral symmetry with bending angle ϕ_R, and rotations about the cubic [110] axis give orthorhombic symmetry with mean bending angle $\phi_O > \phi_R$.

LMO is an antiferromagnetic insulator. It is orthorhombic with lattice parameters a = 5.533 Å, b = 5.722 Å, c = 7.694 Å. The pseudocubic lattice parameter of 3.91 Å is closely matched to that of YBCO. The lattice mismatch of LMO with YBCO is less than 2.50%. In the LMO perovskites, a cooperative Jahn-Teller ordering of the occupied e orbitals at the Mn (III):t^3e^1 ions removes the e-orbital degeneracy and lowers the c:a ratio of the orthorhombic structure.

Biaxially textured Ni and Ni-W (3%) substrates were obtained by mechanically deforming metal rods by more than 95%, followed by annealing at 1100 to 1300°C for 1 h in the presence of Ar/H_2 (4%) gas. The substrates were typically 5 mm wide and 50 μm thick. Prior to annealing, the substrates were cleaned by sonification in isopropanol. Radio-frequency magnetron sputtering and oxide targets were used to deposit the LMO layers. The sputter targets, made from single-phase LMO powders prepared by a solid-state reaction, were loosely packed into a 4-in. copper tray. Typical sputter conditions consisted of 2–5 × 10^{-5} Torr of H_2O and a total pressure of 3 mTorr forming gas (Ar/H_2 4%). The LMO films were grown at a substrate temperature of 575 to 625°C. The water pressure was sufficient to oxidize the film to form stoichiometric LMO. The forming gas was used to reduce any oxide present at the substrate surface during film growth. The LMO film thickness varied from 600 to 3000 Å.

Pulsed laser deposition (PLD) was used to deposit YBCO films on the LMO buffers. During YBCO deposition, substrates were maintained at 780ºC and 120 mTorr of O_2. Typical YBCO film thickness was 2000 Å. The films were analyzed by XRD techniques. SEM micrographs were taken using a Hitachi S-4100 field emission microscope. The thickness and composition of both LMO and YBCO films were determined by RBS. The resistivity and transport critical current density were measured by using a standard four-probe technique. The voltage contact spacing was 0.4 cm. The 1-μV/cm criterion was used to calculate critical-current-density values. SIMS depth-profile analyses were made to determine the nature of the substrate/buffer and buffer/YBCO interfaces.

A typical θ-2θ scan for a 3000-Å-thick LMO film on a Ni (100) substrate is shown in Fig. 1.20. The strong LMO (00*l*) signal revealed the presence of a good out-of-plane texture. A typical RBS spectrum for a 3000-Å-thick LMO film on a Ni (100) substrate

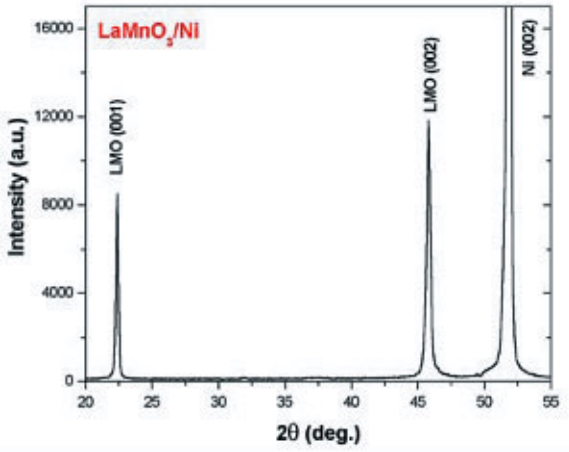

Fig. 1.20. A typical θ-2θ scan for a 3000-Å-thick LMO film on biaxially textured Ni substrates.

is shown in Fig. 1.21. The simulation studies indicate the stoichiometry of La:Mn ratio to be 1:1. As shown in Fig. 1.22, the XRD results from ω and ϕ scans for a 2000-Å-thick YBCO film on $LaMnO_3$/Ni revealed good epitaxial texturing. The FWHM values for Ni (002), LMO (002), and YBCO (005) are 9.0°, 10.3°, and 10.7°, respectively, and those of Ni (111), LMO (111), and YBCO (102) are 9.3°, 10.4°, and 9.2°, respectively. Similarly, textured YBCO/LMO layers were grown on biaxially textured Ni-W substrates. SIMS depth-profile analyses for a 2000-Å-thick YBCO film on 3000-Å-thick LMO-buffered Ni substrates are shown in Fig. 1.23. As can be seen at the YBCO/LMO interface, there is no diffusion of cations into the superconductor. The interface is sharp and very clean. The interface between the Ni and LMO is also clean, proving that there is no diffusion of Ni into the buffer layer. Hence, the LMO buffer layer is shown to be an excellent diffusion barrier for Ni. LMO also provides a very good template for growing high-quality YBCO films.

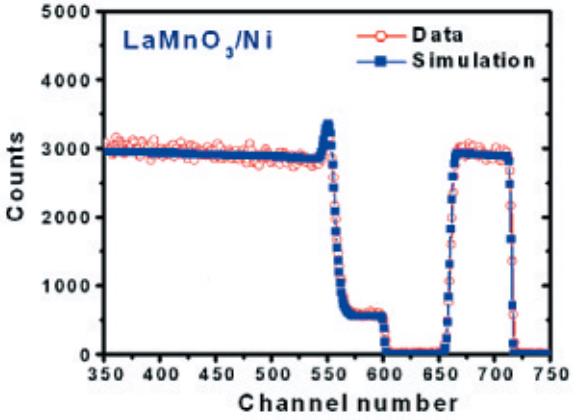

Fig. 1.21. RBS of LMO on Ni (100) substrates.

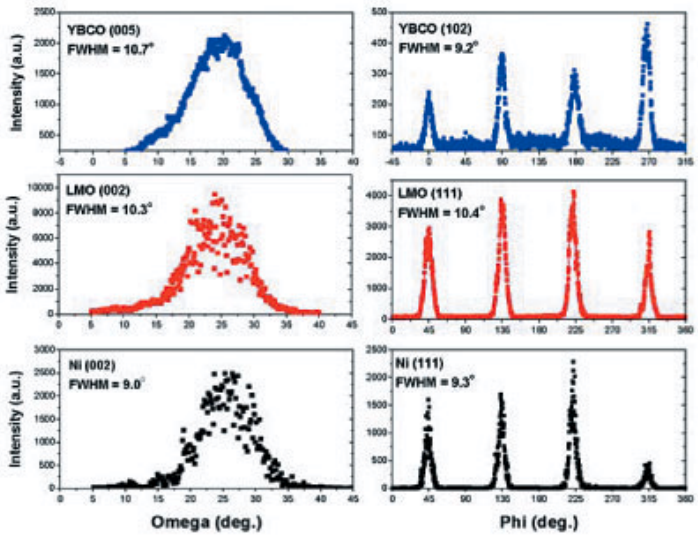

Fig. 1.22. The ω and ϕ scans for a 2000-Å-thick YBCO film on 3000-Å-thick LMO-buffered Ni substrates.

SEM micrographs for a 3000-Å-thick LMO film and a 2000-Å-thick YBCO film on LMO-buffered Ni substrates are shown in Fig. 1.24. As can be seen from Fig. 1.24(a), the Ni grain boundary is very well covered by the LMO layer. The LMO layers are smooth, dense, continuous, and crack-free. The microstructure of the YBCO surface is also dense but with some oxide particles present at the surface [Fig. 1.24(b)]. These features are typically observed in all PLD films. The field dependence of critical current density for YBCO films on LMO-buffered Ni and Ni-W substrates is shown in Fig. 1.25. A zero-field critical current density of 1.0 MA/cm^2 at 77 K was obtained on YBCO films grown on LMO-buffered Ni substrates. A zero-field critical current density of 1.2 MA/cm^2 at 77 K for a 2000-Å-thick YBCO film on 60-nm-thick $LaMnO_3$-buffered Ni-W substrate was obtained. The critical current density at 0.5 T was about 20% of the zero-field critical current density, indicating the presence of a strongly linked YBCO film. Thus, for the first time it has been demonstrated that a YBCO film having a high critical current density can be grown on just a 60-nm-thick LMO layer on a single-buffered Ni-W substrate.

In summary, the growth of high-quality YBCO films with a critical current density of more than 1 MA/cm^2 at 77 K and self-field on LMO/Ni or Ni-W substrates has been demonstrated. Magnetron sputtering was used to grow the LMO layers directly on both Ni and Ni-W substrates. It should be possible to scale up the single-buffer-layer technology to produce long lengths of coated conductors.

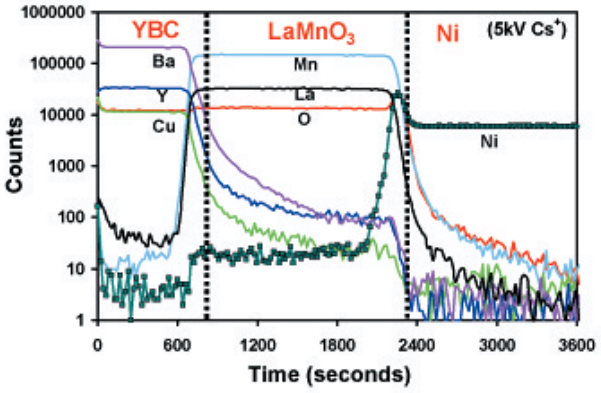

Fig. 1.23. SIMS depth-profile analyses for a 2000-Å-thick YBCO film on 3000-Å-thick LMO-buffered Ni substrates.

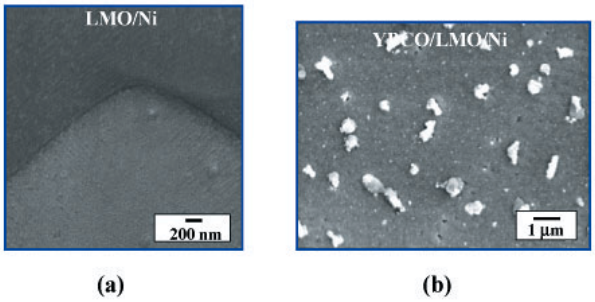

Fig. 1.24. SEM micrographs for (a) 3000-Å-thick LMO film on Ni (100) substrates, indicating the presence of a crack-free and smooth microstructure, and (b) 2000-Å YBCO film on LMO-buffered Ni substrates.

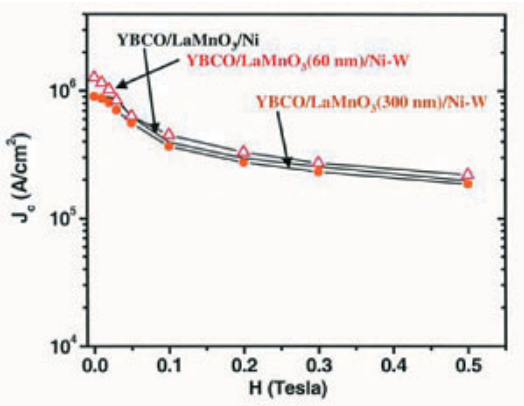

Fig. 1.25. The field dependence of the transport current density for a 2000-Å-thick YBCO film on LMO-buffered Ni and Ni-W substrates.

1.4 ALL-SOLUTION FABRICATION OF Gd_2O_3 BUFFER LAYERS ON BIAXIALLY TEXTURED METAL TAPES FOR YBCO COATED CONDUCTORS

T. Aytug, M. Paranthaman, S. Sathyamurthy, D. B. Beach, C. E. Vallet, C. Cantoni, S. Kang, and D. K. Christen

Recently, good superconducting performance has been demonstrated in continuously processed HTS coated conductors based on RABiTS™. The RABiTS™ technique utilizes the biaxial texture of a metal substrate produced by thermomechanical processing as a template for the epitaxial deposition of one or more buffer layers. These buffer layers then provide a structural template and a chemical barrier for the subsequent epitaxial growth of an HTS coating. To date, buffer-layer studies have focused on multilayers. Generally, deposition of a complete buffer-layer sequence involves a combination of vacuum deposition techniques and exposure of samples to multiple intermediate thermal cycles and ambient environments. These requirements adversely affect the structural and chemical integrity of all individual sublayers and increase the overall complexity of the process. To overcome these difficulties, it is important to develop a single buffer layer that can be fabricated by an easily scalable processing technique. Nonvacuum processes based on chemical solutions, such as sol-gel and MOD, offer many desirable aspects, such as precise control of metal-oxide precursor stoichiometry and composition, mechanical simplicity, and low cost. Recently, it has been reported that various RE_2O_3 (rare-earth; RE = Gd, Yb, and Eu) and $RE_2Zr_2O_7$ (RE = La and Nd) oxide films can grow epitaxially on textured Ni substrates by solution-based methods. Hence, if a single buffer layer based on such materials can be deposited by using a solution approach, it would significantly decrease the processing time and would make the process simpler and more conducive to scaleup to long lengths.

A 2-methoxyethanol solution of gadolinium methoxyethoxide/acetate, prepared by an alkoxide sol-gel synthesis route, was used to coat the Ni tapes. The solution preparation was carried out under an argon

gas atmosphere in a Schlenck-type apparatus. The as-received gadolinium acetate powder was purified to avoid premature hydrolysis, which can induce precipitation. It was purified by dissolving it in a mixture of water and acetic acid at a ratio of 3 to1, filtering, and then evaporating to dryness in an oven maintained at 150°C overnight to remove absorbed moisture. Then the purified gadolinium acetate (about 3.34 g) was dissolved in 40 mL of 2-methoxyethanol in a 250-mL round-bottomed flask. The flask was refluxed for 1 h with an excess of 2-methoxyethanol to exchange the acetic acid ligand with the methoxyethoxide ligand. The final volume was adjusted to 40 mL to produce a 0.5-M Gd_2O_3 precursor solution. The metal substrates were coated with Gd_2O_3 film by spin coating the precursor solution at 2000 rpm for 30 s, followed by annealing at temperatures ranging from 1100 to 1150°C for 1 h in an Ar-4%H_2 atmosphere. The thicknesses of the buffer layers were varied by repeating the coating process up to three times.

The quality of the all-solution Gd_2O_3/Ni structure was then assessed. A XeCl excimer laser system operated with energy density of about 4 J/cm^2 was used to deposit YBCO films by PLD. Typical YBCO film thicknesses were 200 nm. A standard four-point contact technique was applied to measure the superconducting critical temperature and critical current density of the YBCO films. For short samples, the distance between voltage contacts was 4 mm and the critical currrent density values were assigned at a 1-μV/cm criterion. Silver electrical contacts were deposited onto the samples by dc-magnetron sputtering followed by an annealing in 1-atm O_2 for 30 min at 500°C.

Figure 1.26 shows the XRD θ-2θ spectrum of each coat of a typical Gd_2O_3 multicoated film on a textured Ni substrate processed at 1120°C. The increase in the thickness of the samples after each coat was about 150 Å. At a first glance, the presence of only (00*l*) reflections may indicate that for each coat, Gd_2O_3 is oriented with its *c*-axis normal to the plane of the substrate. Even though this may be true for the first and second coat samples, the relative increase of the (004) peak intensity after the third coat was not as high as the increase that was observed after the second coat, implying substantial deterioration in the crystalline quality of the Gd_2O_3 films after the third coat. To investigate this issue, plan-view SEM studies and reflection high-energy electron diffraction (RHEED) analyses were performed on each sample. Figure 1.27 shows the surface morphologies of the one-, two-, and three-coat samples. Although each sample exhibits a crack-free surface morphology, significant surface roughening develops for the two- and three-coat samples. After the second coat, sparsely distributed white features were observed on the surface, which correspond to the randomly oriented Gd_2O_3 grains [Fig. 1.27(b)]. This morphology indicates that the single crystalline orientation of the films gradually changed to polycrystalline. After the third coat, the surface of the samples becomes rougher and the porosity increases [Fig. 1.27(c)]. In fact, this growth behavior can clearly be seen from the RHEED patterns for the same samples [see Fig. 1.27(d), (e), and (f)]. While the single-coat Gd_2O_3 layer exhibits well-defined spots, indicating high crystalline quality (00*l*) orientation, the two-coat sample shows a mixture of spots along with the ring components, implying evolution of polycrystalline Gd_2O_3 components on the surface. After the third coat, the surface of the sample displays entirely polycrystalline growth characteristics. Figure 1.28 shows the atomic-force microscopy (AFM) pictures of the surface of Gd_2O_3 one-, two-, and three-coat samples. As the thickness

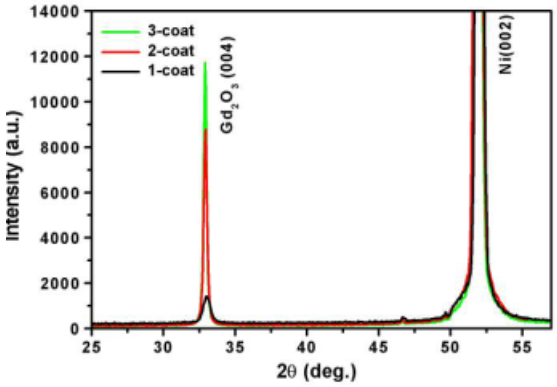

Fig. 1.26. Typical θ-2θ scans for one-, two-, and three-coat layers of Gd_2O_3 on textured Ni substrates.

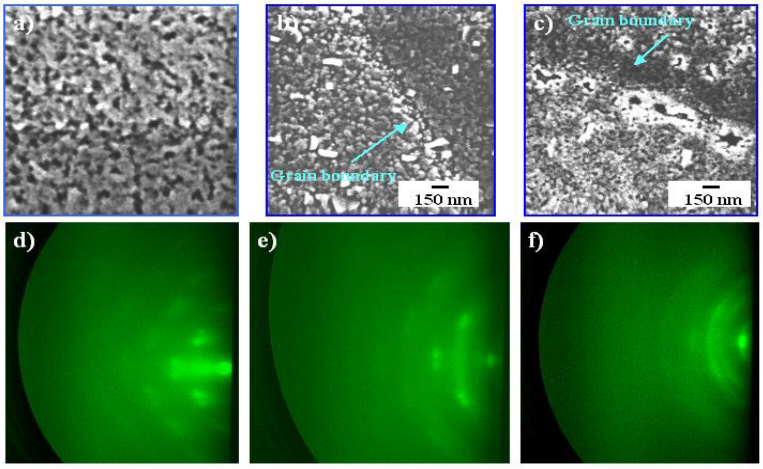

Fig. 1.27. SEM micrographs (a, b, and c) and RHEED images (d, e, and f) for one-, two-, and three-coat layers of Gd_2O_3 on textured Ni substrates.

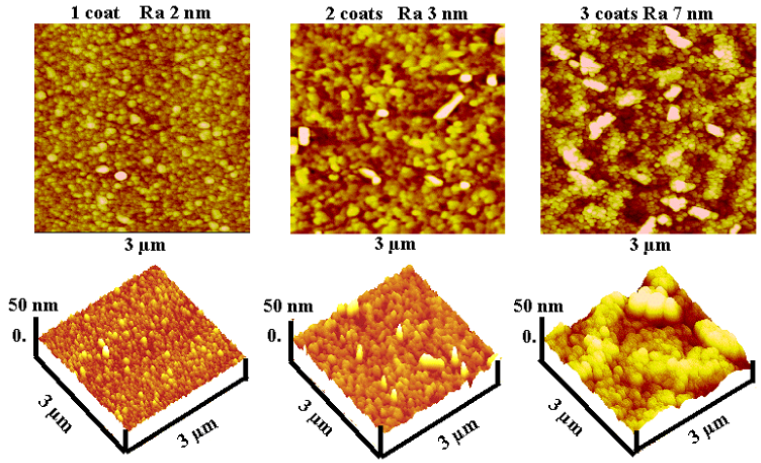

Fig. 1.28. AFM scans on the surface of one-, two, and three-coat layers of Gd_2O_3 on textured Ni substrates.

increased, the surface roughness also increased, from 2 nm for one coat, to 3 nm for two coats, and to 7 nm for three coats.

Because the qualifying test for any coated conductor buffer-layer structure is compatibility with the YBCO coatings, electrical transport and superconducting property measurements were conducted on the same samples. The results of measuring critical current and voltage characteristics for the YBCO films grown on a one-coat (15-nm) and two-coat (35-nm) Gd_2O_3 layers are plotted in Fig. 1.29. The results show that both transition temperature and critical current density improve as the thickness of the buffer layer increases from one coat to two coats. Specifically, the critical current densities of YBCO films deposited on one- and two-coat Gd_2O_3 layers are 150 and 250 KA/cm^2, respectively, and the transition temperature values are 85 and 87 K, respectively. However, the YBCO films grown on the three-coat samples did not have superconducting properties. It is well documented that Ni impurities in the superconducting structure can significantly reduce critical current density and transition temperature. The low critical current density and transition temperature of the three-coat samples most likely result from the combination of Ni diffusion through the thin Gd_2O_3 layers into the YBCO and surface degradation of the Gd_2O_3 as the film thickness increased.

In summary, solution deposition has been used to deposit epitaxial Gd_2O_3 films on textured Ni substrates. The Gd_2O_3 films have been used as a single buffer layer for deposition of YBCO by PLD on these metal substrates. The surface property characterizations of Gd_2O_3 layers revealed deterioration of the surface microstructure as the thickness increased. From the superconducting property characterizations, the critical current density and transition temperature of the YBCO films were found to slightly increase with an increase in Gd_2O_3 thickness up to 350 Å. For thicker Gd_2O_3 layers, the YBCO exhibited nonsuperconducting properties.

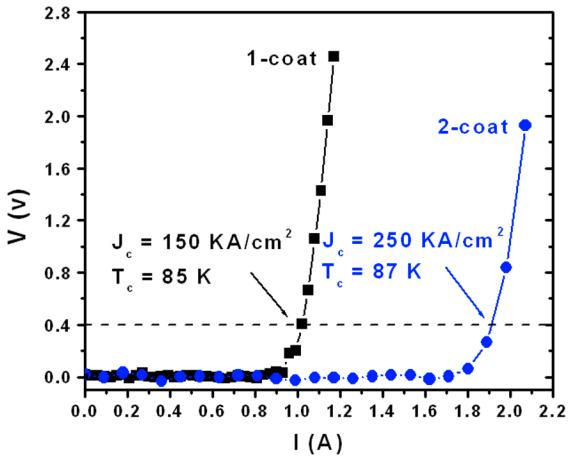

Fig. 1.29. Current-voltage plot for 0.2-µm-thick, PLD-grown YBCO films on one- and two-coat layers of Gd_2O_3.

1.5 LANTHANUM ZIRCONATE: A SINGLE BUFFER LAYER PROCESSED BY SOLUTION DEPOSITION FOR COATED CONDUCTOR FABRICATION

S. Sathyamurthy, M. Paranthaman, H-Y. Zhai, H. M. Christen, P. M. Martin, and A. Goyal

To date, in the processing of high-current coated conductors on RABiTS™, the best reproducible results have been obtained by using two- or three-layer buffer architectures (e.g., CeO_2/YSZ/CeO_2/Ni). There are several reasons why a simpler architecture might be desirable. Typically, deposition of the buffer layer stack involves a combination of vacuum and nonvacuum deposition techniques coupled with the exposure of the samples to thermal cycling and the ambient environment. These requirements could lead to the degradation of the individual buffer layers and could add to the complexity and cost of the overall process. However, if a single buffer layer deposited by a scalable technique were developed, it might significantly decrease processing time and make the process simpler and more conducive to scale-up to long lengths.

The results of using a single lanthanum zirconate [$La_2Zr_2O_7$ (LZO)] buffer layer deposited by sol-gel processing for YBCO coated conductors are reported here. LZO has a cubic pyrochlore structure with a close lattice match with YBCO. Chemical solution deposition techniques have evolved as potentially low-cost, nonvacuum processes for fabrication of long lengths of coated conductors. Flexible metal substrates with a biaxial texture offer an ideal template for these solution processes. Typically, this process involves coating the substrates with a metal-organic precursor solution at room temperature followed by a high-temperature annealing to obtain highly crystalline phases. This process offers precise control of composition and stoichiometry and can yield uniform homogeneous films.

The precursor solution for the deposition of LZO films was prepared by refluxing a stoichiometric mixture of lanthanum isopropoxide and zirconium n-propoxide in 2-methoxyethanol in a Schlenk-type apparatus. A cation concentration of 0.25 M was used throughout this work. As-rolled tapes of Ni and Ni-1.7%Fe-3%W (Ni-W) were cleaned by ultrasonication in isopropanol. The tapes were then annealed in a reducing (Ar-4%H_2) atmosphere for 1 h at 1100°C for Ni and 1300°C for Ni-W to get the desired cube texture. The metal substrates were coated with LZO film by spin coating the precursor solution at 1000 rpm for 30 s, followed by annealing at 1100°C for 1 h in Ar-4%H_2. The process was repeated to get a thicker coating of the buffer layer. PLD at 780°C in 120 mTorr oxygen with an average laser energy of 200 mJ was used to deposit YBCO films on the LZO-buffered metal tape. XRD was used to characterize the phase purity and texture of the samples, and SEM was used to monitor the microstructures of both LZO and YBCO. A standard four-point probe technique was used to measure resistivity and transport critical current density. RBS was used to measure the thicknesses of the LZO and the YBCO films.

The θ-2θ XRD pattern of each coat of a typical LZO multicoated film on a textured nickel and Ni-W substrate indicated the presence of a strong (400) reflection. A small amount of randomly oriented LZO [the (222) reflection in the XRD pattern] was detected in films obtained by three coating/annealing cycles. Therefore, thicker films were not investigated further. Texture measurements were made on these samples by using a four-circle diffractometer; typical values obtained are tabulated in Table 1.2. On a

Table 1.2. Out-of-plane texture (Δω) and in-plane texture (Δϕ) of LZO and YBCO on textured Ni and textured Ni-W substrates

	Δω (degrees)		Δϕ (degrees)	
	Ni	Ni-W	Ni	Ni-W
Uncoated	7.73	5.98	9.2	7.98
LZO (one coat)	7.61	5.93	8.96	8.21
LZO (three coats)	7.72	6.25	9.6	8.4
YBCO	5.96	6.99	10.4	11.1

nickel substrate with an out-of-plane texture of 7.73° and an in-plane texture of 9.2, the LZO shows an out-of-plane texture of 7.61° and an in-plane texture of 8.96° after one coat, and 7.72, and 9.6°, respectively, after three coats. Thus, the texture of the LZO films was as good as that of the nickel tape, showing only a slight deterioration after three coats, which is consistent with the observations based on the θ-2θ patterns. Similarly, on the Ni-W substrates with an out-of-plane texture of 5.98° and an in-plane texture of 7.98°, the LZO showed an out-of-plane texture of 5.93° and an in-plane texture of 8.21° after one coat, increased slightly to 6.25° and 8.4°, respectively, after three coats. SEM micrographs of the multiple coats of LZO film on textured nickel and Ni-W show that each coat of the LZO film had a smooth surface with a dense, fine-grained microstructure. According to RBS results, the LZO layer had a thickness of 500 Å, and the ratio of lanthanum to zirconium was found to be close to 1.

A typical θ-2θ XRD pattern obtained from YBCO deposited on LZO (three coats) buffered nickel substrate is shown in Fig. 1.30. Apart from good *c*-axis texturing of the YBCO, Fig. 1.30 also shows that no detectable amount of nickel oxide formed during the YBCO deposition. This finding suggests that LZO can act as a diffusion barrier to prevent nickel oxidation. Texture measurements on the YBCO were performed by using a four-circle X-ray diffractometer. The out-of-plane and in-plane textures of the YBCO were found to be 5.96° and 10.4°, respectively, on nickel substrates and 6.99° and 11.1°, respectively, on the Ni-W substrates (see Table 1.2). An SEM image showing the microstructure of YBCO on LZO buffered nickel is shown in Fig. 1.31. It is evident from this figure that the YBCO has a dense microstructure similar to that normally observed for PLD-grown YBCO on single-crystal substrates and metal substrates with a three-layer buffer architecture. The YBCO/LZO/Ni samples were analyzed for composition and thickness of the different layers by RBS. The results of this analysis are given in Fig. 1.32. From this analysis it was found that the YBCO film thickness is 2500 Å with a Y:Ba:Cu stoichiometry close to 1:2:3 and that the LZO film thickness is 500 Å with a La:Zr ratio close to 1:1. A good match between the simulation and the data, especially at the nickel surface, suggests that there is no significant oxidation or diffusion of the nickel into the LZO film and is consistent with the XRD results. The field dependence of the critical current density of YBCO on LZO buffered nickel substrates measured by a four-point probe is given in Fig. 1.33. Figure 1.33 compares the performance of the YBCO on all-solution buffered nickel to that of the YBCO on conventional three-layer

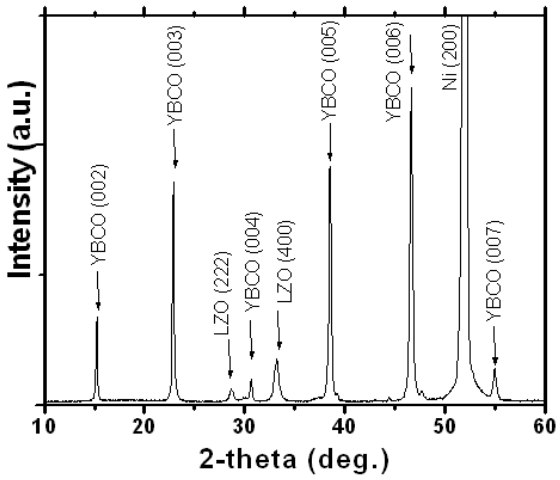

Fig. 1.30. A typical θ-2θ XRD pattern of YBCO/LZO/Ni shows the good *c*-axis texture of YBCO and the absence of NiO phase.

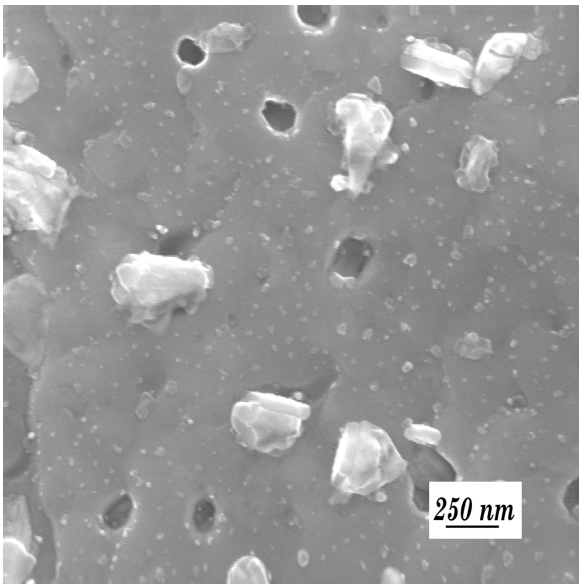

Fig. 1.31. SEM image showing the microstructure of PLD-grown YBCO on LZO-buffered Ni showing good density of the YBCO layer.

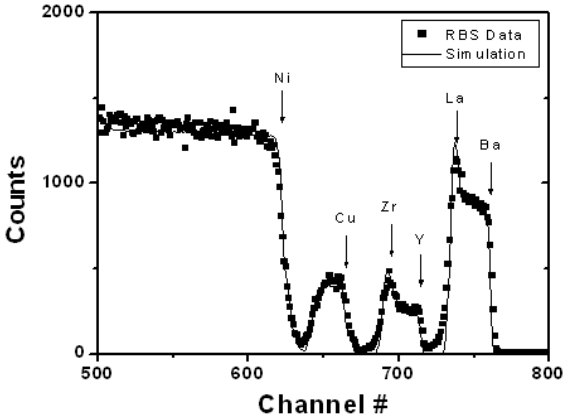

Fig. 1.32. RBS analysis of YBCO/LZO/Ni. The spectrum was measured with 5-MeV He^{2+} ions at near normal incidence and detected at a scattering angle of 160°.

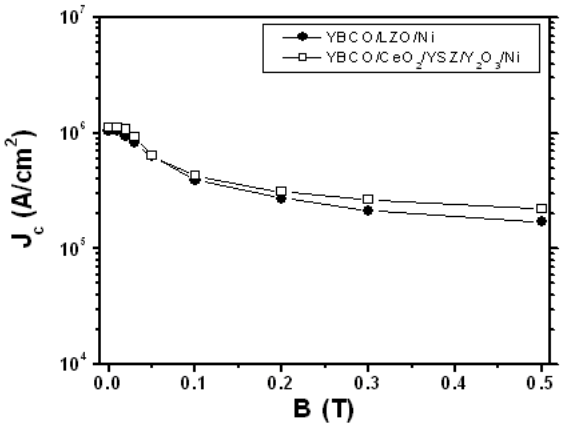

Fig. 1.33. Field dependence of critical current density for YBCO on all-solution LZO-buffered Ni substrate compared with that of YBCO on conventional $CeO_2/YSZ/Y_2O_3$ buffered nickel.

buffers ($CeO_2/YSZ/Y_2O_3$/Ni). A critical current density of 1.1 MA/cm^2 was obtained on YBCO films deposited on all-solution LZO buffered Ni substrate. Figure 1.33 also shows that the performance of the all-solution buffer is comparable to that of the standard three-layer buffers ($CeO_2/YSZ/Y_2O_3$/Ni).

To understand the effect of the buffer layer thickness on the performance of the YBCO films, textured Ni-W substrates were coated with one, two, and three coats of LZO films corresponding to thickness values of 150, 300, and 500 Å. YBCO films were deposited on these samples by PLD, and the transition temperatures and critical current densities of the samples were measured. These results, plotted in Fig. 1.34, show that both the transition temperature and critical current density improve as the thickness of the buffer layer increases. However, no difference in the texture or the microstructure was observed among the samples. With very thin LZO films as buffer layers, some nickel diffusion may be taking place, which could lead to a depression of transition temperature and critical current density while not affecting the texture or the microstructure of the samples. However, with a 500-Å LZO buffer layer, the Ni-W substrates gave a critical current density of 0.83 MA/cm^2 (as compared with the 1.1 MA/cm^2 measured for YBCO deposited on the Ni substrate). The critical current density values obtained on the Ni-W substrates were found to be slightly lower than those obtained on nickel substrates. This may imply that the PLD deposition conditions are not yet optimized for the Ni-W alloy substrates. For example, the higher stiffness of the Ni-W alloy substrates may prevent them from making as good a thermal contact with the heater surface as the Ni substrates during the PLD. Further studies are under way to overcome this issue.

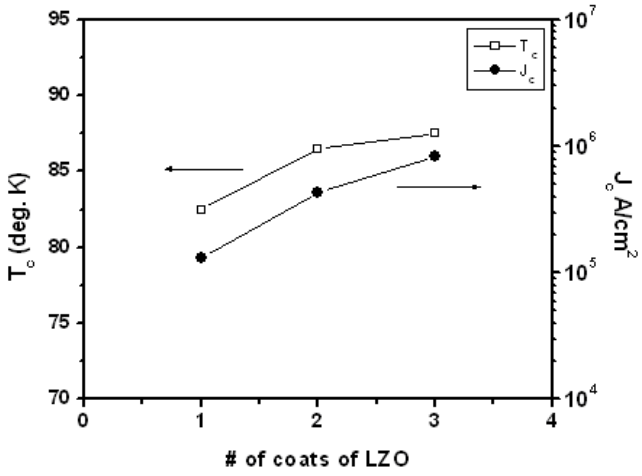

Fig. 1.34. Variation of transition temperature and critical currrent density of YBCO on LZO-buffered Ni-W as a function of the thickness of the LZO layer. Each coat of the LZO layer is about 150 Å.

In conclusion, solution deposition has been used to deposit epitaxial LZO films on both textured Ni and Ni-W substrates. LZO films have been used as single buffer layers for deposition of YBCO by PLD on these metal substrates. Critical current densities greater than 1 MA/cm^2 and 0.83 MA/cm^2 have been measured for the Ni and Ni-W substrates, respectively. The properties of these samples are similar to YBCO deposited on textured nickel with the standard three-layer buffer architecture. These results offer the promise of a scalable process for solution deposition of a single-layer buffer on long lengths of substrates to be used for coated conductor fabrication.

1.6 SINGLE BUFFER LAYERS OF LMO OR LSMO FOR THE DEVELOPMENT OF YBCO COATED CONDUCTORS: A COMPARATIVE STUDY

T. Aytug, M. Paranthaman, H. Y. Zhai, H. M. Christen, S. Sathyamurthy, and D. K. Christen (ORNL); R. E. Ericson (3M)

Potential applications of HTS coated conductors involve the efficient production, distribution, and storage of electrical power. Ideally, conductive-oxide buffer layers are preferred for these applications because they can provide electrical coupling between the thin HTS layer and the thick underlying metal substrate, thereby improving the electrical and thermal stability of the structure against a transient to the dissipative regime. To date however, the buffer layers that have been developed have comprised insulating oxides and multilayers. High-quality YBCO films have been grown reproducibly on the RABiTS™ standard architecture of CeO_2/YSZ/CeO_2/Ni. Development of conductive-oxide buffer layers on RABiTS™ has begun recently with the demonstration of an epitaxial $SrRuO_3$/$LaNiO_3$ bilayer structure on Ni tapes. The YBCO coatings deposited on the $SrRuO_3$/$LaNiO_3$/Ni architecture exhibited good electrical connectivity over the entire structure and yielded values for critical current density (at 77 K, self-field) exceeding 1.2×10^6 A/cm^2.

The fabrication of these multilayered buffer architectures presents major challenges. Generally, deposition of a complete buffer-layer sequence involves a combination of vacuum-deposition techniques and exposure of samples to multiple intermediate thermal cyclings and the ambient environment. These requirements adversely affect the structural and chemical integrity of all individual sublayers and increase the overall process complexity. To overcome these difficulties, it is important to develop a single buffer layer, ideally conductive, that can be fabricated by an easily scalable deposition technique. Recently, the viability of the doped rare earth manganate compound, $La_{0.7}Sr_{0.3}MnO_3$ (LSMO) was investigated as a buffer layer for YBCO coated conductors, due to its electrical conductivity, good thermal stability, and structural compatibility with YBCO. In that study, YBCO films deposited on highly textured LSMO buffer layers on Ni tapes showed superconducting transition temperatures (T_c = 87–89) and critical current density values (77 K, self-field) $\approx 5 \times 10^5$ A/cm^2. These values are somewhat depressed compared with

those obtained on either the standard CeO_2/YSZ/CeO_2/Ni or the conductive $SrRuO_3$/$LaNiO_3$/Ni structure (T_c = 90–92 K, J_c (77 K) ≥1 × 10^6 A/cm^2). The reason for this slight degradation was attributed to low-level Sr contamination of YBCO from the LSMO layers, as documented by SIMS. In light of the above observations, it is reasonable to assume that the parent compound $LaMnO_3$ (LMO), if fabricated epitaxially on Ni and/or mechanically strengthened Ni-(3at%W-1.7at%Fe) (Ni-alloy), would resolve the Sr-contamination issue. LMO is an insulating perovskite oxide whose pseudo-cubic lattice parameter (3.91 Å) is closely matched to that of the orthorhombic YBCO (3.86 Å). These characteristics point to possible viability as a single buffer layer for YBCO coated conductors.

Here is reported for the first time the growth of high-critical-current-density (>1 × 10^6 A/cm^2 at 77 K) YBCO coatings on a single buffer layer, deposited on both biaxially textured Ni and on Ni alloy. A comparative study of the chemical compatibility and the superconducting properties (transition temperature and critical current density) of YBCO films grown on single layers of both LSMO- and LMO-buffered Ni and Ni-alloy tapes is presented.

Biaxially textured Ni (99.99%) and Ni-alloy substrates were obtained by progressive cold rolling of polycrystalline, randomly oriented Ni and Ni-alloy bars followed by a texturing anneal at 1100°C (for pure Ni) and 1250°C (for Ni-alloy). The 1-h heat treatment in a reducing, forming gas (96% Ar + 4% H_2) atmosphere yielded the desired (100) cube texture. Depositions of the LSMO and LMO buffer layers were conducted with an rf-magnetron sputtering system. The sputter targets were made from single-phase LSMO and LMO powders, prepared by solid-state synthesis, and lightly packed into a copper target tray. Typical sputtering conditions consisted of a sputter-gas mixture of forming gas and 2–5 × 10^5 Torr of H_2O at a total pressure of 3 mTorr. Substrate temperatures were in the range of 575 to 625°C. Water vapor provided oxygen for the stability of the oxides, and forming gas helped to suppress the oxidation of the metal tapes. The LMO film thickness was varied in the range of 60 to 300 nm to investigate the effect on microstructure and on the superconducting properties of the HTS layer. The thickness of LSMO layers was maintained at around 300 nm. The deposition rate was ≈ 0.42 Å/s.

The YBCO films were grown by PLD, using a KrF excimer laser system operated at an energy density of ≈2 J/cm^2 and a repetition rate of 15 Hz. During YBCO deposition, the substrates were maintained at 780°C in 120 mTorr of O_2. After deposition, the samples were first cooled to 500°C at a rate of 5°C/min; then the O_2 pressure was increased to 550 Torr, and the samples were cooled to room temperature at the same rate. Typical YBCO film thicknesses were 200 nm. Crystal structures were characterized with a Philips model XRG3100 XRD. Microstructural analyses were conducted on a JOEL model JSM-840 SEM. SIMS depth-profile analyses were made to document possible cation contamination of YBCO. Electrical property characterizations were made by using a standard four-probe technique on samples with dimensions of 10 to 15 mm in length and 3 to 5 mm in width, with values of critical current density assigned at a 1-μV/cm criterion.

A typical XRD θ-2θ scan for a 300-nm-thick LMO layer deposited on biaxially textured Ni is given in Fig. 1.35; the inset shows a logarithmic-scale (111) pole figure of the same LMO film. The presence of only (00*l*) reflections indicates that the LMO is oriented with its *c*-axis normal to the plane of the substrate; the pole figure reveals a single-domain epitaxy with the in-plane LMO[110]//substrate[110].

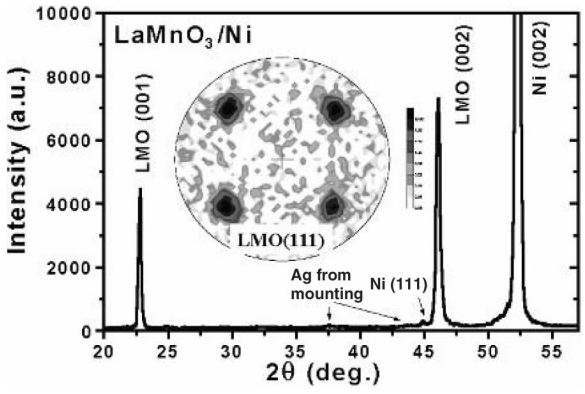

Fig. 1.35. Typical XRD θ-2θ pattern for a 300-nm-thick LMO buffer layer on biaxially textured Ni substrates. The inset shows a (111) logarithmic-scale pole figure of the same film.

The ω-scan rocking curve on the LMO(002) and ϕ-scan on the LMO(111) yielded out-of-plane and in-plane peak-width FWHM of 9° and 10°, respectively. Both distribution widths are comparable to those of the underlying Ni substrate. Similar crystallographic relationships were observed for the growth behavior of LMO films on Ni-alloy tapes.

In addition to excellent crystalline quality, the LMO layers show a crack-free, homogeneous, and dense microstructure. The upper images in Fig. 1.36 show grain-boundary regions for 300-nm-thick LMO-buffered Ni and Ni-alloy substrates. Similar surface morphologies were observed for films deposited at various thicknesses, ranging from 60 to 300 nm. The lower two images show typical surface morphologies of two YBCO films deposited on LMO(300 nm)/Ni and LMO(300 nm)/Ni-alloy substrates, respectively, where dense and uniform microstructures are also observed. Overall, these results on LMO layers are very similar to those previously observed on the LSMO layers.

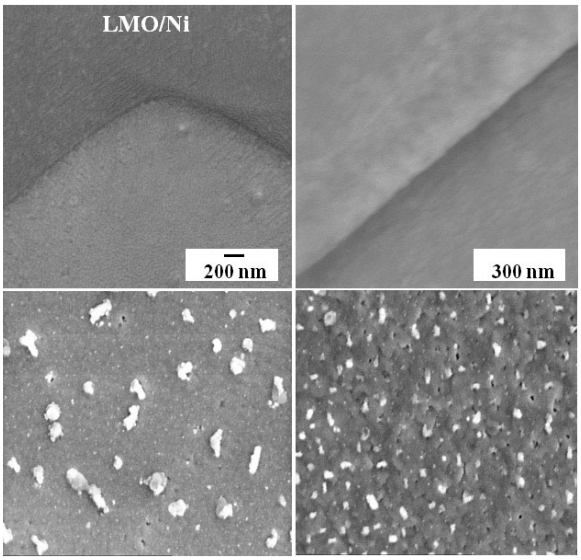

Fig. 1.36. SEM micrographs of 300-nm-thick LMO films deposited directly on biaxially textured (a) Ni and (b) Ni-alloy substrates. The surface morphology of YBCO film grown on LMO buffered (c) Ni and (d) Ni-alloy tapes.

The qualifying test for the suitability of any buffer layer structure on any metal tape is chemical compatibility with the YBCO coatings. Figures 1.37(a) and (b) compare the results of SIMS depth profile measurements on YBCO/LSMO/Ni and YBCO/LMO/Ni, respectively. Both samples show well-resolved interfaces and well-defined layers that effectively block Ni diffusion to within a thickness of few hundred angstroms, as evidenced by the sharp increase of the Ni signal near the buffer-substrate interface. For the YBCO/LSMO/Ni structure [Fig. 1.37(a)], the La and Mn signals remain at the noise level, while a significant broadening of the Sr signal within the YBCO layer indicates contamination. On the other hand, Fig. 1.37(b) clearly shows a YBCO coating on the LMO/Ni structure that is free of cation contamination. In fact, these SIMS results are in accordance with the differences observed in the electrical and superconducting properties of YBCO films deposited on LSMO or LMO buffer layers. In Fig. 1.38, the magnetic field dependence (H||*c*-axis) of the transport critical current density at 77 K for YBCO films deposited on LMO/Ni-(Ni-alloy) is compared with that of LSMO/Ni-(Ni-alloy) architectures. To observe the effect of LMO thickness on the superconducting properties of YBCO layers, the critical current density-magnetic field behavior of two samples having 60- and 300-nm-thick LMO layers is shown. At zero applied field, YBCO films of ~200-nm thickness grown on LMO support high critical current density ($J_c \geq 1.0 \times 10^6$ A/cm^2), whereas the YBCO films on LSMO show approximately half that value. The transport properties are largely independent of LMO thickness in the range of 60 to 300 nm. Specifically, the self-field critical current density of the YBCO/LMO(60 nm)/Ni-alloy is above 1.2×10^6 A/cm^2, which is comparable to the best values obtained on RABiTS™ having both the "standard tri-layer insulating" buffer architecture (CeO_2/YSZ/CeO_2/Ni) and "bi-layer conductive" architecture ($SrRuO_3$/$LaNiO_3$). The present results establish a new benchmark for performance because they were attained on a RABiTS™ structure having a single buffer layer. The inset of Fig. 1.38 shows the superconducting transition region of the temperature-dependent resistivity curves for the same YBCO/LMO/Ni and YBCO/LSMO/Ni samples. Differences in the net resistivity values between two samples are due to the electrical coupling

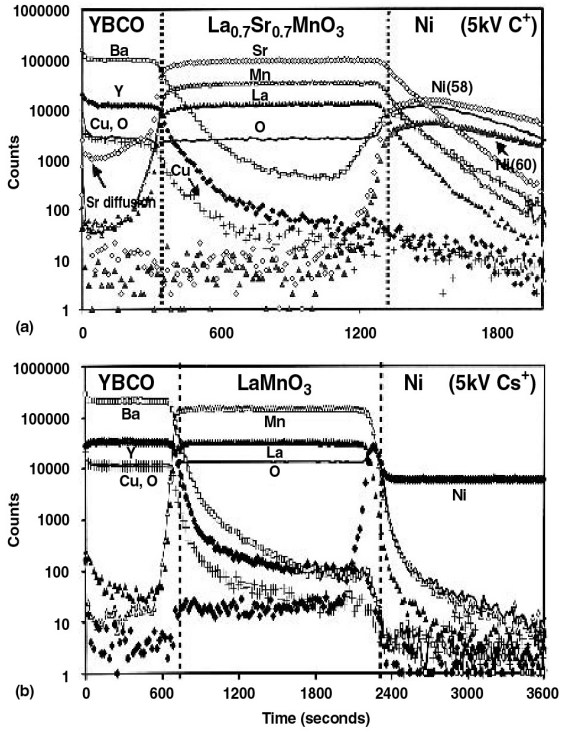

Fig. 1.37. SIMS depth profiles for (a) YBCO/LSMO/Ni and (b) YBCO/LMO/Ni multilayer structures.

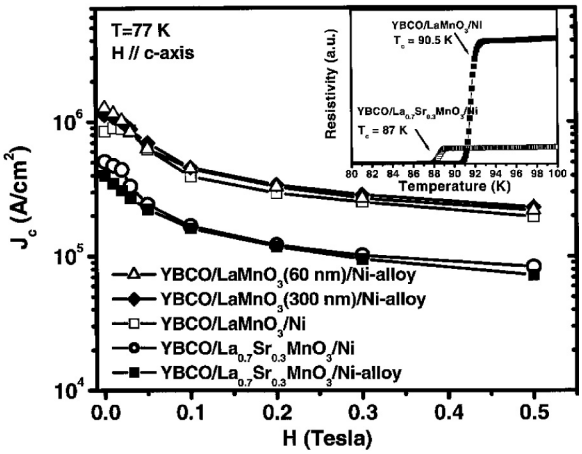

Fig. 1.38. Magnetic field dependence of critical current density measured at 77 K for the YBCO films on LMO buffered Ni and Ni-alloy substrates. Also shown for comparison are typical critical-current-density data (H, 77 K) for YBCO/LSMO/Ni and YBCO/LSMO/Ni-alloy tapes. The inset shows the resistive superconducting transition region of the same YBCO/LMO/Ni and YBCO/LSMO/Ni structures.

between the HTS layer and the metal substrate through the conductive LSMO layer, providing an overall reduced resistivity. While the YBCO/LSMO/Ni exhibits a transition temperature of only 88 K, that of the YBCO/LMO/Ni structure is 91 K, further supporting a low-level of Sr contamination from the LSMO layer. It is well documented that Sr impurities in the superconducting structure can significantly reduce the transition temperature. This conclusion is also consistent with the lower critical current density values observed for the YBCO films on LSMO layers.

In summary, a comparative study is presented of the chemical compatibility and superconducting properties (transition temperature and critical current density) of YBCO films grown on single layers of LSMO- and LMO-buffered biaxially textured Ni and Ni-alloy substrates. Although YBCO films on both buffers have good crystalline structure, the transition temperature and critical current density of the YBCO on LMO layers have shown significantly higher values than those of the YBCO films grown on LSMO layers. These results are observed to be in accordance with the low-level Sr contamination of the YBCO originating from the LSMO layers. The results also indicated that the LMO layer thicknesses in the range of 60 to 300 nm do not significantly affect the superconducting properties of the YBCO coatings. For epitaxial YBCO films on LMO/Ni-(Ni-alloy) tapes, typical self-field critical current density (77 K) values of 1×10^6 A/cm^2 have been achieved. The present results provide initial support for implementation of LMO buffer layers in the development of second-generation HTS wires based on the RABiTS™ approach to fabrication of YBCO coated conductors.

1.7 FABRICATION OF HIGH CRITICAL CURRENT DENSITY YBCO TAPES ON THE NEWLY DEVELOPED LANTHANUM MANGANATE SINGLE BUFFER LAYERS

M. Paranthaman, T. Aytug, S. Kang, R. Feenstra, J. D. Budai, and D. K. Christen (ORNL); P. N. Arendt, L. Stan, J. R. Groves, R. F. DePaula, S. R. Foltyn, and T. G. Holesinger (LANL)

1.7.1 Introduction

Ion-beam-assisted deposition (IBAD) on RABiTS™ has emerged as one of the leading techniques for the fabrication of templates for second-generation YBCO coated conductors. In the RABiTS™ approach, the standard three-layer architecture of CeO_2/YSZ/Y_2O_3/Ni-W is used to produce meter lengths of buffered tapes. The Y_2O_3 seed layer is typically grown by reactive evaporation. Both the YSZ barrier and the CeO_2 cap layers are grown by rf magnetron sputtering. In an effort to develop alternative single-buffer-layer technology for YBCO coated conductors, the growth of YBCO films was recently demonstrated with a critical current density greater than 1.2 MA/cm^2 at 77 K and self-field on LMO-buffered Ni-W substrates. The LMO buffer layer, which has been identified as a good diffusion barrier for Ni, is orthorhombic perovskite with the following lattice parameters: a = 5.533 Å, b = 5.722 Å, and c = 7.694 Å. The pseudocubic lattice parameter of 3.88 Å is closely matched to YBCO. The lattice mismatch of LMO with YBCO is less than 0.8%. Following the successful demonstration of the growth of YBCO films on LMO buffered Ni-W substrates, single-buffer-layer technology was extended to IBAD substrates. Here, the first demonstration of the growth of high-current-density YBCO films on LMO-buffered IBAD MgO template layers is reported.

1.7.2 Experimental

Highly textured IBAD MgO templates on metallic substrates were received from Los Alamos National Laboratory (LANL).[1] To determine the compatibility of LMO with MgO surfaces, LMO buffers were also deposited on MgO (100) single-crystal substrates. The LMO layers were deposited by rf-magnetron sputtering. The sputter targets were single-phase LMO powders loosely packed into a 4-in. copper tray. The powders were prepared by a solid-state reaction. Typical sputter conditions consisted of 2 to 5 × 10^{-5} Torr of H_2O with a total pressure of 3 mTorr forming gas (Ar/H_2 4%). The LMO films were grown at a substrate temperature of 650 to 750°C. The water pressure was sufficient to oxidize the film to form stoichiometric LMO. The forming gas was used to reduce any oxide present at the substrate surface during film growth. The LMO film thickness varied from 60 to 300 nm. The deposition rate was ~0.6 Å/s.

The YBCO films were grown by PLD; a XeCl excimer laser system was used, operated at an energy density of ≈2 J/cm^2 and a repetition rate of 10 to 20 Hz. During YBCO deposition, substrates were maintained at 780°C and 120 mTorr of O_2. Typical YBCO film thickness was 2000 Å. An ex situ BaF_2 process was also used to grow YBCO films. The films were analyzed by a Philips Model XRG3100 XRD; microstructural analyses were conducted on a JOEL Model JSM-840 SEM. The thickness and composition of both LMO and YBCO films were determined by RBS. AFM was used to study the surface roughness of the samples. A standard four-probe technique was used to measure the resistivity and transport critical current density. The voltage contact spacing was 0.4 cm. A 1-μV/cm criterion was used to calculate critical current density values.

1.7.3 Results and Discussion

1.7.3.1 YBCO Films on LMO-Buffered MgO (100) Single-Crystal Substrates

Detailed XRD studies indicated the presence of highly textured YBCO and LMO films on MgO single-crystal substrates. The field dependence of critical current density for YBCO films grown by both PLD and the ex situ BaF_2 process on LMO-buffered MgO substrates is shown in Fig. 1.39. A zero-field critical current density of 4.3 MA/cm^2 at 77 K was obtained. YBCO BaF_2 films carried a critical current of 143 A/cm-width. Critical current density at 0.5 T was about 20% of the zero-field critical current density, indicating the presence of a strongly linked YBCO film.

The microstructure (obtained by SEM) of a PLD YBCO film on an LMO-buffered MgO substrate is shown in Fig. 1.40. It appears to be a very high quality YBCO film. Good uniformity in porosity and surface particulate across the entire film were observed. These results indicate that LMO is highly compatible with both MgO and YBCO.

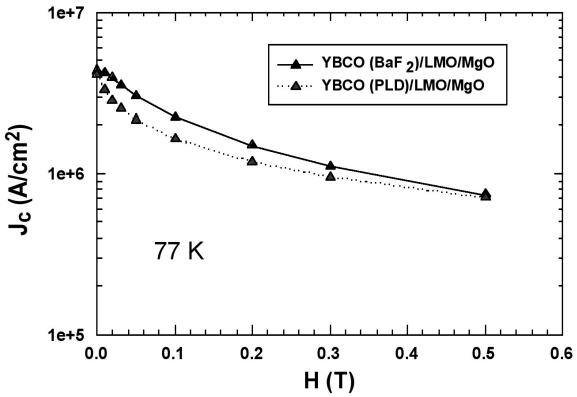

Fig. 1.39. The field dependence of the transport current density (J_c) for both 200-nm-thick PLD YBCO (solid line) and 300-nm-thick BaF_2 YBCO (dashed line) films on LMO-buffered MgO (100) single-crystal substrates.

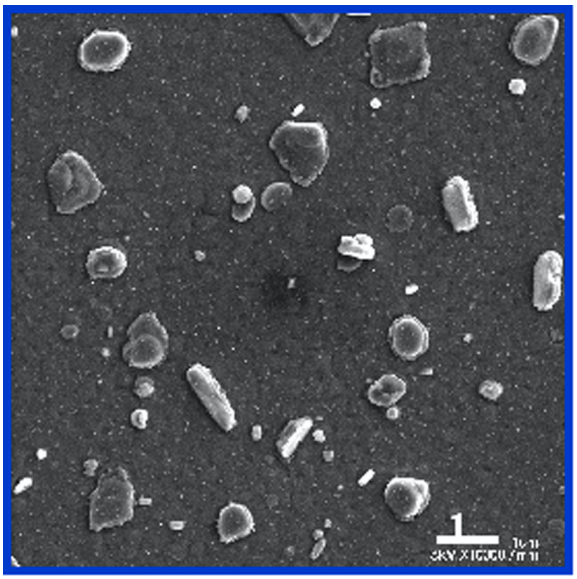

Fig. 1.40. SEM micrograph for a 200-nm-thick PLD YBCO film on LMO-buffered MgO (100) single-crystal substrate.

1.7.3.2 YBCO Films on LMO-Buffered IBAD MgO Templates on Metallic Substrates

A typical θ-2θ scan for a 200-nm-thick YBCO film on LMO-buffered IBAD MgO/Ni-alloy substrate is shown in Fig. 1.41. The strong YBCO (00*l*) signal revealed the presence of a good out-of-plane texture. NiO impurities were not observed. As shown in Fig. 1.42, the XRD results from ω and ϕ scans for a 200-nm-thick YBCO film on LMO/IBAD MgO/Ni-alloy revealed good epitaxial texturing. The FWHM values for LMO (002) and YBCO (005) are 3.2°, and 2.4°, and those of LMO (111) and YBCO (102) are 10.4°, and 8.6°, respectively. MgO diffraction patterns were weak due to the presence of very thin MgO layers.

The field dependence of critical current density for PLD-grown YBCO films on LMO-buffered IBAD MgO templates is shown in Fig. 1.43. A zero-field critical current density of 1.8 MA/cm^2 at 77 K was obtained. YBCO films had very high flux-pinning properties. An irreversibility field of 7.5 T was observed. An SEM image of the microstructure of the film's surface is shown in Fig. 1.44. The image indicates the presence of a dense film. In addition, YBCO films with a thickness of 1.65 μm grown on

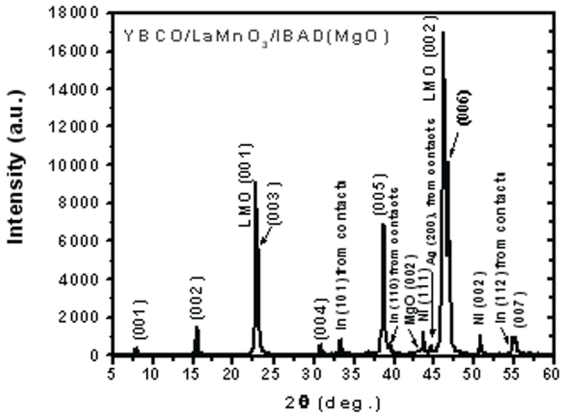

Fig. 1.41. A typical θ-2θ scan for a 200-nm-thick YBCO film on 300-nm-thick LMO-buffered IBAD MgO/Ni-alloy substrate.

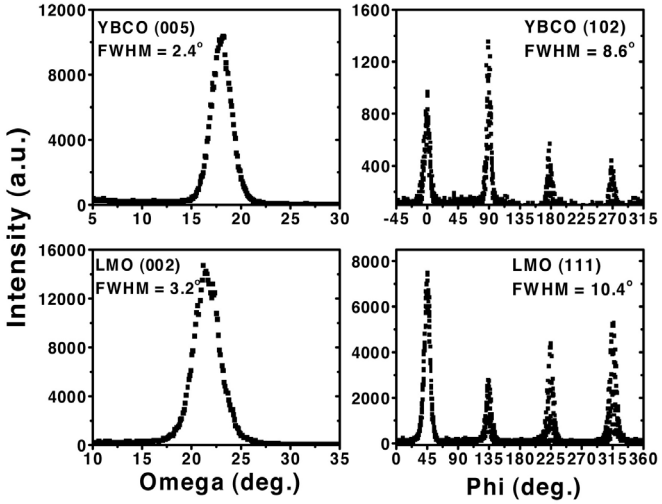

Fig. 1.42. The ω and ϕ scans for a 200-nm-thick YBCO film on 300-nm-thick LMO-buffered IBAD MgO/Ni-alloy substrate.

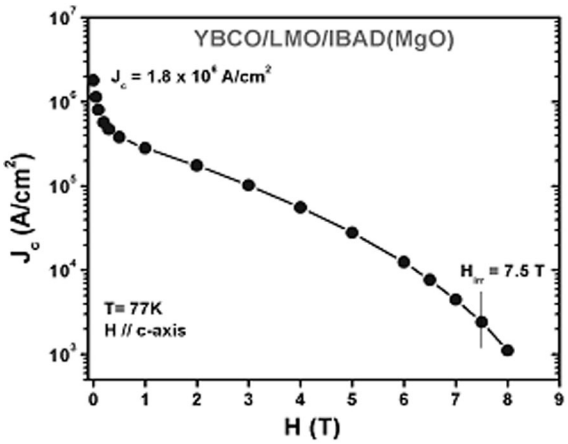

Fig. 1.43. The field dependence of the transport current density (J_c) for a 200-nm-thick YBCO film on 300-nm-thick LMO-buffered IBAD MgO/Ni-alloy substrate.

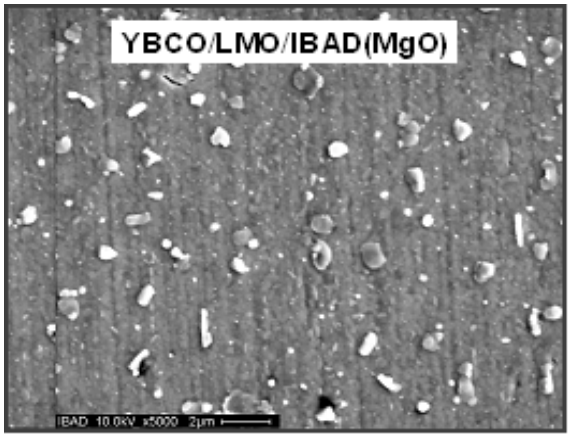

Fig. 1.44. SEM micrograph for a 200-nm-thick PLD YBCO film on 300-nm-thick LMO-buffered IBAD MgO/Ni-alloy substrate.

LMO-buffered IBAD MgO templates carried a critical current of 230 A/cm, demonstrating that LMO is highly compatible with IBAD MgO templates. Efforts are being made to use this architecture to fabricate long lengths of YBCO coated conductors.

1.7.4 Summary

The successful fabrication of high-performance YBCO coatings was demonstrated on a single LMO buffer layer deposited on both MgO single-crystal substrates and IBAD MgO templates on metallic substrates. A critical current of 230 A/cm-width was obtained on YBCO films grown on LMO-buffered IBAD MgO templates. This performance is comparable to the best single-layer results achieved on IBAD MgO substrates, including the $SrRuO_3$ layer newly developed at LANL.

1.7.5. Reference

1. J. R. Groves et al., "High Critical Current Density $YBa_2Cu_3O_{7-\delta}$ Thick Films Using Ion Beam Assisted Deposition MgO Biaxially Oriented Template Layers on Nickel-Based Superalloy Substrates," *J. Mater. Res*. **16**, 2175–81 (2001).

1.8 YBCO COATED CONDUCTORS (AMSC/ORNL CRADA)

M. W. Rupich, U. Schoop, D. T. Verebelyi, C. Thieme, W. Zhang, X. Li, T. Kodenkandath, N. Nguyen, E. Siegal, D. Buczek, J. Lynch, M. Jowett, E. Thompson, J-S. Wang, J. Scudiere, A. P. Malozemoff, Q. Li, S. Annavarapu, S. Cui, L. Fritzemeier, B. Aldrich, C. Craven, and F. Niu (AMSC); A. Goyal and M. Paranthaman (ORNL)

1.8.1 Introduction

The commercial viability of YBCO coated conductor composite (CCC) wire will be determined in a large part by two key factors: performance and cost. A number of potential technologies are under development for the fabrication of the YBCO CCC wires. One particularly attractive combination of technologies involves the RABiTS™ template for the formation of the textured substrate along with MOD of the YBCO layer. The RABiTS™ process is based on deposition of an epitaxial oxide buffer layer (or layers) on a deformation-textured metal or metal alloy substrate. The buffer system functions as a template for the growth of the YBCO superconducting layer and is a barrier to chemical diffusion between the YBCO and the metal substrate. The MOD process is based on the formation of the YBCO layer from a solution-based precursor coated on the surface of the buffered substrate. The combination of the RABiTS™ and MOD technologies is particularly attractive based on the projected price:performance ratio.

Good performance has been demonstrated in short-length samples; however, high critical currents over meter-length RABiTS™ tapes have only recently been reported. In contrast, the combination of YSZ IBAD and PLD-YBCO technologies has shown that greater than 100 A/cm-width can be obtained at 75 to 77 K on 1-m-long tapes. However, the slow texture evolution in YSZ-IBAD and the cost of laser deposition make the IBAD-PLD approach potentially expensive, even compared with the multifilamentary composite Bi-Sr-Ca-Cu-O (BSCCO) tapes currently available in the marketplace.

The current performance capability of a scalable reel-to-reel RABiTS™-MOD process for the fabrication of YBCO CCC wires is presented here.

1.8.2 Experimental

1.8.2.1 Reel-to-Reel YBCO CCC Wire Fabrication

The RABiTS™-MOD architecture for the YBCO CCC wire consists of a cube-textured Ni alloy substrate buffered with cubic oxide buffer layers and a MOD-derived YBCO layer (Fig. 1.45). Fabrication of the YBCO CCC wire, from substrate rolling to application of the Ag cap layer, was carried out entirely by using scalable reel-to-reel processes (Fig. 1.46).

The metal alloy was rolled down to a 50-μm-thick, 1-cm wide tape and was then recrystallized in a reel-to-reel furnace to form the cube-textured template. Epitaxial buffer layers with the structure Y_2O_3/YSZ/CeO_2 were deposited in the reel-to-reel system with continuous processing that is compatible with longer lengths. Prior to the oxide buffer deposition, a 2-μm Ni layer was deposited on the Ni alloy

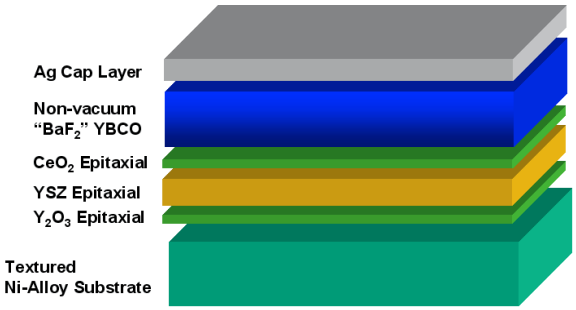

Fig. 1.45. Architecture of the YBCO CCC wire based on the RABiTS™-MOD technologies.

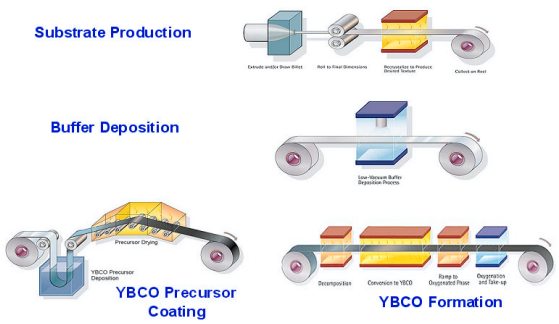

Fig. 1.46. Illustration of the reel-to-reel processing scheme used for fabrication of continuous lengths of YBCO CCC wire based on RABiTS™-MOD technologies.

substrate and sulfurized to enhance the epitaxial nucleation of the Y_2O_3 oxide layer on the metal surface. The 50-nm-thick Y_2O_3 seed layer was deposited by continuous e-beam evaporation while the 300-nm YSZ barrier and 30-nm CeO_2 cap layers were deposited by rf-sputtering.

YBCO films were deposited on the buffered tapes at a loading of 4800 mg YBCO/m^2 of substrate (calculated thickness of 0.8 μm for a 1-cm-wide substrate) by an industrial web-coating process using a trifluoroacetate- (TFA)-based precursor. The MOD film was pyrolyzed at 400°C in a humid oxygen atmosphere to a precursor film with a nominal composition of BaF_2, CuO, and Y_2O_3, then was converted to epitaxial YBCO at 700 to 800°C in an $O_2/H_2O/N_2$ environment. The structure was completed with a 3-μm Ag cap layer and an oxidation step to provide environmental protection and a low resistivity contact to the superconductor. RBS analysis of the final film indicated a YBCO thickness of ~1 μm at the center of the tape.

YBCO films on CeO_2-buffered YSZ single crystals or 1 × 1 cm $CeO_2/YSZ/Y_2O_3$/Ni-alloy substrates were deposited by a spin-coating process. The properties of the precursor solution limit the spin-coated YBCO thickness to less than 1 μm on the 1 × 1 cm substrates. The short samples were processed statically under the same process conditions used for the continuous wires.

1.8.2.2 Measurements

Current densities were determined by transport measurements at 77 K in self-field with a 1-μV/cm criterion. Measurements of YBCO CCC wires were made over the full width and length and at 5-cm intervals. Measurements on single-crystal substrates were made on ~1-mm-wide bridges. Reel-to-reel XRD characterizations were carried out on a system developed at ORNL.

1.8.3 Results and Discussion

1.8.3.1 Characterization of RABiTS™

Compared with pure Ni substrates, the Ni-W alloy has improved mechanical strength and decreased magnetic loss without a loss in texture. The tensile strength of a 1-cm-wide and 75-μm-thick Ni5at%W substrate is 178 MPa at room temperature; a comparable Ni substrate's tensile strength is 34 MPa. Although Ni5at%W has a Curie temperature of 334 K, the magnetic losses are 0.086 W/kA-m (for a 100-A conductor at 60 Hz, 8 mm × 50 μm substrate), a factor of 5 lower than that for a Ni substrate and significantly less than the loss associated with a 1 MA/cm^2, 2.5-μm-thick YBCO film at 77 K (based on the standard Norris formula).

Figure 1.47 shows the grain boundary misorientation distribution (GBMD) of a typical Ni-5at%W substrate. The GBMD shows a relatively sharp distribution with a maximum at 5.8°. Corresponding X-ray texture analysis indicates a Δθ (in-plane) texture of 7.0° and a Δω (out-of-plane) texture of 6.9°. Subsequent growth of the buffer and YBCO layers results in similar textures (Table 1.3).

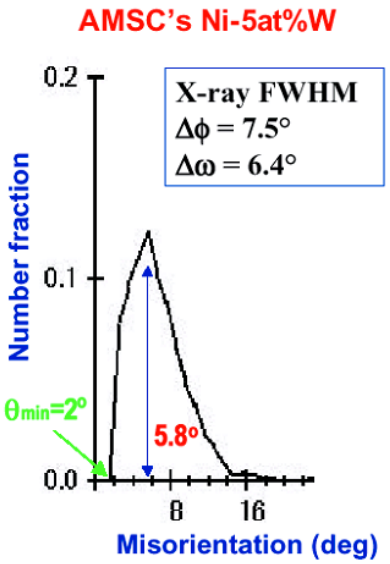

Fig. 1.47. Grain boundary misorientation distribution of a Ni-5at%W substrate. Analyzed area was 1 mm^2.

1.8.3.2 Performance of MOD-Based YBCO Films on Single Crystal and Oxide Buffered Metal Substrates

Critical current densities of YBCO films derived from TFA-based processes vs film thickness are shown in Fig. 1.48. Critical-current-density values for YBCO films on CeO_2 buffered YSZ single crystals are compared with values reported earlier. Previously reported data showed a significant drop in critical current density with increasing film thickness. Improvements to solution-based YBCO growth processes have considerably increased the performance of YBCO films in thicknesses of up to 1 μm. Critical current density values of greater than 4 MA/cm^2 have been obtained with 0.9-μm-thick YBCO films on single-crystal substrates.

Critical current density data on fully buffered, short RABiTS™ have been included in Fig. 1.48 for comparison. For increasing YBCO thickness, the maximum observed value for critical current density is ~40% of the single-crystal values for the same thickness. On the current RABiTS™, the overall supercurrent is limited by the YBCO growth process and by the local texture of the substrate. Maximum critical currrent density values on the RABiTS™ relative to that on single-crystal substrates can be predicted by the percolation theories of the critical currents across a network of grain boundaries. Those calculations assume tape width, grain size, and random grain distribution related to a particular in-plane FWHM. When those calculations are applied to our RABiTS™ (Δθ = 6.4°, grain size = 25 μm and 1-cm tape width), the results predict a critical current density of ~40% of the single-crystal value. This value coincides nicely with the critical current densities reported in Fig. 1.48 for short RABiTS™ and single-crystal substrates.

The observed thickness dependence of critical current density on single crystals as well as on metal substrates demonstrates the potential of achieving commercial performance levels of critical currents by a combination

Table 1.3. In-plane textures (Δθ) and out-of-plane textures (Δω) of layers in YBCO CCC

Composite layer	Δθ (degrees)	Δω (degrees)
Ni-W	7.0	6.9
YSZ	6.5	6.7
CeO_2-Y_2O_3	6.7	7.0
YBCO	6.4	6.0

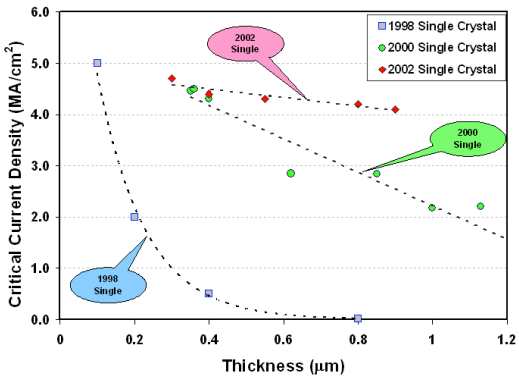

Fig. 1.48. Historical improvement in critical current density (77 K, self-field) of YBCO films grown from a TFA-based precursor on CeO_2/YSZ(sc) substrates (1 × 1 cm) and CeO_2/YSZ/Y_2O_3/NiW substrates (1 × 1 cm) as a function of film thickness.

of inexpensive processes such as solution-based growth of the HTS layer and deformation of textured substrates. For commercial applications, performance levels of 300 A/cm-width are targeted. The data reported here indicate that these levels can be achieved by either increased HTS layer thickness or improved substrate texture. Most likely, a combination of both will result in a commercial process for the fabrication of YBCO CCC.

1.8.4 Performance of Continuously Processed YBCO CCC Wires

Figure 1.49 shows the critical current vs length along a 1.25-m-long YBCO conductor. The end-to-end critical current was 112 A/cm-width with an n value of 31. The inset in Fig. 1.49 provides the statistics from the critical current data measured in 5-cm intervals over the length of the tape. The end-to-end result is in very good agreement with the critical current density values obtained in static processing on short metal samples for 1-μm-thick YBCO films and demonstrates the scalability of the YBCO deposition process.

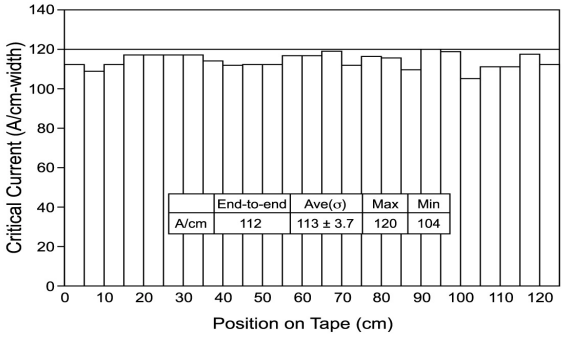

Fig. 1.49. Critical current vs length for a 1.25-m YBCO superconducting tape with Ni-5atm%W substrate. Statistical data are included for critical current measurements at 77 K, self-field, taken at 5-cm intervals.

To assess the reproducibility of the reel-to-reel RABiTS™-MOD process, ten sequential 1-m-long YBCO CCC wires were processed under nominal conditions. Figure 1.50 is a histogram of the average critical current from each of ten consecutive 1-m tapes, measured at 5-cm intervals; the standard 1-μV/cm criterion was used. The average critical current of the ten runs is 98 A. The highest end-to-end critical current of the ten wires was 118 A/cm-width. Although occasional regions of reduced critical current were measured, each correlated directly to a visually detected handling defect recorded prior to measurement of critical current. The high average critical current and narrow distribution between wires demonstrates the robustness and consistency of both the RABiTS™ and MOD processes.

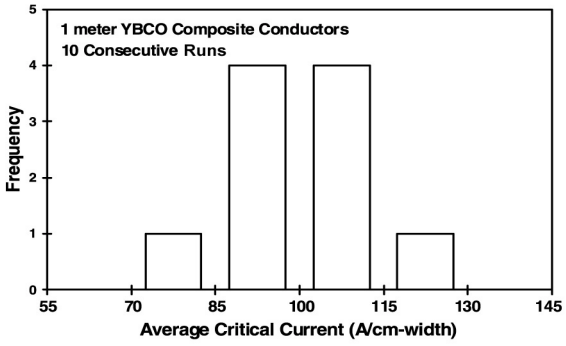

Fig 1.50. Critical current measured at 77 K, self-field, averaged from 5-cm segments on ten consecutive 1-m runs. The average critical current for the ten runs was 98 A, with a standard deviation of 14 A. Standard deviation of individual runs was lower.

In addition, current models of YBCO CCC performance over length predict a degradation of critical current density over length, depending on the width of the CCC substrate in numbers of grains across. However, even with the assumption of statistical grain distribution in a RABiTS™ tape, a reduction in critical current density of only 15% is predicted over 1000-m conductor length with a FWHM between 6 and 7° for a conductor that is at least 100 grains wide. These observations are confirmed in the recent work of Nakamura et al.[1] Commercial conductors with a width of 0.4 cm and a grain size of 50 μm fall in this regime where the conductor is about 100 grains wide. Hence, current modeling that assumes a random grain distribution predicts no significant reduction in critical current density for commercial conductor length scales.

1.8.4.1 Characterization of MOD YBCO Films

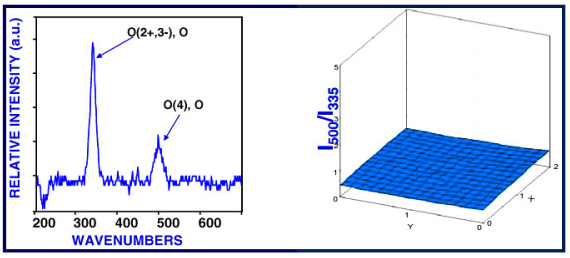

Fig. 1.51. Raman microprobe spectrum (left) of the YBCO layer from a 112-A/cm-width YBCO CCC wire processed in a 1.25-m length. Contour map (right) shows out-of-plane texture analyzed over a 4-mm² area.

Raman microprobe analysis of a sample cut from a meter-length wire, displayed in Fig. 1.51, shows a phase-pure YBCO film consistent with X-ray data. There is no evidence of cation disorder of second phases from the Raman data. The 335 cm^{-1} and 500 cm^{-1} bands correspond to the in-plane and out-of-plane O-vibrational mode, respectively. The out-of-plane texture of the YBCO film can be assessed by the ratio of the intensities of the 500/335 wave number bands. The calculated out-of-plane texture contour map in Fig. 1.51 shows that the film is highly textured and that the texture is uniform over the tape surface. Corresponding X-ray texture analysis of the film shows a $\Delta\theta$ (in-plane) texture of 6.0° and a $\Delta\omega$ (out-of-plane) texture of 6.4°, consistent with the Raman analysis.

1.8.5 Conclusion

In this work, the current capability of the combined low-cost RABiTS™-MOD process was demonstrated for the reproducible fabrication of high critical current YBCO CCC wire by using scalable reel-to-reel manufacturing processes.

The solution-based process for the deposition of YBCO films has been successfully extended to continuous processing of high critical current films. The feasibility of achieving critical currents greater than 100 A/cm-width has been demonstrated by depositing 1-µm-thick YBCO films.

No indication of critical current degradation with length has been observed over multiple tapes, indicating that the RABiTS™-MOD process can be used directly for the production of commercial-length YBCO CCC wires.

1.8.6 Reference

1. Y. Nakamura, T. Izumi, and Y. Shiohara, "Percolation Analysis of the Effect of Tape Length on the Critical Current Density of 123 Coated Conductors," *Physica C* **371**, 275–84 (2002).

1.9 THE PROGRESS ON LOW COST, HIGH QUALITY, HIGH TEMPERATURE SUPERCONDUCTING TAPES DEPOSITED BY THE COMBUSTION CHEMICAL VAPOR DEPOSITION PROCESS

S. S. Shoup, M. K. White, S. L. Krebs, N. Darnell, A. C. King, D. S. Mattox, and I. H. Campbell (MicroCoating Technologies, Inc.); K. R. Marken, S. Hong, and B. Czabaj (Oxford Superconducting Technology); M. Paranthaman, H. M. Christen, H.-Y. Zhai, and E. Specht (ORNL)

1.9.1 Introduction

High-temperature superconductors hold great promise for offering tremendous energy and cost savings to the electric power industry. Over the past several years, scientists have investigated the

potential YBCO coated conductors have to offer and have achieved very high current densities on single-crystal substrates as well as coupon-sized flexible metallic substrates. Efforts are turning toward scaling the deposition process to obtain practical lengths of coated conductors and to begin investigating “real product” usage. Once these trials have succeeded, the focus will be on achieving long-length, large-volume production at a cost that will be competitive with copper. Scaling is a task in itself with many factors to consider in maintaining the high quality over the long length while providing coated conductors at a viable cost.

The innovative combustion chemical vapor deposition (CCVD) technology has considerable potential to overcome many of the shortcomings of traditional vapor deposition techniques while yielding equal or better quality coatings at a lower cost. As a result, capital requirements and operating costs are reduced at least tenfold when compared with competing vacuum-based technologies (e.g., sputtering and metal oxide CVD). The ability to deposit thin films in a nonvacuum atmosphere enables continuous, production-line manufacturing. Consequently, throughput potential is far greater with CCVD than with conventional thin-film technologies, most of which are generally restricted to batch processing. Such advantages can help decrease the cost of fabricating HTS tape over traditional deposition technologies and thus help meet DOE's target cost goals for making HTS tape competitive with copper.

1.9.2 Experimental Details

In the traditional CCVD process (Fig. 1.52), precursors are dissolved in a solvent that typically acts as the combustible fuel. This solution is atomized to form submicron droplets by means of the “Nanomiser” technology (patent pending), proprietary to MicroCoatings Technology, Inc. (MCT). These droplets are then convected by an oxygen stream to the flame, where they are combusted. A substrate is coated by simply drawing it through the flame plasma. The heat from the flame provides the energy required to evaporate the droplets and for the precursors to react and to vapor-deposit on the substrates. The temperature of the nickel substrate is an independent process parameter that can be varied to actively control the film's microstructure, epitaxy, and substrate oxidation. In the case of buffer-layer depositions, a localized reducing atmosphere is also used to prevent nickel oxidation, and a solvent system with lower carbon content is used to minimize carbon deposition. Dynamic seals allow for continuous substrate passage between the open air and the localized reducing atmosphere.

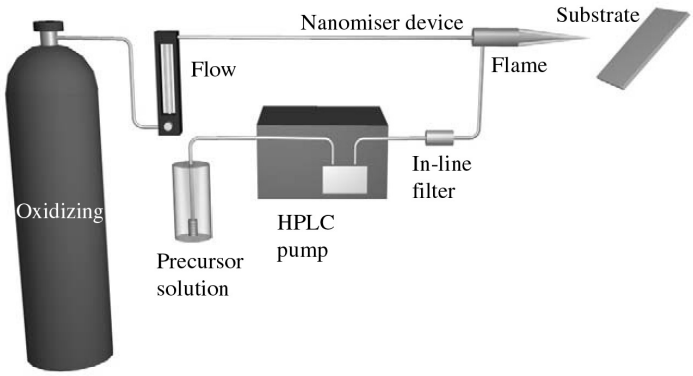

Fig. 1.52. Schematic representation of CCVD technique.

One of the largest challenges in tailoring the CCVD system for deposition of YBCO was the removal of all carbon sources from the process. Once formed, barium carbonate is difficult to remove and is detrimental to the performance of the superconductor coating. The process was modified to allow for use of aqueous solutions in the deposition of YBCO. A new Nanomiser for the atomization of aqueous solutions and the use of a hydrox flame resulted in successful YBCO depositions on single-crystal substrates.

1.9.3 Discussion

1.9.3.1 Buffer Layers: Optimization and Scaling

Buffer-layer depositions were initiated on single-crystal substrates to prove the viability of using CCVD to deposit layers that could be used as suitable templates for the growth of high-performance YBCO. Critical current densities greater than 3.5 MA/cm^2 were obtained on CCVD buffer layers on single-crystal substrates. The focus then moved to depositing layers onto textured metal substrates. MCT partnered with Oxford Superconducting Technology, which supplies the substrates and is in the process of scaling the textured metal to lengths greater than 100 m. Several architectures of buffer layers have been deposited by CCVD; $SrTiO_3$, CeO_2, YSZ, and $LaAlO_3$ have been used, $SrTiO_3$ and CeO_2 being the only layers to be grown epitaxially directly on Ni. The architecture enabling the highest-performance PLD YBCO has been a 250-nm $SrTiO_3$ layer with a 40-nm CeO_2 cap layer. Phi scans performed on an architecture of $SrTiO_3$ with a CeO_2 cap layer yield average FWHM phi values of 8.3° and 8.7° for $SrTiO_3$ (111) and CeO_2 (111), respectively; (002) omega values are 9.8° and 8.0°. MCT has continued to refine the deposition temperature, thickness, and microstructure of the buffer layers and, in conjunction with ORNL, has demonstrated that PLD YBCO with a critical current density greater than 1 MA/cm^2 can be deposited onto CCVD RABiTS™ (Fig. 1.53).

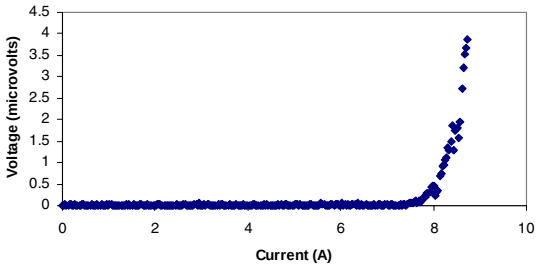

Fig. 1.53. Critical current as a function of applied voltage for PLD YBCO/CCVD buffer/Ni: I_c = 7.944 A, 0.44-cm-wide sample and 170-nm-thick YBCO translates into a critical current density of 1.06 MA/cm^2.

Ceria seed layers can also be grown on Ni and yield a misorientation of about 1%. Alternative architectures will be explored using this seed layer in the future. Sulfur content on the surface has been found to be an important factor in determining the amount of misorientation that is grown in the initial seed layer. X-ray photoelectron spectroscopy (XPS) has been used to detect the amount of surface sulfur, and a correlation has been drawn between the percentage of sulfur and the percentage of misorientation. XPS is now used as a diagnostic technique to screen batches of Ni, and Oxford is investigating the metal-rolling and heat-treatment processing steps required to achieve consistent diffusion of sulfur to the surface.

With successful coupon-sized samples of CCVD RABiTS™ fabricated, MCT focused on scaling the technology to meter lengths of tape. A meter length of tape was first made by using the same single Nanomiser system used to produce the small samples. A thin layer of $SrTiO_3$ (estimated to be about 5 nm thick based on time and solution concentration ratios) was deposited in two passes to provide the seed epitaxial layer. A higher concentration of $SrTiO_3$ solution was then used to deposit a growth layer of the desired thickness (~250 nm) in the second pass. A third pass deposited the CeO_2 cap layer (~40 nm). XRD analyses (Table 1.4) taken from small samples on each end of the sample indicate that there is a minor amount (<3.5%) of both in-plane and out-of-plane misorientation in the $SrTiO_3$ layer but no detectable misorientation in the CeO_2 cap layer. PLD YBCO deposition onto one of these end pieces (performed by ORNL) resulted in a critical current density of 937,000 A/cm^2 as measured by ORNL.

Reel-to-reel XRD analyses (Fig. 1.54) indicate fairly good uniformity along the length of the sample; a higher degree of in-plane and out-of-plane misorientation in CeO_2 and in-plane misorientation in $SrTiO_3$ was seen at about 50 cm. The cause is unknown, and uniformity rebounds slightly after this position. The XRD analyses in Fig. 1.54 show the in-plane uniformity of the CeO_2 along three different lengths of tape

Table 1.4. Epitaxy characterization for meter lengths

Run ID	Out-of-plane				In-plane			
	CeO_2		$SrTiO_3$		CeO_2		$SrTiO_3$	
	Misorientation (%)	(002) ω FWHM	Misorientation (%)	(002) ω FWHM	Misorientation (%)	(111) ϕ FWHM	Misorientation (%)	(111) ϕ FWHM
IIF-99I	0.00	9.51	2.15	7.23	0.00	7.92	3.36	8.49
						8.34		9.10
LL-22D	26.01	∞	23.35	11.25	47.0	14.73	~0	10.15
LL-33F	2.93	9.56	3.48	7.35	0.00	10.77	0.00	8.60
						8.33		8.32
LL-44E	0.00	8.80	1.82	6.97	7.96	8.69	9.91	8.62
						7.98		8.30
LL-49D	0.00	12.46	1.36	11.09	0.00	8.64	0.00	7.46
LL-50D	11.39	8.84	4.53	7.59	6.75	9.21	13.86	7.75

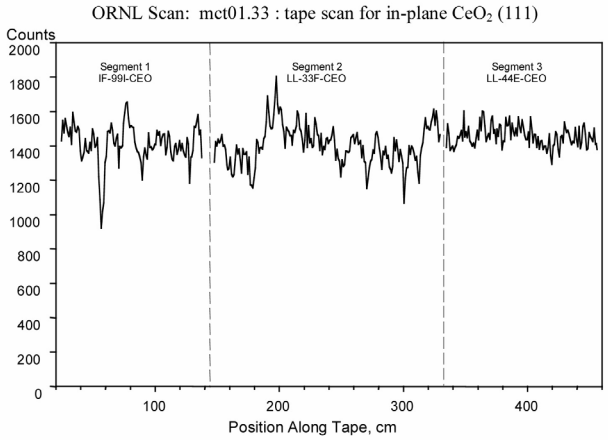

Fig. 1.54. CeO_2 cap in-plane texture uniformity for 3-m-plus buffered lengths.

(different deposition runs) that have been spliced together for ease of analysis. The first segment is the piece made from the single Nanomiser system described above.

The next scaling step was to replicate the current setup to yield a four-unit Nanomiser system to decrease deposition time and thus increase throughput. In most cases, two of the Nanomisers provided the seed layer, and then the tape was rewound and traversed through the system again with three Nanomisers delivering the growth $SrTiO_3$ layer and the last Nanomiser providing the CeO_2 cap. Several runs have been made with this system, and XRD analyses have been performed (Table 1.4). Slight changes in deposition parameters, including the rate at which the tape moved (and thus the number of Nanomisers providing the layer) and the concentration of the solution, account for the varying degrees of misorientation and FWHM changes among the different tapes. The second and third segments in Fig. 1.54 are tapes made with the four-unit Nanomiser system. The last segment shown has the lowest FHWM values and is the most uniform along the length. Coupons of the ends of this segment will be coated with PLD YBCO to determine their effectiveness as buffer templates. Attempting to deposit the desired thickness and architecture in a single pass through the four-unit Nanomiser system required increasing to 1.5× the concentration of the solution that provided the $SrTiO_3$ growth layer. This increase resulted in the largest amount of misorientation, as can be seen in Table 1.4 for the tape with the ID number LL-50D. Ideally, a five-unit Nanomiser system would be required to deposit a desired thickness in a single pass under the current deposition conditions. Further increasing the number of Nanomisers would increase the deposition rate.

1.9.3.2 Superconductor Optimization on Single Crystals and CCVD RABiTS™

YBCO deposited onto single crystals by CCVD has achieved the benchmark performance: a critical current density value of 1 MA/cm^2 (Fig. 1.55). The deposition was performed in the open atmosphere, using an aqueous solution of nitrates. Although additional oxygen can be entrained from the surrounding

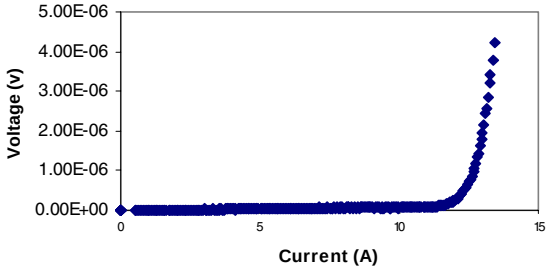

Fig. 1.55. Critical current as a function of applied voltage for CCVD YBCO/LAO single crystal: I_c = 12.22 A, 0.3-cm-wide sample, and 380-nm-thick YBCO translates into a critical current density of 1.07 MA/cm².

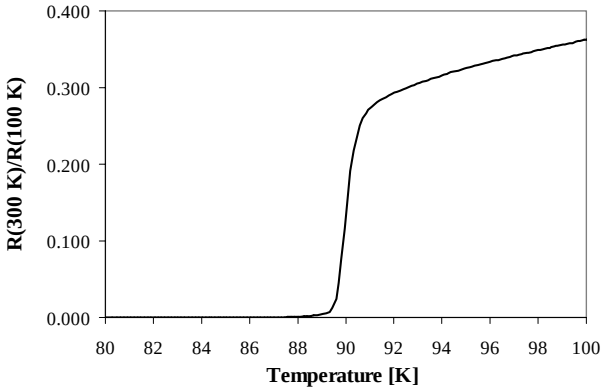

Fig. 1.56. Resistance as a function of temperature for a YBCO coating deposited by CCVD.

air during deposition, the best critical current densities were obtained when the sample was annealed in flowing oxygen for 50 min in an in-line furnace at 500°C immediately after deposition and then quenched to room temperature. Without the anneal, critical current density values were about 850,000 A/cm². Critical transition temperatures for such samples are typically between 85 and 91 K (Fig. 1.56).

Depositing CCVD YBCO on CCVD RABiTS™ is currently under investigation. A localized reducing atmosphere, or at the least an inert atmosphere, is still required, even in the presence of the buffer layer, to minimize the oxidation of the metal substrate. The traditional challenges of abating NiO formation during YBCO growth along with epitaxy and compositional control have been prevalent, and some deposition conditions cause breakdown of the buffer layer and thus cause the formation of excessive, random $BaCeO_3$ or $BaTiO_3$ when $SrTiO_3$ and CeO_2 layers are used. In these cases, the original buffer layers have been randomized or appear with significantly reduced intensities.

Conditions have been identified in which the buffer layer remains intact and functional, and thus minimal NiO formation is seen. Work will continue in this area as variables such as composition, deposition rate, and formation temperature are investigated further. It may also be necessary to modify the architecture or thickness of the CCVD RABiTS™ from that used with PLD YBCO to obtain the highest-performance CCVD YBCO possible.

1.9.4 Conclusions

Scaling the CCVD buffer-layer deposition process to longer and longer lengths will remain a preeminent focus for MCT. More XRD analyses will be necessary to determine the quality along the length as deposition parameters are changed during investigation. Additional PLD YBCO deposition on coupons from these meter lengths will be needed to determine their effectiveness as growth templates for high-performance superconductors. Ultimately, it is desirable to have PLD YBCO deposited on an entire meter-length piece to gauge performance. CCVD buffer-layer deposition onto alloy substrates has begun with promising initial results and will continue on short samples before being scaled to longer lengths.

Research on CCVD YBCO on CCVD RABiTS™ is encouraging and will continue with a goal of achieving critical current density values greater than 1 MA/cm².

1.10 GROWTH OF OXIDE SEED LAYERS ON Ni AND OTHER TECHNOLOGICALLY INTERESTING METAL SUBSTRATES: ISSUES RELATED TO FORMATION AND CONTROL OF SULFUR SUPERSTRUCTURES FOR TEXTURE OPTIMIZATION

C. Cantoni, D. K. Christen, A. Goyal, L. Heatherly, F. A. List, G. W. Ownby, D. M. Zehner, H. M.Christen, and C. M. Rouleau

1.10.1 Introduction

Progress in the understanding of the epitaxial seed layer nucleation on a face-centered cubic lattice (fcc) cube-textured metal is reported. A PLD system was used, combined with in situ reflection RHEED, AES, and XRD to study the surface of textured nickel, Ni alloy, and palladium substrates during annealing and oxide film growth. The experiments revealed the existence of a sulfur superstructure on the textured Ni (or Ni alloy) surface that forms after surface segregation of S contained as a common impurity in the bulk metal. During the high-temperature texturing anneal, S atoms diffuse to the surface of the tape and are arranged in a centered (2×2) superstructure. Depending on the initial S concentration and/or specific annealing conditions, the superstructure layer can exhibit different coverage.

The effect of such superstructure on the nucleation of several oxide layers on Ni, Ni-alloy, and Pd surfaces is discussed. Issues are examined related to incomplete superstructure coverage and a method for controlling the S surface concentration is described.

1.10.2 Seed Layers on {100}<100> Ni

Among the various materials compatible with YBCO, the seed layers used in RABiTS™ (adopting various in situ and ex situ techniques) are oxides with perovskite structure ($SrTiO_3$, LMO), fluorite structure (CeO_2, YSZ), pyrochlore structure ($La_2Zr_2O_7$), and RE_2O_3 structure (Gd_2O_3, Y_2O_3, Eu_2O_3). The last two groups exhibit a crystal structure that differs from the fluorite by having vacancies in the oxygen sublattice and cation order (in pyrochlores). The oxide seed layers investigated in this study are CeO_2, YSZ, Gd_2O_3, LMO, and $SrTiO_3$ (STO). For all these materials deposition on the *c* (2×2) S template consistently produced highly textured (200) films but that deposition on a clean Ni surface always produced films with a different orientation.

To produce clean Ni surfaces with the sulfur template, previously textured Ni tapes were heated to 550°C in high vacuum ($P_{base} = 1 \times 10^{-8}$ Torr) for 1 h to remove weakly bound species that had adsorbed on the surface after air exposure. This step was effective in removing any traces of hydrocarbons and oxygen on the sample surface. A stable S superstructure was at this point observed by using RHEED and AES. Examples of RHEED patterns are shown for two different orientations, with the incident electron beam parallel to the <100> and to the <110>, in Figs. 1.57(a) and (b), respectively. The pattern in Fig. 1.57(a) shows two extra streaks (indicated by arrows) in addition to the reflections observed for a clean Ni (001) surface pattern. The extra streaks are positioned halfway

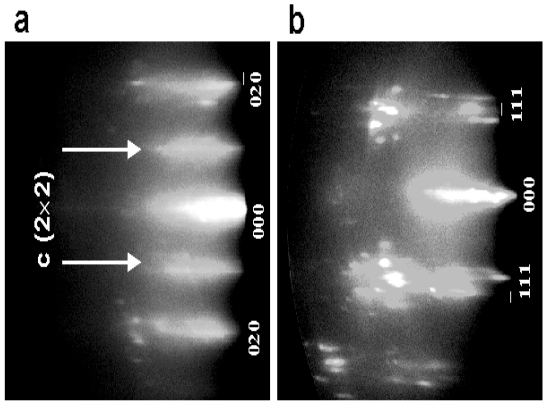

Fig. 1.57. RHEED patterns obtained from the {100}<100> Ni surface after 1-h anneal at 500°C with the incident electron beam (a) along <100> and (b) along <110>. The Ni reflections are indexed, and arrows indicate the superstructure streaks.

between the Ni streaks and are not observed in the <110> pattern. This is consistent with the existence of a *c* (2 × 2) S superstructure with S atoms occupying alternating fourfold hollow sites on the Ni surface lattice. AES spectra showed that the concentration of S on the surface was uniform across the sample and constant with temperature up to 1000°C in ultrahigh-vacuum conditions. Ni surfaces free from sulfur were obtained by depositing a Ni film on the textured Ni tapes in situ by PLD. AES and RHEED analyses of the laser-deposited Ni overlayers indicated that the films did not contain any detectable amount of S. In these samples, segregation of sulfur to the surface and consequent formation of a *c* (2 × 2) superstructure were observed only after the S atoms had diffused through the entire Ni overlayer as a consequence of anneals at temperatures of 750°C or higher. However, RHEED observations indicated that the formation of the sulfur superstructure on the Ni films (500–1000 Å thick) is a very slow process with a time constant of the order of 1 h or more. This finding justified the use of the samples with Ni overlayers as clean Ni surfaces in the seed layer deposition experiments. All seed layers were deposited by laser ablation of stoichiometric ceramic targets on the *c* (2 × 2)/{100}<100> Ni surface and on the superstructure-free Ni overlayers that had been previously deposited in situ. The films were grown under the same conditions and with the same procedure for both types of samples while the process was monitored with RHEED. The deposition temperature ranged between 600 and 800°C.

In the case of YSZ and STO, after an initial ~100-Å-thick layer was deposited in vacuum ($P_{base} \leq 5 \times 10^{-8}$ Torr), $P(O_2)$ was increased to 1×10^{-5} Torr and a final film was grown. CeO_2 and Gd_2O_3 seed layers were grown at a constant $P(H_2O)$ of $1–5 \times 10^{-5}$ Torr. LMO was grown at a $P(H_2O)$ of 3 to 6 mTorr. Figure 1.58 shows an XRD ϕ scan of the (111) peak for a CeO_2 seed layer deposited on the *c* (2 × 2)-S template. The first XRD peak appears at 0°, indicating that the CeO_2 film had grown with a 45° in-plane rotation on the Ni substrate. This was also the case for YSZ and Gd_2O_3 seed layers; STO and LMO grew cube-on-cube on the *c* (2 × 2) S template. Deposition of the same buffer layers on clean Ni surfaces produced films with (111) orientation in the case of YSZ, CeO_2, and Gd_2O_3 (<001>seed//<001>Ni), but it produced multiple in-plane domains in the case of STO and a (110) orientation for LMO.

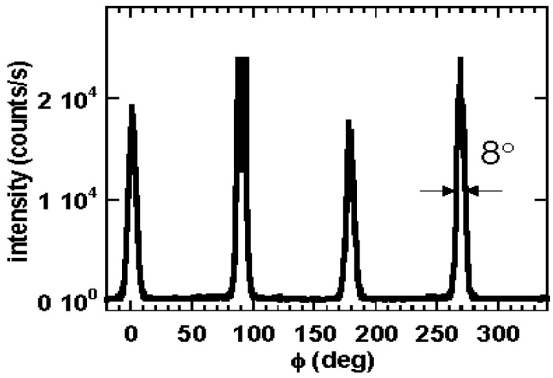

Fig. 1.58. XRD ϕ-scan of the (111) peak for a CeO_2 seed layer deposited on the *c* (2 × 2) sulfur template chemisorbed on {100}<100> Ni.

1.10.3 Quantification and Control of the S-Superstructure

It is evident that the *c* (2 × 2) S superstructure plays a very important role in the nucleation of an oxide buffer layer on Ni. The effect of the S superstructure can be partially explained on the basis of structural and chemical considerations. The S layer behaves like a template that matches and mimics the arrangement of the oxygen atoms in (001) sublattice planes for all the seed layers considered in this study, as shown in Fig. 1.59. Sulfur belongs to the VI group and is chemically very similar to oxygen, often exhibiting the same electronic valence. The presence of such an ordered S template thus facilitates the bonding of the oxide cations in specific sites and promotes the (001) epitaxial nucleation of the film.

In cases for which the bulk S content of particular batches of Ni was much lower than 30 ppm by weight, the seed layer deposition process produced films with degraded texture or partial (111) orientation. In those cases, as recent AES analyses have revealed, S was depleted in the near-surface

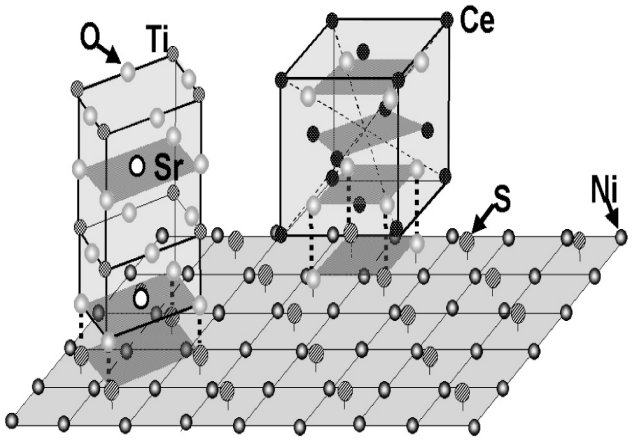

Fig. 1.59. Schematic model for the nucleation of CeO_2 and STO on a (001) Ni surface with a chemisorbed *c* (2 × 2) sulfur superstructure. The dashed lines indicate correspondence between oxygen sites in (001) planes of the seed layer and sulfur sites on the Ni surface. The seed layer cations impinging on the Ni surface bond easily to the sulfur atoms present on the metal surface, promoting the (001) orientation of the growing film. In the STO case, there is a 1:1 correspondence between oxygen atoms in the SrO plane and sulfur atoms on the Ni surface. Therefore, it is plausible that Ti ions initially bond to the S surface atoms to form the first TiO_2 plane of the STO structure. In the CeO_2 case, two of four oxygen ions per unit cell match the sulfur atoms of the *c* (2 × 2) superstructure. During nucleation of CeO_2, oxygen atoms may fill in the empty fourfold Ni hollows and the Ce cations subsequently bond to the template formed by S and O.

layer during a high-temperature texturing anneal (~1100°C). This depletion may be the result of the formation and subsequent desorption of SO_2 in the presence of a sufficient $P(O_2)$. Sulfur depletion impeded formation of a continuous *c* (2 × 2) layer across the entire Ni surfaces, drastically modifying the oxide film nucleation.

The abovementioned considerations illustrate a connection between the quality of the seed layer texture and the degree of coverage of the *c* (2 × 2) superstructure on Ni. To investigate this, combined AES and RHEED experiments were conducted, aimed at quantifying the coverage of the *c* (2 × 2) structure on different Ni samples.

During AES experiments, depending on the material under test and the beam energy, Auger electrons escaped and were detected from a layer 5 to 10 Å deep below the surface. Therefore, the S concentration from AES can differ from the actual atomic concentration of the top monolayer of the surface. They differ (1) because of the uncertainty related to the measurement itself and (2) because, after segregation, S could exhibit a concentration gradient in the layer tested by AES. This ambiguity was resolved by comparing the AES results obtained on typical samples with those obtained on superstructure-free samples on which the *c* (2 × 2) superstructure was intentionally grown through S adsorption. In these experiments, a clean Ni surface was first produced by depositing a Ni layer in situ. Subsequently, a small amount of H_2S with a partial pressure of 5×10^{-7} to 1×10^{-6} Torr was introduced in the vacuum chamber at a substrate temperature of 700 to 800°C for few minutes and was then pumped away. As shown by several other surface studies, the H_2S molecules dissociated at the Ni surface and S atoms chemisorbed to form a superstructure with a coverage that saturated at 0.5 ML [1 ML ≡ (number of surface adsorbate atoms)/(number of surface substrate atoms)], corresponding to one complete atomic layer of the *c* (2 × 2) S superstructure. Exposures to H_2S as low as a few langmuir (1 langmuir ≡ 10^{-6} Torr-s) produced very strong *c* (2 × 2) reflections in the RHEED patterns [see Fig. 1.60(a)]. The sulfur superstructure was stable at 800°C after the H_2S was removed. CeO_2 and YSZ seed layers deposited in situ after S adsorption were highly oriented with a percentage of cube texture very close to 100%, as indicated by the (111) pole figure [Fig. 1.60(b)]. Longer exposure of the Ni surface to H_2S (≥1800 langmuir) did not produce any degradation of the RHEED pattern that could be attributed to either adsorption of surface S in excess of 0.5 ML or formation of a Ni sulfide phase. After exposure to air at room temperature and consequent reheating of the sample in a vacuum, the as-grown superstructure was found to be stable and reproduced the same initial RHEED pattern. AES experiments performed in situ

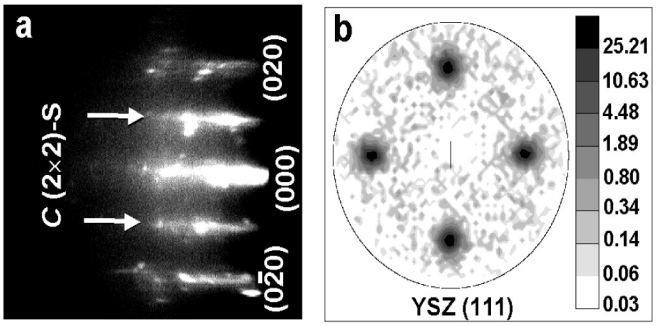

Fig. 1.60. (a) RHEED pattern showing strong *c* (2 × 2) reflections obtained after exposing a clean {100}<100> Ni surface to a few langmuir of H_2S at 800°C. (b) Logarithmic (111) pole figure of a YSZ seed layer grown in situ on the *c* (2 × 2) S superstructure shown in (a). For this sample the X-ray background signal was eliminated by subtracting a second pole figure obtained after changing the Bragg angle by 1°. The calculated percentage of cube texture for this film was 99.96%.

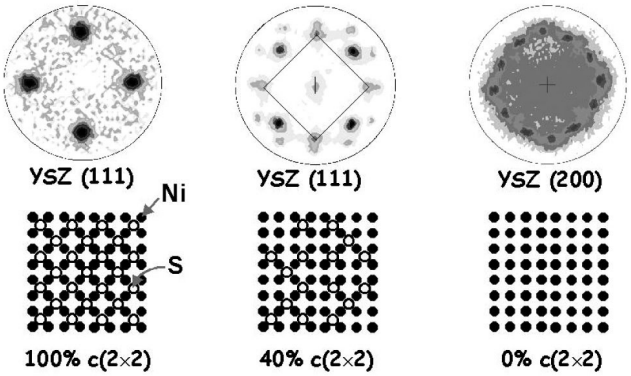

Fig. 1.61. Comparison between pole figures of three STO films grown on {100}<100> Ni substrates having different sulfur coverage. Left: 100% of a *c* (2 × 2) layer (or θ = 0.5 ML); middle: 40%; and right: 0%.

after S adsorption yielded a sulfur signal of about 25% at saturation. The same value was obtained on samples where the *c* (2 × 2) S superstructure had formed as a consequence of segregation and showed RHEED patterns identical to those acquired in the S adsorption experiments. From these observations, an AES value of ~25% was associated with a full layer of *c* (2 × 2) S superstructure on the Ni surface. Consequently, the S surface content was quantified in cases in which the superstructure did not cover the entire Ni surface and the *c* (2 × 2) reflections in the RHEED pattern were less intense than in fully covered samples.

Figure 1.61 is a comparison of pole figures for a YSZ seed layer grown on three different types of Ni substrates. In the first case, the substrate shows a complete S superstructure and the (111) logarithmic pole figure of the YSZ seed shows a perfect cube texture. In the second case, the substrate superstructure exhibits a partial coverage (~40%) that translates to multiple orientations for the YSZ film. In the third case, the surface of the substrate does not contain any S and the YSZ film shows only a (111) texture. In cases in which the substrate's S coverage was between 40 and 80% of a full *c* (2 × 2) layer, we observed a cube texture with XRD peaks broader than those observed in seed layers grown on substrates with 100% *c* (2 × 2) superstructure.

The improvement in the texture of the seed layer determined by the S superstructure corresponds to an enhancement in critical current density of the YBCO film subsequently deposited on the completed (seed plus buffer layer) RABiTS™. This relation is illustrated in Fig. 1.62, which plots the critical current density of four YBCO/CeO_2/YSZ/CeO_2/Ni samples vs the S surface content of the Ni substrate prior to seed layer deposition. In this experiment, the first sample was obtained by selecting a meter-long textured Ni tape showing only 40% of the S coverage corresponding to a full *c* (2 × 2) monolayer; the other samples were exposed to H_2S in a subsequent anneal. In this case (the texturing anneal), sulfurization and seed layer (CeO_2) deposition were carried out continuously in situ, in a reel-to-reel vacuum system equipped with an AES. The H_2S partial pressure was varied during the sulfurization treatment in such a way that different portions of the tape would show different S surface coverage at the end of the process. After deposition,

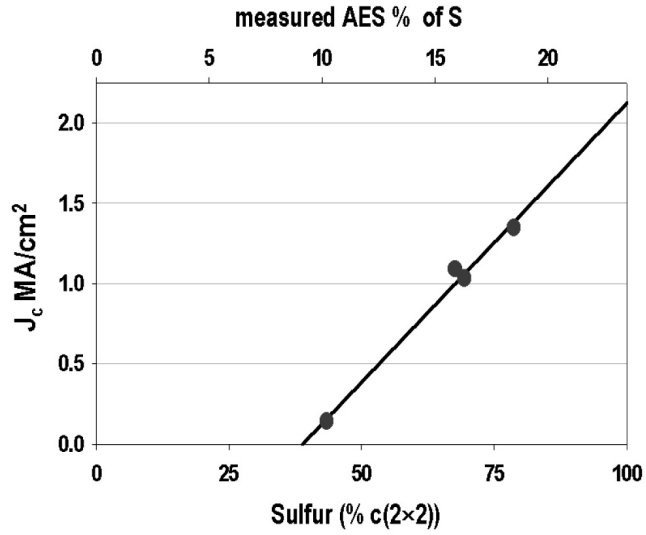

Fig.1.62. Critical current density vs initial substrate S concentration for four YBCO/CeO_2/YSZ/CeO_2/Ni RABiTS™ samples.

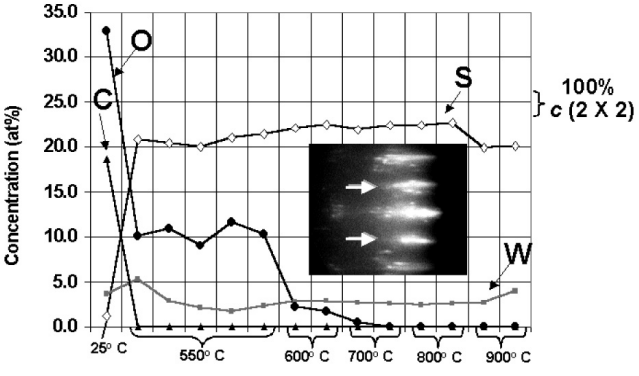

Fig. 1.63. AES data collected on a biaxially textured Ni-3%W alloy substrate after heating to different temperatures and holding for 10 or 60 min. The inset shows the RHEED pattern obtained after heating to 550°C.

four sections of the tape corresponding to four different S surface concentrations were cut and YBCO was deposited on them by PLD.

Sulfur adsorption experiments provide a method for quantifying the S coverage on the Ni surface after the texturing anneal. But, more importantly, H_2S exposure provides a rapid and efficient way to obtain a full coverage of the *c* (2 × 2) S superstructure on textured Ni and consequently optimizes the seed layer texture without being restricted by the amount of S present in the bulk, which depends upon the less-efficient segregation process. H_2S exposure has been successfully introduced in a continuous process for texturing and applying a CeO_2 coating on meter-long Ni tapes, yielding highly oriented and reproducible long lengths of RABiTS™. YBCO films deposited on short sections of these RABiTS™ tapes by PLD and the ex situ BaF_2 method have consistently shown critical current densities larger than 1 MA/cm^2.

1.10.4 Results of Seed Layer Growth on Ni-3%W, Ni-13%Cr, and Pd

Because of the magnetic properties of Ni, coated conductors fabricated with Ni tape show losses in alternating-current (ac) electromagnetic fields, which may be an issue for certain applications. Alloying Ni with small quantities of metals like W and Cr results in lower or practically zero magnetization at liquid-nitrogen temperatures (the latter is the case of the Ni-13%Cr alloy). In addition, Cr and W add strength to the tape, making handling of lengths easier.

The importance of the S superstructure for epitaxial seed layer growth on Ni is known, so it is natural to wonder whether the superstructure plays the same role in textured Ni alloys. Figure 1.63 shows Auger data and a RHEED pattern for a textured Ni-3%W substrate heated up to 900°C in high vacuum. It is evident that, just as for Ni, S surface segregation during texturing had resulted in a *c* (2 × 2) superstructure with complete coverage. The oxygen and carbon signals in the Auger plot derive from air exposure after the texturing anneal, and these species desorb easily with mild heating. As expected from these observations, high-quality buffer layers were deposited on such Ni-W surfaces.

Figure 1.64 shows the RHEED pattern of a Gd_2O_3 seed layer grown by PLD on a textured Ni-3%W substrate at a temperature of 600°C and a P(H_2O) of 1×10^{-5} Torr. The figure indicates that the seed layer

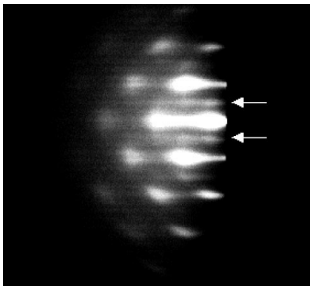

Fig. 1.64. RHEED pattern for a 100-nm-thick Gd_2O_3 film on Ni-3%W.

has grown epitaxially with (004) orientation. The weaker streaks marked by the arrows are superlattice reflections originated by the periodicity of the large cubic cell (a = 10.813 Å) of Gd_2O_3. Fully textured CeO_2, YSZ, and Y_2O_3 seed layers have also been deposited on c (2 × 2)-S/Ni-3%W by PLD or other vapor deposition techniques under the same growth conditions established for deposition on Ni. Because the reactivity of O_2 with W is higher than its reactivity with Ni, careful control of background oxygen is important during buffer layer deposition on Ni-W alloys. RHEED observations showed that the Ni-3%W surface is stable in the presence of a $P(H_2O)$ in the range of 10^{-5} Torr; pressures in the range of 10^{-4} Torr or higher cause changes in the diffraction patterns that can be interpreted as oxide formation. The surface of pure Ni remained stable against oxidation at water pressures as high as tenths of mTorr.

The reactivity with oxygen is substantially higher for Ni-13%Cr substrates. In fact, attempts to deposit typical seed layers like CeO_2 or Y_2O_3 by several vapor deposition techniques on Ni-13%Cr have failed. A combination of RHEED and Auger measurements on these substrates has shown that C and O species are strongly bound to the Ni-Cr surface after air exposure, and high-temperature anneals (700–750°C) in 200 mTorr of forming gas before deposition are necessary to clean the surface and expose the underlying S superstructure. Once cleaned, the Ni-13%Cr surfaces with the top c (2 × 2) S superstructure are stable in background oxygen pressures lower than 1×10^{-8} Torr. Above this value, oxidation of the substrate occurs, rapidly disrupting seed layer growth. The deposition conditions for most of the seed layers used for RABiTS™ involve a $P(H_2O)$ of 10^{-5} Torr or higher. Such a H_2O pressure in the deposition chamber gives rise to an equilibrium oxygen pressure in the range of 10^{-7} Torr, as indicated by a quadrupole mass spectrometer, and therefore is sufficient to oxidize the Ni-13%Cr surface. The only successful attempt of oxide seed layer growth on the bare c (2 × 2)/Ni-Cr surface by PLD was obtained by using YSZ. Unlike other seed layers, YSZ can be deposited from a ceramic target in an oxygen background pressure as low as 10^{-10} Torr. Cube-textured YSZ films were grown on Ni-13%Cr at a temperature of 600°C by ablation of a YSZ target in the base pressure of the vacuum chamber (P_{base} = 0.5–1 × 10^{-8} Torr) corresponding to an O_2 $P(O_2)$ of 0.5 to 1 × 10^{-10} Torr). In addition to the (002) reflections, these films showed a small (111) component with no preferential in-plane orientation. The (111) component was not observed when the initial part of the YSZ deposition was conducted in a partial pressure of H_2S equal to 2 × 10^{-6} Torr. Figure 1.65 shows the logarithmic YSZ (111) pole figure for a 170-nm-thick film that was grown by using H_2S for the initial layer of 70 nm in thickness. Although the background X-ray signal was subtracted to highlight possible secondary orientations, the pole figure shows only cube-texture reflections and the percentage of cube texture was 93%. Despite the chamber's low background oxygen pressure, activated oxygen species present in the ablation plume probably led to local formation of CrO_x, and consequently partial nucleation of YSZ with non-cube orientation. The presence of H_2S during the first stage of film growth reduced the amount of oxygen in the plume by forming SO_2 molecules. Consequently, the substrate oxidation rate decreased, allowing a well-textured YSZ film to be deposited. After YSZ deposition, an 80-nm-thick CeO_2 cap layer was grown in situ at 660°C in an $P(O_2)$ of 5 × 10^{-4} Torr. A 200-nm-thick

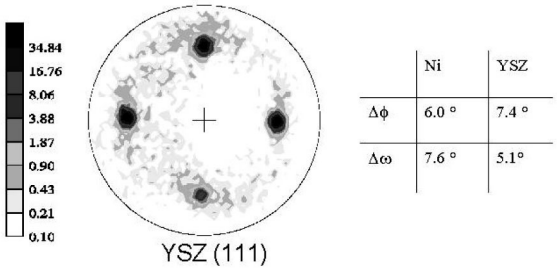

Fig. 1.65. Logarithmic (111) pole figure of a YSZ film deposited on c (2 × 2)/Ni-13%Cr.

YBCO film grown on this sample by PLD showed a critical current density of 0.44 MA/cm^2 at 77 K and in self magnetic field.

The structural model presented for the S effect on seed layer epitaxy should in principle apply to any fcc metal surface that forms a *c* (2 × 2) superstructure and has a good lattice match with the seed layers used in RABiTS™ fabrication. Pd also forms a *c* (2 × 2) superstructure, and, just like for Ni, CeO_2, and STO, seed layers can be grown epitaxially on the S template. The Pd (001) surfaces were obtained by depositing thick epitaxial Pd films on (001) STO single crystals by e-beam evaporation. The as-grown films were free of sulfur and the *c* (2 × 2) superstructure was grown by in situ H_2S exposure, as was done for Ni substrates. Figure 1.66 shows a comparison of RHEED patterns acquired during the nucleation of a CeO_2 film on a *c* (2 × 2)-S/Pd surface and on a clean Pd surface. In the latter case, the RHEED pattern shows additional spots attributable to crystal domains oriented (111) and rotated 45° that are not observed when CeO_2 is deposited on the S-covered metal surface.

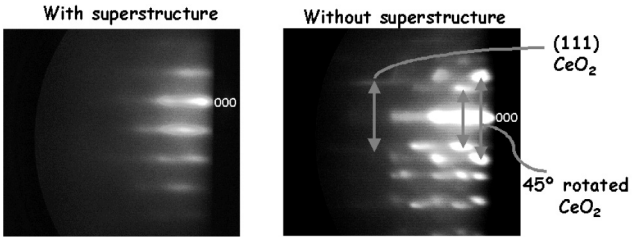

Fig. 1.66. RHEED patterns with e-beam parallel to the substrate <100> for a CeO_2 film nucleated on (left) a Pd (001) surface with the S superstructure and (right) on a clean, S-free, Pd (001) surface.

1.10.5 Conclusion

In conclusion, the *c* (2 × 2) S superstructure present on {100}<100> Ni also forms also on the surface of biaxially textured Ni-alloys, such as Ni-3%W and Ni-13%Cr, and on Pd. In all cases, the *c* (2 × 2) S superstructure acts like a template that enables the epitaxial growth of oxide seed layers on the metal, and a complete coverage of this chemically stable layer is necessary to replicate the substrate texture in the buffer layer. Annealing the Ni, Ni-alloy, or Pd substrates at seed layer deposition temperature in the presence of a small amount of H_2S is sufficient to produce a stable *c* (2 × 2) S with a coverage of 0.5 ML. This simple step creates a complete S template independent of the coverage obtained through segregation. Implementing this step in a continuous RABiTS™ fabrication process allows the initial Ni/Ni-alloy texturing anneal to be carried out at conditions that yield the best texture (and often involve high temperatures and consequent S evaporation) without being limited by the S segregation process.

1.11 THICKNESS DEPENDENCE OF THE CRITICAL CURRENT DENSITY IN EX SITU YBCO COATED CONDUCTORS WITH VARIABLE SUBSTRATE TEXTURE

R. Feenstra, D. K. Christen, A. Goyal, A. A. Gapud, P. M. Martin, E. D. Specht, J. D. Budai, M. Paranthaman, D. F. Lee, L. Heatherly, F. A. List, H. Hsu, and D. M. Kroeger (ORNL); D. T. Verebelyi (American Superconductor Corp.); B.-W. Kang (Pohang University, S. Korea); T. G. Holesinger, P. N. Arendt, J. R. Groves, and R. F. DePaula (Los Alamos National Laboratory); D. M. Feldmann, and D. C. Larbalestier (University of Wisconsin)

For a coated conductor with a fixed critical current density value, the critical current normalized to conductor width K_c scales proportionally with the HTS layer thickness *t* [$K_c \equiv I_c/w = t\,J_c$ (units: amperes per centimeter)]. An appealing aspect of coated conductors is that, due to the dominant substrate thickness, relevant variations in thickness leave the conductor dimensions practically unchanged. On the

other hand, the YBCO production rate scales inversely with thickness. Furthermore, the thickness of a subsequently deposited stabilizing overlayer, designed to match the critical current, has been estimated to be of similar magnitude as the substrate-YBCO composite, adding a further consideration with respect to conductor geometry.

In practice, critical current density is not a constant, but it exhibits a negative derivative: dJ_c/dt. This behavior appears to be largely dependent on processing but is predicted from intrinsic effects related to flux pinning in two-dimensional systems as well. Practical considerations associated with cost of superconductor processing vs substrate preparation, as well as constraints on the engineering critical current density (J_E) ($J_E = K_c/t$), thus will likely determine the configuration best suited for meeting critical-current targets (e.g., using a single HTS coating or a multiple-ply geometry). Irrespectively, it is evident that the most flexible situation for a successful technology development lies in using as thin a YBCO layer as possible (i.e., maximizing the critical current per width of conductor for a single-layer conductor and consuming the least amount of HTS processing).

A parameter with a profound effect on critical current density, but heretofore not systematically considered in studies that relate critical current density to thickness, is the quality of the substrate's biaxial texture. Through the intrinsic dependence of critical current density on grain boundary orientation, by virtue of the epitaxial relationship, critical current density and associated transport networks depend strongly on the grain boundary distribution of the substrate being used. Although a complete mapping of such networks is difficult to achieve, an important consequence is that the critical current per unit width of coated conductors cannot be meaningfully compared with critical current density without reference to the substrate texture. A potentially larger issue at hand is whether the benefits of a well-textured substrate, evident in thin YBCO coatings ($t < 0.5$ μm), are maintained in the thick-film regime as well. On the nanometer scale, where grain boundaries affect the local superconducting properties, practically no information exists regarding the interaction between growth-induced defects and dislocation cores of the grain boundary. The possibility could thus arise that growth-induced disorder in thick YBCO coatings diminishes the texture advantage, depriving the technology of an important tool for improving critical current performance.

The study reported here addresses this issue, expanding on the previous investigations in two significant ways. First, a comparison is made between epitaxial YBCO deposits on a number of coated-conductor substrates. As a result of differences in their preparation, buffer layer chemistry, and texture, these substrates enable a range of performance levels, characterized by distinct optimized critical current density values in thin (0.33-μm) YBCO coatings. Three varieties of RABiTS™ and one template containing YSZ biaxially textured by IBAD were used. Onto these substrates, *c*-axis–oriented YBCO coatings with thicknesses up to 3 μm were successfully grown, enabling a cross-correlation between thickness- and texture-related effects. A recent report by Foltyn et al.[1] compared YBCO coatings of various thicknesses on IBAD-YSZ with epitaxial films on (100) YSZ single crystals. The YBCO was grown by PLD. Although the current-limiting role of substrate-propagated grain boundaries was implicitly in evidence, the observed differences as a function of conductor thickness could not be attributed to texture-related effects because a strong structural deterioration was observed for the coated conductors. This deterioration was identified in the form of so-called "dead layers" (contributing negligibly to critical current) located at either the substrate interface or the film surface. The latter involved essentially all material beyond a critical YBCO thickness of 1.5 to 2 μm. No dead layers were identified for the epitaxial films on single-crystal substrates.

Contrasting with this study, the present report involves a two-step precursor approach, using an ex situ anneal to bring about the epitaxial growth. Distinguished by the incorporation of BaF_2 as a precursor constituent, this approach is considered advantageous for large-scale coated-conductor production.

Indeed, a solution-based variant of this process involving trifluoroacetates is currently under active pursuit by various research groups around the globe. Although use of the BaF_2 ex situ process for successful formation of 5-μm-thick YBCO films on (100) STO single crystal substrates has previously been demonstrated, this is the first reported study of critical current density in the 0.3- to 3-μm thickness range on coated-conductor substrates. Considering the importance of the growth mechanism for thick epitaxial coatings, a detailed comparison with PLD-deposited YBCO is both scientifically and technologically of interest. Such a comparison is made in the second part of this report, following the introduction of an enabling normalization step. While significant parallels are found with respect to $J_c(t)$, important differences are identified as well. A common mathematical model to fit $J_c(t)$ dependence is used to determine how materials-related effects may be reflected in this dependence and relevant fitting parameters.

A summary of the coated-conductor substrates used in this study is presented in Table 1.5. Listed are buffer layer architectures and compositions of the metallic RABiTS™ template as well as texture information in the form of FWHM values of substrate and YBCO reflections in XRD ϕ-scans. Although the latter information is insufficient to predict critical current density, good qualitative agreement with Δϕ was observed. All substrates featured a thin (<30-nm) CeO_2 cap layer to provide a compatible interface with the YBCO. Identified as the first buffer layer material onto which high critical current density YBCO coatings could be successfully grown by the ex situ BaF_2 process, this material still provides the most suitable template despite a nonnegligible degree of reactivity.

Table 1.5. Summary of coated-conductor substrate structure and performance characteristics

Substrate	Architecture[a]	Δϕ (degrees)[b]		J_c (0.33 μm) (MA/cm^2)[c]	Max $K_c(t)$ (A/cm)		t_0[e]
		YSZ	YBCO[c]				
RABiTS™, Ni(1)	Ni/C/Z/C	10.6	10.3	1.0	116	(2.5 μm)[d]	2.33
RABiTS™, NI(2)	Ni/C/Z/C	8.1	7.3	1.55	164	(2.1 μm)[d]	2.40
RABiTS™, Ni-W	Ni(W,Fe)/Ni/Y/Z/C	7.9	6.5	1.5	176[f]	(2.6 μm)[d]	2.78
IBAD, YSZ	Ni-alloy/Z(IBAD)/C	12.9	5.4	2.7	239[f]	(2.9 μm)[d]	2.24
					270[g]	(2.9 μm)[d]	

[a]C = CeO_2, Z = $(Zr,Y)O_2$, Y = Y_2O_3.
[b]In-plane texture, FWHM.
[c]0.33-μm-thick YBCO.
[d]Corresponding YBCO thickness for maximum $K_c(t)$.
[e]Characteristic "decay" constant, t_0, of the J_c thickness dependence obtained from a simple exponential fit in the interval 0.3 to 3 μm: $J_c = J_c(0)\exp(-t/t_0)$.
[f]Inferred by extrapolation from the H-field dependence of the critical current density.
[g]Measured on a patterned bridge.

The YBCO coatings were grown from precursors containing controlled mixtures of Y, BaF_2, and Cu. The precursors were deposited by simultaneous evaporation from three e-beam sources in a vacuum environment (10^{-6} to 10^{-5} Torr). The precursors were annealed (without intermediate processing) in a furnace, in flowing gas mixtures at atmospheric total pressure. Because of a limited source supply, multiple deposits were used for precursors thicker than 1 μm. However, all films were converted into YBCO during a single heat treatment. Annealing temperatures ranged between 740 and 790°C; the duration was adjusted according to precursor thickness and an average YBCO growth rate of ~1 Å/s. The oxygen partial pressure was set at 200 to 300 mTorr. Added H_2O vapor, needed to initiate YBCO formation, was kept to partial pressures less than 5 Torr. Ballast gas was either nitrogen or helium. Flow rates were adjusted to plug-flow velocities of ~4 m/min (measured at room temperature).

A narrow range of suitable processing conditions has been gradually identified for thin, high critical current density YBCO coatings (on CeO_2); the processing of thicker coatings was found to depend even more on the processing conditions. The combination of H_2O pressure and flow velocity proved to be especially important for controlling the kinetics of growth. Because the proper annealing conditions had not been identified previously, a considerable part of this research involved process optimization. This report reflects a stabilization of this optimization process, providing a baseline for future process improvements. The epitaxy of the YBCO coatings, for all thicknesses, is appropriately described as predominantly or exclusively oriented to the *c*-axis. The normal-state resistivity (ρ) is commensurate with this epitaxy. Generally, ρ (300 K) is less than 300 μΩ.cm for YBCO on RABiTS™, often reaching values as low as ~220 μΩ.cm, and exhibiting overall a minor dependence on thickness. Somewhat higher ρ values resulted on IBAD-YSZ. A standard four-probe geometry was used to measure critical currents. Reported values refer to a 1-μV/cm criterion, self-field, and 77.3 K. Measurements were performed over the full substrate width (3 to 6 mm). In selected cases (primarily RABiTS™-NiW), self-field critical current readings could not be directly measured due to instrumental limitations. Extrapolated values from measurements in applied magnetic fields (H || c) were used in those instances. The YBCO thickness was inferred from a calibration of the evaporation rate monitors against RBS readings and a Tencor profilometer.

The thickness dependence of critical current density for YBCO coatings on each of the four templates is presented in Fig. 1.67. Depicted are the best critical current density values at the various thickness values for either substrate type. Also included are representative data for 0.33-μm-thick YBCO on (100) STO and (CeO_2 buffered) YSZ single-crystal substrates and a single datum for the intragranular critical current density for YBCO on RABiTS™-Ni(1) (measured via micropatterning). A comparison of these thin-film data clearly highlights the limiting role of substrate-propagated low-angle grain boundaries. Notably, the substrate-related distinction persists with increasing YBCO thickness. In the semi-log plot of Fig. 167, the dependences are nearly parallel, indicating a similar fractional reduction in critical current density independent of the "starting" value in thin YBCO coatings.[2] It follows that the substrate-propagated grain boundaries that limit critical current density in thin YBCO coatings also limit the critical current densities in the thicker coatings. Although the intragranular critical current density value also is expected to decrease with thickness, actual information about this dependence cannot be inferred from the data. This is a significant conclusion because most descriptions favor intragranular critical current density. The simplest scenario consistent with the observations is that whatever defects cause intragranular critical current density to decrease with increasing thickness, there is no interaction with the grain boundary dislocation cores. In this scenario, intragranular critical current density would decrease as shown in Fig. 1.67. On the other hand, a stronger

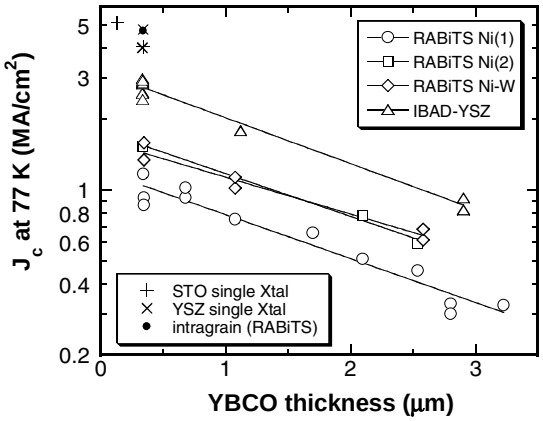

Fig. 1.67. Thickness dependence of the critical current density in ex situ YBCO films on four coated conductor substrates as well as thin coatings on $SrTiO_3$ (labeled STO) and YSZ single-crystal substrates. Intragranular value of critical current density for a thin coating on RABiTS™ Ni(1) was measured after micropatterning (ref. Feldmann et al.). Lines represent 120 exponential fits with t_0 values as indicated in Table 1.5 according to $J_c(t) = J_c(0)\exp(-t/t_0)$.

thickness dependence of intragranular critical current density could make its influence felt for coatings on better-textured substrates. To rule out this uncertainty and to obtain a consistent understanding, it would be valuable to determine the thickness dependence of intragranular critical current density independently, for example, by reexamining epitaxial films on single crystal substrates.

The lines depicted in Fig. 1.67 represent simple exponential fits to the data according to $J_c = J_c(0) \exp(-t/t_0)$. Values of the t_0 "decay" constants, ranging between 2.2 and 2.8 μm for the various substrate materials, are included in Table 1.5. An unsatisfactory aspect of this fit is the prediction that critical current density would tend toward zero with increasing thickness. Accordingly, K_c reaches a maximum for $t = t_0$. To examine the thickness dependence of critical current density in more detail, a combined dataset for the four coated-conductor substrates was created by normalizing thickness dependence of critical current density by the average measured value at t = 0.33 μm for YBCO coatings on the same substrate. This normalization effectively eliminates effects related to texture and/or substrate. The normalized data are plotted in Fig. 1.68 on a linear scale.[1]

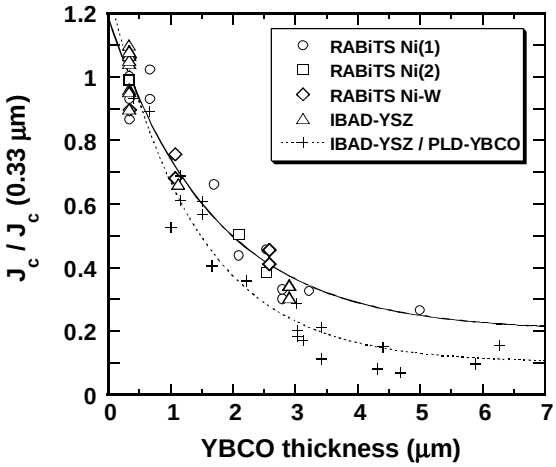

Fig. 1.68. Thickness dependence of the critical current density normalized by its value for a thickness of 0.33 μm for YBCO coatings on the four coated conductor substrates included in this study. The solid line represents a fit according to Eq. (1.1) in the text with $A = 0.2$, $B \cong 1$, and $t_0 = 1.67$ μm. Data for PLD-deposited YBCO on IBAD-YSZ reported by Foltyn et al. are included for comparison, normalized by $J_c(0.33\ \mu m) = 2.79$ MA/cm^2. The dashed line through these data represents a fit according to Eq. (1.1) with $A = 0.1$, $B = 1.18$, and $t_0 = 1.37$.

Consistent with the near-parallel dependences of Fig. 1.67, the data are seen to collapse onto a "universal" thickness dependence of critical current density, which we have fitted by using a more generalized expression originally proposed by Foltyn et al.:

$$J_c(t)/J_c(0.33\ \mu m) = A + B \exp(-t/t_0) \quad . \qquad (1.1)$$

In this expression, the parameter A describes a limiting critical current density value in thick YBCO coatings (beyond the present range of investigation) relative to thin-film critical current density values on the same substrate. $A = 0$ corresponds to the simple exponential fit described above, providing a technically acceptable fit over the experimental interval. However, small increments in A do not significantly affect the quality of fit. The extra term is accommodated by a decreasing t_0. An upper limit of $A = 0.2$ (with $t_0 = 1.67$ μm) was determined for the available data set. The calculated dependence is indicated in Fig. 1.68. A preliminary result from subsequent research beyond the 3-μm range [YBCO on RABiTS™-Ni(1)] agrees well with the predicted trend.

Using a similar normalization, data from the study of Foltyn et al. for YBCO on IBAD-YSZ are also included in Fig. 1.68. A normalizing value of $J_c(0.33\ \mu m) = 2.79$ MA/cm^2 was inferred from the data in Fig. 1.68 in the corresponding reference, consistent with a high degree of biaxial texture similar to the IBAD-YSZ template used here. A normalized plot of $K_c(t)/J_c(0.33\ \mu m)$ for the two data sets is presented in Fig. 1.69.[1]

A remarkable consistency in thickness dependences of critical current density is observed for t < 1.5–2 μm. For either YBCO processing technique, critical current density decreases by about 30% when the YBCO thickness is increased from 0.33 to 1 μm. The results diverge, however, for thicker

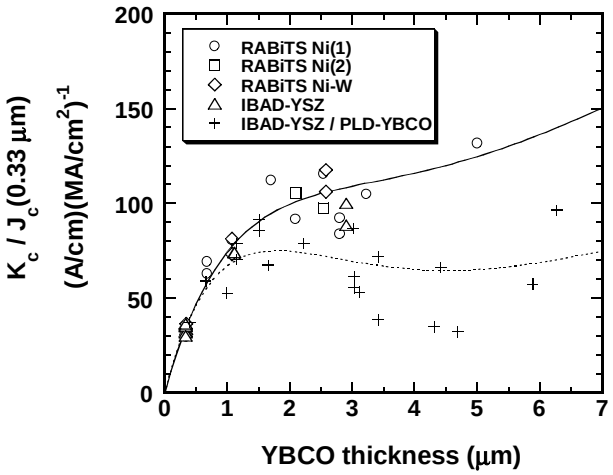

Fig. 1.69. Thickness dependence of the critical current K_c per centimeter conductor width normalized by the value of critical current density for a thickness of 0.33 μm for ex situ YBCO films on four coated conductor substrates and PLD-deposited YBCO on IBAD-YSZ from Foltyn. The solid and dashed lines were calculated from the fits presented in Fig. 1.68.

coatings, with the PLD data seemingly tending toward a lower "saturation" value. A fit according to Eq. (1.1) with $A = 0.1$, indeed, gives a satisfactory representation of the PLD data (optimized toward high critical current densities in the range $t > 3.5$ μm). Clearly, the parameter A delineates important tendencies of the material system associated with imperfect growth or film-substrate reactions. For example, $A = 0$, describing a $K_c(t)$ function that tends toward zero for large values of t, could depict catastrophic effects such as cracking or a chemical contamination of the YBCO (perhaps leading to a reduced transition temperature) due to material transport from the metallic substrate. A commonly observed deteriorative mechanism is that of a delayed film-substrate reaction involving only the top (CeO_2) buffer layer. Such reaction may disable a layered region in the YBCO in the substrate vicinity, leading to local dead layer. This scenario is potentially well described by a critical current density saturation value of $A = 0.1$. At intermediate thickness values, in the course of the deposition process, the loss of well-textured YBCO due to a gradual film-buffer reaction could lead to a net negative derivative dK_c/dt. After the reacting buffer layer material is depleted, however, additional deposits could eventually gain the upper hand, leading to a subsequent K_c increase for very thick YBCO coatings. Structural characterization of the interface region of the PLD YBCO coatings is consistent with this scenario; however, the additional surface dead layer apparently limits K_c to maximum values already reached at the critical thickness of 1.5 to 2 μm.

The ex situ YBCO films, by comparison, appear less influenced by substrate- and/or growth-induced dead layers. This is reflected in the larger A value and the observed monotonic $K_c(t)$ dependence. First indications from electron microscopy and critical current density–ion-milling studies currently in progress indeed confirm the absence of significant dead layers in these YBCO coatings. The YBCO structure is dense at least to a thickness of 2.9 μm. The derivative dK_c/dt, however, is nonmonotonic (predicted to reach a minimum at $t \cong 3.3$ to 3.4 μm according to the fit with $A = 0.2$), suggesting that materials-related effects still dominate. A subtle but significant difference between in situ and ex situ processes with respect to the interpretation of the thickness dependence of critical current density lies in the fact that, in the case of in situ growth, the initial and intermediate stages of growth are independent of the intended final thickness. A time evolution of deteriorative processes thus may be inferred from the comparison of films with different thicknesses. For ex situ films, similar time-dependent effects could occur; however, due to material transport inside the precursor layer that facilitates epitaxial YBCO nucleation at the substrate interface, the precursor thickness itself becomes a parameter of the growth process. The observation of the thickness dependence of critical current density described by Eq. (1.1) with reduced saturation values A, then, does not strictly point toward a deteriorative film-substrate reaction but could also reflect an overall less-optimized growth process (e.g., a process with enhanced secondary phase segregation). The results of improved processing in this scenario should be reflected in a gradually increasing A value.

We conclude this analysis with a discussion of the consequences of a reduced critical current density in thick YBCO deposits relative to the effect of an improved substrate texture. The representation of Fig. 1.69 allows such comparison. If an arbitrary goal of K_c = 450 A/cm for a single YBCO coating were set (exceeding the currently achieved performance of first-generation multifilamentary composites), and a highly textured substrate such as the IBAD-YSZ featured in this study [J_c(0.33 μm) ≅ 3 MA/cm^2] were used, Fig. 1.69 would indicate that ex situ YBCO coatings of about 7 μm thick would be needed to meet the K_c target (it is assumed that the fit with A = 0.2 accurately describes the thick-film regime). If a better substrate texture quality were available, however, approaching single-crystal limits even further by enabling J_c(0.33 μm) ≅ 4 MA/cm^2, the corresponding YBCO thickness would shrink to ~3 μm. Such performance may already be achievable with the presently optimized annealing conditions. These predictions are an immediate consequence of the texture-invariant thickness dependence of the critical current density witnessed in this study.

1.11.1 References

1. S. R. Foltyn et al., High-T_c Coated Conductors—Performance of Meter-Long YBCO/IBAD Flexible Tapes," *IEEE Trans. on Appl. Supercond.* **9**, 1519 (1999) and references therein.
2. Feldmann, D. M., et al., "Inter- and Intragrain Transport Measurements in $YBa_2Cu_3O_{7-x}$ Deformation Textured Coated Conductors," *Appl. Phys. Lett.* **79**, (24) 3998–4000 (2001).

1.12 Ni-Cr TEXTURED SUBSTRATES WITH REDUCED FERROMAGNETISM FOR COATED CONDUCTOR APPLICATIONS

J. R. Thompson (ORNL, University of Tennessee, Knoxville); A. Goyal, D. K. Christen, and D. M. Kroeger (ORNL)

1.12.1 Introduction

Pure nickel lends itself well to fabrication of substrates with the desired {100}<100> texture needed for the RABiTS™ approach to coated conductors; however, its ferromagnetism, with a transition temperature of 627 K and a saturation magnetization of 57.5 emu/g at T = 0, complicates the design of high-field magnets for critical applications (e.g., magnetic resonance imaging, accelerators). Furthermore, use of Ni-based tapes in ac applications runs the risk of increased energy loss due to hysteretic loss in the magnetic material. The actual magnetic energy loss per cycle of applied magnetic field is given by the area enclosed within a magnetization loop, and this varies with the magnetic "hardness" of the ferromagnet.

With these considerations, it is clearly desirable to develop suitable alloys with reduced ferromagnetism that can also be successfully biaxially textured. The difficulty in forming such substrates stems from the fact that even minor additions of alloying additions greatly affect the ability to produce a dominant biaxial texture in pure fcc metals. Recently, methods have been developed to fabricate cube-textured alloy substrates with reduced magnetism. The magnetic properties of a series of Ni-Cr alloys possessing lower Curie temperatures and lower saturation magnetization (M_{sat}) are reported here. As demonstrated in this section, these materials reduce or eliminate the potentially undesirable ferromagnetism of pure Ni while retaining the ability to be biaxially textured.

1.12.2 Experimental Aspects

A series of alloys was prepared from 99.99% purity starting elements. Appropriate mixtures were vacuum-arc melted and dropped into copper moulds to form rods of the appropriate composition. $Ni_{1-x}Cr_x$ materials were investigated with nominal compositions x = 0, 7, 9, 11, and 13 at. % Cr. Details of composition, obtained by inductively coupled plasma analysis, are given in Table 1.6. The materials were biaxially textured by rolling deformation followed by annealing at 1050°C for 2 h in vacuum with a $P(O_2)$ less than 10^{-7} Torr. For magnetization measurements, the 0.13-mm-thick sheets were cut into 5 × 5 mm pieces. Generally, a stack of three to five pieces was mounted in a thin plastic tube for magnetic measurements. The magnetic field was applied parallel to the plane of the sheets to minimize demagnetizing effects. In an additional experiment to assess the magnitude of energy loss due to ferromagnetic hysteresis after a representative amount of work-hardening, a foil of $Ni_{93}Cr_7$ was controllably deformed. The foil was wrapped around a 9-mm mandrel, flattened, then reverse-wrapped, and again flattened for one deformation cycle. It was studied at 77 K with the magnetic field applied either parallel or perpendicular to the plane of the foil. For comparison, the hysteretic loss in biaxially textured Ni after three complete deformation cycles was investigated as well.

Table 1.6. Summary of alloy composition and magnetic properties of Ni-Cr alloys

Nominal composition	Cr x (at. %)	T at peak ($d\chi/dT$) (K)	T_c (K)	θ_p (K)	M_{sat} (G-cm^3/g)
Pure Ni	0		627	–	57.5
Cr-7 %	7.2	245	248	~260	23.1
Cr-9 %	9.2	120	115	155	12.6
Cr-11 %	11.1	17	20	37	4
Cr-13 %	13.2	–	<10	–	0.4

The magnetic studies were conducted in a superconducting quantum interference device (magnetometer) at temperatures between 5 and 300 K, in magnetic fields up to 65 kOe. The isothermal mass magnetization loop at various temperatures and the "susceptibility" (M/H vs T) in fixed field were measured; normally, H = 1 kOe. Dimensionally, the mass magnetization M [M = (magnetic moment)/(mass of alloy)] has units of emu per gram; M = G-cm^3/g. To record powder diffraction patterns, a Philips model XRG3100 diffractometer and Cu K_α radiation were used. A Picker four-circle diffractometer was used to determine the texture of the films by omega and phi scans. Pole figures were collected to determine the percentage of cube texture.

1.12.3 Magnetic Properties of Textured NiCr Alloys

Figure 1.70 shows the temperature dependence of the mass magnetization [$M(T)$] of the $Ni_{1-x}Cr_x$ alloys measured in a 1-kOe applied magnetic field. Qualitatively, it is evident that magnetization decreases quickly with the addition of Cr. Also, the transition temperature, noted on the figure, steadily diminishes. The transition temperature values were obtained from the following relation: spontaneous magnetization $M \propto (T_c - T)^\beta$ with β = 1/3.10. Figure 1.71 illustrates this dependence by plotting M^3 vs T, wherein a linear extrapolation to $M^3 = 0$ yields values for transition temperature. In this process, data very close to the transition temperature were ignored, where M is influenced by presence of the applied field. The power law dependence describes the data rather well for a substantial temperature range below the transition temperature (see Fig. 1.70 and Table 1.6 for data from all alloys).

For coated-conductor applications, one anticipates that the materials will be employed in the presence of large magnetic fields and for generating such fields. Thus it is useful to examine the field-dependent

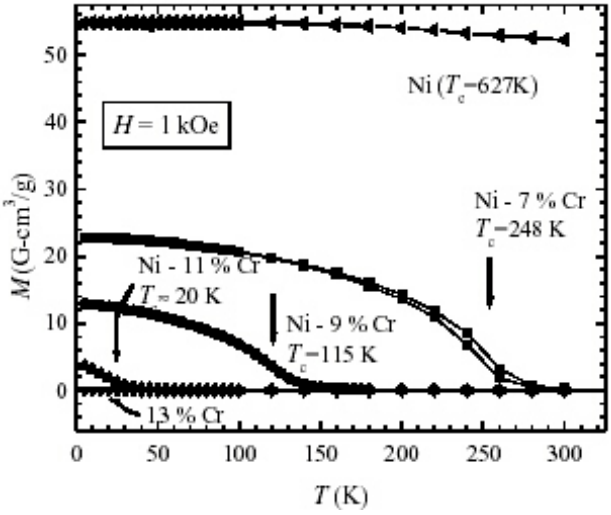

Fig. 1.70. The mass magnetization of $Ni_{1-x}Cr_x$ alloys vs temperature, measured in an applied field H = 1 kOe applied parallel to the plane of the foils. Nominal Cr concentration x is given in atomic percent.

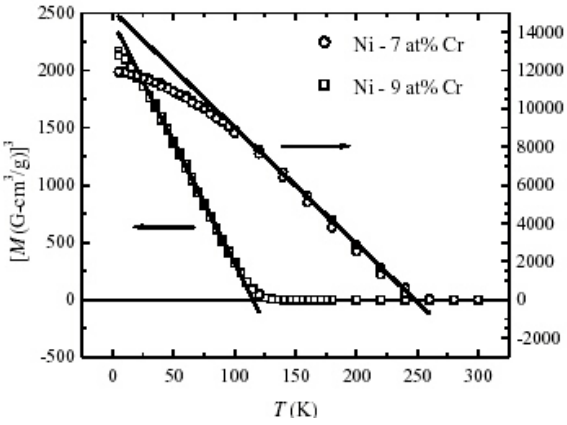

Fig. 1.71. A plot of M^3 vs temperature T. Straight lines show the extrapolation to M = 0 used to define the transition temperature.

magnetization at representative temperatures of 40 and 77 K (see Fig. 1.72). At these temperatures, it is evident from the "square" response of the 7 and 9 at. % Cr alloys that they are ferromagnetic. In contrast, the alloys with higher Cr content are paramagnetic and have significantly lower magnetization. From similar studies at 5 K, the M_{sat} values listed in Table 1.6 were obtained. Included in Fig. 1.72 are data for annealed type 304 stainless steel, a common construction material in cryogenic applications; a comparison shows that the magnetization of the Ni-11 at. % Cr alloy is comparable with the type 304 stainless steel and that the 13 at. % Cr alloy is even lower.

For the paramagnetic state above the transition temperature, for an applied field that is not too large (here H = 1 kOe), the ratio of magnetization to applied magnetic field (M/H) closely approximates the initial differential susceptibility $\chi_{mass} = dM/dH$. Thus the data may be analyzed by using a Curie-Weiss dependence,

$$M/H = C/(T - \theta_p) \quad , \tag{1.2}$$

where the Curie constant $C = N_A \mu_B^2 \, p_{eff}^2/3k_B$,
θ_p is the paramagnetic Weiss temperature,
N_A is Avogadro's number,
μ_B is the Bohr magneton,
p_{eff} is the effective magnetic moment per atom,
k_B is Boltzmann's constant.

The reciprocal H/M vs T is plotted in Fig. 1.73, which shows a reasonable description of the data. The resulting values for the Weiss temperatures are shown in Table 1.6. At higher temperatures, some samples deviate from the simple Curie-Weiss relationship; this may be due to deviations from the overly simple temperature dependence of Eq. (1.2) or to the presence of an additional paramagnetic contribution or contributions (e.g., nominally temperature-independent orbital terms not included in this expression). As is frequently the case for ferromagnetic materials, the values for the paramagnetic Weiss temperature lie near the respective transition temperatures but rarely coincide exactly. In Table 1.6, along with the paramagnetic Weiss temperatures, are values of the temperature at which $d(M/H)/dT$ is largest; the latter

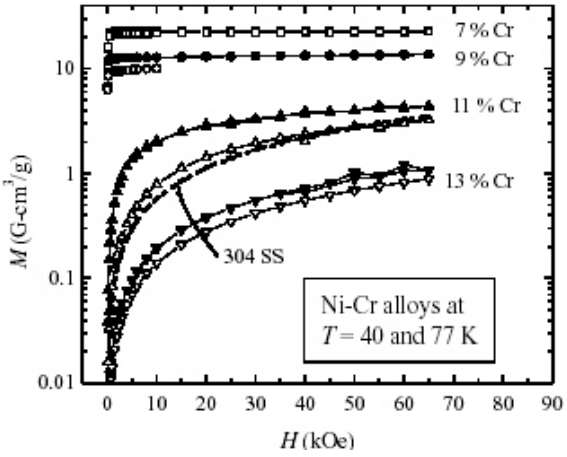

Fig. 1.72. The field dependence of the magnetization of $Ni_{1-x}Cr_x$ materials at 40 K (closed symbols) and at 77 K (open symbols). For comparison, the magnetization of annealed Type 304 stainless steel at 77 K is shown as a dotted line.

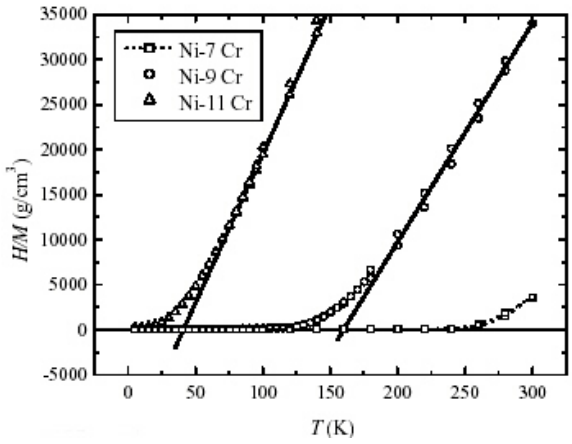

Fig. 1.73. The inverse "susceptibility" *H*/*M* vs temperature *T* for three ferromagnetic NiCr alloys. The straight lines show a simple Curie-Weiss dependence for alloys with 9 and 11 at % Cr.

provides a rough estimate of the transistion temperature, provided that the applied field (here 1 kOe) is not too large.

Some qualitative dependencies on Cr content are already apparent. More quantitative features are presented in Fig. 1.74. In Fig. 1.74(a) is the transition temperature that decreases quite linearly with Cr content, as shown by the solid line fitted to the present data. A simple linear extrapolation to the axis at $T_c = 0$ intersects at critical Cr concentration of 11.5 ± 0.4 at. %. This value lies slightly below the critical concentration of 13 at. % Cr deduced previously by Besnus et al.[1] These authors, whose results are included in Fig. 1.64, observed a "tail" in the dependence of transition temperature on Cr content near the critical Cr concentration. Included, too, are earlier results from the compendium of Bozorth,[2] in which many values were obtained by extrapolating from higher temperatures. The present results for the biaxially textured substrate materials lie close to those from some earlier studies but significantly below the values reported in Bozorth. Figure 1.74(b) presents the M_{sat} at T = 5 K. Again a linear decrease with Cr content is observed, as illustrated by the solid line, with an intersection at a Cr concentration of 12.0 ± 0.2 at. %. As in Fig. 1.74(a), the present results lie below the earlier data from Bozorth and agree within experimental error with the data of Besnus et al. Next were considered the hysteretic energy loss of two controllably deformed ferromagnetic substrate materials, the Ni-7 at. % Cr alloy and, for comparison, a biaxially textured strip of pure Ni. For the alloy, a foil of Ni-7 at. % Cr was wrapped around a 9-mm mandrel, flattened, reverse wrapped, then again flattened to simulate the work hardening that might be encountered in fabricating a superconducting component. The magnetization of the material is shown in Fig. 1.75 with the field applied either parallel to plane of the foil (steep curves related to a small demagnetizing factor) or normal to the surface (a flatter curve with much stronger demagnetizing effects). In either case, the material is relatively reversible, qualitatively indicating a modest energy loss due to magnetic hysteresis. Numerical integration of the loop area gives a hysteretic energy loss per cycle of 160 erg/g (1400 erg/cm^3) with the applied field parallel to the plane of the foil and 230 erg/g (2000 erg/cm^3) with the applied field normal to the surface. The coercive field at 77 K is 4 Oe.

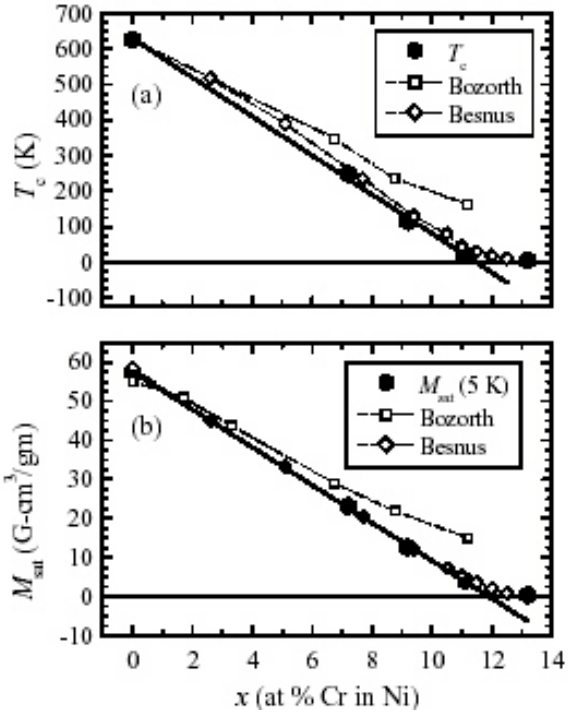

Fig. 1.74. Variation of magnetic properties of $Ni_{1-x}Cr_x$ alloys with Cr content *x*. (a) The transition temperature T_c obtained here and those reported by Bozorth (R. P. Bozorth, *Ferromagnetism* (IEEE Press, Piscataway, N.J., 1978), and Besnus et al. (M. J. Besnus, Y. Gottehrer, and G. Munshy, *Phys. Stat. Sol. B* **49**, 597, 1972). The line is a linear dependence fitted to the present $T_c(x)$ data. (b) The saturation magnetization at T = 5 K vs x.

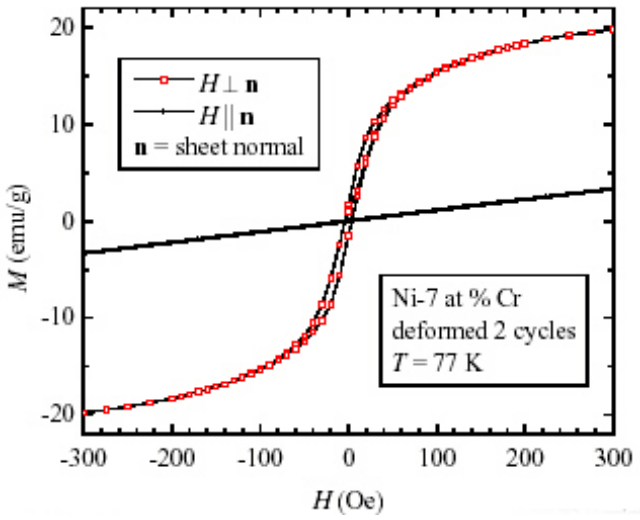

Fig. 1.75. Magnetization loops (expanded scale) for a deformed $Ni_{93}Cr_7$ foil at 77 K with magnetic field applied parallel or perpendicular to the plane of the foil. The magnetization is relatively reversible, with limited hysteretic energy loss per cycle.

The corresponding hysteretic loss was measured in an unalloyed tape of pure biaxially textured Ni. A 4 × 5 mm^2 foil was subjected to three complete cycles of deformation, also around a 9-mm mandrel. Its magnetization loop was measured at 77 K in the range ±800 Oe (the field was limited to this interval to avoid trapping flux in the superconductive magnet, which would distort the measurement.) The results are shown in Fig. 1.76. The steeper curve, with the applied field normal to the surface, approaches saturation. Integrating the area within this loop gives an energy loss per cycle of 2050 erg/g (18,200 erg/cm^3) and a coercive field of 7 Oe. The flatter curve parallel to the plane of the sample does not approach saturation, due to the large demagnetizing factor in this orientation and the higher saturation magnetization of pure Ni (57.5 emu/g = 512 G at T = 0). With this minor hysteresis loop, the area is notably lower, giving a loss per cycle of 500 erg/g (4450 erg/cm^3). The inset in Fig. 1.76 shows magnetization in applied fields large enough to saturate the material.

It is informative to compare the hysteretic losses in these substrates with the hysteretic loss arising from the superconductive material per se. For an estimate, assume a 50-µm-thick metal substrate, a typical RABiTS™ tape architecture, and an 8-mm-wide tape coated with 2.5 µm of YBCO. With a critical current density of 1 × 10^6 A/cm^2 at 77 K, this gives a critical current of 200 A; for ac operation at 60 Hz, assume a peak ac current of 100 A ($I_0 = I_c/2$ = 100 A). To estimate the superconductive energy loss, the theory of Norris[3] is used, which applies to a long isolated conductor with a critical current density that is independent of field. This theory, for the case of a round or elliptical wire, has been shown to provide a good description of the ac loss in YBCO coated conductors on Ni and on Hastalloy. For the

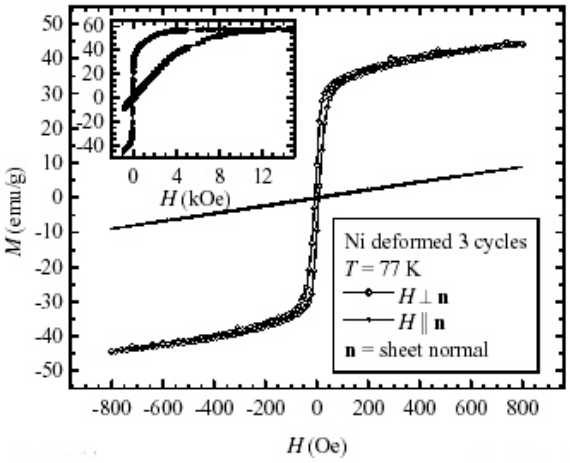

Fig. 1.76. Magnetization loops (expanded scale) for a deformed biaxially textured Ni foil at 77 K with magnetic field applied parallel or perpendicular to the plane of the foil. Inset: magnetization in large fields.

extreme case ($I_0 = I_c$), the Norris expression gives a loss per cycle per meter (SI units) of $L_c = (1/2p)m_0 I_0^2$ =, or 8 mJ/m-cycle; for $I_0 = I_c/2$, the loss is smaller by a factor of ~17 according to Norris (Table 3),[3] giving an L_c of 0.46 mJ/m-cycle. To obtain the common figure of merit for a coated conductor, the power loss per kiloampere-meter of composite material, one multiplies by the ac frequency (60 Hz) and the current ratio (1000 A/I_0) = 10. This yields a superconductive component to the hysteretic loss of 0.27 W/kA-m at $I_c/2$. At I_c, the Norris expression gives a loss of 0.012 W/kA-m × (I_c/1 A) at f = 60 Hz, yielding the value 2.4 W/kA-m at $I_o = I_c$ = 200 A.

In this example, there is 0.4 cm^3 of alloy per meter of tape. Assuming that the ambient ac field is sufficiently strong to carry the substrate around the entire hysteretic part of its magnetization loop, one has a ferromagnetic loss per cycle per meter of 0.07 mJ/m for the 7 at. % Cr alloy and 0.7 mJ/m for the pure Ni substrate. The corresponding power losses are 0.043 W/kA-m and 0.43 W/kA-m, respectively. Thus the alloy substrate increases the loss at $I_c/2$. by ~16 %, whereas the loss from the Ni substrate is comparable with that in the superconductor.

This example illustrates the magnitude of losses that might be encountered in power line applications. However, for peak currents near the critical current, the superconductive energy loss increases rapidly with peak currrent, faster than I_0^3, while it varies as $(I_0/I_c)^3$ when the current is small. Because the superconductive and ferromagnetic losses have different dependencies on peak current, their relative magnitude depends on how near the critical current the coated conductor is driven. In addition, the above illustration assumes the worst case, namely that the ferromagnetic loss is maximized: in a conductor and field configuration where the substrate experiences smaller ac field amplitudes, the ferromagnetic loss component diminishes. This decrease is evident in the lower loss per cycle for the Ni material with the applied magnetic field normal to the surface, where H < 800 Oe. Thus the total loss will depend both on the choice of substrate materials and on the operating conditions, I_0/I_c, and the conductor layout that affect the ac field experienced by the conductor.

Before concluding, it is useful for perspective to consider briefly the losses in the first-generation Ag-clad BSCCO tapes. These materials, too, are reasonably well described by the Norris expressions for the elliptical conductors presented in this section. For example, the predicted loss at the critical current is 0.012 W/kA-m × (I_c/1 A) for f = 60 Hz, which increases with critical current. The critical currents in typical BSCCO conductors give losses of 0.2 to 0.6 W/kA-m; these values are lower than those cited for YBCO because the critical current values are lower. For various power transmission projects using superconductive cables, the targeted maximum loss (which has been achieved with these materials) is 1 W/m at 2 kA$_{rms}$, corresponding to a specific loss of 0.35 W/(kA$_{peak}$-m). In the end, of course, a high critical current is desirable because it allows one to operate at a lower relative current, where losses decrease rapidly.

Overall, it appears that 7 at. % Cr alloy should be entirely satisfactory for many applications, obviating the need for higher Cr contents, for which the biaxial texturing is more difficult. The hysteretic losses in the deformed pure Ni are more significant, and their impact must be evaluated in light of the intended application and the ac field environment.

1.12.4 Texture in Ni-Cr alloys

All alloy compositions studied were successfully textured to obtain ~100% cube texture. In Fig. 1.77, this is illustrated by the background-corrected (111) pole figure for a Ni-13 at. % Cr substrate annealed at 1050°C for 2 h. Only four crystallographically equivalent peaks, corresponding to the {100}<100> cube orientation, are present in the pole figure. Quantification of the pole figure suggests ~100 % cube texture in the sample. Figure 1.78 shows a ϕ-scan revealing the degree of in-plane texturing in the substrate. The FWHM as determined from the ϕ-scan is 7.8°. Figure 1.79 shows ω-scans to demonstrate the degree of out-of-plane texturing in the same substrate as Fig. 1.76. Figure 1.79(a) was obtained with the sample rotated in the rolling direction. The FWHM of the texture is 5.7°. Figure 1.79(b) shows an ω scan with the sample rotated about the rolling direction, for which the FWHM is 8.9°. Clearly, these results demonstrate that Ni-Cr alloys with Cr contents as high as 13 at. % Cr can be thermomechanically processed to form substrates with very sharp and fully formed cube texture.

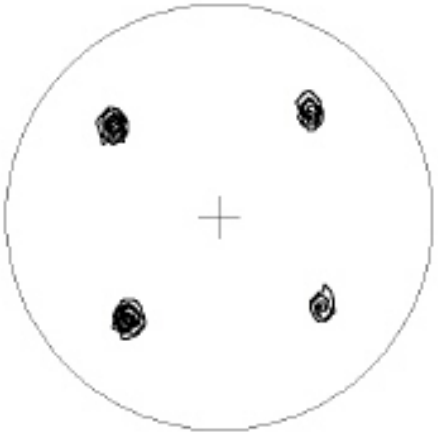

Fig. 1.77. A (111) pole figure for a Ni-13 at. % Cr substrate that was annealed at 1050°C for 3 h.

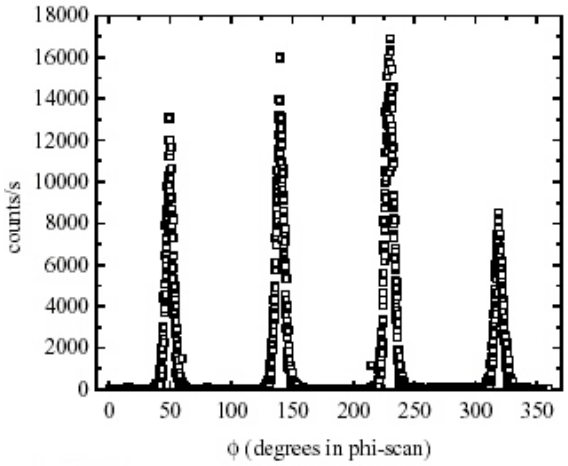

Fig. 1.78. A ϕ-scan showing the in-plane texturing in the substrate (same as Fig. 7). The FWHM is 7.8°.

1.12.5 Conclusions

This work shows that Ni-Cr alloys with much reduced or nonexistent ferromagnetism can be fabricated and successfully processed to have biaxial cube texturing. The hysteretic loss in a deformed sample of alloy was measured and compared with that in pure Ni; the results suggest that the magnetic loss of the 7 at. % Cr substrate in a coated conductor should be small compared with that in first-generation Bi-cuprate tapes and small compared with hysteretic losses in the superconductive coating.

1.12.6 References

1. R. P. Bozorth, *Ferromagnetism,* IEEE Press, Piscataway, N.J. (1978), pp . 307–308.
2. M. J. Besnus, Y. Gottehrer, and G. Munshy, *Phys. Stat. Sol.* B **49**, 597 (1972).
3. W. T. Norris, *J. Phys. D* **3**, 489 (1970).

1.13 PULSED ELECTRON DEPOSITION OF RE-BCO AS AN ALTERNATIVE TO PULSED LASER DEPOSITION

H. M. Christen, H. Y. Zhai, and A. Goyal

Despite the great advances of numerous YBCO deposition techniques, PLD still appears most promising for the deposition of thick films. Unfortunately, the technique suffers from the comparatively

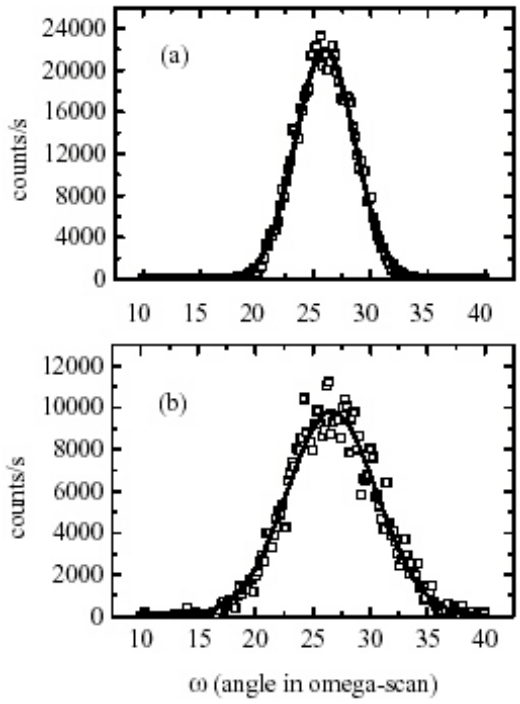

Fig. 1.79. Angular ω-scans showing the degree of out-of-plane texturing. (a) Sample rotated in the rolling direction, giving a FWHM of the texture of 5.7°. (b) Sample rotated about the rolling direction with FWHM of 8.9°.

high cost of excimer lasers. A technique that combines some of the advantages of PLD with a lower-cost method of producing an energetic deposition plasma would hold great promise for the production of coated conductors.

To understand the costs involved in PLD, we have developed a simple cost model to calculate the expense related to the production of laser energy as needed for the deposition of YBCO. Published and privately communicated information (S. R. Foltyn, Los Alamos National Laboratory; H. C. Freyhardt, University of Göttingen; Y. Iijima, Fujikura Ltd.) shows that under current conditions, 33 kJ of optical energy is needed to deposit a YBCO volume measuring 1 m × 1 cm × 1 μm. Using information provided by Lambda Physik, the current cost of producing 1 MJ of optical energy is approximately $100 if guaranteed (rather than expected) lifetimes for all components are assumed. If a critical current density of 1 MA/cm^2 is achieved, these numbers indicate a cost of $33/kA·m for the optical energy alone. Costs for other steps, such as tape production, buffer layer deposition, tape handling, and passivation, are assumed to be similar for all coated-conductor approaches and thus are not considered here. When the guaranteed laser component lifetimes are replaced with more realistic, expected values, the cost drops to $23/kA·m, and increased collection efficiencies in the PLD arrangement could reduce costs to $12/kA·m. For this cost to be reduced further, the critical current density will have to be increased significantly. For example, to reduce the cost of the required optical energy to less than $5/kA·m, a critical current density of 2.5 MA/cm^2 is required.

Pulsed electron deposition (PED) has only recently gained interest as a promising alternative to PLD for thin-film growth. The technique was first developed by C. Schultheiss and co-workers at the Max Planck Institute in Karlsruhe, Germany, and had then been applied to the growth of YBCO (see Fig. 1.80).[1] Since then, the technique has been improved significantly, and Neocera, Inc. (of Beltsville, Md.) introduced a commercial PED source to the market in 2000.

PED is conceptually similar to PLD except that an energetic electron beam (rather than a laser pulse) results in the formation of an ablation plume and that the excimer laser is replaced by a comparatively simple and cost-effective electron source. For the propagation of the electron beam in the deposition chamber, the

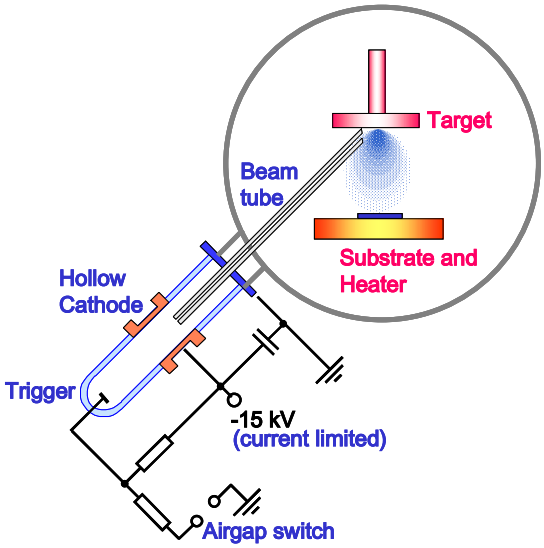

Fig. 180. Schematic representation of the pulsed electron deposition process.

background pressure has to be kept in the range of 5 to 30 mTorr, possibly the most stringent restriction on the approach. Much less information is available about the ablation process and plume-heating mechanisms in PED than in PLD, and pulse-to-pulse variations currently present one of the most significant issues.

In May 2002, a Neocera PED unit was installed at the Accelerated Coated Conductor Initiative (ACCI) facility. The unit was integrated into a chamber according to ORNL's design. A target-rastering mechanism had to be designed and built because the position of the electron beam remains fixed, unlike the PLD laser beam, which can be scanned across the target to prevent uneven target wear. Figure 1.81 shows the vacuum system and its main components.

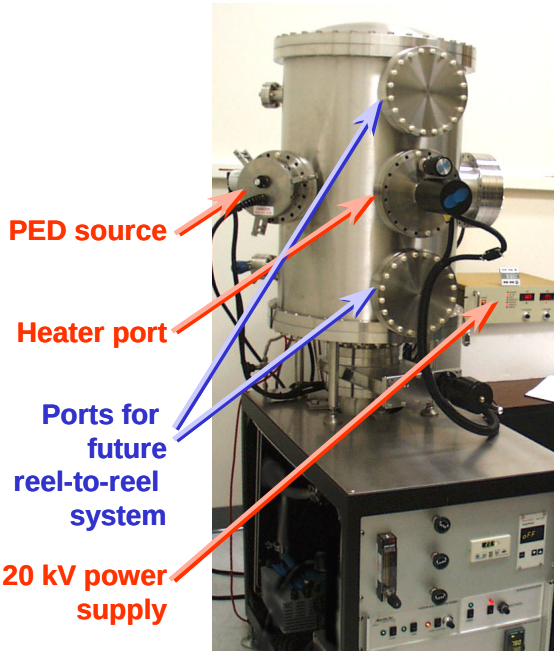

Fig. 1.81. PED system installed at ORNL.

A series of growth experiments clearly indicated the strong dependence of the film quality and growth rate on specific parameters of the method. Pulses are typically fired at 15 kV, and the "spark" is then guided to the target via a ceramic beam tube. Most importantly, a very strong dependence of the ablation rate on the distance from the beam tube to the target has been observed; only a narrow range of distances and background pressures have resulted in the formation of a strong ablation plasma (see Fig. 1.82).

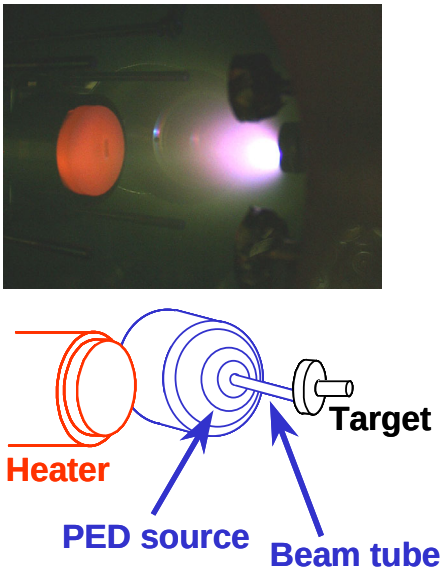

Fig. 1.82. Photograph of a PED ablation plume (YBCO) and schematic representation of the visible components.

Preliminary results for YBCO grown on STO are shown in Fig. 1.83, where a transition at 89.9 K with a width of $\Delta T_c \approx$ 2.5K is observed together with a room-temperature resistivity of about 300 μΩcm, which is indicative of the quality of the material. Additionally, GdBCO was grown both on STO substrates and on buffered Ni-W tapes (CeO_2/YSZ/Y_2O_3/Ni/Ni-W); the XRD results are shown in Fig. 1.84. These films are clearly of inferior quality compared with those produced here by PLD, and a careful investigation of the differences between these approaches is required.

On single-crystal STO substrates, YBCO with critical current densities exceeding 1.5 MA/cm^2 have been obtained, clearly showing the promise of the technique. However, these samples were deposited at 820°C, a temperature at which oxidation of the nickel tapes typically occurs. Although superconductivity was observed on GdBCO films deposited on buffered tapes, the corresponding critical current densities were negligibly small.

In collaboration with Neocera, GdBCO films were deposited at Neocera onto RABiTS™, onto which buffer layers had been deposited by PLD at ORNL. In this configuration, comparatively high

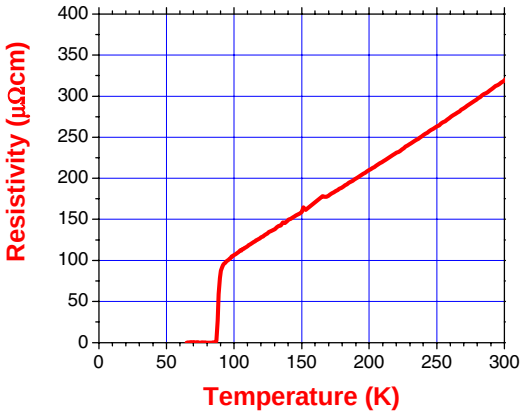

Fig. 1.83. Resistivity as a function of temperature for a YBCO film on an STO substrate.

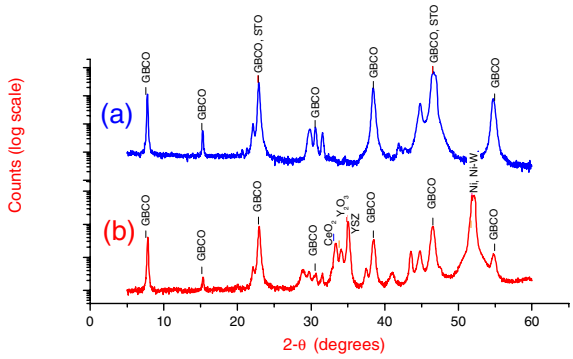

Fig. 1.84. XRD data for GdBCO on an STO substrate (a) and a buffered Ni-W RABiTS™ tape (b).

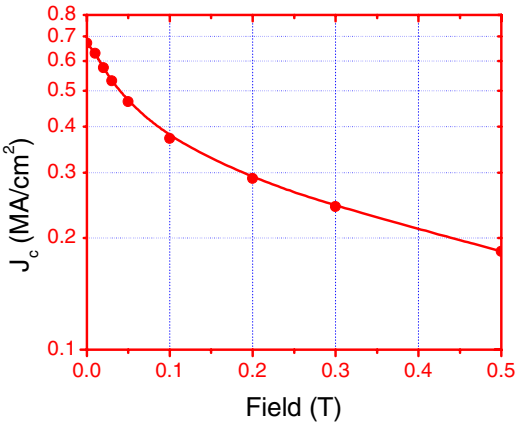

Fig. 1.85. Critical current density as a function of magnetic field for a GdBCO film grown onto a buffered Ni RABiTS™ tape. The GdBCO film was PED-deposited at Neocera, whereas the CeO_2/YSZ/CeO_2 buffer layer stack was deposited by PLD at ORNL.

critical current densities (0.8 MA/cm^2) were obtained. Figure 1.85 shows data for critical current density as function of magnetic field for one of these samples.

It is currently not clear why GdBCO results in better properties than YBCO. Figure 1.86 compares the microstructure of two films grown on $SrTiO_3$ substrates at 820°C and 20 mTorr of oxygen. The target-substrate distance was 3.5 cm, and the electron pulse repetition rate was 7 Hz. The deposition of 4000 to 4500 shots yielded a film with a thickness of 300 nm. The microstructure of the YBCO film is typical for what would be expected in the case of YBCO deposited at this elevated temperature.

To understand some of the differences between PLD and PED, we installed an ion probe to measure the kinetics of the deposition plume. Ion probes have been used extensively in PLD.[2] In the simple configuration used here, a negatively biased coaxial probe records the ion density in the plasma. Plotting the response as a function of time for different probe-target distances yields information about the velocity of expansion and thus the energetics of the deposition species. Figure 1.87 shows results for the PED and PLD systems. (The data for both systems were obtained at 20 mTorr, although typical film growth in PLD occurs at 100 mTorr or higher.) Clear differences are apparent between the two sets of curves. Most strikingly, a sharp maximum at around 8 μs is observed for PED, and this maximum appears not to scale with distance and hence is not simply related to the expansion of a gaseous plume. A secondary maximum is clearly traceable, but its velocity is much lower than that of the PLD plume. Further investigation of these phenomena is currently in progress.

To summarize, an initial study of using PED to grow RE-BCO showed that superconducting films can be obtained on single-crystal substrates. However, growth on buffered tapes has proven difficult due at least in part to the requirement of relatively elevated deposition temperatures. Experiments are currently

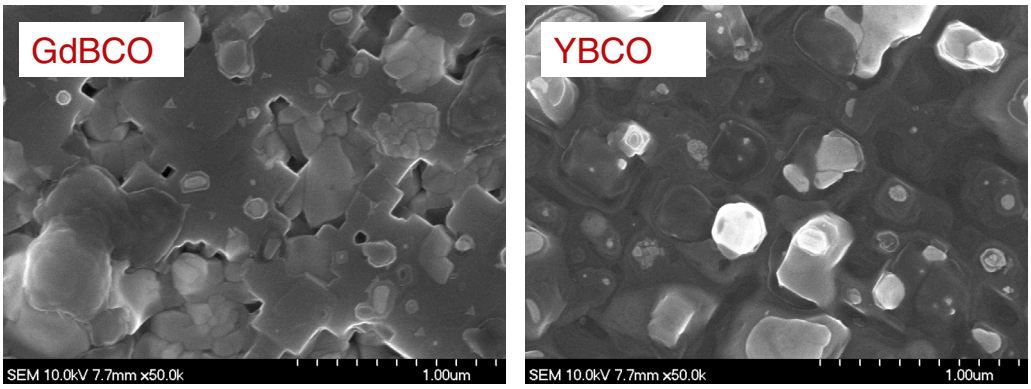

Fig. 1.86. SEM images comparing the microstructure of PED-grown GdBCO (left) and YBCO (right).

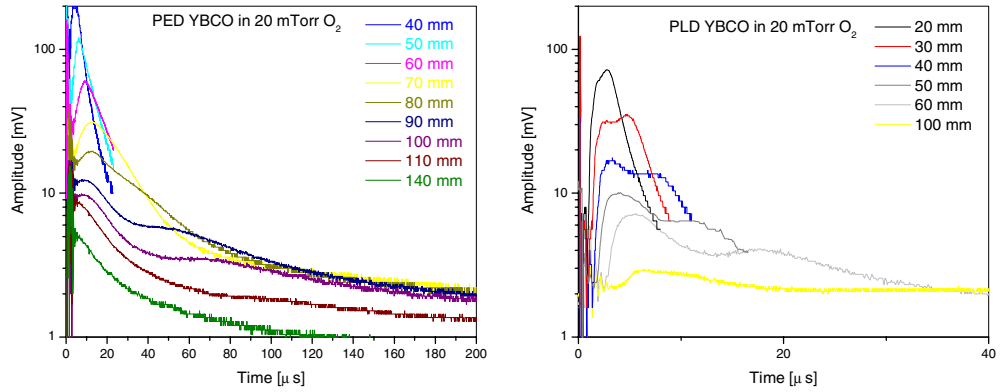

Fig. 1.87. Ion probe traces for different probe-target distances for PED (left) and PLD (right). The time scales differ. Both data sets were taken at 20 mTorr of oxygen.

being pursued to understand the differences between PED and PLD, including microstructural analysis and an ion probe investigation into the plume dynamics. Understanding the detailed differences between the cost-effective PED process and the highly successful PLD technique should allow us to determine the parameters under which PED can be used successful for large-scale coated-conductor fabrication.

The fruitful collaboration with L. Zhang (ORNL Engineering Science and Technology Division), C. M. Rouleau and D. B. Geohegan (ORNL Solid State Division), K. S. Harshavardhan and M. Strikovski (Neocera, Inc.), and the continued help of S. Sathyamurthy, D. F. Lee, D. M. Kroeger, F. A. List, and P. M. Martin is gratefully acknowledged.

1.13.1 References

1. Q. D. Jiang, et al., "Deposition of $YBa_2 Cu_3 O_{7-x}$ Thin Films by Channel-Spark Pulsed Electron Beam Ablation," *Thin Solid Films* 241, 100 (1994).
2. D. B. Geohegan, "Diagnostics and Characteristics of Pulsed Laser Deposition Laser Plasmas," in *Pulsed laser Deposition of Thin Films*, ed. D. B. Chrisey and G. K. Hubler, Wiley, New York, 1994.

1.14 ORNL'S NEW ROLLING MILL FOR THE ACCL ARRIVES

A. Goyal

ORNL received its new, custom-designed rolling mill (Fig. 1.88). We performed the first rolling on it during the week of April 15, 2002.

It is a four-high mill with 10-in.-diam × 8-in.-wide backup rolls. The carbide work rolls are 2.25 in. diam × 8 in. wide. The roll speed is 60 ft/min. The mill has a 40-hp, variable speed motor. Its approximate weight is 11,500 lb. It occupies about 84 × 96 × 108 in. of space (see Figs. 1.89 and 1.90).

The mill is expected to allow ORNL to investigate in detail the limits of the texture that can be obtained in long lengths of metals and alloys. It will also allow CRADA partners to explore sophisticated rolling procedures because most functions are either automated or mechanized.

The following are the descriptions of critical parts of the mill.

- **Housings and mill heads:** The rolling housings are amply proportioned steel designed for good rigidity in finished rolling. The rolling mill heads are chrome plated.
- **Rolls:** The mill is furnished with alloy steel rolls. The ends of the roll faces have a 45° bevel and are taper-ground about 0.01 in. from the end of the rolls.
- **Roller bearings:** Heavy-duty roller bearings equipped with antifriction thrust bearings prevent lateral movement of the rolls.
- **Roll adjustment:** The mill is furnished with double outboard gear. This double outboard gear adjustment is used for fine roll adjustment. An interlocking device is used for simultaneous or individual adjustment of the adjusting screws. The screws are made of alloy steel with hardened steel plates on the top of the boxes to take the thrust.
- **Screw-down mechanism:** A sophisticated power screw-down mechanism with feedback is provided for precise positioning of the roll separation.
- **Pinion gear:** A specially designed hardened alloy steel pinion gear equipped with heavy-duty antifriction bearings provides a very smooth finish.

Fig. 1.88. The new rolling mill arrives at ORNL.

Fig. 1.89. Mill and slitting unit placed in the ACC laboratory.

Fig. 1.90. Side view of the mill.

- **Mill drive:** The mill motor is coupled to combination reducer and herringbone pinion stand. The reducer and pinion stand are equipped with antifriction bearings. Drive is provided to the rollers from the reducer and pinion stand through universal joint couplings.
- **Entry and exit tables:** The entry and exit tables are fastened to the housings for alignment. They are readily adjustable vertically by adjusting screws plus plain side guides and cleaning pads.
- **Double recoiler assembly:** Rated for 50-lb capacity, the double recoiler assembly is mounted to the base extension of the mill. It maintains perfect alignment between the recoiler and rolls. The recoiler shaft is keyed and complete with a constant-torque electromechanical clutch/brake system. A welded steel base of heavy plate construction encloses the motor gear reducer, pinion gear box, rolling head, and recoiler for easy operation.
- **Load cells:** The mill is equipped with two load cells to accurately measure the downward pressure on the rolls.
- **Coil hold-down:** This device is used to ensure safety of the operator when working with large coils.
- **Filtration system:** The mill is equipped with a 2-μm, circulating-oil absolute filtration system to ensure prompt removal of particles.
- **Tensioning system load cells:** The mill is equipped with two load cells on either end to accurately control and measure the applied tension during reel-to-reel rolling.

1.15 CRYSTALLINE PHASE DEVELOPMENT DURING VACUUM CONVERSION OF BARIUM FLUORIDE PRECURSOR ON METALLIC SUBSTRATES

F. A. List, E. D. Specht, L. Heatherly, K. J. Leonard, D. F. Lee, and D. M. Kroeger

1.15.1 Introduction

A vacuum conversion system with in situ XRD has been developed to identify ranges of process parameters that lead to more rapid and complete conversion of precursor to high-performance YBCO superconductor tape. Conversions have been performed in this system for a variety of conversion times, temperatures, ramp rates, water vapor pressures, and oxygen pressures. Only a subset of the results is presented and discussed in this section. Although the results of this effort are strictly applicable to only those precursors and buffered substrates considered here, processing trends might be more generally applicable to many YBCO conductors derived from precursor conversion.

1.15.2 Experimental

All samples were cut to a length of 3 cm from the same continuously processed 1-cm-wide, 50-μm-thick, ~1-m-long tape. The tape consisted of a biaxially textured Ni-3at%W substrate on which epitaxial buffer layers of Y_2O_3 (~200 Å), YSZ (~2500 Å), and CeO_2 (~200 Å) were deposited. The Y_2O_3 was deposited at ~600°C by e-beam evaporation of metallic yttrium in a vacuum containing ~5×10^{-5} Torr H_2O. The YSZ and CeO_2 were deposited at ~650°C by magnetron rf sputtering of oxides in the presence of ~3×10^{-5} Torr H_2O. BaF_2 precursor (~3000 Å) was then deposited at ~100 to 200°C on the buffered tape by e-beam co-evaporation of metallic yttrium, BaF_2, and copper with ~2×10^{-5} Torr H_2O. RBS confirmed the precursor thickness and cation ratio (Y:Ba:Cu = 1:2:3).

Each sample was spot-welded to nickel leaders of similar cross section and was suspended between two water-cooled copper electrodes. A slight tension was provided to the sample with counterweights (~100 g) attached to each leader. A new, 75-μm-diam, type K thermocouple pair was spot welded to the edge of each sample to monitor substrate temperature. Resistance heating of the metallic substrate

controlled the temperature of the sample. A zero-crossing, phase-angle-fired, 60-Hz current controller was used to reduce thermocouple offset and noise. Linear ramp rates to the maximum conversion temperature were typically 25°C/min and ranged from 5 to 500°C/min. The maximum conversion temperature was varied from 620 to 820°C. The temperature stability at the maximum conversion temperature was ~0.5°C, and the average quench rate following conversion was >20°C/s to below 200°C.

Conversion of the BaF_2 precursor to YBCO was accomplished in a sealed, all-metal, hydrocarbon-free vacuum chamber. A base pressure of $\sim 5 \times 10^{-7}$ Torr was attained after a pumpdown of ~2 h. A quadrupole mass spectrometer revealed that water vapor was the major component of the residual gas. During conversion, the $P(O_2)$ and $P(H_2O)$ were controlled with manual precision leak valves. Either a capacitance diaphragm manometer (for pressures ≥ 0.5 mTorr) or a cold cathode ionization gauge (for pressures < 0.5 mTorr) was used to first establish water vapor pressure (generally 0.01 to 5 mTorr). Next, the capacitance diaphragm manometer was used to establish the $P(O_2)$ (generally 1 to 200 mTorr). During conversion, the oxygen leak valve was manually adjusted to maintain the desired total pressure. After conversion, the oxygen leak valve was closed and the water vapor pressure was checked for drift throughout the conversion. Drift of water vapor pressure was found to be typically less than ±10%.

Energy dispersive X-ray diffraction (EDX) continuously monitored the development of crystalline phases during precursor conversion. A fixed tungsten anode, operated at 40 kV and 30 mA, generated X rays. Collimating slits provided white radiation to the sample through a 250-μm-thick beryllium vacuum window at a 15° incident angle. Scattered radiation at a 15° take-off angle was detected with an energy-dispersive germanium detector through another beryllium window and Soller slits.

Figure 1.91 (upper) shows an X-ray spectrum for a converted sample obtained in 20 min with the EDX system. For comparison, Fig. 1.91 (lower) shows an X-ray spectrum for the same sample obtained in the same time with a standard θ-2θ diffractometer by using a 50-kV, 30-mA copper anode and a scintillation detector. Although both spectra show similar diffraction features, the EDX spectrum shows lower 2θ resolution and fluorescence peaks. The two major advantages of this EDX system are its simplicity (no moving components) and the fact that spectra are collected simultaneously for the full range of 2θ. Scanning dead time, timing offset, and failure to monitor unexpected peaks are thus reduced. Throughout precursor conversion, complete EDX XRD spectra were recorded every 2 min for each sample. Following conversion, standard θ-2θ spectra were recorded for each sample.

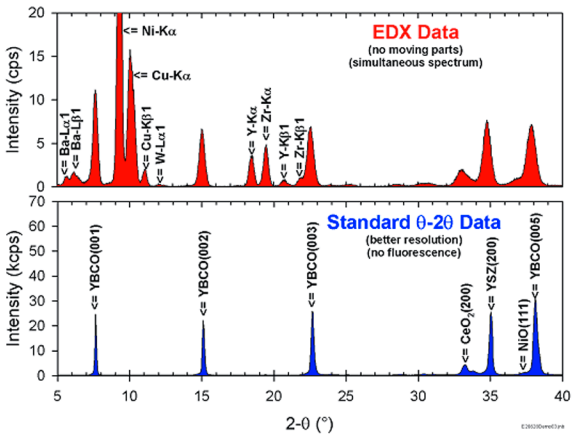

Fig. 1.91. Comparison of data obtained for the same YBCO tape using EDX and standard θ-2θ X-ray techniques.

Transport critical current was measured in liquid nitrogen (~77 K) and self-field by the standard four-probe technique with a voltage probe spacing of 0.4 cm and a 1-μV/cm criterion for critical currrent. Prior to the critical-current measurements, samples were sputter-deposited with silver (~1 μm thick) for electrical contacts and were oxygenated at 510°C in flowing pure oxygen at 1 atm for 60 min.

1.15.3 Results and Discussion

Conversion of the BaF_2 precursor to YBCO involves thermally ramping the precursor to an elevated temperature (typically ~740°C) in the presence of oxygen and water vapor and maintaining that

temperature for a time sufficient for conversion to complete. Oxygen is required to maintain thermodynamic stability of the YBCO, and water vapor participates in the removal of fluorine from the precursor. Process parameters investigated in this work include conversion time, ramp rate, water vapor pressure, oxygen pressure, and temperature. In this report, only results for variable conversion temperature for fixed conversion time, ramp rate, water vapor pressure, and oxygen pressure are presented and discussed. All processing has been conducted in the absence of a carrier gas.

Figure 1.92 shows EDX results obtained for five precursor samples for which the conversion temperature was varied. The conversion temperature ranged from 650 to 770°C. Samples were heated at a linear ramp rate of 25°C/min to the conversion temperature in 200 mTorr oxygen and 0.05 mTorr water. The total conversion time was generally 210 min. The total conversion time was extended to 270 min for the lowest conversion temperature to ensure complete conversion. At approximately the time at which the conversion temperature is first reached (time = 0 min in Fig. 1.92), the YBCO (002) intensity begins to rise from zero at a rate that is roughly linear with respect to time. The rate of rise of the YBCO (002) intensity decreases with decreasing conversion temperature.

Figure 1.92(b) shows the EDX intensity for a diffraction peak corresponding to a d-spacing of 3.58 Å as a function of time. This peak may arise from scattering from (111) planes of both BaF_2 and Y-Ba oxyfluoride. Wu et al.[1] have shown that crystalline Y-Ba oxyfluoride plays a significant role during precursor conversion. The crystal structure and lattice parameter for the Y-Ba oxyfluoride are indistinguishable from those for BaF_2 by standard techniques. For all conversion temperatures, the intensity of the d = 3.58 Å peak passes through a maximum within ~10 min after reaching the conversion temperature and then decays to zero at the same time that the YBCO (002) intensity reaches a plateau.

Figure 1.93 shows θ-2θ intensities, precursor conversion rate, and critical current as a function of conversion temperature for the five samples. The precursor conversion rate is taken to be the precursor thickness (3000 Å) divided by the time at the conversion temperature required to reach the plateau for the

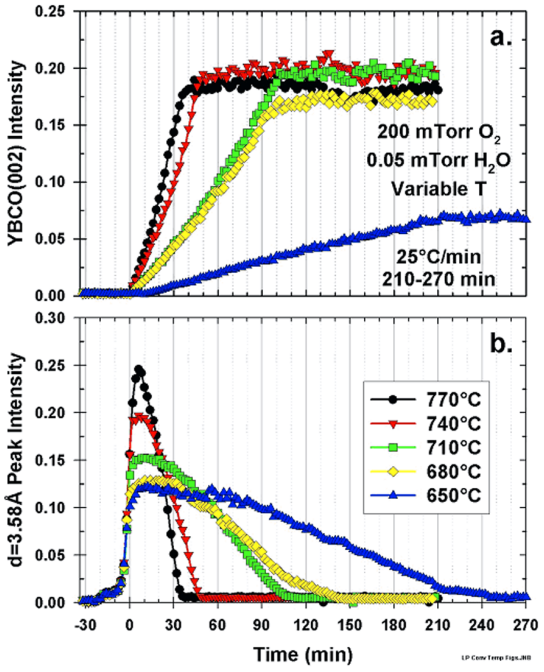

Fig. 1.92. EDX diffraction data obtained during precursor conversion for different conversion temperatures.

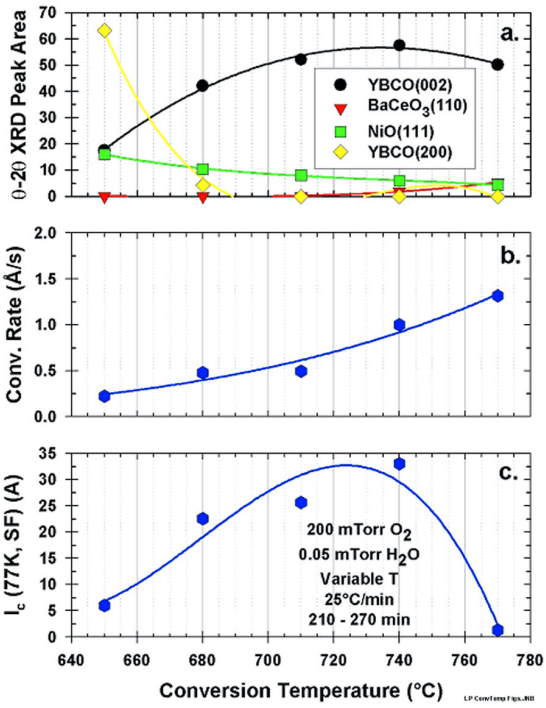

Fig. 1.93. Some properties of YBCO tapes prepared at different conversion temperatures.

YBCO(002) intensity. For this range of temperature, the precursor conversion rate increases as conversion temperature increases. The critical current exhibits a maximum for a conversion temperature of 740°C (I_c = 33.0 A, J_c = 1.20 Ma/cm^2). Low critical current, high NiO (111), and high YBCO (200) (a⊥ YBCO) are observed after conversion for low conversion temperature. For high conversion temperature, low critical current and high $BaCeO_3$ (110) are observed.

Rapid conversion of BaF_2 precursor to high-performance YBCO requires process optimization involving many process variables. Presented here are a few results of a more extensive investigation to better understand the limitations of the BaF_2 precursor route to YBCO coated conductor fabrication. A complete presentation of results is forthcoming.

1.15.4 Reference

1. L. Wu et al., "Nucleation and Growth of $YBa_2Cu_3O_x$ on $SrTiO_3$ and CeO_2 by a BaF_2 Postdeposition Reaction Process," *J. Mater. Res*. **16**(10), 2869–84 (2001).

1.16 SURFACE ROUGHNESS MEASUREMENTS FOR THE DEVELOPMENT OF YBCO COATED CONDUCTORS

F.A. List

A commercially available laser scatterometer (Model 5872, Optical Dimensions, LLC) has been equipped with a tape handler to evaluate the optical surface roughness of lengths of conductor at various stages of completion and thus to assist in the development of YBCO coated conductors. Thus far, nearly 500 m of tape have been evaluated with this equipment for our industrial collaborator and for our internal use. Measurements of surface roughness have contributed to improvements in both processing and quality control.

The scatterometer measures roughness for a 1×5 mm region at a rate of ten readings per second. Average roughness ranging from 2.5 to 1000 nm RA can be measured. Typical tape speed is 1 m/h, and tape capacity is 40 m of 50-μm-thick tape. Figure 1.94 shows typical roughness data obtained for an 11-m length of annealed nickel tape. The raw roughness data for this tape consists of ~5×10^5 readings. Distribution analysis of the raw data leads to a mean roughness of 9.6 nm and a standard deviation of 1.4 nm. Spectral (Fourier transform) analysis reveals no cyclic components to roughness. These data provide part of a baseline to which other roughness data can be compared.

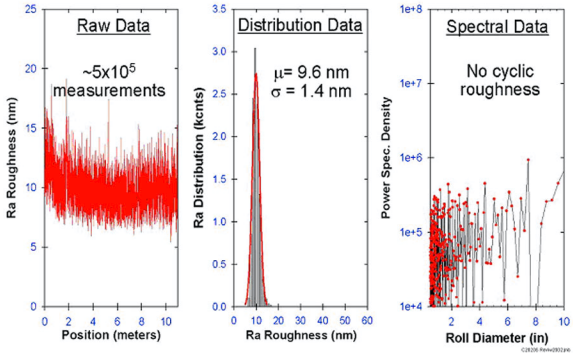

Fig. 1.94. Typical surface roughness data for an 11-m annealed nickel tape.

An example of the use of surface roughness measurements to control quality during conductor processing is illustrated in Fig. 1.95. Periodic spikes in roughness are visible over the entire length of an 8-m piece of fully buffered tape. Spectral analysis of the roughness data indicates that the fundamental period of the spikes is 28.25 cm. Knowing the precise period of the spikes facilitates identification of their origin. Specifically, a once-around defect for a 3.54-in.-diam roll leads to a defect on the tape every 28.25 cm. Examination of the equipment used to process this tape revealed a defective 3.53-in.-diam idle roll. Repair of the defective idle roll eliminated the spikes in roughness.

A second example of the use of surface roughness measurements to control quality is illustrated in Fig. 1.96. The roughness was unusually high for a 7.5-m length of fully buffered tape (μ = 33.3 nm) and displayed a bimodal distribution. Microscopic examination showed the surface of the tape to have a mottled appearance suggestive of scattered residue associated with liquid droplet drying. A defective tape-cleaning process was subsequently identified as the cause of this abnormal surface roughness.

Figure 1.97 shows an example of the role played by surface roughness measurements in annealing metallic substrate tapes to develop biaxial texture. A 4.2-m length of Ni-3%W tape that had been annealed at three different temperatures along its length was characterized by diffraction and surface roughness. Although texture improved (lower $\Delta\omega$ and $\Delta\phi$) as anneal temperature increased, surface roughness increased. Better epitaxy and ultimately better conductor performance are believed to arise from substrates showing better texture and lower roughness. Figure 1.97 quantitatively illustrates the trade-off between crystalline texture and surface roughness associated with optimization of heat treatment for metallic substrate tapes.

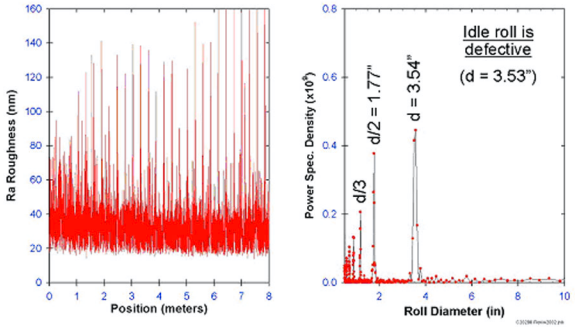

Fig. 1.95. Roughness data obtained for a fully buffered tape when using a defective idle roll during processing.

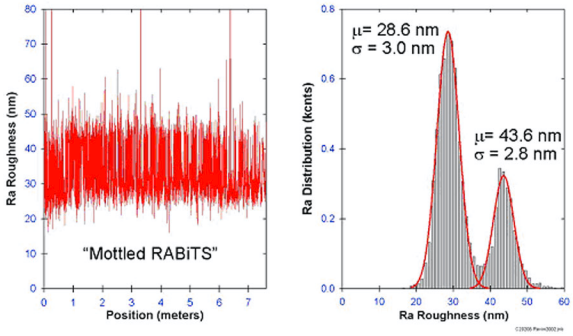

Fig. 1.96. Roughness data obtained for a fully buffered tape when using a defective cleaning process.

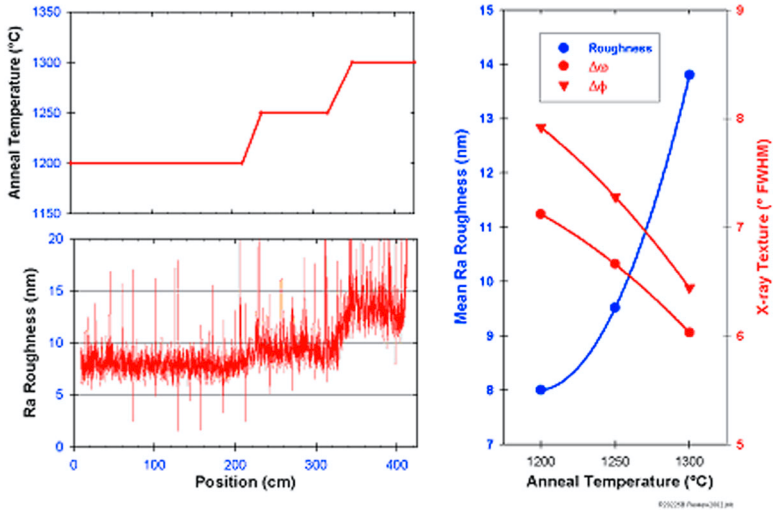

Fig. 1.97. Surface roughness and X-ray crystalline texture for a Ni-3% W tape annealed at three temperatures.

1.17 MICROSTRUCTURE CHARACTERIZATION OF THE THICKNESS DEPENDENCE OF CRITICAL CURRENT DENSITY OF YBCO ON RABiTS™

K. J. Leonard, B. W. Kang, A. Goyal, D. M. Kroeger, J. W. Jones, S. Kang, N. Rutter, M. Paranthaman, and D. F. Lee

1.17.1 Introduction

YBCO deposition on RABiTS™ has been well established. RABiTS™ consists of layers of metal oxide buffers epitaxially deposited with either a cube-on-cube or rotated cube-on-cube orientation to the {100}<100> textured Ni or Ni-alloy substrates. These ceramic buffer layers act as a barrier against Ni diffusion from the base metal substrate into the YBCO layer while providing a template of reduced lattice mismatch between YBCO and Ni for epitaxial growth. Although different deposition methods exist for the epitaxial growth of YBCO on substrates, all have significant barriers in developing thick YBCO films. In this investigation, YBCO layers of varying thicknesses were deposited by PLD on RABiTS™.

The PLD method has been widely used as a process for producing high-quality YBCO films on various substrates; however, growth of thicker YBCO films that maintain good *c*-axis alignment is difficult. The mechanisms that lead to degradation in the films can stem from both the conditions under which deposition takes place and the type of substrate used for deposition. Film deposition temperatures at or below 600°C can lead to random or *a*-axis aligned grains due to decreased add-atom mobility at the growth interface, and the favoring of the faster non-*c*-axis growth directions. Similarly, higher deposition rates have also produced non-*c*-axis orientations in the growing film. Whether random or *a*-axis growth occurs depends on the temperature of deposition and on the substrate. Development of *a*-axis growth is common on single-crystal substrates even at relatively high deposition temperatures, due to the small difference in *a*, *b*, and *c*/3 lattice constants of YBCO and those of the substrates. In addition, the formation at the YBCO/substrate interface of disordered Y-Ba-Cu-O perovskite structures with $3a_p \cong c_{YBCO}$ lattice constants can further lead to easier nucleation and growth of *a*-axis-oriented grains.

The effect of decreasing the surface temperature of a growing film during the deposition process is another obstacle to the development of thicker films. Although complete *c*-axis-aligned films of up to 2 μm have been grown on various substrates, a loss in texture associated with temperature drop occurs after a given point. The mechanism behind the temperature drop was theorized as the change in the surface emissivity resulting from a roughening of the surface as it grows, producing a temperature drop of as much as 100°C or more for a given film thickness. As the thick film is grown, reactions between the YBCO layer and the buffer layer can result in the formation of nonsuperconducting phases. The phases formed vary with the type of substrate/buffer architecture used; $BaCeO_3$, BaO, $YCuO_2$, Y_2BaCuO_5, Y_2O_3, and CuO have been identified. Foltyn et al. observed in 3.0-μm and 4.7-μm-thick films a 0.25-μm-thick layer at the substrate that was degraded and carried no current.[1]

It is the purpose of this investigation to identify through microstructural characterization the causes of the reduction in critical current density with thickness in YBCO films on RABiTS™. For this purpose, films ranging from 0.19 to 3.0 μm in thickness were characterized through cross-sectional electron microscopy. The critical-current and critical-current-density measurements, along with X-ray characterization of these samples are briefly summarized; they have recently been reported on in greater detail elsewhere.

1.17.2 Results and Discussion

1.17.2.1 Results for 0.19-µm-Thick YBCO

The critical current density and critical current values from previous work are plotted as a function of YBCO thickness in Fig. 1.98 along with the values for YBCO deposited on single-crystal STO substrates for comparison.[2] The measured properties of the films and their textures determined through XRD are listed in Table 1.7. The surface of the 0.19-µm-thick YBCO layer [Fig. 1.99(a)] was found to be relatively smooth with only slight deviations in height associated with individual *c*-axis-oriented subgrains or growth columns. However, a number of particles were observed on the surface. The number density of these was approximately one to two outgrowths for every 100 µm^2 of surface area, with sizes typically ranging from 0.5 to 1.8 µm diam, with an average size of approximately 0.8 µm diam. These particles were determined through EDS to be YBCO with no secondary phases found adjacent to or associated with them. These particles were similar to those reported for PLD-deposited YBCO on CeO_2 buffered r-cut (1-102) Al_2O_3 substrates and on STO substrates. Based on the density of the surface outgrowths and their average diameter, the percentage of *c*-axis-oriented surface area is near the 98.8% value measured for cube texture that was determined through XRD (see Table 1.7). Due to the low number density of the outgrowths, they were not observed in the two cross-sectional TEM samples prepared from the 0.19-µm-thick film.

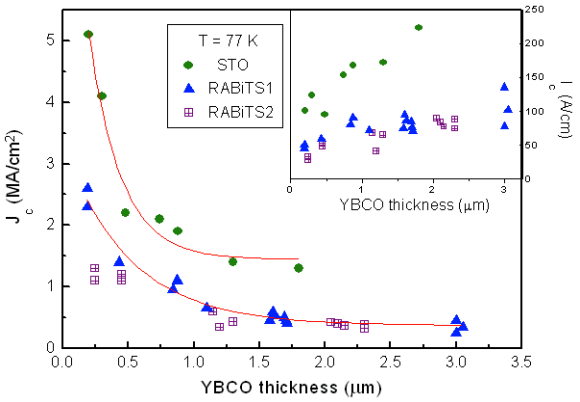

Fig. 1.98. The critical current density (J_c) as a function of YBCO film thickness on RABiTS™ and on (100) STO substrates. [Ref. S. R. Foltyn et al., *J. Mater. Res.* **12**(11), 2941 (1997)]. Inset shows the calculated critical current (I_c) as a function of film thickness for a 1-cm-wide sample. The solid J_c curves are based on the empirical fit of the exponential decay function, from which I_c data were calculated.

The 0.19-µm YBCO films examined in cross section [Fig. 1.99(b)] showed complete *c*-axis orientation throughout the thickness and no secondary phases or porosity. The YBCO layers consisted of *c*-axis-oriented subgrains, separated by anti-phase boundaries observable when tilted away from the [010] YBCO zone axis along the 001 direction. The deviation in orientation across the boundaries was negligible; no mosaic spreading of the diffracted intensities was observed during analysis. The mismatch

Table 1.7. The properties and texture of YBCO films of different thicknesses on RABiTS™

Sample	Thickness (µm)	J_c (MA/cm^2)	I_a/I_c	t_a (µm)	t_c (µm)	t_a/t_c	Δϕ (°)[a]	Δω (°)[b]	Cube (%)[c]
BWK-53C	0.19	2.6	0	0	0	0	1.07	0.73	98.8
BWK-70B	0.43	1.4	0	0	0	0	1.04	0.7	90.4
BWK-73B	0.84	1.2	0.06	0.03	0.81	0.04	1.17	0.66	90.4
BWK-96B	1.2	0.54	0.03	0.02	1.18	0.02	1.07	0.73	90.5
BWK-88A	1.6	0.59	0.05	0.05	1.55	0.03	1.03	0.76	89.7
BWK-93A	3.0	0.45	0.07	0.14	2.86	0.05	1.08	0.73	79.9

[a]In-plane texture measured from the FWHM ratio of YBCO(103) / Ni(111).

[b]Out-of-plane texture measured from the FWHM ratio of YBCO(005) / Ni(200)

[c]Cube percentage calculated from the YBCO(113) pole figure.

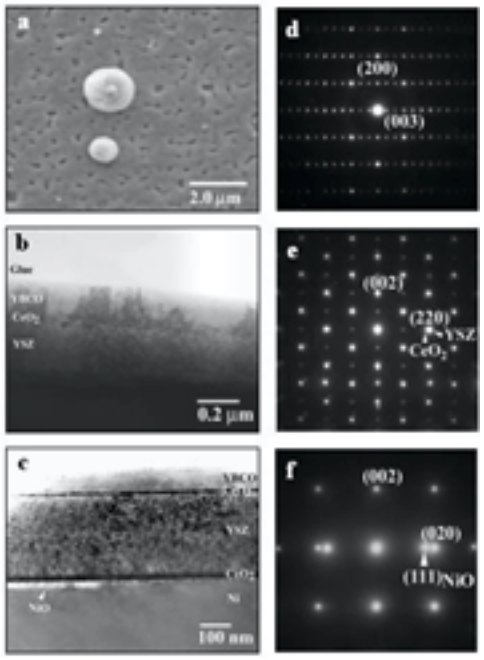

Fig. 1.99. Electron micrographs from the 0.19-μm-thick YBCO sample. (a) SEM image of the surface morphology showing outgrowth formations. TEM cross-section images of (b) the YBCO film, and (c) the architecture of RABiTS™, including the NiO layer formed during the PLD growth of the YBCO layer. Selected area diffraction patterns illustrating the epitaxial relationship between the layers in the RABiTS™ structure: (d) the YBCO [010] pattern, (e) the CeO_2 [110] and YSZ [110] zone axis patterns, and (f) the Ni [100] pattern with NiO {111} reflections.

across the boundaries was found to be associated with the presence of stacking faults within the *c*-axis grains, producing local deviations across the boundaries of only a fraction of the *c*-axis unit cell dimension. Stacking faults and dislocations within the grains, producing the darker contrast within the film, were found to be higher in density near the YBCO/CeO_2 interface. Examination of the interface showed no evidence of reactions between the YBCO and $CeO_2$and no presence of any disordered perovskite layer within the YBCO as reported to occur in PLD and ex situ grown films on single-crystal and metal substrates.

Epitaxial orientation of the YBCO and buffer layers can be seen within Fig. 1.99(c) along with the corresponding selected area diffraction patterns [Fig. 1.99(d–f)], showing the YBCO[010]//CeO_2[110]//YSZ[110]//Ni[100] orientation relationship. A 10- to 15-nm-thick NiO layer that developed within the cross section showed a (111) orientation to the Ni (010) substrate and CeO_2 (110) seed layer. XRD before and after YBCO deposition indicates that the NiO layer forms during deposition of the YBCO layer.

1.17.2.2 Results for 0.5-μm-Thick YBCO

Cross-section examination of the 0.5-μm-thick YBCO sample [Fig. 1.100(a)] revealed a number of interesting details on the growth of the YBCO film and on the subsequent formation of secondary and reaction phases. In general, the cross section of the YBCO contained *c*-axis growth columns, separated by anti-phase boundaries, with stacking faults emanating from them and growing across the *c*-axis columns. The *c*-axis column height traversed the entire film thickness and was found to contain no porosity. The film showed the formation of randomly oriented grains near the top of the film surface, contributing to the drop in cube texture from 98.8% in the 0.19-μm-thick film to 90.4% (Table 1.7). Despite some twinning within the random grains, they remained typically defect-free compared with the c⊥ grains of the film.

The most interesting feature within the sample was the presence of an outgrowth grain. The grain was observed to peak at approximately 0.2 μm above the surface of the film, with a head diameter of 0.4 μm, typical of what had been seen during SEM examination of the surface and in the 0.19-μm-thick film. The grain extended down into the film to a depth of approximately 150 nm above the CeO_2 cap layer interface [Fig. 1.100(b)] Present at the bottom of the outgrowth grain were numerous anti-phase boundaries, which extended further toward the CeO_2 cap layer but remained disconnected. The outgrowth grain itself was found to have a ~2.2° tilt in its *c*-axis direction relative to the surrounding film region and a rotation of the grain about the [010] direction [Fig. 1.100(c)]. One side of the outgrowth grain displayed a long, relatively straight interface, while the other showed a larger deviation to the adjacent grain and was decorated by numerous CuO particles. No defects within the buffer layers or Ni substrate below the

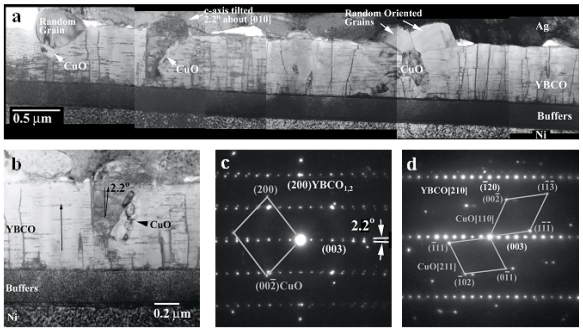

Fig. 1.100. (a) Cross-section TEM bright-field composite image of the 0.5-μm-thick YBCO sample taken along the g = 001 condition, showing the anti-phase boundaries between c⊥ columns and stacking fault structures within the YBCO film. Random grain formations are now being observed. (b) Close-up image of the outgrowth grain and (c) the [010] selected area diffraction patterns of the outgrowth and c⊥ grains, illustrating the 2.2° tilting of the *c*-axis of the outgrowth grain. Also present is the CuO [010] pattern from one of the secondary phase particles along the interface. (d) The [110] and [210] patterns from CuO particles oriented along the [210] direction of one of the misaligned YBCO grain formations.

outgrowth grain were found to account for the formation of this grain.

The formation of the outgrowth grains is not believed to have been a result of the formation of CuO grains that are present along its side and not the result of the formation of any secondary phase formed during the film deposition. The region directly below the grains is also free of any interface reaction phases formed between the YBCO and CeO_2 layer. In fact, CuO particles appear along the interfaces between the randomly oriented grains and the *c*-axis grains as well. Investigation of possible orientation relationships between the CuO and the YBCO grains revealed multiple growth directions possible for CuO [Fig. 1.100(d)], which were different from those observed previously.[3] It was also found that within the locations of CuO formation, some particles held orientation relationships to the *c*-axis grains, while others were linked to the randomly oriented grains.

In addition to the formation of CuO at the interfaces between the misoriented and c⊥ grains, other secondary phase formations were found within the 0.5-μm-thick film. Reaction between the YBCO and CeO_2 cap layer resulted in the precipitation of 10- to 20-nm $BaCeO_3$ particles partially embedded within the CeO_2 layer [Fig. 1.101(a)]. Through high-resolution TEM it was found that the particles held a $BaCeO_3$ [100]//CeO_2 [110], $BaCeO_3$ (012)//CeO_2 (220) orientation relationship. These reactions were found occurring at random intervals along the interface. A Y_2O_3 particle was also observed within a c⊥ grain near the CeO_2 interface [Fig. 1.101(b)], although no $BaCeO_3$ was found immediately nearby. The Y_2O_3 particle held an orientation of Y_2O_3 [110]// YBCO [010], Y_2O_3 (110)//YBCO (100) to the c⊥ grain. Y_2O_3 particles appearing within the bulk of the YBCO and having the same orientation relationship have been reported previously as Type A Y_2O_3 particles.[4,5] These particles are different from the smaller Type B particles, which generally appear near the top of the YBCO film and hold a Y_2O_3 (110)//YBCO (001) relationship. Type B particles were not detected within the YBCO films examined in this work.

1.17.2.3 Results for 1.7-μm-Thick YBCO

Characterization of the 1.6-μm film by XRD and the 1.7-μm film by TEM showed a significant change in comparison to the half-micron film. While a small drop in the percentage of cube texture was determined (Table 1.7), the critical current density value was more than halved in comparison to the half-micron film. The microstructure of the 1.7-μm film showed relatively undisturbed c⊥ grains in the lower portion of the YBCO film [Fig. 1.102(a)]; however, the misoriented grains were more numerous near the top of the film surface [Fig. 1.102(b)]. Unlike YBCO films grown by PLD on IBAD YSZ buffered substrates, the misoriented grains do not completely cover the top of the film as observed in both TEM and SEM images [Fig. 1.103(a)]. Most of the misoriented grains were formed in groups that typically

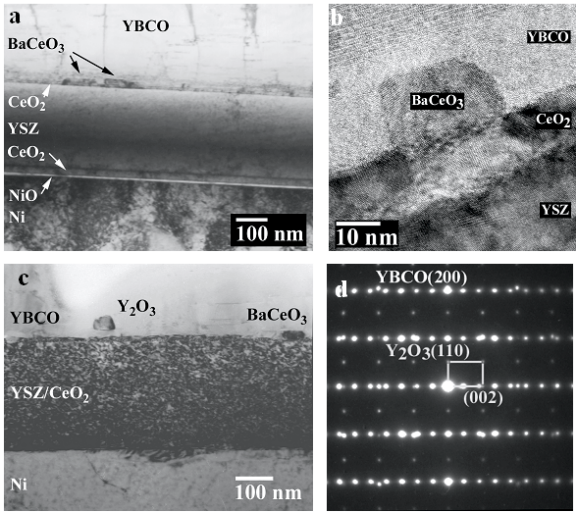

Fig. 1.101. Secondary phase formation within the 0.5-μm-thick YBCO film. (a) Bright-field and (b) high-resolution images of $BaCeO_3$ grain formations along the YBCO/CeO_2 interface. The amorphous region within the YBCO around the $BaCeO_3$ particle was caused by electron beam damage. (c) A Y_2O_3 particle formed in the bulk but near the interface having (d) a Y_2O_3 [110]// YBCO [010] orientation relationship.

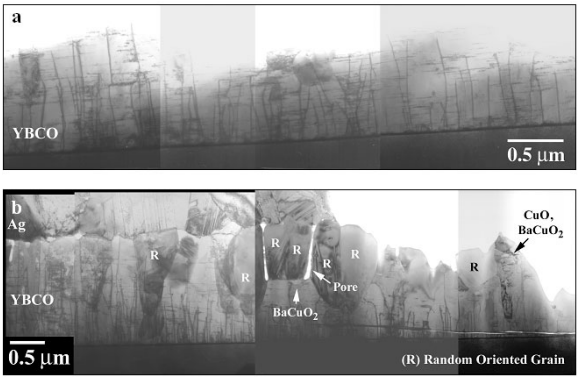

Fig. 1.102. Cross-section composite images of the 1.7-μm-thick YBCO sample showing (a) good c⊥ grain development near the buffer interface, and (b) random grain and secondary phase formations near the top surface of the film.

shared a common twin boundary. The presence of porosity within the microstructures was also beginning to be seen, but it was usually associated with the large mismatches between the c⊥ and randomly oriented grains. These regions, however, may have contained secondary phases that were removed during sample preparation. CuO particles at the interfaces between the two types of grain orientations were also present in addition to $BaCuO_2$.

The polished cross section of the sample viewed through SEM [Fig. 1.103(a)] showed a more roughened film surface than that of the thinner films due to the increased population of randomly oriented grains near the film surface. In comparison with the TEM images, the randomly oriented grains began to form at a film thickness of about 0.45 μm, consistent with observations of the 0.5-μm-thick YBCO film. Large surface outgrowths were also viewed in the cross section in addition to the outlines of V-shaped grains. These were determined through TEM to be *a*-axis-aligned grains [Fig. 1.103(b)], which were first detected in the θ-2θ scans of films greater than 0.5 μm in thickness. The darker regions outlining the a⊥ grains imaged in SEM are believed to be secondary phase formations, although the presence of any secondary phases was not detected through EDS or diffraction analysis. The inset in Fig. 1.103(b), taken during TEM examination, suggests particle pullout during sample preparation.

$BaCeO_3$ was again observed along the interface between YBCO and CeO_2 [Fig. 1.103(c)] in an amount more than that occurring within the 0.5-μm sample. A thin layer of $BaCeO_3$ along the interface between the large separated particles was identified. However, diffraction analysis of the interface revealed the presence of the CeO_2 cap layer, indicating that it had not completely reacted.

1.17.2.4 Results for 3.0-μm-Thick YBCO

The thickest of the characterized samples suffered from the largest degradation in cube texture. Imaging of the sample cross section by SEM [Fig. 1.104(a)] revealed a very rough surface with little or no smooth areas associated with the top of the YBCO film. Imaging of the film by TEM [Fig. 1.104(b, c)] confirmed the presence of porosity within the microstructure. Pores were found to be associated with the

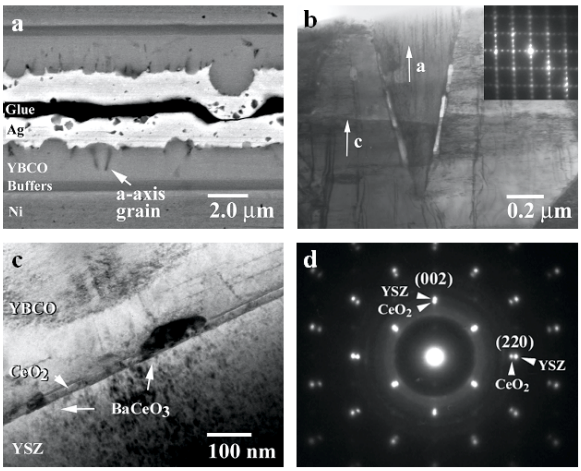

Fig. 1.103. (a) SEM image of cross section revealing the presence of outgrowth, a-axis and random oriented grain formations in the 1.7-μm-thick sample. TEM images of (b) an a-axis-oriented grain formation with insert showing [100] and 90° rotated [010] patterns of the c⊥ and a⊥ grains, respectively. (c) $BaCeO_3$ formation along the cap layer interface, and (d) the CeO_2 and YSZ [110] zone axis patterns, confirming that some of the cap layer is still present.

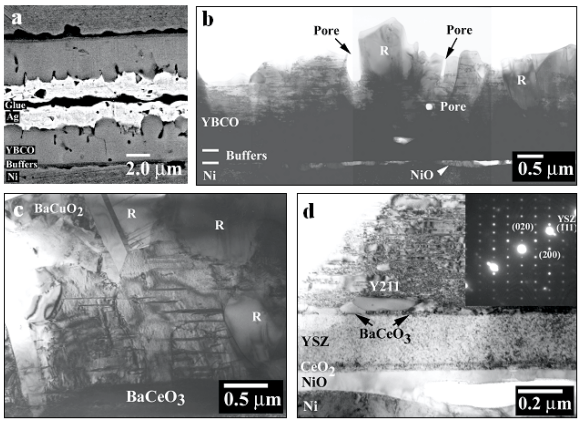

Fig. 1.104. (a) SEM and (b) TEM cross-section images from the 3.0-μm-thick YBCO sample, showing an increase in surface roughness due to random and secondary phase formations. TEM bright field images of (c) random and $BaCuO_2$ grain structures within the film, and (d) $BaCeO_3$ and Y_2BaCuO_5 phases produced from the reactions between the YBCO and CeO_2 layers. Insert in (d) shows the [001] diffraction pattern of the Y_2BaCuO_5 phase with additional YSZ reflections from the buffer.

formation of random grains but were also found in areas with no apparent structural deviations in the c⊥ grain orientation or secondary phase precipitation. It is possible that the pores are the result of either the relief in volumetric changes associated with the formation of secondary phases or the removal of quenched-in vacancies, depending on location.

Formation of CuO along the interfaces of the YBCO grains was again present within the 3.0-μm films, but a dramatic increase in the amount of $BaCuO_2$ was observed. The $BaCuO_2$ regions contained microstructures of fine plates, which appeared to be a mix of random and twin-related orientations. The $BaCuO_2$ phase formations were located near the top surface of the YBCO film as well as at intermediate depths.

The reaction between YBCO and the CeO_2 cap layer appeared to be complete within the 3.0-μm sample. Investigation of the interface region through both diffraction and composition analysis could not identify any distinct CeO_2 layer remaining, suggesting that the cap layer has been completely reacted to form $BaCeO_3$ [Fig. 1.104(d)]. In examining the relationship between YBCO and CeO_2 cap layer, the chemical reaction can be written as follows:

$$2YBa_2Cu_3O_7 + 4CeO_2 \rightarrow 4BaCeO_3 + 2YCuO_2 + 4CuO + O_2 \quad , \tag{1.3}$$

to which it is expected that $YCuO_2$ and CuO are produced with $BaCeO_3$. Although reactions between $BaCeO_3$ and YBCO that produce $YCuO_2$ have been reported within CeO_2 buffered films, $YCuO_2$ was not found in the samples examined. However, Y enrichment resulting from the formation of $BaCeO_3$ produced Y_2BaCuO_5 grains along the interface between YBCO and $BaCeO_3$, as verified by electron diffraction [see the insert in Fig. 1.104(d)].

It was demonstrated in work by Scotti di Uccio and coworkers that a competition between the Y_2BaCuO_5 and Y_2O_3 phases can occur within Y-rich YBCO films deposited on MgO buffered STO.[6] From their work, the two competing reactions, based on 50% excess in Y for simplicity, can be written as follows:

$$(1.5Y + 2Ba + 3Cu + xO) \rightarrow YBa_2Cu_3O_7 + 1/4Y_2O_3 \qquad (1.4)$$

$$(1.5Y + 2Ba + 3Cu + xO) \rightarrow 5/6YBa_2Cu_3O_7 + 1/3Y_2BaCuO_5 + 1/6CuO \ . \qquad (1.5)$$

From the rate equations, a greater amount of the Y_2BaCuO_5 phase is expected. In their work, they determined that the nucleation of Y_2O_3 took place homogeneously within the YBCO film, whereas the Y_2BaCuO_5 phase only nucleated at the buffer interface. They concluded that the formation of Y_2BaCuO_5, despite being more thermodynamically stable than Y_2O_3, was inhibited within the YBCO grains unless a suitable interfacial nucleation site existed. This is due to the higher surface energy of the Y_2BaCuO_5 nucleus, making homogeneous nucleation in the YBCO bulk unfavorable. This is why the Y_2O_3 precipitate is frequently observed within YBCO thin films, when in fact the Y_2BaCuO_5 phase is at equilibrium with YBCO at PLD deposition temperatures under a reduced oxygen environment.

1.17.2.5 Defect Structures

The dark-field and bright-field images of the 1.7- and 3.0-μm films in Figs. 1.105(a) and (b), respectively, reveal numerous faults emanating from the anti-phase boundaries within the *c*-axis grains. Also visible is the dense dislocation network located near the YBCO/CeO_2 interface. The fault structures have previously been shown to form from excess atoms, typically Y and Cu, released from the interfacial reactions between YBCO and CeO_2, which diffuse up through the grain boundary columns and intercalate into single layers within the YBCO lattice. These defects create single unit cell thick layers of $Y_2Ba_4Cu_8O_y$, $Y_2Ba_4Cu_7O_y$, or $Y_2Ba_2Cu_4O_y$, which emanate from the c⊥ boundaries. High-resolution imaging of the fault structures occurring in each of the films were studied individually; they showed an extra Cu-O layer inserted into the YBCO stacking sequence [Fig. 1.105(c)]. Measurement of the unit cell height in the <001> direction of these layers found that the addition of the extra material increased the *c*-axis parameter from 11.7 to 13.3 Å, matching the $Y_2Ba_4Cu_8O_y$ lattice parameter. Similar results have been observed before, along with the presence of other off 123 compounds; however, in this study only the $Y_2Ba_4Cu_8O_y$ structure was found.

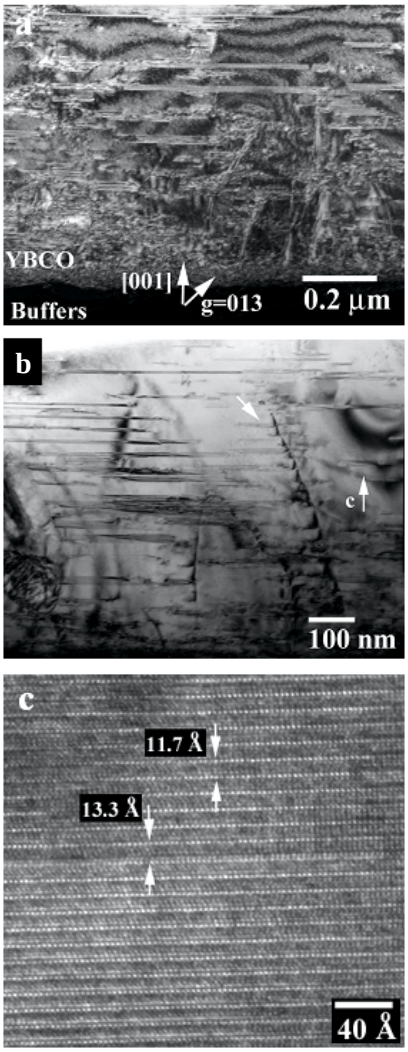

Fig. 1.105. (a) Dark-field and (b) bright-field images, g = 013 near the [100], showing stacking-fault and defect structures within the 1.7- and 3.0-μm-thick YBCO films, respectively. The arrow within the 3.0-μm film points out a smaller sized fault structures emanating from the c⊥ grain boundary. (c) High-resolution image of stacking fault structure within the 0.5-μm-thick YBCO film. The change in *c*-axis lattice constant from 11.7 Å to 13.3 Å indicates the intercalation of a $Y_2Ba_4Cu_8O_y$ layer within the Y123 grain.

In investigating these faulted structures in the YBCO films, it was found that the lengths of these structures tended to increase with their distance away from the interface. This finding is in contradiction to an earlier work reporting an inversely proportional relationship between the intercalate length and its distance from the interface. This discrepancy suggests that some of the stacking faults within the films were produced during the deposition process, rather than as a result of interfacial reactions occurring at the YBCO/cap layer interface. That the faults formed during deposition is supported by the evidence of faults present within the 0.19- and 0.5-μm-thick films, which developed little or no interfacial reactions. However, it is still possible that some faults were created from the excess Cu-O produced from the interfacial reactions that had formed the Y_2BaCuO_5 phase [Eq. (1.5)]. The arrow within Fig. 1.105(b) indicates such possible formations because the sizes of the faults emanating from the boundary are much smaller than those nearby.

1.17.2.6 Results for Aged 0.2-μm-Thick YBCO

The effects of deposition time on the formation of secondary phases within the YBCO, specifically along the cap layer interface, were investigated by preparing an additional 0.2-μm-thick YBCO sample and soaking in the 790°C deposition temperature under 120 mTorr O_2 for an extended time (approximately 2 h of aging) to simulate the conditions for growth of a 1.0-μm-thick sample. A 25% decrease in critical current density was measured for the aged sample in comparison with a standard 0.2-μm-thick film on the same substrate. When viewed by SEM, the surface of the aged 0.2-μm sample did not reveal any features that were different from what had been observed on the standard 0.19-μm sample. The number density and distribution of outgrowth grains were found to be similar to those of the unaged sample.

The big difference between the two samples was found when viewed in cross section by TEM. The 0.2-μm aged sample showed a significant increase in the misorientation between adjacent subgrains. These deviations were clearly evident when the sample was viewed along the g = 001 vector near the [010] zone axis [Fig. 1.106(a)]. The variation in orientation produced the changes in image contrast from one subgrain to the next. These changes were not the result of Ni grain boundaries as they all took place within a single grain, nor were they produced by changes within the CeO_2 cap layer orientation or thickness over the surface. Some of these subgrains still contained a few anti-phase boundaries within them and could be considered to be a collection or grouping of subgrains. However, many of the larger subgrains were relatively free of defects (including stacking faults). While examination of these anti-phase boundaries in the unaged 0.19-μm sample revealed no measurable tilt or rotation of the c⊥ grains across the boundaries, a rotation between 5 and 8° about the *c*-axis was measured between the larger subgrains in the aged material. This large deviation was evident when the boundary was examined at higher magnifications [Fig. 1.107(a)]. In the high-resolution image, it appears as if the

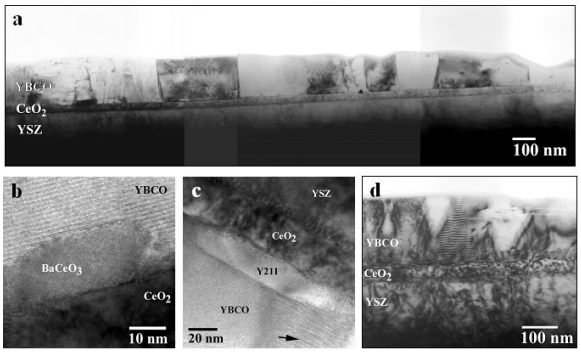

Fig. 1.106. Cross-sectional TEM images of the 0.2-μm-thick film aged an additional 2 h at 790°C under 120 mTorr O_2.
(a) Composite image of the film cross section showing contrast changes in c⊥ grains due to changes in orientation. (b) $BaCeO_3$ and (c) Y_2BaCuO_5 phases formed at the interface between the YBCO and CeO_2 layers, arrow in (c) points to a c⊥ boundary. (d) Fresnel fringes imaged between mismatched c⊥ grains, illustrating the increasing deviation closer to the buffer interface.

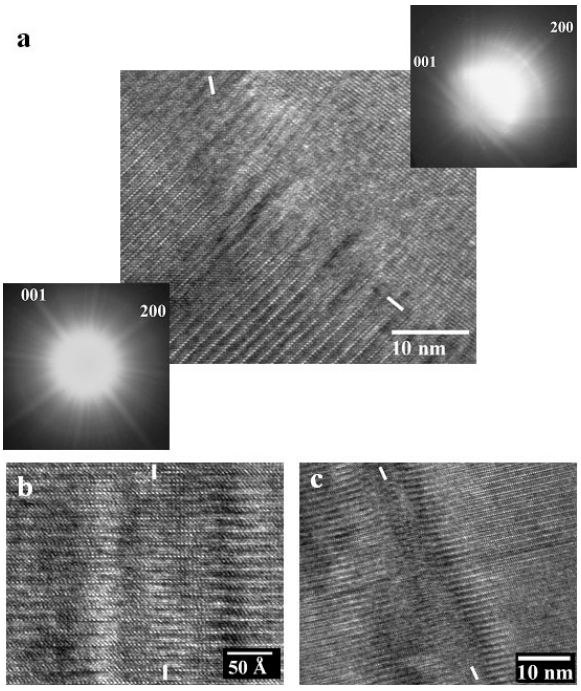

Fig. 1.107. High-resolution image of the interfaces between two c⊥ grains within (a) the aged 0.2-µm-thick film showing an 8° rotation of one of the grains about the *c*-axis as illustrated by the convergent beam patterns from each side of the boundary, (b) the 0.5-µm-thick film with very little change across the interface, and (c) the 3.0-µm-thick film showing an increased amount of mismatch, relative to the 0.5-µm film.

boundary is between grains of c⊥- and a⊥-oriented material. However, the grain on the right side of the image has been rotated about the *c*-axis direction approximately 8°. The displayed convergent beam patterns taken on either side of the boundary under the same tilt conditions lend further visual aid.

This dramatic change across the boundary of two c⊥ grain columns was only found within the aged sample. For comparison, high-resolution images taken of the anti-phase boundaries within the 0.5-µm and 3.0-µm samples are shown in Figs. 1.107(b) and (c), respectively. Very little change occurs across the interface within the 0.5-µm sample. Although an increase in the deviation was observed within the 3.0-µm film, the deviation was still less than that of the aged sample. The lateral mismatch across the boundaries was associated with the presence of stacking faults, displacing the opposing sides to an amount of only a fraction of the unit cell height of the YBCO structure. Bals et al. have recently shown that the origins of the anti-phase boundaries within rare earth oxide films ($REBa_2Cu_3O_7$) were derived at the oxide/substrate interface due to changes in the initial nucleating layer of the *c*-axis stacking sequence of the crystal structure.[7] They claim that the additions of successive numbers of stacking faults can lead to the annihilation of these anti-phase boundaries.

The 0.19-µm sample showed no evidence of reaction between the YBCO and CeO_2 layer. Reactions did occur, however, within the aged 0.2-µm sample. Along the interface of the thinned sample, several grains of $BaCeO_3$ [Fig. 1.106(b)] and one grain of Y_2BaCuO_5 [Fig. 1.106(c)] were identified. The amount of reaction between the YBCO and CeO_2 was limited to only a few distinct locations with no evidence of a $BaCeO_3$ film detected along the cap layer interface. The $BaCeO_3$ particles were similar in appearance and in growth orientation to those observed within the 0.5-µm and thicker films. The Y_2BaCuO_5 grain was different from that observed within the 3.0-µm sample, in that it was found without an accompanying $BaCeO_3$ particle. However, the grain was located at a misoriented subgrain boundary, which can be seen within the high-resolution image and is also denoted by the arrow within Fig. 1.106(c). A closer investigation of the Y_2BaCuO_5 relationship with the cap layer and subgrain interface is being conducted.

The misorientation between the c⊥ subgrains within the aged 0.2-µm sample was determined to be greater near the CeO_2 cap layer interface than at the top of the YBCO film. Although this was true for all of the film thicknesses examined, it was particularly apparent from the widening of Fresnel fringes within the aged material along these interfaces [Fig. 1.106(c)]. The large misorientation between c⊥ subgrains is believed to be the result of strain relief associated with the localized mismatch between CeO_2 and YBCO, either from the increased strain resulting from chemical reactions at the interface or a reduction in the

energy associated with the dislocation density within the YBCO film near the interface. A larger number of stacking faults and defects were found near the YBCO/cap layer interface than near the free surface of the YBCO layer, suggesting that a higher strain state was present in the film due to the mismatch in lattice parameter between CeO_2 and YBCO. Furthermore, it had been observed that the anti-phase boundaries within the 3.0-μm samples were found to be much wider with greater misorientation across the interface than in the thinner films, suggesting that some relief had taken place due to the longer time at deposition temperature. However, this is complicated by the fact that much of the original interface region had been destroyed by the reactions between YBCO and CeO_2 (with the Y_2BaCuO_5 and $BaCeO_3$ particles consuming at least 0.1 μm of the YBCO film). In addition, the subgrains within the 0.2-μm aged sample revealed much fewer stacking faults, dislocations, and short-range variations within the *c*-axis lattice constant than within the as-deposited 0.19-μm sample.

A similar test on PLD-deposited YBCO on IBAD YSZ buffered Inconel 625 was noted by Foltyn et al., in which a 0.46-μm film was deposited and aged at 775°C in 0.2 Torr O_2 for 1 h.[2] The reported critical current density was one-tenth that of the non-aged film. Impurity diffusion from the substrate into the YBCO layer adjacent to the interface was cited as the cause of the drop in critical current density. No microstructural characterization was presented.

1.17.3 Conclusions

In combining the microstructural investigation of the YBCO films with the previously reported X-ray characterization data, one of the main causes of the loss of critical current density was found to be degradation of the cube texture in the thicker films. The formation of randomly oriented grains near the top of the YBCO film began around a thickness of 0.45 μm under the given PLD conditions and RABiTS™ architecture. The amount of non-*c*-axis grain formation increased with film thickness, along with the formation of *a*-axis-oriented grains beginning within the 1.7-μm-thick film. Although the random grain formations dominated the upper portion of the film, they did not create a dead layer preventing *c*-axis growth up to the surface of the YBCO film. In addition to the development of randomly oriented grains, extended time at deposition temperatures led to the formation of secondary phases produced from reactions between YBCO and the CeO_2 cap layer and the increase in misalignment between the *c*-axis grain columns. This effect was observed to be the strongest within the 0.2-μm-thick YBCO film aged under deposition conditions for an additional 2 h, in which subgrain misalignments of up to 8° were measured through electron diffraction. The driving force for the changes occurring near the buffer interface appears to be related to either the amount of strain associated with the mismatch between YBCO and the CeO_2 buffer or in the removal of excess dislocation and defect energy produced from the strain relaxation during the growth of the YBCO film.

The development of secondary phases along the interfaces also played a significant role in the reduction of YBCO film properties. The formation of $BaCeO_3$ began to appear as distinct particles along the YBCO/CeO_2 interface within the 0.5-μm-thick film, leading to the eventual removal of the CeO_2 buffer within the 3.0-μm-thick film. In addition to the $BaCeO_3$ formation, Y_2BaCuO_5 particles were also found at the interface in both the 3.0-μm-thick and aged 0.2-μm-thick films. Although seen for the first time in CeO_2 buffered substrates instead of Y_2O_3, the formation of the more thermodynamically stable Y_2BaCuO_5 phase was only possible through heterogeneous nucleation along the interface. The combined thickness of the $BaCeO_3$ and Y_2BaCuO_5 phases within the 3.0-μm sample constituted at least 0.1 μm of the YBCO film near the buffer surface, approaching a thickness near to that of the thinnest YBCO layer investigated in this study.

Along with the formation of reaction phases at the interface, increases in the amount of CuO and $BaCuO_2$ were observed with increasing YBCO thickness. These phases formed along the interfaces between the *c*-axis-oriented and randomly oriented grain formations. Formations of YBCO outgrowths, which have been frequently reported on in literature, were also observed.

1.17.4 References

1. S. R. Foltyn et al., "Relationship between Film Thickness and the Critical Current of $YBa_2Cu_3O_{7-\delta}$ Coated Conductors," *App. Phys. Lett.* **75**(23), 3692–94 (1999), and references therein.
2. S. R. Foltyn et al., "Influence of Deposition Rate on the Properties of Thick $YBa_2Cu_3O_{7-ä}$ Films," *J. Mater. Res*. **12**(11), 2941 (1997).
3. A. L. Vasiliev et al., "Single Variant Orientational Growth of $YBa_2Cu_3O_{7-x}$ on Vicinal (011) $SrTiO_3$ Substrates Observed by Electron Microscopy**,"** *Physica C* **289**(3–4), 243–50 (1997).
4. K. Verbist, A. L. Vasiliev, and G. Van Tendeloo, "Y_2O_3 Inclusions in $YBa_2Cu_3O_{7-\delta}$ Thin Films," *Appl. Phys. Lett.* **66**(11)1424–26 (1995).
5. A. Catana et al., "Identification of Epitaxial Y_2O_3 Inclusions in Sputtered $YBa_2Cu_3O_7$ Films: Impact on Film Growth," *Appl. Phys. Lett.* **60**(8), 1016–18 (1992).
6. U. Scotti di Uccio et al., "Phase Competition between Y_2BaCuO_5 and Y_2O_3 Precipitates in Y-Rich YBCO Thin Films, *Physica C* **321**(3–4), 162–76 (1999).
7. S. Bals et al., "Optimisation of Superconducting Thin Films by TEM," *Physica C* **372–76**(2), 711–14 (2002).

2. Technical Progress in Applications Development

2.1 SOUTHWIRE-ORNL HTS CABLE SUPERCONDUCTIVITY PARTNERSHIP INITIATIVE (SPI)

J. W. Lue, M. J. Cole, J. A. Demko, R. C. Duckworth, A. R. Ellis, P. W. Fisher, M. J. Gouge, D. R. James, P. M. Martin, A. L. Qualls, I. Sauers, S. W. Schwenterly, and J. P. Stovall

2.1.1 Triaxial Cable R&D: Initial Testing of 5-m Cable

In 2001, the ORNL-Southwire cable team designed, built, and tested a 1.5-m-long prototype triaxial cable. Each phase consisted of two layers of BSCCO-2223 HTS tapes. Electrical tests of the cable included the direct current (dc) voltage-current curve and ac loss measurements. The three-phase ac loss was close to the sum of the losses of the three individual phases. There was no measurable excess ac loss due to the presence of the other concentric phases. A total three-phase ac loss of about 1 W/m was measured at the design operating current of 1250 A rms. Encouraged by the positive test results from the prototype cable, in FY 2002 the Southwire-ORNL team conceived, designed, and built a 5-m triaxial cable with associated three-phase terminations.

The basic cable configuration used in the 1.5-m and 5-m cables, in which three concentric phase conductors are separated by liquid-nitrogen-impregnated dielectric tape, is shown in Fig. 2.1. For the 5-m cable, the design phase current is 1300 A rms at 77 K and the design phase-to-phase voltage is 15 kV. The phase conductors are BSCCO-2223 silver-alloy tapes wound in a helical manner on a 35.6-mm former; each phase has two layers of tapes. The dielectric material is Cryoflex™ tape immersed in liquid nitrogen. For equal currents in each phase, the current in the copper shield should be about zero. The induced current in the shield for unbalanced three-phase currents measured in the 1.5-m prototype cable was found to be small. The liquid nitrogen used for cable cooling flows inside the cryostat. The cryostat has a vacuum space with superinsulation for reducing the heat load from ambient; the design heat in-leak is 2 W/m. The outer diameter of the cryostat is 143 mm.

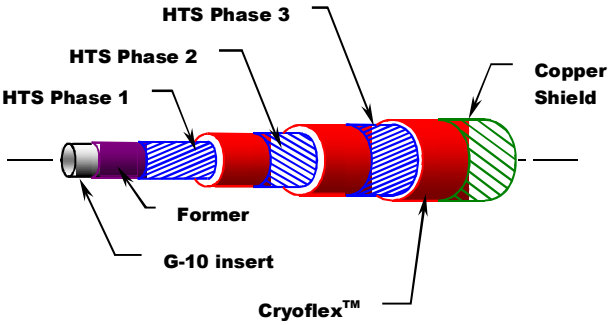

Fig. 2.1. Schematic of the triaxial cable.

The 1.5-m prototype cable operated only at low voltage and did not require a termination. The 5-m triaxial cable is a full-scale demonstration of the technology and has a full-scale, three-phase termination. The termination provides for ambient temperature connections to the three phases and the shield. It makes the temperature transition from liquid-nitrogen temperature to ambient temperature in the three copper-pipe phase conductors as well as the copper braid shield conductor. For the phase conductors, the design approach of McFee is used to select the cross-sectional area and length of the copper pipes given the 1300-A-rms design current. The design axial conduction loss at full current is on the order of 50 W/phase. Although internal cooling is possible in the termination, it was decided to take the more challenging approach of cooling the termination from the outside only. This approach has the advantage that the cooling circuit is at ground potential but the disadvantage that adequate radial heat conduction from the three electrical phases must pass through the termination cross section out to the flowing liquid nitrogen coolant at the wall. In particular, the dielectric material between the phase conductors and between the outer phase and the shield conductor has to be a material with adequate thermal conductivity at 77 K and

300 K and must have acceptable electrical insulation and mechanical strength performance over this temperature range. The 15-kV operating voltage must be accommodated, and the termination should be designed for a 50-kV withstand (1 min, dry) and 110-kV basic-impulse-level voltages per the requirements of the Institute of Electrical and Electronics Engineers, Inc. (IEEE). The present termination is designed for the above operating voltage, but only limited high-voltage testing is planned for this termination design iteration. A radial model of the three-phase termination was developed, and the ANSYS code was used to evaluate it. Thermal conductivities (at 77 K) of the termination insulation in the range 0.25 to 2 W/m-K were evaluated; the material eventually chosen had a thermal conductivity at 77 K of about 75% of the value at 273 K. Because the cable's dielectric system merges with the termination, it is important to keep the temperature at the cold end of the termination low enough to ensure that no nitrogen bubbles nucleate in the taped dielectric. If the nitrogen were at 5 atm (a typical lower value) then one would have to be below 94 K. This is possible if the external cooling configuration is used. The entire termination was modeled with ANSYS. Figure 2.2 shows the model predictions for temperature distribution for the termination.

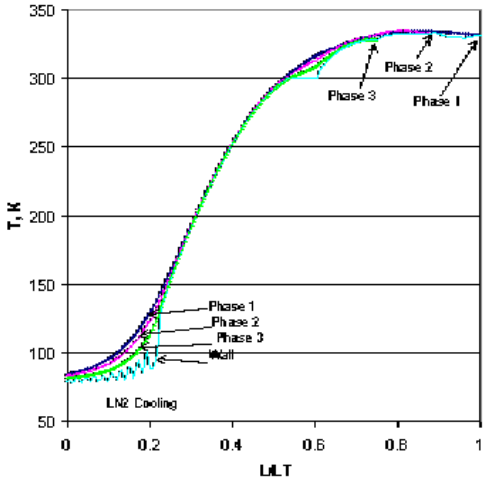

Fig. 2.2. Temperature profiles in the termination predicted by ANSYS.

The model can be used to fine-tune the cooling scheme, which does not meet the ideal conditions of the McFee assumptions (i.e., no radial temperature gradient and no heat input from the system beyond the termination). The cable is spliced to the termination in the region to the left of zero, where the temperature is low and consistent with cable operation. Large radial temperature gradients occur in the region cooled by liquid nitrogen, but this is in a part of the termination where liquid nitrogen is not used as a dielectric. The jagged temperature in the wall cooled by liquid nitrogen is from discrete cooling channels. Temperature control is provided at the ambient temperature end of the termination for two reasons: to intercept some of the heat generated by warm parts of the termination during full-power operation and to heat the warm end during conditions of less than full power operation or when the system is idle. The points marked Phase 1, 2, and 3 on the right-hand side of Fig. 2.2 designate points where power is connected to the system. The three-phase termination is cooled separately from the 5-m triaxial cable because one of the objectives of the 5-m cable test program is a thermal measurement of ac losses while running the cable with currents in all three phases. A separate liquid nitrogen cooling path for the cable allows a more sensitive measurement of ac losses in the cable. Figure 2.3 is a photograph of the assembled three-phase termination showing with liquid nitrogen connections for termination cooling and the three warm bushings on the right side. The start of the triaxial cable is on the extreme left side.

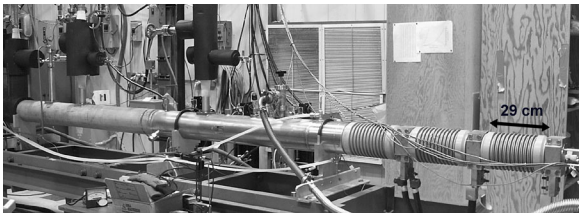

Fig. 2.3. Photograph the triaxial cable and termination.

A comprehensive test program is under way to quantify the potential benefits of this HTS cable. The first tests after gaseous nitrogen filling and purging were a controlled cooldown over about 4.5 h from ambient temperature while monitoring temperature

gradients and mechanical contractions. Since the start of the test program, the cable has experienced more than six cool-down to operating temperature and warm-up cycles. After a steady state had been reached at the cable operating temperature, the cable and termination heat load at a standby condition (zero current) was measured. The cable was also operated at constant ac and dc currents for several extended time intervals, during which thermal losses were measured in the terminations and cable. Measurements of the mass flow rate of liquid nitrogen through the terminations and the cable as well as the temperatures of the inlet and outlet streams were used to determine the heat loads on the different parts of the system. The system reached thermal equilibrium at approximately 5 h after starting a circulating flow through the cable and terminations. Then, dc voltage-current measurements were made on each of the three-phase conductors to determine the critical current of each phase. The critical currents at the measured temperature of 83.6 K and extrapolated to 77 K using the known temperature dependence of critical current were phase 1 (inner phase): 1400/1928 A; phase 2 (middle phase): 1570/2163 A and phase 3 (outer phase) 1610/2218 A. The voltage-current curve for phase 1 at 83.6 K is shown in Fig 2.4. The *n*-value was 12.6 for phase 1, 13.3 for phase 2, and 10.5 for phase 3.

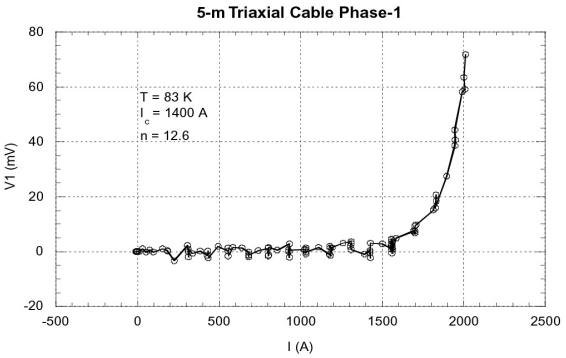

Fig. 2.4. Direct-current voltage-current curve of phase 1.

Phase 1 of the triaxial cable was also subjected to an overcurrent hold test to determine its steady-state overcurrent limit. Figure 2.5 shows the voltage drop across the cable as phase-1 current was stepped above its critical current of 1400 A at 83.6 K and held for about 2 min each at currents of 1500 to 1800 A. No appreciable voltage increase was observed at each of the successive current hold points until the last hold at 1800 A. At about 1800 A, there was a controlled thermal runaway after about 1 min. There was only a very small voltage rise at 1750 A. At that current limit, the voltage across phase 1 was about 19.5 mV. Therefore, a heat load of about 5.6 W/m on phase 1 appears to be the limit for the present cable configuration and cooling condition.

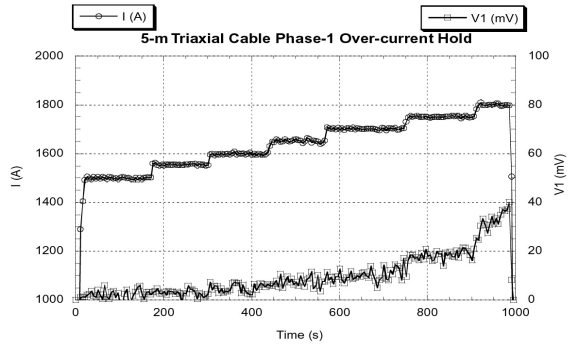

Fig. 2.5. Voltage across phase 1 at successively higher current holds.

Next the ac losses in the phase conductors were measured. For this purpose a three-phase power supply with a current capability of up to 2000 A per phase was connected to the cable. It was verified with a Rogowski coil that the three electrical phases were 120 electrical degrees apart. For measurement of ac losses in that configuration, an electrical measurement (using a Rogowski coil with a lock-in amplifier) is not possible due to the coupling between phases. Therefore, a thermal measurement (from the liquid nitrogen flow rate and the temperature rise) was used to measure ac losses in both single-phase and three-phase operation. The measurement was corrected for the heating due to the induced current in the copper shield. The measured ac losses were about 0.45 to 0.50 W/m per phase (1.42 W/m total) at an operating current of ~1100 A rms in all three phases and at a temperature of ~84 K. At this temperature the critical current of phase 1 is about 1400 A. The monoblock

theory, which does not address the interaction between phases, was used to calculate the HTS losses given the operating current, the critical current, and the phase conductor radial geometry. The simple sum of the losses of the three phases calculated with the monoblock theory was very close to measured total of 1.42 W/m. Based on the monoblock theory, the total ac loss at the design current of 1300 A would be about 1.7 W/m when the cable is cooled to 77 K. The lowest loss per phase is for balanced three-phase operation; ac losses with an applied current in only a single phase are about twice the loss per phase of three-phase operation. This may be the result of eddy current loss in the cryostat and other metallic structures due to imperfect current shielding in the present short cable configuration. In general, even for drastic imbalances in the phase current, the currents in the shield are typically 10 to 15% of the phase current. This finding is consistent with previous measurements on the 1.5-m triaxial cable.

The next development step, planned for 2003, will be a 5-m triaxial cable with a current rating of about 3 kA per phase. Future work includes evaluation of this higher-current cable and termination high-voltage dielectric system per the IEEE requirements.

2.1.2 HTS Cable Aging

Work on studying the aging of model HTS cables immersed in liquid nitrogen is continuing with an emphasis on correlating the aging with partial discharge. A plot of time to breakdown as a function of the applied voltage is shown in Fig. 2.6, showing the log-log dependence and the corresponding *n* value. For breakdown times longer than about one day, cables show a wide variation in breakdown times, depending on the amount of partial discharge observed. The cable ages more slowly when the partial discharge level is low at a given applied voltage. The following section discusses efforts made to study sources of partial discharge in the cable.

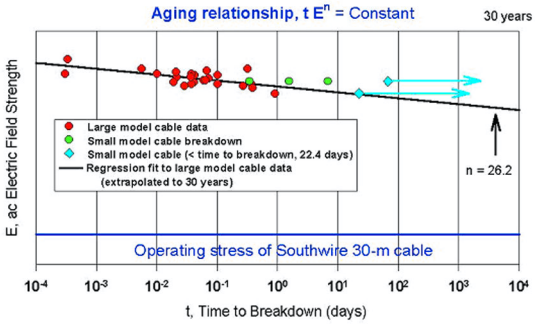

Fig. 2.6. Plot of time-to-breakdown as a function of applied ac field stress on model cable wrapped with Cryoflex™ insulation and immersed in liquid nitrogen. An "*n*" value of 26.2 was determined from a linear regression fit to the breakdown data.

2.1.3 Partial Discharge in Model Cables

Measuring partial discharge (PD) in model cables is complicated by the fact that there can be multiple sources of PD coming from the cable, bushing, power supply, and other high-voltage components. Additionally, there may be noise generated by other equipment (e.g., motors, pumps, switches) that also contributes to PD pulses measured by the PD detection system. A considerable effort has been put into eliminating unwanted PD noise and correctly identifying and measuring true PD coming from the cable.

A model cable (designated S-10) was made with split grounds to establish that PD was coming from the cable itself. One ground tape covers the central region of the cable, and the other section covers both the transition from cable to stress cone and the stress cone region. The grounds are separated from each region by about 2 mm and are wrapped over a continuous semiconducting layer. The two stress cone grounds are tied together and are connected to a lead exiting the cryostat through a feedthrough. A separate lead from the central region passes through another feedthrough. A custom-made PD detector box and preamplifier are connected in series to each signal lead, which goes to a separate channel on a

Power Diagnostix ICM digital detector. If a PD pulse occurs in the cable in the stress cone region, it should appear much stronger on the channel for that ground and vice versa. PD occurring elsewhere in the system should be detected equally by both channels. Also for this series method, pulses occurring in the cable have the same polarity as the waveform (i.e., one observes a negative PD pulse on the negative half cycle and a positive pulse on the positive half cycle. If a PD occurs elsewhere in the system, such as on the high-voltage lead for example, the pulse will be of opposite polarity to the half cycle. This series method (the detector is in series with the test sample) thus provides more information than the standard parallel method, in which the polarity of the PD pulse is always opposite that of the waveform whether it comes from within the sample or external to it.

With the improved setup, it was possible to observe PD from the cable itself. The polarity of the PD pulses for the series mode was the same as the applied-voltage waveform, indicating that the signal was indeed coming from within the cable itself. There was general agreement with the standard ICM arrangement in the parallel mode when the ground leads were tied together. However, there is some discrepancy when comparing only the stress cone region with the ICM method. The reason for this is not understood at present, but we believe there may be some ringing or bleed-over of signal when the grounds are isolated. Further work is planned to resolve this issue. However, with the grounds tied together, some interesting patterns are observed as the voltage is raised. On the negative half cycle three distinct regions of PD evolve, which may indicate three different sources or mechanisms occurring in the insulation (see Fig. 2.7). To observe the patterns, the ICM system was set up to take 1-min scans every 5 min with the voltage held constant, which provided a time evolution of PD. At a given voltage, the number of pulses of PD often start out high and then diminish, as is also observed in the literature. The number of counts and magnitude of PD pulses is being analyzed to determine correlations with the applied voltage. Cable S-10 failed at 52 kV after two scans (corresponding to about 10 min of operation at that voltage). The data leading up to breakdown are currently being analyzed.

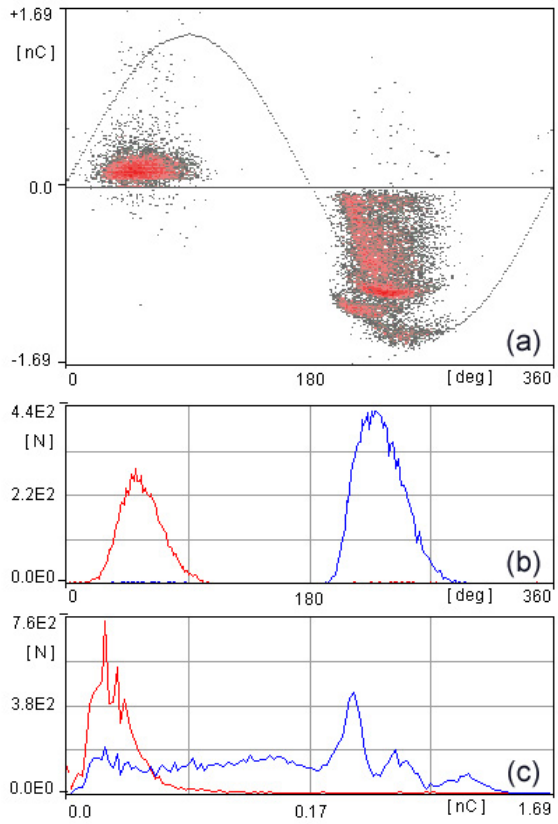

Fig. 2.7. Partial discharge profile obtained on model cable wrapped with Cryoflex™ insulation and immersed in liquid nitrogen at an applied voltage of 52 kVAC rms just prior to breakdown. Polarity of the pulses indicate that the discharge originates from within the cable itself, most likely in the butt gaps. (a) 2-D partial discharge pattern superimposed on a high-voltage waveform, where pulse intensity ranges from low (black) to high (red). (b) Plot of pulse rate as a function of phase angle (red: positive half cycle, blue: negative half cycle). (c) Plot of pulse rate as a function of pulse amplitude (red: positive half cycle, blue: negative half cycle).

2.2 WAUKESHA ELECTRIC SYSTEMS/SUPERPOWER/ROCHESTER GAS & ELECTRIC HTS UTILITY TRANSFORMER SPI

S. W. Schwenterly, J. A. Demko, R. C. Duckworth, I. Sauers, D. R. James, and A. R. Ellis

2.2.1 5/10-MVA Transformer Cooling Module Fabrication

Shop fabrication, final assembly, and proof testing were completed on the 5/10-MVA transformer cooling module. All internal systems were successfully pressure tested and leak checked satisfactorily to 10^{-9} atm-cc/sec. All instrumentation was checked and verified for proper operation. Two defective temperature sensor diodes were discovered; they were replaced by Lakeshore Cryotronics. The completed module and dummy load were crated and shipped to Waukesha Electric Systems (WES) in late March 2002 and arrived in good condition. They will be installed in the WES vacuum test tank for cooling tests in April 2002. Figure 2.8 is a top view of the completed module. The two cryocoolers can be seen in the foreground. The MLI-wrapped heat shield that encloses the thermal-coupling components is below the flange at the bottom of the picture.

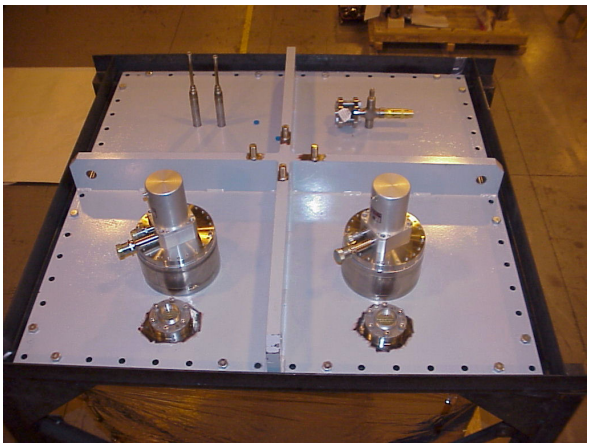

Fig. 2.8. Completed transformer cooling module.

2.2.2 5/10-MVA Transformer Cooling Module Testing

2.2.2.1 Cooling Module Description

A 5/10-MVA, 24.9-kV/4.2-kV prototype HTS transformer is now being fabricated for tests on the utility grid at the WES plant site. The cryogenic system comprises two self-contained modules that bolt into the top plate of the transformer. A cryocooler module provides 25 to 45 K refrigeration to the HTS coils, and a liquid nitrogen tank module supplies liquid nitrogen to the current lead heat sinks and radiation shields on the cold mass. The nitrogen tank has its own cryocooler to recondense boiloff. The HTS coil-cooling module for this transformer was designed by ORNL and fabricated by the private sector in collaboration with SuperPower. Figure 2.9 shows an external view of the cooling module. Two Cryomech AL-330 cryocoolers are mounted on the top flange. Bellows couplings provide vibration isolation and to allow the coolers to deflect slightly with thermal contraction of the internal transformer components. The bellows assemblies are supported by preloaded springs that resist atmospheric pressure when the tank is

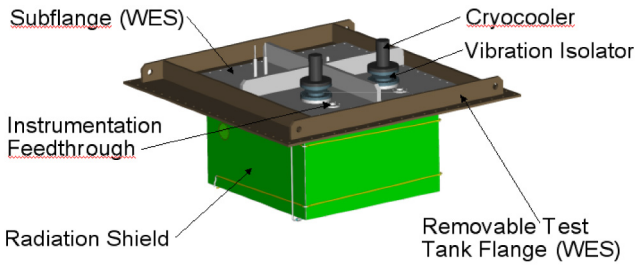

Fig. 2.9. External view of cooling module.

evacuated. A liquid-nitrogen-cooled copper shield with multiple-layer superinsulation (MLI) hangs below the top flange, surrounding the cryocooler cold heads and the components that couple them to the coils.

The thermal coupling system contains several proprietary design innovations. A dummy load with an array of six electric heaters hangs below the radiation shield. The heaters closely reproduce the thermal contact area of the HTS coils. The dummy load is arranged for easy removal before the module is installed in the 5/10-MVA transformer. Temperatures on the cold heads, coupling components, and dummy load are measured by Lakeshore Cryotronics DT-470 diodes calibrated with 0.25-K precision. Radiation shield temperatures are monitored by type T thermocouples. All data were recorded with a Hewlett-Packard data-logging system that downloaded to a computer. Cooling for the cold head compressors was provided by a 3-ton (roughly 10.5-kW) water chiller circulating a glycol solution in a closed loop so that the whole system was completely self-contained. Figure 2.10 shows the finished cooling module being installed in the vacuum test tank at WES. The radiation shield is about to enter the tank, and the MLI-covered dummy load can be seen below the shield toward the back edge of the tank.

Fig. 2.10. Installation of cooling module in vacuum test tank.

2.2.2.2 Performance Requirements

During operation of the 5/10-MVA transformer, the cooling module is required to maintain the coils at temperatures below 50 K, with total heat loads of up to 100 W in normal operation at 100% rated current and 280 W at the 200% overload current. Most of the heat load comes from lead conduction in normal operation and from ac losses in the conductor in the overload condition. After continuous stable operation of the transformer has been demonstrated at the lowest temperatures achievable, it is expected that only one cooler will be operated at higher temperatures in order to increase efficiency. In that situation, the second cooler will have to turn on if a 2× overload suddenly occurs, without allowing the coil temperature to exceed 45 K.

2.2.2.3 Test Results

Following installation of the transformer in the vacuum test tank, the tank was pumped down overnight and a good vacuum in the low 10^{-6} torr range was achieved. After the two cryocoolers were started, the tank was valved off from the vacuum pumping system, and no further pumping was needed. Liquid nitrogen was supplied to the heat shield from an external dewar because the internal liquid nitrogen tank for the transformer would not fit into the vacuum test tank. The shield cooled to 77 K in about 2 h. The coolers ran quietly. The main noise was a hissing sound from the helium lines, which could be easily suppressed with sound insulation. This is an important consideration for utility installations, which are often near residences. The cooling rate during most of the cooldown was about 12 K/h. After about 25 h, the system reached a temperature of 22 to 24 K on the dummy load. Cooldown was completely automatic, and the only operator adjustment needed was an occasional adjustment of the liquid nitrogen flow to the shield. (This adjustment will not be needed on the transformer because it will have the internal gravity-flow liquid nitrogen tank.) Over the next several days, several runs were made with various heating rates on the dummy load. The system stability at all heat loads was excellent, with

no sign of temperature oscillation. The system operated unattended in overnight runs with no problems. On the weekend, the coolers were shut down and the system was allowed to warm in order to gauge the background heat loads. This gave an estimated background load of about 100 W, which is consistent with the rated cooling capacity of the two coolers at the minimum temperature of 22 to 24 K that was reached with no heat on the dummy load. This relatively high background load is mainly radiation from the warm walls of the tank to the dummy load, which had no 77-K shield. The background load of the cooling system itself, excluding the dummy load radiation, is estimated at less than 15 W. Figure 2.11 plots the temperatures maintained on the coolers and dummy load for various values of the total heat load. (including the 100-W background). The lower set of curves was taken with both coolers running; the upper set was taken with only one cooler running. In each set, the upper two lines indicate the range of temperatures on the dummy load, and the lower line gives the temperatures on the cryocooler cold heads. The maximum total load applied to the system was 340 W. This raised the maximum dummy load temperature to 53 K. At that point, the coolers were running 9 to 10 K colder than the dummy load. This total temperature drop is actually somewhat smaller than the values calculated in the original engineering analysis.

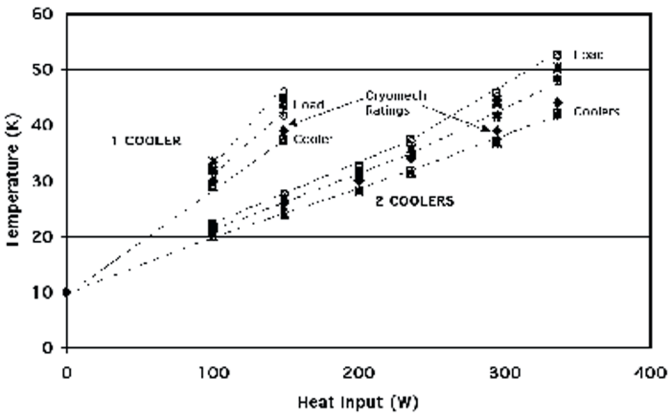

Fig. 2.11. Temperatures maintained vs total heat load.

The six heaters on the dummy load could be controlled individually. To simulate operation of the transformer with unbalanced phase loads, the system was run with 125 W on the first pair of heaters and 100 W on each of the other two pairs. No temperature instability was observed during a few hours of operation in this mode, and dummy load temperatures remained very uniform. The system also ran successfully with a single cooler. As shown in the upper curves on Fig. 2.11, it reached a minimum dummy load temperature of 34 K with the 100-W background load. An additional load of 50 W could be applied without exceeding a load temperature of 45 K. The minimum cryocooler temperature with the 100-W background was 29 K. This is only about 1 K higher than the temperature reached with both coolers and 200 W. This shows that the shutdown cooler does not add more than about 5 W of extra heat load to the system. The black diamond symbols in Fig. 2.11 show Cryomech's published rated temperatures for one and two coolers at the heat inputs used for the tests. The observed cooler temperatures at all loads were actually somewhat lower than the Cryomech ratings, which are probably conservative. The observed cooler temperature plots extrapolate to a zero-heat-load value of about 12 K, which is consistent with Cryomech's ratings.

Figure 2.12 shows the time behavior of the system at a jump in heat load simulating the transition to 2× overload operation. The system was first run with one cooler for several hours at the 100-W background load. During that time, the cooler that was off (Cooler 2) was at just below 35 K, the same as the maximum load temperature. Cooler 1 was running at 30 K. At about 16.5 h, the dummy load was suddenly increased to 200 W, giving a total load of 300 W. The second cooler was now turned on. Within minutes, it cooled down to the same temperature as Cooler 1 and picked up its share of the load with no temperature overshoot. The whole system then slowly warmed up over the next 4.5 h, reaching a maximum temperature of about 46 K. At 21 h, the dummy load was shut off and the system cooled back

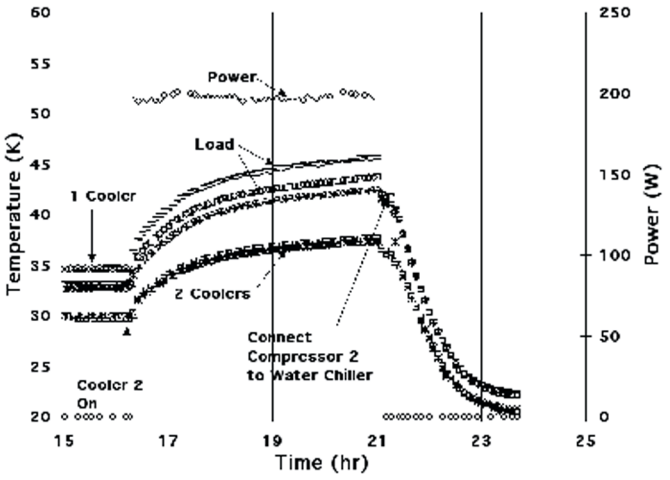

Fig. 2.12. Temperatures vs time in transition from single-cooler mode to both coolers operating. A step increase in dummy load power from 0 to 200 W occurs at 16.5 h.

down. The slope of the cooling curve between 21 and 21.5 h is less steep because Cooler 2 was shut down briefly to connect its compressor to the water chiller. It had earlier been running in open-loop with city water because of some uncertainty that the chiller could handle both compressors.

2.2.2.4 Conclusion

A self-contained, closed-loop cryogenic cooling system for a 5/10-MVA HTS power transformer has been designed, fabricated, and tested. The system worked completely reliably with minimal operator adjustment. It ran successfully over several nights unattended. Acceptable load temperatures were maintained with one cooler at normal operation loads and with both coolers under anticipated overload conditions. The system transitioned smoothly from single-cooler to dual-cooler operation and handled unbalanced heat loads with no problems. The tests show that the heat-transfer efficiency of the system is adequate for the expected loads of the transformer at temperatures up to 50 K. The system is also expected to be applicable to future production transformers with much higher ratings in the 30-MVA range. Use of a better HTS conductor in these units will allow operation with higher currents and voltages at the same total thermal load levels.

2.2.3 MLI Blanket Design

Design of the MLI blankets for the 5/10-MVA transformer coil set was completed. The blankets were designed to use several identical sections; thus design and fabrication costs were reduced. Adjacent blanket sections are electrically isolated from each other to prevent a shorted loop of the conductive aluminized Mylar™ around any or all of the core legs. Before the blankets were ordered, full-size drawings were sent to WES. Simulated blanket patterns were cut from inexpensive material and were checked for proper fit on the frame that supports the phase coils and their radiation shield. The blankets will be procured by SuperPower.

2.2.4 Alternating Current Loss Tests

Further ac loss tests were carried out on the fourth sample coil that was received from SuperPower. The data system capacity was upgraded to measure all of the temperature sensors in the coil so that a more detailed profile of losses vs turn location could be determined. The 60-Hz losses for the superconductor showed the expected cubic dependence on current, as shown in Fig. 2.13. More extensive variable-frequency tests verified the linear dependence of ac losses on frequency, as shown in Fig. 2.14. Thus hysteresis is expected to be the major loss mechanism. The dc critical current of the coil, measured at 44 K, was about 160 A. This gives confidence that the 5/10-MVA unit will be able to operate at 2× overload with ample margins. A final report on the sample was submitted to SuperPower.

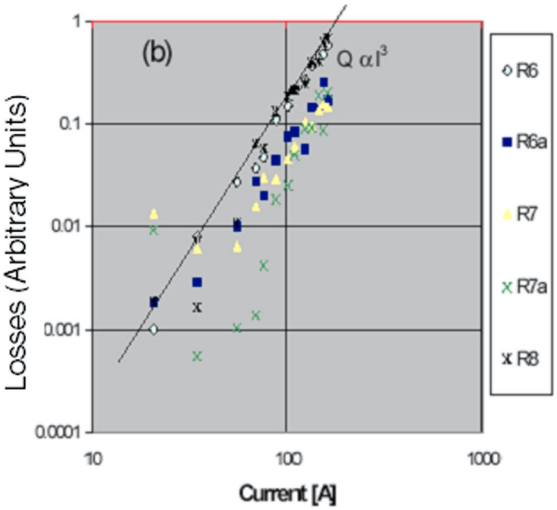

Fig. 2.13. Sample Coil 4: 60-Hz ac losses vs current at 28 K.

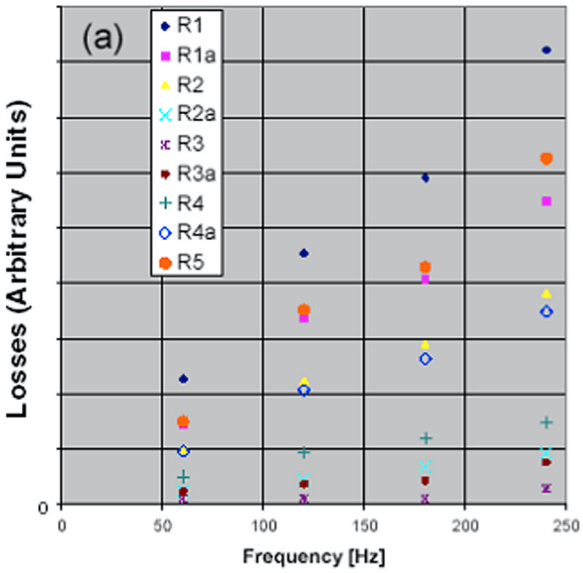

Fig. 2.14. Sample Coil 4: ac losses vs frequency at 39 K and 120 A.

2.3 GENERAL ELECTRIC CO. HTS GENERATOR PROGRAM SPI

J. A. Demko, R. C. Duckworth, M. J. Gouge, and S. W. Schwenterly

A CRADA statement of work for this new SPI project was developed by General Electric (GE) and ORNL staff; the CRADA was approved by GE and the U.S. Department of Energy (DOE) with an effective period from August 2, 2002, through July 31, 2005. The ORNL part of the work scope includes HTS tape and coil testing, cryogenic system R&D/design support, modeling the grid impact of HTS rotors, second-generation conductor compatibility, and general technical support. To support the GE HTS generator development, ORNL has been asked to investigate the effects of small amounts of contamination on the thermal radiation heat transfer between selected surfaces that are relevant to the generator design. Contaminants present in ambient air (e.g., water vapor, nitrogen) have been shown to increase the surface emissivity and, in turn, to increase the thermal radiation heat exchange. A preliminary test plan for the surface emissivity measurements requested by GE has been prepared, and a test arrangement as shown in Fig. 2.15 has been proposed. This facility uses a helium research dewar as the vacuum chamber and a Cryomech AL330 cryocooler

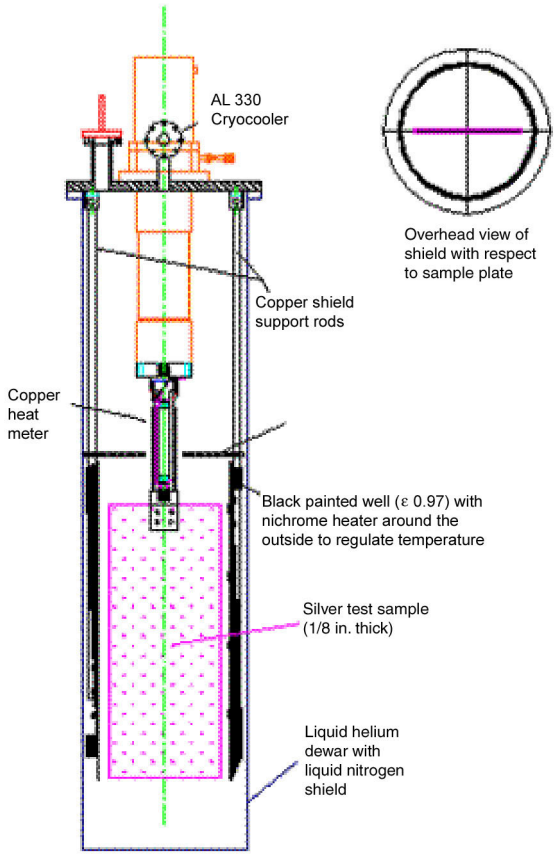

Fig. 2.15. Layout of the proposed emissivity experimental setup.

to cool the test sample plate to the required temperature. With the shield providing an isothermal surface, the heat load to the cooled sample will be measured by a specially designed heat meter. From this measured heat load, the effect of the contaminants on the surface emissivity will be determined. The SINDA/FLUINT Thermal Desktop was used to conduct an initial series of thermal analyses that provided estimates of the magnitude of the heat transfer that can be expected for the geometry shown in Fig. 2.15. The temperature distribution on the test sample as calculated for one case by the Thermal Desktop is shown in Fig. 2.16. Table 2.1 lists emissivities and the calculated variation of the heat transfer for them in this geometry.

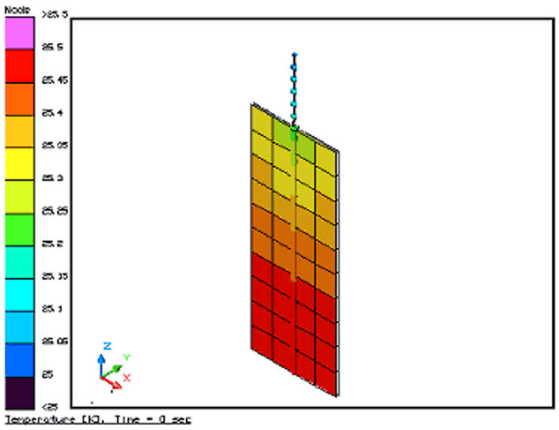

Fig. 2.16. 20 × 51 cm sample plate with 1.3-cm-diam rod and ε_{warm} = 0.95, ε_{cold} = 0.01.

2.4 STRATEGIC R&D: SOLID DIELECTRICS FOR HTS APPLICATIONS: BREAKDOWN STRENGTHS OF STYCAST AND CIBA EPOXIES

I. Sauers, A. R. Ellis, and D. R. James

Additional samples of Stycast Blue (2850 FT) with 24LV catalyst were tested for ac breakdown strength to provide better statistics, particularly at room temperature, where only one breakdown value had been obtained previously. The additional samples run at both room temperature (13 samples) and in a liquid nitrogen bath (24 samples). The data were plotted and were found to follow a weak-link (Weibull statistics) model as shown in Fig. 2.17. The plots can be characterized by a most likely value E_0 and a slope β. Table 2.2 gives the Weibull plot parameters, along with mean rms breakdown values. A 15% decrease in strength was observed in going from room temperature to 77 K.

An epoxy that increases in dielectric strength as the temperature is decreased is highly desirable for high-voltage HTS applications. It has been reported in the literature that nonpolar materials do not exhibit the increase in breakdown strength that is seen in polar materials. The Stycast epoxy used here might be characterized as a relatively nonpolar material, which would be consistent with the observed temperature dependence. In contrast to the Stycast, the Ciba epoxy (now referred to as Araldite 5808) studied previously exhibits a significant increase in strength from room

Table 2.1. Calculated heat loads on the 8-in.-wide, 20-in.-long sample

ε_{warm}	ε_{cold}	Q (W)
0.95	0.01	0.89
0.95	0.02	1.77
0.95	0.03	2.66

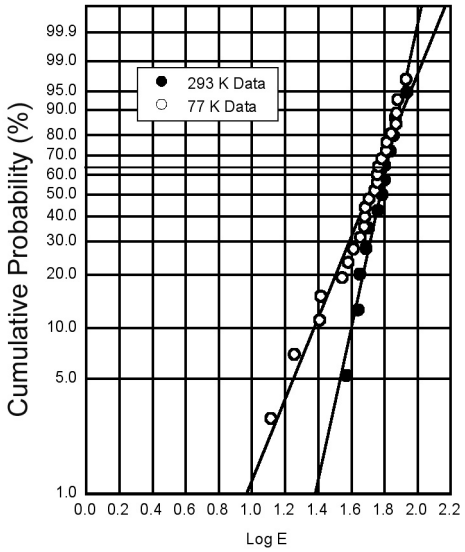

Fig. 2.17. Weibull plot breakdown data for Stycast 2850 FT epoxy at 293 K (solid points) and 77 K (open points). Solid lines through the data are linear regression fits to the data. The heavy horizontal line denotes the Weibull 63.2% probability.

Table 2.2. Statistical data on breakdown in epoxies at room temperature and liquid nitrogen temperature

Temperature (K)	E_0 (kV/mm) Weibull 63.2%	Shape parameter, β (slope)	Number of samples	Arithmetic mean E_{mean} (kV/mm)
		Stycast epoxy		
293	65.9	4.7	13	59.1
77	54.7	2.5	24	51.1
		Araldite cast epoxy		
293	87	4.9	9	70.3
77	166	2.5	7	142.3

temperature to 77 K. A reexamination of the Araldite data using the Weibull analysis is shown in Fig. 2.18 with the two Weibull parameters summarized in Table 2.2. It is not yet known how polar this material is, but the data would suggest that it should be more polar than the Stycast. This point will be investigated further in the future.

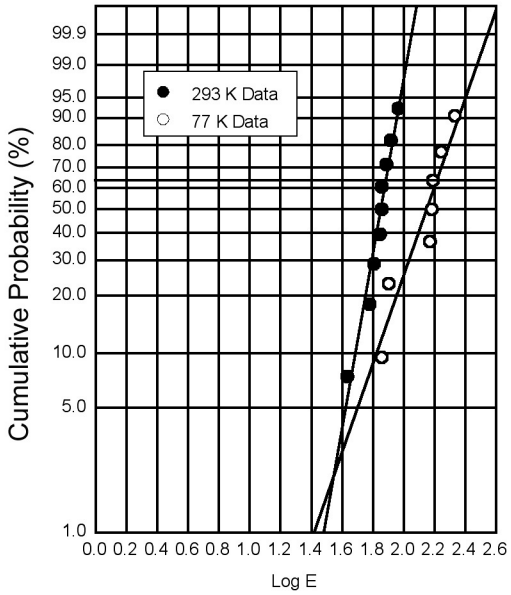

Fig. 2.18. Weibull plot of breakdown data for Ciba epoxy at 293 K (solid points) and 77 K (open points). Solid lines through the data are linear regression fits to the data. The heavy horizontal line denotes the Weibull 63.2% probability.

2.5 STRATEGIC R&D: SHORT SAMPLE CRITICAL CURRENT MEASUREMENTS OF BSCCO TAPES IN EXTERNAL MAGNETIC FIELDS

J. A. Demko (ORNL); M. Young and R. Grabovickic (ORNL and UTK)

Tests continued on silver-alloy BSCCO tapes in this quarter and were extended to measurements in parallel fields from 0 to 5 T. Results are shown in Figs. 2.19 and 2.20. The *n*-values were approximated from the voltage-current characteristic curves by applying the power law to the resistive transition portion of the curve. Figure 2.20 plots the approximated *n*-value as a function of temperature at incremented applied magnetic field magnitudes.

2.6 STRATEGIC R&D: YBCO QUENCH AND STABILITY STUDIES

R. Grabovickic, J. W. Lue, R. C. Duckworth, and M. J. Gouge

Thermal stability and quench propagation in a composite tape made of YBCO superconductor has been studied experimentally. Several 10- to 20-cm-long RABiTS™ YBCO tapes were tested at ORNL. The YBCO tape sample was mounted between a Kapton-tape-insulated Cu block and a G-10 block. It was then affixed to the first-stage cold head of a Cryomech GB-37 cryocooler for conduction cooling to about 40 K. A distribution of critical currents of 12 to 17 A was measured at 78 K, and 62 to 75 A at 43 K. As shown in Fig. 2.21, critical currents increase linearly as the operating temperature decreases.

115A AMSC tape characteristics influenced by externally applied parallel magnetic fields.

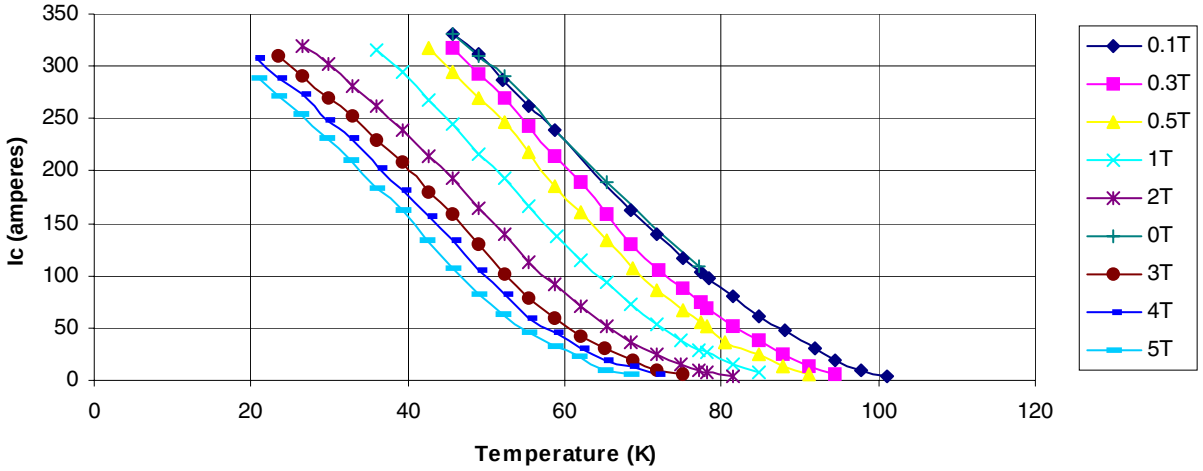

Fig. 2.19. Measurements of the critical current of AMSC HTS tape under background parallel fields from 0 to 5 T.

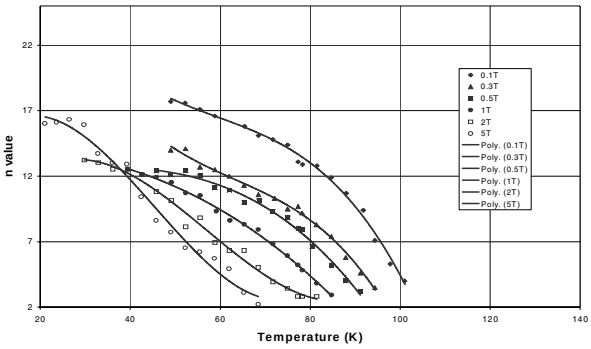

Fig. 2.20. Measured *n* values as a function of temperature at incremented values of an externally applied parallel field.

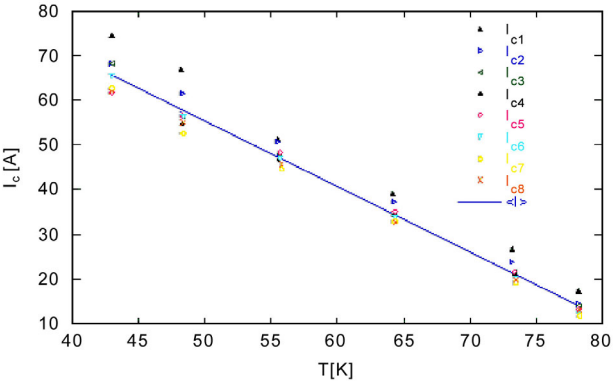

Fig. 2.21. Critical currents of eight different zones of the YBCO tape as a function of operating temperature.

Stability margins were measured from 45 to 80 K. Quench propagation in each test was initiated by applying a sequence of a short overcurrent pulse followed by a longer pulse at a typical operating current for the tape. The resulting change in resistivity due to internal heating was measured through voltage taps across different zones of the tape. Measurements were performed as a function of both initial overcurrent and operating current for several operating temperatures between 45 K and 80 K. At 45 K, for example, a 2.1-s overcurrent pulse (peak current of 117.4 A) followed by a 33.7-A operating current (Fig. 2.22) caused a quench while a peak current of 116.5 A did not (see Fig. 2.23).

The measured stability margins of 16 to 120 J/cm^3 are close to or higher than Cp-integral to transition temperature as shown in Fig. 2.24. It can be seen in Fig. 2.24 that for an operating temperature up to 60 K, the calculated values for stability margin on both curves are much lower than the measured values.

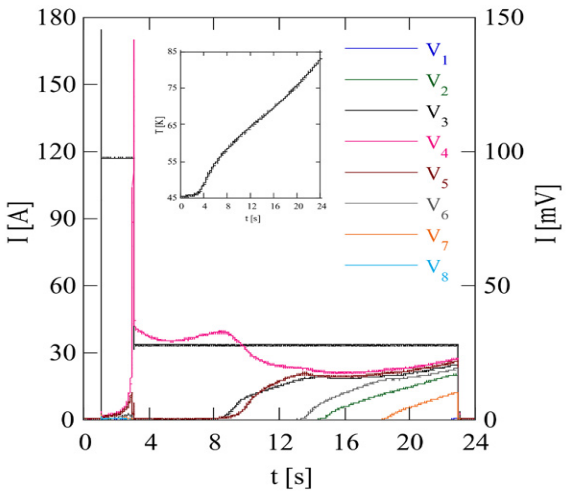

Fig. 2.22. Quench propagation at 45.4 K from zone 4 to zones 3, 2, and 1, and from zone 5 to zones 6 and 7 at 117.4 A overcurrent pulse for 2.1 s followed by a 33.7-A operating current. The inset shows temperature at the middle of the tape as a function of time.

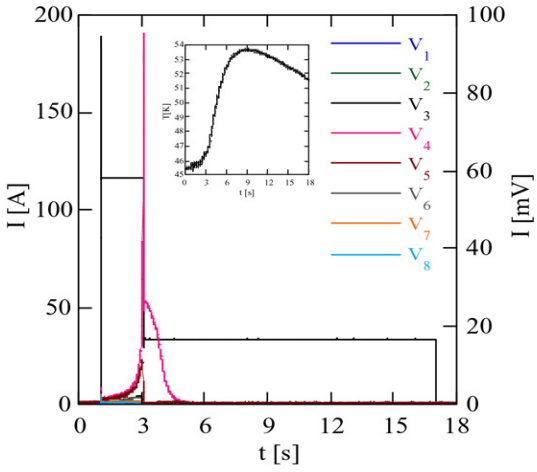

Fig. 2.23. Full recovery at 45.4 K for an overcurrent pulse with a magnitude of 116.5 A and a duration of 2.1 s followed by a 33.7-A operating current.

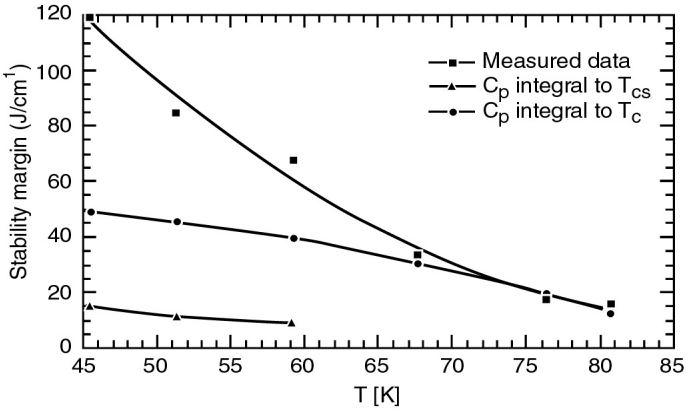

Fig. 2.24. Stability margin as a function of operating temperature.

The higher measured stability margins probably originate from a considerable amount of conduction cooling, which is proportional to the difference between the local temperature of the sample and the operating temperature. There is also some margin provided at $I_t > I_c$ due to the low n value of the YBCO tape ($n \approx 5$–10 from 44 K to 80 K). The cooling effect starts to decrease at the operating temperatures above 60 K, which results in an adequate agreement between measured and calculated values of the stability margin.

The "minimum propagation current" is the operating current below which there is no normal zone propagation, even for overcurrent pulses with an energy exceeding the stability margin. The values for minimum propagation current as a function of operating temperature are plotted in Fig. 2.25. The minimum propagation current was also estimated by extrapolated values from the intercept on the operating-current axis, where the quench propagation velocity was equal to zero. It can be seen in the figure that the extrapolated values for minimum propagation current compare favorably with the corresponding experimentally obtained values.

Distinctive normal zone propagation was observed at all measuring temperatures. Propagation velocity is defined as the ratio between the zone length and the time necessary for a sharp voltage increase in that zone to arrive in the adjacent zone. Normal zone propagation velocities were found to increase linearly with the current as shown in Fig. 2.26. No more than 10 mm/s of propagation velocity

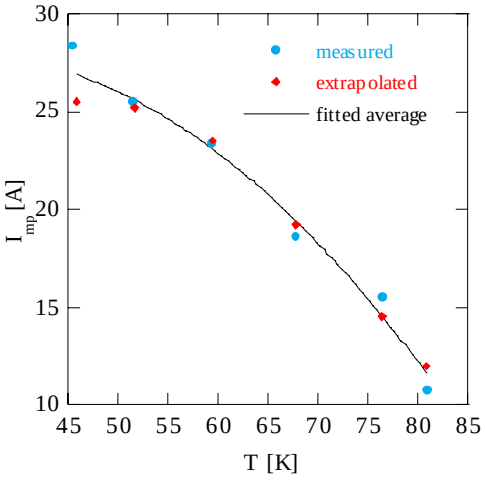

Fig. 2.25. Minimum propagation current as a function of operating temperature.

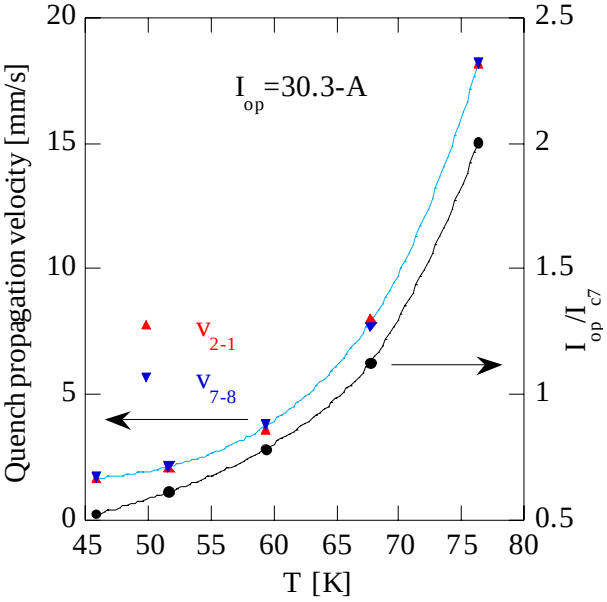

Fig. 2.26. Propagation velocities v_{2-1} and v_{7-8} as a function of temperature ranging from 45.8 K to 76.4 K at an operating current of 30.3 A.

was measured when the operating current was set below the critical current. As can be observed from Fig. 2.26, an increase in temperature resulted in a rapid rise in quench propagation velocity at fixed operating current. The reason for this can be attributed to the decrease in the difference between the transition temperature and the operating temperature.

2.7 STRATEGIC R&D: CRYOGENICS ASSESSMENT TASK

J. A. Demko, M. J. Gouge, and B. W. McConnell

DOE and the national laboratory, industrial, and university teams working on electric system HTS applications have long recognized the importance of cryogenics as an enabling technology. Cryogenics workshops were held at the 1998 and 1999 DOE peer reviews. These workshops examined the state-of-the-art in cryogenic components and estimated performance requirements when used with HTS electric power systems. The key issues in employment of cryogenic support technology were identified as efficiency, reliability, and cost. The participants developed a cryogenic roadmap and a companion implementation plan. Building on this planning base, the principal objectives of this present effort are as follows:

- determination of the characteristics of the cryogenic refrigeration systems for use in HTS electric power applications;
- critical appraisal of the state of cryogenic refrigeration technology, comparing how well this technology matches the needs of the HTS power applications;
- determination of deficiencies in cryogenic technology that must be mitigated;
- identification of the R&D program elements that should be undertaken to fulfill the needs of the HTS power applications; and
- development of an appropriate programmatic approach, involving contributions from government, industry, and academia, to ensure that cryogenic refrigeration technology will be adequately mature to enable practical HTS power applications.

Technical interviews were completed with staff who are active in cryogenics research in the cryogenic industry, the SPI teams, utilities, national laboratories, and universities. Based on their input, a draft report was developed and a presentation of status and initial recommendations was made at the January 2002 Wire Development Workshop. Subsequent draft reports were distributed in February and March, and a final draft report was provided to DOE with recommendations in early April. After the relevant cryogenic technology and the needs of the HTS electric applications were reviewed, the following recommendations were made in the report.

- A specific SPI-type program targeted to cryogenic support systems for HTS electric applications is recommended. Cryogenic equipment vendors should lead the effort because they are the center of expertise and represent the future industrial base to support HTS electric applications. It may be possible to leverage similar efforts in the U.S. Department of Defense.
- Standardization across devices is strongly recommended where feasible. This appears possible for motors, generators, transformers, fault-current limiters, HTS coils, and perhaps cables. This approach will enable the focused R&D resources to benefit the most applications.
- The Stirling (valveless) pulse tube shows promise; it has no moving parts in the cold section of the pulse tube, and it has drive units that can be oil-free with non-wearing internal parts. Reliability and efficiency have the potential to approach the Cryogenic Roadmap goals.
- Single-stage GM cryocoolers are the workhorses of the present SPIs, and their potential needs to be determined relative to that of pulse-tube cryocoolers.
- For HTS cables, the availability of cryocoolers that can provide 1 to 2 kW at 70 to 80 K with performance near Cryogenic Roadmap goals would be an attractive solution relative to the physically larger Brayton and Claude Cycles with helium or nitrogen as the cycle fluid.
- A parallel program must be considered, especially for cables, on lowering cryostat heat losses (i.e. lower the system heat load-W/m) and improving cryostat reliability (by solving the problem of high-vacuum degradation). The initial effort led by NASA-Kennedy Space Center shows promising results for flexible cryostats.

Based on the positive response from the community and DOE program staff, ORNL developed a statement of work for a request for proposal (RFP) and presented it at the 2002 DOE HTS Peer Review (oral presentation and poster) and at the 2002 Applied Superconductivity Conference (poster). There was a broad consensus on the suitability of the work statement. DOE concurred with the RFP for the initiative, and ORNL issued it in late August 2002. Proposals were due in November 2002. ORNL is leading a multiple-laboratory team to evaluate the proposals. This DOE national program effort has also been coordinated with technical staff from Department of Defense laboratories that would benefit from R&D in this cryogenic enabling technology for superconducting applications. The assessment report that the statement of work is based on is available at the following website: http://www.ornl.gov/HTSC/pdf/CryoAssessRpt.pdf.

3. Summary of Technology Partnership Activities

3.1 BACKGROUND

Oak Ridge National Laboratory (ORNL) is a key participant in the U.S. Department of Energy's (DOE's) national effort on electric power applications of high-temperature superconductivity (HTS). ORNL has formed effective teams that combine the resources of the Laboratory with the entrepreneurial drive of private companies. New technology partnership mechanisms, a feature of the ORNL Superconducting Technology Program for Electric Power Systems since its inception in 1988, have resulted in 42 superconductivity "pilot center" cooperative agreements and 9 cooperative research and development agreements (CRADAs). Seven cooperative agreements and three interagency agreements were active during FY 2002. In addition, licensing agreements, joint inventions, and joint publications with the private industry partners have ensured that there *is* technology transfer throughout the program.

Technology partnering on Laboratory-industry teams can occur in several ways. In the ORNL program, the cooperative development level of technology partnering is emphasized: joint Laboratory-industry teams work on problems that (1) require combined resources and expertise and (2) have a clear objective of precompetitive research and technology development. For the project to succeed, each partner depends on the success of the other. Most of the cooperative projects with private industry and the Laboratory precompetitive research and development (R&D) projects involve developing key technology in which commercialization of the results is expected to occur after a minimum of 3 to 5 years.

3.2 RELATIONSHIP TO THE DOE MISSION

The ORNL program mission is that of its program sponsor, DOE's Office of Distributed Energy and Electric Reliability, Superconductivity Program: to develop the technology base necessary for industry to proceed to commercialization of electric energy applications of HTS. HTS will enable new energy-efficient motors, transformers, and transmission lines and will also provide electric power equipment manufacturers with strategic technology for global competitiveness. Electric utilities can defer acquisition of new transmission rights-of-way with successful introduction of superconducting cables. System stability and protection will be enhanced with the introduction of fault-current limiters. Distributed utility systems in the future, which will include distributed generation systems, will benefit from the small size and light weight of the next generation of electric power equipment. In addition, oil-free power transformers and cables will provide a cost-effective, more environmentally friendly option for the utility sector.

3.3 FUNDING

DOE funding for the ORNL program, a summary of funds-out cooperative agreements, and subcontracting activities in 2002 are shown in Tables 3.1, 3.2, and 3.3. Funds-out to industry, universities, and other federal agencies (e.g., the National Institute of Standards and Technology and the National Science Foundation) was more than $3.7 million in FY 2002.

Table 3.1. Superconducting Technology Program funding: authorization and outlay by fiscal year

	New budget authorization/outlay ($\$ \times 1000$)				
	1998	1999	2000	2001	2002
Direct scientific and technical[a]	5,356	5,416	5,616	8,989	6,494
Management and outreach	400	400	400	400	420
Subtotal—ORNL	**5,756**	**5,816**	**6,016**	**9,389**	**6,914**
Subcontracts[b]	2,437	3,244	4,099	4,680	3,330
Funds-out cooperative agreements[c]	589	795	585	945	370
Total program	8,782	9,855	10,700	15,014	10,614

[a]Includes ORNL capital equipment ($1.4 M in FY 2001 for ACCI facility).

[b]Details are provided in separate table.

[c]Includes interagency agreements (National Institute of Standards and Technology, National Aeronautics and Space Administration, and the National Science Foundation).

3.4 TECHNOLOGY PARTNERSHIP APPROACH

An interdisciplinary approach uses many of the resources available at ORNL to meet the program goals for joint Laboratory-industry development of HTS technology for electric power applications. The superconductivity agreement mechanism interlinks R&D projects with industry and universities that optimize utilization of facilities, expertise, and program resources for the benefit of all participants. This program also coordinates the ORNL activities with the other national laboratories, government agencies, university centers, and industry groups.

Cooperative agreements ensure that technology development is industry-driven. The ORNL Office of Technology Transfer and Economic Development and patent counsel work together to place these agreements. Where appropriate, these efforts are coordinated with projects within ORNL that are funded by the DOE Office of Science as well as Work for Others and ORNL Laboratory Director's R&D Fund projects.

Effective funds-out to industry is used to supplement industry cost share. In FY 2002, $3.7 million in funds-out to industry and universities was provided through cooperative agreements and subcontracts. To keep industry involved from the start of the program and to ensure commercialization potential, all of these technology-partnering mechanisms are augmented by CRADAs, user agreements, and licensing activities.

Responsiveness to American industry has high priority in this program. An ORNL ad hoc technical review committee, consisting of a project manager, a scientific coordinator, a manager for conductor development, and a manager for applications development, reviews all inquiries from industry and recommends projects for possible funding. This review ensures that (1) the proposed work fits the program mission, (2) the work is collaborative, (3) there is legitimate commercial interest, and (4) the work is feasible. Substantial private-sector cost share is required on cooperative agreements.

ORNL provides support to the DOE Headquarters (DOE-HQ) Superconductivity Program for Electric Power Systems by identifying, guiding, and monitoring R&D at ORNL and ORNL subcontractor sites and by performing coordination, analysis, and planning of activities related to the national program.

ORNL works with the other program laboratories to address such issues as communication among program participants, workshop and meeting implementation, planned competitive solicitations and superconductivity agreements, and coordination of technical and economic assessments.

Table 3.2. Superconductivity Program summary of cooperative agreements as of September 30, 2002

Participant[a]	Approved term	Type[b]	Total agreement cost share ($K)			Technology area
			By DOE		By industry	
			To ORNL	To industry		
American Superconductor	4/5/01–4/4/05	C	2,400	0	2,400	HTS conductors for electric power applications; BSCCO-2223 Wire Development Group; and YBCO wires
General Electric Company	8/2/02–7/31/05	C	650	0	650	Design and development of a 100-MVA HTS generator
NIST-Gaithersburg	12/1/00–11/30/2002	IAG	0	300	300	YBCO phase diagram research
NIST-Boulder	3/98–12/31/2004	IAG	0	907	907	Electromechanical properties for superconductor applications
NSF Sci & Tech. Policy Inst (RAND)	4/15/2000–10/30/2002	IAG	0	300	0	HTS critical issues study
Neocera	8/1/2001–9/30/2003	FO	250	205	260	Pulsed e-beam deposition as a viable method for HTS coated conductor development
Oxford Instruments	1/94–1/31/2004	C	1,450	0	1,675	Develop technology for RABiTS™ metal template
Southwire Company	2/1/97–9/30/2005	FO	12,066	500	12,631	Develop HTS cable technology
3M-Southwire-LANL-ORNL	4/3/97–12/31/2002	C				Development of HTS wire using coated conductor technologies
3M					2,758	
Southwire					580	
LANL				2,480[c]	3,338	
ORNL			2,600			
Waukesha Electric Systems	6/15/97–3/31/2003	FO	3,197	250	2,556.4	HTS transformer
Total active agreements			22,613	2,462	24,717.4	
Total completed agreements			14,524	6,030.6	18,898.7	
TOTALS			37,137	8,492.6	43,616.1	

[a]LANL = Los Alamos National Laboratory, NSF = National Science Foundation, NIST = National Insititute of Science and Technology.
[b]C = CRADA, FO = funds-out, IAG = interagency agreement.
[c]DOE to LANL.

Table 3.3. FY-2002–2003 active subcontracts ($K)

Subcontractor	Term	Obligated		Subject
		FY 2002	Cumulative	
Imtech	10/3/94–2/29/00		358	Assist research on HTS materials
	3/1/2000–2/28/01		66	
	3/2/2001–2/28/02		81	
	3/1/02–3/31/03	47	47	
Massachusetts Institute of Technology (competed)	6/1/00–12/31/02	46	236	Stability and quench protection
Florida State University (competed)	6/1/00–12/31/02	36	161	Stability and quench protection
Oak Ridge Institute for Science and Education (competed)	Ongoing	945	945	Postdoctoral research fellowships
Energetics, Inc. (competed)	4/18/00–3/31/01		432	Technical and analytical support to ORNL/LANL/ANL
	4/1/01–9/30/02	190	600	
	9/30/02–3/31/03			
Bob Lawrence & Associates (competed)	3/15/99–10/30/02	160	845	Technological and economic benefits assessment and market study; HTS outreach
	10/1/02–9/30/05	20		
University of South Carolina	7/1/99–9/30/02		20	High-temperature conductor development and characterization
Stanford University (competed)	10/1/98–3/31/02		1465	Ion-beam-assisted deposition of buffer layers and in situ deposition of YBCO by electron-beam evaporation
Boston College	6/28/99–2/18/01		99	Dev. epitaxial film growth and properties
	2/19/01–7/31/02	10	69	
MicroCoating Technologies (competed)	11/1/99–3/31/03	400	2075	Coated conductor research
3M (competed)	2/1/00–3/31/03	750	1877	Coated conductor research
IGC (competed)	6/7/00–3/9/03	508	950	Coated conductor research
TMS	5/3/02–11/30/03	55	55	Technical assistance to HTS
University of Florida	10/1/00–9/30/02		53	HTS films and buffers on biaxially textured copper
University of Kansas	5/00–7/15/02		98	Hg-based HTS coated conductors
University of Cincinnati	9/15/01–9/14/03		60	Nonfluorine sol-gel synthesis of YBCO thin films on flexible substrates for developing coated conductors

An Industrial Overview Committee is charged with reviewing program activities and advising Laboratory management as to program progress, policy, and direction. The committee consists of representatives of electric utilities, original equipment manufacturers, and HTS wire manufacturers. This committee meets occasionally at ORNL, Argonne National Laboraory, or Los Alamos National Laboratory.

3.5 PROGRAM INVENTIONS

A summary of the new invention disclosures for FY 2002 is shown in Table 3.4. Patents issued in FY 2002 are shown in Table 3.5, and all patents issued since 1994 are shown in Table 3.6.

Table 3.4. Invention disclosures in FY 2002

ID No.	Subject	Submitted by
1002	Method to fabricate biaxially textured articles	A. Goyal
1036	Method of depositing a buffer layer on magnesium oxide templates and articles formed thereby	M. Paranthaman, T. Aytug (ORISE), D. K. Christen, R. Feenstra
1040	Method of fabricating epitaxial films of superconducting MgB_2	A. Goyal, H. M. Christen, H.-Y. Zhai (ORISE)
1041	Method of fabricating flexible, semiconductor-based devices	A. Goyal
1042	Method of fabricating biaxially textured substrates	A. Goyal
1043	Buffer layers and articles for electronic devices	A. Goyal
1047	Buffer layer suitable for synthesis of high-J_c YBCO coatings by the BaF_2 ex situ method	R. Feenstra, M. Paranthaman, T. Aytug, D. K. Christen
1074S	Alloyed magnesium-boron superconductor with transition temperature above 100 K (subcontract)	D. C. Larbalestier, C.-B. Eom, S. D. Bu, J.-H. Choi, S. Patnaik, A. V. Gurevich, L. D. Cooley, E. E. Hellstrom, and A. A. Squitieri (University of Wisconsin)
1112S	Method of fabricating YBCO thin and thick films via sol-gel processing (subcontract)	A. Goyal (ORNL) and Y. Xu (Univ. of Cincinnati)
1128	Rapid, low-pressure conversion of high-temperature superconductor precursor	F. A. List III
1129C	Method, composition, and article pertaining to superconductor on textured metal substrate (CRADA)	A. Goyal (ORNL), C. Thieme (American Superconductor)
1132C	Ternary nonmagnetic alloys for biaxially textured substrates (CRADA)	C. L. H. Thieme (American Superconductor)
1146	Termination for a high-temperature superconducting triaxial cable	P. W. Fisher, C. A. Foster, M. J. Cole, and M. J. Gouge (ORNL) and D. T. Lindsay (Southwire)
1155C	New precursor route to produce epitaxial oxide buffers on biaxially textured metal and alloy substrates (CRADA)	M. Paranthaman, S. Sathyamurthy, T. Aytug, and M. W. Rupich (American Superconductor)

Table 3.5. Patents issued in FY 2002

Patent No./ID No.	Date Issued	Title
6,296,701 B1 (296)	October 2, 2001	Method of Depositing An Electrically Conductive Oxide Film on a Textured Metallic Substrate and Articles Formed Therefrom
6,331,199 B1	December 18, 2001	Biaxially Textured Articles Formed by Powder Metallurgy
6,375,768 B1 (312)	April 23, 2002	Method for Making Biaxially Textured Articles by Plastic Deformation
6,385,835 B1	May 14, 2002	Apparatus for Fabricating Continuous Lengths of Superconductor
6,399,154 B1 (734)	June 4, 2002	Laminate Article
6,440,211 B1 (649)	August 27, 2002	Method of Depositing Buffer Layers on Biaxially Textured Metal Substrates
6,447,714 B1 (316)	September 10, 2002	Method for Forming Biaxially Textured Articles by Powder Metallurgy
6,451,450 B1 (749)	September 17, 2002	Method of Depositing a Protective Layer over a Biaxially Textured Alloy Substrate and Composition Therefrom

Table 3.6. Cumulative list of patents issued

Patent No./ID No.	Date Issued	Title
5,357,756 (1185-X)	Oct. 25, 1994	Bipolar Pulse Field for Magnetic Refrigeration
5,395,821 (1039-X)	March 7, 1995	Method of Producing Pb-Stabilized Superconductor Precursors and Method of Producing Superconductor Articles Therefrom
5,525,583 (1471-X) (with AMSC)	June 11, 1996	Superconducting Magnetic Coil
5,546,261	August 13, 1996	Hermetically Sealed Superconducting Magnet Motor
5,646,097	July 8, 1997	Method of Fabricating a (1223) Tl-Ba-Ca-Cu-O Superconductor
5,739,086 (1640-X)	April 14, 1998	Structures Having Enhanced Biaxial Texture and Method of Fabricating Same
5,741,377 (1640-X)	April 21, 1998	Structures Having Enhanced Biaxial Texture and Method of Fabricating Same
5,830,828 (1193-X)	November 3, 1998	Process for Fabricating Continuous Lengths of Superconductor
5,846,912 (1512-X)	December 8, 1998	Method for Preparation of Textured $YBa_2Cu_3O_x$ Superconductor
5,898,020 (1640-X)	April 27, 1999	Structures having Enhanced Biaxial Texture and Method of Fabricating Same

Table 3.6 (continued)

Patent No./ID No.	Date Issued	Title
5,958,599 (1640-X)	September 28, 1999	Structures Having Enhanced Biaxial Texture
5,964,966	October 12, 1999	Method of Forming Biaxially Textured Alloy Substrates and Devices Thereon
5,968,877 (18-19)	October 19, 1999	High-T_c YBCO Superconductor Deposited on Biaxially Textured Ni Substrate
5,972,847 (458)	October 26, 1999	Method for Making High-Critical-Current-Density $YBa_2Cu_3O_7$ Superconducting Layers on Metallic Substrates.
6,055,446 (1193)	April 25, 2000	Continuous Lengths of Oxide Superconductors
6,077,344 (223)	June 20, 2000	Sol-Gel Deposition of Buffer Layers on Biaxially Textured Metal Substances
6,106,615 (368)	August 22, 2000	Method of Forming Biaxially Textured Alloy Substrates and Devices Thereon
6,114,287 (534) (HTSPC-023)	September 5, 2000	Method of Deforming a Biaxially Textured Buffer Layer on a Textured Metallic Substrate and Articles Therefrom
6,150,034 (467)	Nov. 21, 2000	Buffer Layers on Rolled Nickel, or Copper as Superconductor Substrates
6,156,376 (467)	Dec. 5, 2000	Buffer Layers on Metal Surfaces having Biaxial Texture as Superconductor Substrates
6,159,610 (467)	December 12, 2000	Buffer Layers on Metal Surfaces having Biaxial Texture as Superconductor Substrates
6,180,570 B1 (312)	January 30, 2001	Biaxially Textured Articles Formed by Plastic Deformation
6,256,521 B1 (1784, new 148)	July 3, 2001	Preferentially Oriented, High-Temperature Superconductors by Seeding and a Method for their Preparation
6,261,704 B1 (218)	July 17, 2001	MGO Buffer Layers on Rolled Nickel or Copper as Superconductor Substrates
6,70,908 B1 (734)	August 7, 2001	Rare Earth Zirconium Oxide Buffer Layers on Metal Substrates
6,286,194 B (1193)	September 11, 2001	Apparatus for Fabricating Continuous Lengths of Superconductor
6,296,701 B1 (296)	October 2, 2001	Method of Depositing An Electrically Conductive Oxide Film on a Textured Metallic Substrate and Articles Formed Therefrom
6,331,199 B1 (316)	December 18, 2001	Biaxially Textured Articles Formed by Powder Metallurgy
6,375,768 B1 (312)	April 23, 2002	Method for Making Biaxially Textured Articles by Plastic Deformation
6,385,835 B1 (Div of 5830828)	May 14, 2002	Apparatus for Fabricating Continuous Lengths of Superconductor
6,399,154 B1 (734)	June 4, 2002	Laminate Article
6,440,211 B1 (649)	August 27, 2002	Method of Depositing Buffer Layers on Biaxially Textured Metal Substrates
6,447,714 B1 (316)	September 10, 2002	Method for Forming Biaxially Textured Articles by Powder Metallurgy
6,451,450 B1 (749)	September 17, 2002	Method of Depositing a Protective Layer over a Biaxially Textured Alloy Substrate and Composition Therefrom

4. Events, Honors, and Awards

4.1 CARL KOHRT VISITS THE COATED CONDUCTOR RESEARCH LABORATORY

Carl Kohrt, Battelle's president and chief executive officer, made his first visit to ORNL in January 2002. While at ORNL, Dr. Kohrt toured the ACCL, where he observed the operation of ORNL's unique reel-to-reel X-ray diffraction facility, which is used to analyze the crystalline alignment of HTS substrates. In Fig. 4.1, ORNL staff member Eliot Specht is showing him the results for a RABiTS™ sample produced by Microcoating Technologies, Inc.

Fig. 4.1. Eliot Specht shows the results of reel-to-reel XRD analysis of a RABiTS™ sample to Battelle President and CEO Carl Kohrt.

4.2 DOE RECOGNIZES PATRICK MARTIN AS "OUTSTANDING MENTOR"

DOE's Office of Science recently named Patrick Martin, a member of ORNL's Metals and Ceramics Division and key contributor in the ORNL Superconductivity Program, an "outstanding mentor" for his service as mentor in the summer of 2001 for the Energy Research Undergraduate Laboratory Fellowships (see Fig. 4.2). Mr. Martin was a mentor for Frank Partica, an undergraduate student from the Juniata College in Pennsylvania. The output from the 10-week summer internship included development and demonstration of a new system to measure the critical current of long-length superconducting tapes, a system that is in constant use today at ORNL. The system design was transferred to 3M Company, which duplicated it for its use in St. Paul, Minnesota. Patrick received a plaque from Dr. Peter Faletra, the Office of Science's assistant director for education, during his visit to ORNL on February 26, 2002.

Fig. 4.2. Patrick Martin receives the "Outstanding Mentor" award from UT-Battelle's Deputy Director for Science and Technology Lee Riedinger (left) and DOE's Office of Science Assistant Director for Education Dr. Peter Faletra.

4.3 VISITING FACULTY

Professor John Pfotenhauer, from the University of Wisconsin-Madison, arrived in early March 2002 for a 3-month sabbatical at ORNL. He worked on an Office of Science program on changing the cooling mechanism for solid hydrogen extruders from liquid helium to a closed system that uses GM cryocoolers. He also assisted with the final stages of the cryogenic assessment task.

4.4 SUPERCONDUCTIVITY PRESENTED AT SCIENCE AND HUMANITIES SYMPOSIUM

ORNL's Superconductivity Program Manager Bob Hawsey presented a talk and demonstration entitled "Superconductivity: Going for the Cold" on March 1, 2002, at the American Museum of Science and Energy (Fig. 4.3). The talk was part of the Thirty-Seventh Annual Tennessee Junior Science and Humanities Symposium, one of more than 42 such symposia conducted nationally. Approximately 85 science students and instructors from 10 Tennessee high schools attended the talk. The objectives of the symposia are

Fig. 4.3. Going for the cold!

- to promote research and experimentation in the sciences, mathematics, and engineering at the high school level;
- to recognize the significance of research in human affairs and the importance of humane and ethical principles in the application of research results;
- to search out talented youth and their teachers, recognize their accomplishments at symposia, and encourage their continued interest and participation in the sciences, mathematics, and engineering;
- to expand the horizons of research-oriented students by exposing them to opportunities in the academic, industrial, and governmental communities;
- to enlarge the number of future adults capable of conducting research and development; and
- to encourage more active participation of females and other minorities in the sciences, mathematics, and engineering.

4.5 SUMMER INTERNS

The ORNL Superconductivity Program again participated in the summer intern programs conducted by the Oak Ridge Institute for Science and Education. (See Table 4.1 and Fig. 4.4).

Table 4.1. Summer interns and their ORNL mentors

Intern		Mentor	
Name	College	Name	Division
Arpan Basu	Tennessee Technological University	Parans Paranthaman	Chemical Sciences
Daniel Deschenes	California State University Fresno	Isidor Sauers	Fusion Energy
Nicholas Early	Indiana University of Pennsylvania	Patrick Martin	Metals and Ceramics
Peter Hellenbrand	University of Wisconsin-Madison	Parans Paranthaman	Chemical Sciences
Jenny Tobin	Albion College	David Christen	Condensed Matter Sciences
Marcus Young	University of Tennessee	Jonathan Demko	Fusion Energy

Fig. 4.4. The 2003 summer interns in ORNL's Superconductivity Program: (left to right) top: Daniel Deschenes, Arpan Basu, and Peter Hellenbrand; bottom: Nicholas Early, Marcus Young, and Jenny Tobin.

4.6 INDUSTRIAL PARTNERS USE COATED CONDUCTOR RESEARCH LABORATORY AT ORNL

4.6.1 MicroCoating Technologies

E. D. Specht

As U.S. companies develop high-temperature superconducting wires for electric power applications, a measure of the "texture," or in-plane crystallographic alignment, is an important indicator of the quality of a long-length sample. An important tool used to measure this property and other like properties is X-ray diffraction. Staff from MicroCoating Technologies (MCT), of Chamblee, Georgia, a key industrial partner in the Superconductivity Program for Electric Power, visited ORNL to use this diagnostic tool for superconducting wire research (Fig. 4.5). MCT brought four 1-mm-long samples of coated conductor template to ORNL to gain first-hand experience with the new reel-to-reel X-ray diffraction system recently brought on line at ORNL's coated-conductor research laboratory. MCT used its proprietary combustion chemical vapor deposition process to produce the templates. The X-ray diffraction measurements showed that MCT's templates are of excellent quality and exhibit a high degree of in-plane grain alignment, a necessary condition for high-performance superconductor deposition.

Fig. 4.5. Dr. Marvis White using the ORNL equipment. Dr. White is MCT's scientist responsible for developing on-line quality assurance diagnostic tools.

4.6.2 American Superconductor

A. Goyal and P. Paranthaman

Cees Thieme and Steve Hancock of American Superconductor (AMSC, Westborough Mass.) spent the week of September 16, 2002, at ORNL in order to use a new "four-high" state-of-the-art rolling mill (see Fig. 4.6). The mill was installed earlier this year as part of the ORNL's ACCL facilities, which are dedicated to working with U.S. industry to accelerate the scale-up of next-generation high-temperature superconductors for electric power applications. During the week the visitors used the mill to roll nickel alloy materials for use as the starting template for HTS coated conductors based on ORNL's patented RABiTS™ technology.

Fig. 4.6. Cees Thieme (AMSC), Parans Paranthaman (ORNL), and Steve Hancock (AMSC).

4.7 TMS, ACS PRESENT AWARDS TO AMIT GOYAL

During FY 2002, TMS presented Amit Goyal a recognition award for making a "significant contribution as a plenary speaker in the Fundamentals of Materials for Energy Conversion Symposium at the 131st TMS annual meeting. A certificate was also presented to Goyal by the American Ceramics Society for organizing a symposium at the 104th annual meeting in 2002.

4.8 AMSC PRESENTS AWARDS TO ORNL STAFF MEMBERS

John Scudiere, General Manager, Advanced Conductors, at AMSC, visited ORNL on September 27, 2002. During the visit, Mr. Scudiere presented recognition awards to the three ORNL principal investigators with whom AMSC has worked over the past few years. He thanked the entire ORNL "coated conductor team" for helping AMSC achieve world-record performance of next-generation high-temperature superconducting wire based in part on ORNL's patented RABiTS™ technology (see Fig. 4.7). Scudiere also announced that, in partnership with AMSC, the performance of the YBCO wires had increased by 15% since July to more than 140 amperes over a one-meter length, with outstanding uniformity along the length.

Fig. 4.7. Left to right: John Scudiere (AMSC), Everett Bloom and Amit Goyal (Metals and Ceramics Division), John Cooke and Claudia Cantoni (Condensed Matter Sciences Division), Paarans Paranthaman and Michelle Buchanan (Chemical Sciences Division), and Jim Roberto (Associate Lab Director for Physical Sciences).

4.9 ORNL CO-HOSTS INTERNATIONAL WORKSHOP ON PROCESSING AND APPLICATIONS OF SUPERCONDUCTORS

The Materials Research Society (MRS) sponsored International Workshop on Processing & Applications of Superconductors was held in Gatlinburg, Tennessee, on July 31–August 2, 2002. Organized by M. Parans Paranthaman (Chair), Amit Goyal, and Ron Feenstra of Oak Ridge National Laboratory, Teruo Izumi of ISTEC, Japan, and Venkat Selvamanickam of IGC-SuperPower, it presented work from an international group of 50 scientists from industry, national laboratories, and academia who are key players in the field of high temperature superconductivity. Among the 100 workshop attendees were academics, researchers, and engineers from countries all the over the world, including Japan, Germany, France, Korea, and Spain. This workshop also provided overviews of the status of the second-generation YBCO coated conductors in the United States, Japan, and Europe. A pre-workshop tour of ORNL's Accelerated Coated Conductor laboratories was a highlight for the visitors (see Figs. 4.8–4.10).

Fig. 4.8. ORNL Superconductivity Facility tour group, July 31, 2002.

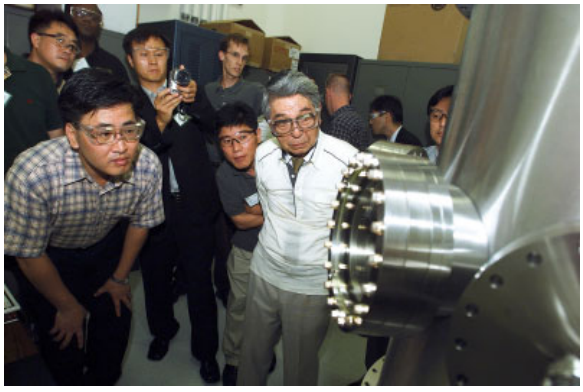

Fig. 4.9. Dr. S. Tanaka (white jacket), vice-president of the International Superconductivity Technology Center in Japan, tours ORNL's Accelerated Coated Conductor Research Laboratory.

Fig. 4.10. Left: MRS Workshop on Superconductivity, Gatlinburg. Right: MRS Workshop poster session.

5. Presentations/Publications

PUBLISHED

Agassi, D., S. J. Pennycook, D. K. Christen, G. Duscher, A. Franceschetti, and S. T. Pantelides, "Critical Currents at Grain Boundaries in High Temperature Superconductors," pp. 253–58 in *Materials for High-Temperature Superconductor Technologies*, ed. M. Paranthaman, M. W. Rupich, K. Salama, J. Mannhart, and T. Hasegawa, Symposium Proceedings Vol. 689, Materials Research Society, Warrendale, Pa., 2002.

Andreone, A., A. Cassinese, C. Cantoni, E. Di Gennaro, G. Lamura, M. G. Maglione, M. Paranthaman, M. Salluzzo, and R. Vaglio, "Study of the Microwave Electrodynamic Response of MgB_2 Thin Films," *Physica C* **372–376**, 1287–90 (2002).

Annavarapu, S., N. Nguyen, S. Cui, U. Schoop, C. Thieme, M. W. Rupich, T. Kodenkandath, D. Verebelyi, W. Zhang, X. Li, Q. Li, M. Paranthaman, A. Goyal, C. Cantoni, M. Kowalewski, and F. A. List, "Program Towards a Low-Cost Commercial Coated Conductor," pp. 231–37 in *Materials for High-Temperature Superconductor Technologies*, ed. M. Paranthaman, M. W. Rupich, K. Salama, J. Mannhart, and T. Hasegawa, Symposium Proceedings Vol. 689, Materials Research Society, Warrendale, Pa., 2002.

Aytug, T., M. Paranthaman, H. Y. Zhai, H. M. Christen, S. Sathyamurthy, D. K. Christen, and R. E. Ericson, "Single Buffer Layers of $LaMnO_3$ or $La_{0.7}Sr_{0.3}MnO_3$ for the Development of $YBa_2Cu_3O_{7-\delta}$ Coated Conductors: A Comparative Study," *J. Mater. Res.* **17**(9), 2193–96, (2002).

Aytug, T., Y.-Y. Xie, J. Z. Wu, and D. K. Christen, "Growth Characteristics of $HgBa_2CaCu_2O_6$ Superconducting Films on CeO_2-Buffered YSZ Single Crystals: An Assessment for Coated Conductors," *Physica C* **363**, 107–112 (2001).

Aytug, T., M. Paranthaman, S. Sathyamurthy, B. W. Kang, D. B. Beach, C. E. Vallet, E. D. Specht, D. F. Lee, R. Feenstra, A. Goyal, D. M. Kroeger, K. J. Leonard, P. M. Martin, and D. K. Christen, "High-J_c YBCO Coatings on Reel-to-Reel Dip-Coated Gd_2O_3 Seed Buffer Layers Epitaxially Fabricated on Biaxially Textured Ni and Ni-(3at%W-1.7at%Fe) Alloy Tapes," pp. 211–16 in *Materials for High-Temperature Superconductor Technologies*, ed. M. Paranthaman, M. W. Rupich, K. Salama, J. Mannhart, and T. Hasegawa, Symposium Proceedings Vol. 689, Materials Research Society, Warrendale, Pa., 2002.

Bugoslavsky, Y., Y. Miyoshi, G. K. Perkins, A. V. Borenov, Z. Lockman, J. L. MacManus-Driscoll, L. F. Cohen, A. D. Caplin, H. Y. Zhai, M. P. Paranthaman, H. M. Christen, and M. Blamire, "Structure of the Superconducting Gap in MgB_2 from Point-Contact Spectroscopy," *Supercon. Sci. Technol.* **15**, 526–32 (2002).

Bugoslavsky, Y., L. Cowey, T. J. Tate, G. K. Perkins, J. Moore, Z. Lockman, A. Berenov, J. L. MacManus-Driscoll, A. D. Caplin, L. F. Cohen, H. Y. Zhai, H. M. Christen, M. P. Paranthaman, D. H. Lowndes, M. H. Jo, and M. G. Blamire, "Effective Vortex Pinning in MgB_2 Thin Films," *Supercond. Sci. Technol.* **15**, 1392–97 (2002).

Callcott, T. A., L. Lin, G. T. Woods, G. P. Zhang, A. Andreone, J. LeCochec, A. Gauzzi, C. Cantoni, M. Paranthaman, D. K. Christen, H. M. Christen, G. Giunchi, and S. Ceresara, "Magnetic Penetration Depth Measurements in MgB_2 Sintered Pellets and Thin Films," *Phys. Rev. B* **65** 20506 (2001).

Cantoni, C., D. K. Christen, R. Feenstra, A. Goyal, G. W. Ownby, D. M. Zehner, and D. P. Norton, "Reflection High-Energy Electron Diffraction Studies of Epitaxial Oxide Seed-layer Growth on Rolling-Assisted Biaxially Textured Substrate Ni(001): The Role of Surface Structure and Chemistry," *Appl. Phys. Lett.* **79**(19), 3077–79 (2001).

Cantoni, C., D. K. Christen, A. Goyal, L. Heatherly, G. W. Owenby, D. M. Zehner, D. P. Norton, C. M. Rouleau, and H. M. Christen, "Effect of Sulfur Surface Structure on Nucleation of Oxide Seed Layers on Textured Metals for Coated Conductor Applications," pp. 349–54 in *Materials for High-Temperature Superconductor Technologies*, ed. M. Paranthaman, M. W. Rupich, K. Salama, J. Mannhart, and T. Hasegawa, Symposium Proceedings Vol. 689, Materials Research Society, Warrendale, Pa., 2002.

Cantoni, C., D. K. Christen, L. Heatherly, M. M. Kowalewski, F. A. List, A. Goyal, G. W. Ownby, D. M. Zehner, B. W. Kang, and D. M. Kroeger, "Quantification and Control of the Sulfur c (2 × 2) Superstructure on $\{100\}_2$, and $SrTiO_3$ Seed Layer Texture," *J. Mater. Res.* **17**(10), 2549–54 (2002).

Christen, D. K., C. Cantoni, J. R. Thompson, M. Paranthaman, M. F. Chisholm, H. R. Kerchner, and H. M. Christen, "Superconducting Properties of High-$J_c MgB_2$ Coatings," pp. 25–31 in *Materials for High-Temperature Superconductor Technologies*, ed. M. Paranthaman, M. W. Rupich, K. Salama, J. Mannhart, and T. Hasegawa, Symposium Proceedings Vol. 689, Materials Research Society, Warrendale, Pa., 2002.

Feldmann, D. M., D. C. Larbalestier, W. Zhang, Q. Li, G. N. Riley, R. Feenstra, A. Goyal, D. F. Lee, M. Paranthaman, D. M. Kroeger, and D. K. Christen, "Inter- and Intragrain Transport Measurements in $YBa_2Cu_3O_{7-x}$ Deformation Textured Coated Conductors," *Appl. Phys. Lett.* **79**, (24) 3998–4000 (2001).

Hawsey, R. A., "Overview of the U.S. Department of Energy Superconductivity Program for Electric Power," pp. 201–10 in *Materials for High-Temperature Superconductor Technologies*, ed. M. Paranthaman, M. W. Rupich, K. Salama, J. Mannhart, and T. Hasegawa, Symposium Proceedings Vol. 689, Materials Research Society, Warrendale, Pa., 2002.

Jin, R., M. Paranthaman, H. Y. Zhai, H. M. Christen, D. K. Christen, and D. Mandrus, "Unusual Hall Effect in Superconducting MgB_2 Films," *Phys. Rev. B* **64** 220506 (2001).

Kaindl, R. A., M. A. Carnahan, J. Orenstein, and D. S. Chenia (Lawrence Berkeley National Laboratory), H. M. Christen, H. Y. Zhai, M. Paranthaman, and D. H. Lowndes (ORNL), "Far-Infrared Optical Conductivity Gap in Superconducting MgB_2 Films," *Phys. Rev. Lett.* **88(**2), 027003 (2002).

Kang, B. W., A. Goyal, D. F. Lee, J. E. Mathis, E. D. Specht, P. M. Martin, D. M. Kroeger, M. Paranthaman, and S. Sathyamurthy, "Comparative Study of Thickness Dependence of Critical Current Density of $YBa_2Cu_3O_{7-\delta}$ on (100) $SrTiO_3$ and on Rolling-Assisted Biaxially Textured Substrates," *J. Mater. Res.* **17**(7), 1750–57 (2002).

Kerchner, H. R., C. Cantoni, M. Paranthaman, D. K. Christen, H. M. Christen, J. R. Thompson, and D. J. Miller, "Heavy-Ion Damage to Magnesium Diboride Films: Electrical Transport-Current Characterization," pp. 133–38 in *Materials for High-Temperature Superconductor Technologies*, ed. M. Paranthaman, M. W. Rupich, K. Salama, J. Mannhart, and T. Hasegawa, Symposium Proceedings Vol. 689, Materials Research Society, Warrendale, Pa., 2002.

Kim, I., P. N. Barnes, A. Goyal, S. A. Barnett, R. Biggers, G. Kozlowski, C. Varanasi, I. Maartens, R. Nekkanti, T. Peterson, T. Haugan, and S. Sambasivan, "Growth of YBCO Thin Films on TiN(001) and CeO_2-Coated TiN Surfaces, *Physica C* **377** 227–34 (2002).

Lamura, G., E. D. Gennaro, M. Salluzzo, A. Andreone, J. L. Cochec, A. Gauzzi, C. Cantoni, M. Paranthaman, D. K. Christen, H. M. Christen, G. Giunchi, and S. Ceresara, "Magnetic Penetration Depth Measurements in MgB_2 Sintered Pellets and Thin Films," *Phys. Rev. B* **65**, 020506 (2002).

Norton, D. P., K. Kim, D. K. Christen, J. D. Budai, B. C. Sales, M. F. Chisholm, D. M. Kroeger, A. Goyal, and C. Cantoni, "$(La,Sr)TiO_3$ as a Conductive Buffer for RABiTS Coated Conductors," *Physica A* **372–376**, 818–20 (2002).

Paranthaman, M. P., T. Aytug, H. Y. Zhai, S. Sathyamurthy, H. M. Christen, P. M. Martin, D. K. Christen, R. E. Erickson, and C. L. Thomas, "Single Buffer Layer Technology for YBCO Coated Conductors," pp. 323–28 in *Materials for High-Temperature Superconductor Technologies*, ed. M. Paranthaman, M. W. Rupich, K. Salama, J. Mannhart, and T. Hasegawa, Symposium Proceedings Vol. 689, Materials Research Society, Warrendale, Pa., 2002.

Sathyamurthy, S., and K. Salama, "Processing Aspects of MOD Strontium Titanate Buffer Layers for Coated Conductor Applications," *Physica C* **377**, 208–16 (2002).

Sathyamurthy, S., M. Paranthaman, T. Aytug, B. W. Kang, P. M. Martin, A. Goyal, D. M. Kroeger, and D. K. Christen, "Chemical Solution Deposition of Lanthanum Zirconate Buffer Layers on Biaxially Textured Ni-1.7% Fe-3% W Alloy Substrates for Coated-Conductor Fabrication," *J. Mater. Res.* **17**(6),1543–49 (2002).

Sathyamurthy, S., M. Paranthaman, B. W. Kang, H. Y. Zhai, T. Aytug, H. M. Christen, E. D. Specht, M. M. Kowalewski, A. Goyal, and P. M. Martin, "Fabrication of High J_c $YBa_2Cu_3O_{7-\delta}$ Coated Conductors Using Sol-Gel Buffer Layers on Nickel and Nickel Alloy Substrates," pp. 357–62 in *Materials for High-Temperature Superconductor Technologies*, ed. M. Paranthaman, M. W. Rupich, K. Salama, J. Mannhart, and T. Hasegawa, Symposium Proceedings Vol. 689, Materials Research Society, Warrendale, Pa., 2002.

Sathyamurthy, S., M. Paranthaman, H Y. Zhai, H. M. Christen, P. M. Martin, and A. Goyal, "Lanthanum Zirconate: a Single Buffer Layer Processed by Solution Deposition for Coated Conductor Fabrication," *J. Mater. Res.* **17(**9), 2181–84 (2002).

Sheahen, T. P., B. W. McConnell, and J. W. Mulholland, "Method for Estimating Future Markets for High-Temperature Superconducting Power Devices," in *IEEE Transactions on Applied Superconductivity*, Vol. 12, No. 2, June 2002.

Shoup, S. S., M. K. White, S. L. Krebs, N. Darnell, A. C. King, D. S. Mattox, I. H. Campbell, K. R. Marken, S. Hong, B. Czabaj, M. Paranthaman, H. M. Christen, H.-Y. Zhai, and E. D. Specht, "The Progress on Low-Cost, High-Quality, High-Temperature Superconducting Tapes Deposited by the Combustion Chemical Vapor Deposition Process," pp. 239–44 in *Materials for High-Temperature Superconductor Technologies*, ed. M. Paranthaman, M. W. Rupich, K. Salama, J. Mannhart, and T. Hasegawa, Symposium Proceedings Vol. 689, Materials Research Society, Warrendale, Pa., 2002.

Specht, E. D., and F. A. List, "Texture by the Kilometer," pp. 277–82 in *Materials for High-Temperature Superconductor Technologies*, ed. M. Paranthaman, M. W. Rupich, K. Salama, J. Mannhart, and T. Hasegawa, Symposium Proceedings Vol. 689, Materials Research Society, Warrendale, Pa., 2002.

Specht, E. D., F. A. List III, D. F. Lee, K. L. More, A. Goyal, W. B. Robbins, and D. O'Neill, "Uniform Texture in Meter-Long $YBa_2Cu_3O_7$ Tape," *Physica C* **382**, 342–48 (2002).

Thompson, J. R., A. Goyal, D. K. Christen, and D. M. Kroeger, "Ni-Cr Textured Substrates with Reduced Ferromagnetism for Coated Conductor Applications," *Physica C* **370**, 169–76 (2002).

Wong-Ng, W., L. P. Cook, J. Suh, I. Levin, M. Vaudin, R. Feenstra, and J. P. Cline, "Phase Relationships and Phase Formation in the System BaF_2-BaO-Y_2O_3-CuO_x-H_2O," pp. 337–48 in *Materials for High-Temperature Superconductor Technologies*, ed. M. Paranthaman, M. W. Rupich, K. Salama, J. Mannhart, and T. Hasegawa, Symposium Proceedings Vol. 689, Materials Research Society, Warrendale, Pa., 2002.

Xie, Y. Y., J. Z. Wu, T. Aytug, and D. K. Christen, "Diffusion Mechanism of Cations and Anions in Cation-Exchange Process for Fabrication of High-T_c Superconducting $HgBa_2CaCu_2O_{6+\delta}$ Films," pp. 107–12 in *Materials for High-Temperature Superconductor Technologies*, ed. M. Paranthaman, M. W. Rupich, K. Salama, J. Mannhart, and T. Hasegawa, Symposium Proceedings Vol. 689, Materials Research Society, Warrendale, Pa., 2002.

Yang, C.-Y., S. E. Babcock, A. Ichinose, A. Goyal, D. M. Kroeger, D. F. Lee, F. A. List, D. P. Norton, J. E. Mathis, M. Paranthaman, and C. Park, "Microstructure of Pulsed Laser Deposited $YBa_2Cu_3O_{7-\delta}$ Films on Yttria-Stabilized Zirconia/CeO_2 Buffered Biaxially Textured Ni Substrates," *Physica C* **377**, 333–47 (2002).

Zhai, H. Y., H. M. Christen, C. Cantoni, A. Goyal, and D. H. Lowndes, "Epitaxial Titanium Diboride Films Grown by Pulsed-Laser Deposition," *Appl. Phys. Lett.* **80**(11), 1963–65 (2002).

Zhukov, A. A., A. Purnell, Y. Miyoshi, Y. Bugoslavsky, Z. Lockman, A. Berenov, H. Y. Zhai, H. M. Christen, M. P. Paranthaman, D. H. Lowndes, W. H. Jo, M. G. Blamire, L. Hao, J. Gallop, J. L. MacManus-Driscoll, and L. F. Cohen, "Microwave Surface Resistance of MgB_2," *Appl. Phys. Lett.* **80**(13), 2347–49 (2002).

SUBMITTED FOR PUBLICATION

Aytug, T. , M. Paranthaman, S. Kang, H. Y. Zhai, H. M. Christen, C. E. Vallet, S. Sathyamurthy, A. Goyal, and D. K. Christen, "$LaMnO_3$: A Single Oxide Buffer Layer for High-J_c $YBa_2Cu_3O_{7-\delta}$ Coated

Conductors," submitted to the proceedings of the 2002 Applied Superconductivity Conference, August 4–9, Houston, Texas, and will be published in *IEEE Trans. on Appl. Supercond.*

Aytug, T., M. Paranthaman, S. Sathyamurthy, B. W. Kang, D. B. Beach, E. D. Specht, D. F. Lee, R. Feenstra, A. Goyal, D. M. Kroeger, K. J. Leonard, P. M. Martin, and D. K. Christen, "Reel-to-Reel Continuous Chemical Solution Deposition of Epitaxial Gd_2O_3 Buffer Layers on Biaxially Textured Metal Tapes for the Fabrication of $YBa_2Cu_3O_{7-\delta}$ Coated Conductors," *Journal of American Ceramic Society* (in press).

Cantoni, C., D. K. Christen, A. Goyal, L. Heatherly, F. A. List, G. W. Ownby, D. M. Zehner, H. M. Christen, and C. M. Rouleau, "Growth of Oxide Seed Layers on Ni and Other Technologically Interesting Metal Substrates: Issues Related to Formation and Control of Sulfur Superstructures for Texture Optimization," submitted to the proceedings of the 2002 Applied Superconductivity Conference, August 4–9, Houston, Texas, and will be published in *IEEE Trans. on Appl. Supercond*.

Cheggour, N., J. W. Ekin, C. C. Clickner, D. T. Verebelyi, C. L. H. Thieme, A. P. Malozemoff, R. Feenstra, A. Goyal, and M. Paranthaman, "Transverse Compressive Stress Effect in Y-Ba-Cu-O Coatings on Biaxially Textured Ni and Ni-5at.%W Substrates," submitted to the proceedings of the 2002 Applied Superconductivity Conference, August 4–9, Houston, Texas, and will be published in *IEEE Trans. on Appl. Supercond*.

Demko, J. A., J. W. Lue, M. J. Gouge, D. Lindsay, M. Roden, D. Willen, M. Daumling, J. E. Fesmire, and S. D. Augustynowicz, "Cryostat Vacuum Thermal Considerations for HTS Power Transmission Cable Systems," submitted to the proceedings of the 2002 Applied Superconductivity Conference, August 4–9, Houston, Texas, and will be published in *IEEE Trans. on Appl. Supercond*.

Duckworth, R. C., J. W. Lue, D. F. Lee, R. Grabovickic, and M. J. Gouge, "The Role of Nicel Substrates in the Quench Dynamics of Silver Coated YBCO Tapes," submitted to the proceedings of the 2002 Applied Superconductivity Conference, August 4–9, Houston, Texas, and will be published in *IEEE Trans. on Appl. Supercond*.

Fisher, P. W., M. J. Cole, J. A. Demko, C. A. Foster, M. J. Gouge, R. W. Grabovickic, J. W. Lue, and J. P. Stovall, "Design, Analysis, and Fabrication of a Tri-Axial Cable System," submitted to the proceedings of the 2002 Applied Superconductivity Conference, August 4–9, Houston, Texas, and will be published in *IEEE Trans. on Appl. Supercond.*

Grabovickic, R., J. W. Lue, M. J. Gouge, J. A. Demko, and R. C. Duckworth, "Measurements of Temperature Dependence of the Stability and Quench Propagation of a 20-cm-long RABiTS Y-Ba-Cu-O Tape," submitted to the proceedings of the 2002 Applied Superconductivity Conference, August 4–9, Houston, Texas, and will be published in *IEEE Trans. on Appl. Supercond*.

Paranthaman, M. P., T. Aytug, S. Sathyamurthy, D. B. Beach, A. Goyal, D. F. Lee, B. W. Kang, L. Heatherly, E. D. Specht, K. J. Leonard, D. K. Christen, and D. M. Kroeger, "Bulk Solution Techniques to Fabricate High J_c YBCO Coated Conductors," *Physica C* (accepted for publication).

Paranthaman, M., D. K. Christen, H. M. Christen, J. R. Thompson, H. R. Kerchner, C. Cantoni, and H. Y. Zhai, "Growth of High Current Density MgB_2 Films Using Ex Situ Precursor Approach," *Physica C* (submitted).

Paranthaman, M. Parans, T. Aytug, S. Kang, R. Feenstra, J. D. Budai, D. K. Christen, P. N. Arendt, J. R. Groves, R. F. DePaula, S. R. Foltyn, and T. G. Holesinger, "Fabrication of High J_c YBCO Tapes using the Newly Developed Lanthanum Manganate Single Buffer Layers," submitted to the proceedings of the 2002 Applied Superconductivity Conference, August 4–9, Houston, Texas, and will be published in *IEEE Trans. on Appl. Supercond.*

Rupich, M. W., U. Schoop, D. T. Verebelyi, C. Thieme, W. Zhang, X. Li, T. Kodenkandath, N. Nguyen, E. Siegal, D. Buczek, J. Lynch, M. Jowett, E. Thompson, J.-S. Wang, J. Scudiere, A. P. Malozemoff, Q. Li, S. Annavarapu, S. Cui, L. Fritzemeier, B. Aldrich, C. Craven, F. Neu, A. Goyal, and M. Paranthaman, "YBCO Coated Conductors," submitted to the proceedings of the 2002 Applied Superconductivity Conference, August 4–9, Houston, Texas, and will be published in *IEEE Trans. on Appl. Supercond*.

Sathyamurthy, S., M. P. Paranthaman, H.-Y. Zhai, H. M. Christen, C. Cantoni, A. Goyal, and P. M. Martin, "Solution Processing of Lanthanum Zirconate Films as Single Buffer Layers for High I_c YBCO Coated Conductors," submitted to the proceedings of the 2002 Applied Superconductivity Conference, August 4–9, Houston, Texas, and will be published in *IEEE Trans. on Appl. Supercond*.

Schwenterly, S. W., M. J. Cole, D. W. Hazelton, and E. F. Pleva, "Performance of a Prototype HTS Power Transformer Cooling Module," submitted to the proceedings of the 2002 Applied Superconductivity Conference, August 4–9, Houston, Texas, and will be published in *IEEE Trans. on Appl. Supercond*.

Schwenterly, S. W., S. P. Mehta, M. S. Walker, and R. H. Jones, "Development of HTS Power Transformers for the 21st Century: Waukesha Electric Systems/IGC-SuperPower/RG&E/ORNL SPI Collaboration," submitted to proceedings of the US-Japan Workshop on High-T_c Superconductors, Santa Fe N.M., Dec. 2–5, 2001, and accepted for publication in *Physica C*.

Specht, E. D., F. A. List III, D. F. Lee, K. L. More, A. Goyal, W. B. Robbins, and D. O'Neill, "Uniform Texture in Meter-Long $YBa_2Cu_3O_7$ Tape," *Physica C* (submitted).

Verebelyi, D. T., U. Schoop, C. Thieme, S. Annavarapu, S. Cui, X. Li, W. Zhang, T. Kodenkandath, L. Fritzemeier, Q. Li, A. P. Malozemoff, N. Nguyen, D. Buczek, J. Lynch, J. Scudiere, M. Rupich, A. Goyal, L. Heatherly, and M. Paranthaman, "Uniform Performance of Meter Long YBCO on Textured Ni Alloy Substrates," *Supercond. Sci. Technol.* (submitted).

Xu, Yongli, A. Goyal, N. A. Rutter, D. Shi, M. Paranthaman, S. Sathyamurthy, P. M. Martin, and D. M. Kroeger, "Fabrication of High J_c $YBa_2Cu_3O_{7-\delta}$ Films Using a Fluorine-Free Sol Gel Approach," *Applied Physics Letters* (submitted).

Young, M. A., J. A. Demko, M. J. Gouge, M. O. Pace, J. W. Lue, and R. Grabovickic, "Measurements of the Performance of BSCCO HTS Tape under Magnetic Fields with a Cryocooled Test Rig,"

submitted to the proceedings of the 2002 Applied Superconductivity Conference, August 4–9, Houston, Texas, and will be published in *IEEE Trans. on Appl. Supercond.*

Zhai, H. Y., H. M. Christen, P. M. Martin, L. Zhang, and D. H. Lowndes, "Direct Electrical Heating of Metal Tape Substrates for Coated Conductor Deposition," submitted to the proceedings of the 2002 Applied Superconductivity Conference, August 4–9, Houston, Texas, and will be published in *IEEE Trans. on Appl. Supercond.*

ABSTRACTS SUBMITTED FOR CONFERENCES AND WORKSHOPS

Aytug, T., M. Paranthaman, S. Kang, H.-Y. Zhai, S. Sathyamurthy, H. M. Christen, D. K. Christen, and R. E. Ericson, "Assessment of Insulating $LaMnO_3$ and Conductive $La_{1-x}A_xMnO_3$ (A = Sr,Ca) Perovskites as Single Oxide Buffer Layers for $YBa_2Cu_3O_{7-\delta}$ Coated Conductors," submitted to 2002 MRS Fall Meeting, Boston Mass, December 2–6, 2002.

Burdette, Don, M. Pace, D. R. James, I. Sauers, and A. Ellis, "Partial Discharge in Voids in Epoxy in Liquid Nitrogen," submitted to the Conference on Electrical Insulation and Dielectric Phenomena (CEIDP), Cancun, Mexico, October 20–24, 2002.

Cantoni, C., D. K. Christen, L. Heatherly, F. A. List, A. Goyal, G. W. Ownby, and D. M. Zehner, "Control of the Sulfur *c* (2×2) Superstructure on {100}<100>-Textured Metals for RABiTS Applications," 104th American Ceramic Society Meeting, St. Louis, Missouri, April 25–May 1, 2002.

Christen, D. K., C. Cantoni, R. Feenstra, T. Aytug, M. P. Paranthaman, L. Heatherly, M. M. Kowalewski, F. A. List, A. Goyal, G. W. Ownby, D. M. Zehner, and D. M. Kroeger, "Strategic Research at ORNL for the Development of Advanced Coated Conductors: Part 1," invited abstract submitted to the Korean Institute of Applied Superconductivity and Cryogenics (KIASC) Conference, 2002, Gyungju, South Korea, February 23, 2002.

Christen, D. K., C. Cantoni, R. Feenstra, T. Aytug, M. P. Paranthaman, L. Heatherly, M. M. Kowalewski, F. A. List, A. Goyal, G. W. Ownby, D. M. Zehner, and D. M. Kroeger, "Strategic Research at ORNL for the Development of Advanced Coated Conductors: Part 1," invited presentation to the Korean Atomic Energy Research Institute, Daejeon, South Korea, February 25, 2002.

Christen, D. K., C. Cantoni, R. Feenstra, T. Aytug, M. P. Paranthaman, L. Heatherly, M. M. Kowalewski, F. A. List, A. Goyal, G. W. Ownby, D. M. Zehner, and D. M. Kroeger, "Strategic Research at ORNL for the Development of Advanced Coated Conductors: Part 1," invited presentation to the Korean Electrotechnology Institute (KERI), Changwon, South Korea, February 26, 2002.

Christen, D. K., C. Cantoni, R. Feenstra, T. Aytug, M. P. Paranthaman, L. Heatherly, M. M. Kowalewski, F. A. List, A. Goyal, G. W. Ownby, D. M. Zehner, and D. M. Kroeger, "Strategic Research at ORNL for the Development of Advanced Coated Conductors: Part 1," invited presentation to the Department of Materials Science and Engineering, Seoul National University, Seoul, South Korea, February 27, 2002.

Christen, D. K., C. Cantoni, J. R. Thompson, M. Paranthaman, H. R. Kerchner, H. M. Christen, and H.-Y. Zhai, "Fabrications and Properties of High-J_c MgB_2 Coatings, invited abstract submitted to the American Ceramics Society 104th Meeting, St. Louis Missouri, April 28–May 1, 2002.

Christen, H. M., "Calculating the Cost of Pulsed Laser Deposition," submitted to 2002 MRS International Workshop on Processing and Applications of Superconductors, Gatlinburg, Tennessee, August 1–2, 2002.

Feenstra, R., A. A. Gapud, D. K. Christen, A. Goyal, F. A. List, L. heatherly, P. M. Martin, D. M. Kroeger, D. M. Feldmann, D. C. Larbalestier, T. G. Holesinger, P. N. Arendt, J. R. Groves, and R. F. DePaula, "Thickness Dependence of J_c of YBCO Coatings Produced by a BaF_2 ex situ Process," submitted to 2002 MRS Fall Meeting, Boston, Massachusetts, December 2–6, 2002.

Feldmann, D. M., S. I. Kim, D. C. Larbalestier, R. Feenstra, A. A. Gapud, D. K. Christen, A. Goyal, F. A. List, L. Heatherly, P. M. Martin, and D. M. Kroeger, "Intra-Granular J_c Versus Grain-Boundary J_c as a Function of YBCO Thickness," submitted to 2002 MRS Fall Meeting, Boston, Massachusetts, December 2–6, 2002.

Gapud, A. A., D. K. Christen, J. R. Thompson, and M. Yethiraj, "Electrical Transport, Magnetic, and Structural Properties of the Vortex Lattice in Superconducting V_3Si," American Physical Society March Meeting, Indianapolis, Indiana, March 18–22, 2002.

Gapud, A. A., D. K. Christen, J. R. Thompson, and M. Yethiraj, "Electrical Transport, Magnetic, and Structural Properties of the Vortex Lattice in Superconducting V_3Si," paper submitted for proceedings of the 23rd International Conference on Low Temperature Physics of Advanced Materials, Hiroshima, Japan, August 20–27, 2002.

James, D. R., I. Sauers, M. Pace, and A. Ellis, "High Voltage Breakdown of Some Solid Epoxies at Room Temperature and in Liquid Nitrogen," submitted to the Conference on Electrical Insulation and Dielectric Phenomena, Cancun, Mexico, October 20–24, 2002.

Lee, D. F., K. J. Leonard, J. Yoo, L. Heatherly, Jr., F. A. List III, P. M. Martin, E. D. Specht, M. P. Paranthaman, and D. M. Kroeger, "Continuous Reel-to-Reel, Ex-Situ Processing of YBCO on Textured Substrates," submitted to 2002 MRS International Workshop on Processing and Applications of Superconductors, Gatlinburg, Tennessee, August 1–2, 2002.

Pace, M., I. Sauers, D. R. James, and A. R. Ellis, "Aging of Lapped Tape Insulated Cable at Cryogenic Temperature," submitted to the Conference on Electrical Insulation and Dielectric Phenomena, Cancun, Mexico, October 20–24, 2002.

Paranthaman, M., S. Sathyamurthy, T. Aytug, D. B. Beach, S. Kang, A. Goyal, H.-Y. Zhai, H. M. Christen, and D. K. Christen, "Development of Low-Cost Alternative Buffer Layer Architectures for YBCO Coated Conductors," submitted to 2002 MRS Fall Meeting, Boston, Massachusetts, December 2–6, 2002.

Sathyamurthy, S., M. Paranthaman, D. B. Beach, H.-Y. Zhai, H. M. Christen, S. Kang, P. M. Martin, and A. Goyal, "Long Length All-Solution Coated Conductor Fabricated Using a Reel-to-reel Dip-Coating Process," submitted to 2002 MRS Fall Meeting, Boston, Massachusetts, December 2–6, 2002.

Sauers, I., M. Pace, D. R. James, and A. Ellis, "Surface Flashover of Fiberglass Reinforced Plastic in Vacuum at Cryogenic Temperature," submitted to the Conference on Electrical Insulation and Dielectric Phenomena, Cancun, Mexico, October 20–24, 2002.

Schwenterly, S. W., "Development of Power Transformers for the 21st Century: Waukesha Electric Systems/IGC-SuperPower/RGE/Oak Ridge National Laboratory SPI Collaboration," presentation to US-Japan Workshop on High-T_c Superconductors, Santa Fe, New Mexico, Dec. 2–5, 2001 (***Invited***).

Thompson, J. R., K. D. Sorge, C. Cantoni, D. K. Christen, and M. Paranthaman "High Current Stability and Sharp *E(J)* Curves in High-J_c Polycrystalline MgB_2 Films," 2001 Vortex Physics Workshop, Bariloche, Argentina, November 25–December 1, 2001 (***Invited***).

Thompson, J. R., A. Goyal, B. W. Kang, K. D. Sorge, and D. K. Christen, "Coated Conductors on Textured Ni-Cr Alloys with Reduced Ferromagnetism: Substrate Properties and YBCO Current Conduction," 2001 US-Japan Workshop on High-T_c Superconductors, Santa Fe, New Mexico, Dec. 2–5, 2001. (***Invited***)

Thompson, J. R., K. D. Sorge, C. Cantoni, D. K. Christen, and M. Paranthaman "High Current Stability and Sharp *E(J)* Curves in High-J_c Polycrystalline MgB_2 Films," submitted to American Physical Society March Meeting, Indianapolis, Indiana, March 18–22, 2002.

Wong-Ng, W., I. Levin, M. Vaudin, L. P. Cook, J. P. Cline, and R. Feenstra, "Phase Formation of $Ba_2YCu_3O_{6+x}$ in the Ba-Y-Cu-F-O-OH System," submitted to 2002 MRS Fall Meeting, Boston, Massachusetts, December 2–6, 2002.

Zhai, H.-Y., and H. M. Christen, "Comparison Between Pulsed Electron Deposition and Pulsed Laser Deposition of RE-BCO Films for Coated Conductor Applications," submitted to 2002 MRS Fall Meeting, Boston, Massachusetts, December 2–6, 2002.

INTERNAL DISTRIBUTION

1. D. B. Beach
2. M. A. Brown
3. D. K. Christen
4. L. M. Dickens
5. R. G. Gilliland
6. M. J. Gouge
7–16. R. A. Hawsey
17–21. W. Koncinski
22. D. M. Kroeger
23. M. Paranthaman
24. R. D. Quinn
25. J. P. Stovall
26. R. Quinn, OTTD
27. J. Johnson, OTIC

EXTERNAL DISTRIBUTION

28. N. Aversa, Consultant, Waukesha Electric Systems, 400 S. Prairie Ave., Waukesha, WI 53186-5937
29. U. Balachandran, Argonne National Laboratory, ET/212, 9700 South Cass Avenue, Argonne, IL 60439-4838
30. P. N. Barnes, Air Force Research Laboratory, AFRL/PRPG, 2645 Fifth Street, WPAFB, OH 45433-7919
31. R. Bhattacharya, National Renewable Energy Laboratory, 1617 Cole Boulevard, Golden, CO 80401
32. J. W. Bray, Physicist/Program Manager, General Electric Corporate Research and Development, P.O. Box 8, Schenectady, NY 12301
33. H. S. Chhabra, EE2D, U.S. Department of Energy, 6H-034/FORS, 1000 Independence Avenue, S.W., Washington, DC 20585
34. P. G. Clem, Sandia National Laboratories, MS 1411, P.O. Box 5800, Albuquerque, NM 87185-1405
35. J. G. Daley, EE2D, U.S. Department of Energy, 6H-034/FORS, 1000 Independence Avenue, S.W., Washington, DC 20585
36. N. Dickman, Waukesha Electric Systems, 400 S. Prairie Ave., Waukesha, WI 53186-5937
37. D. Driscoll, Rockwell Automation, 24800 Tungsten Road, Cleveland, OH 44117
38. J. Ekin, National Institute of Standards and Technology, 325 Broadway, Boulder, CO 80303
39. R. E. George, EE2D, U.S. Department of Energy, 6H-034/FORS, 1000 Independence Avenue, S.W., Washington, DC 20585
40. H. Harshavardhan, Neocera, 10000 Virginia Manor Rd., Beltsville, MD 20705
41. P. A. Hoffman, EE-2D, U.S. Deptartment of Energy, 1000 Independence Ave., S.W., Washington, DC 20585
42. X. Huang, General Electric Corporate Research and Development, EP-113, P. O. Box 8, Schenectady, NY 12301
43. R. L. Hughey, Jr., Southwire Company, P. O. Box 1000, Carrollton, GA 30119
44. A. T. Hunt, MicroCoating Technologies, 3901 Green Industrial Way, Chamblee, GA 30341
45. R. H. Jones, Rochester Gas and Electric, 89 East Avenue, Rochester, NY 14649-0001
46. D. C. Larbalestier, University of Wisconsin–Madison, Applied Superconductivity Center, 1500 Engineering Drive, Madison, WI 53706-1687

47. W. C. Lin, U.S. Department of Energy, Office of Assistant Manager for Energy Research and Development, Oak Ridge Field Office, P.O. Box 2008, Oak Ridge, TN 37831-6269
48. D. Lindsay, Southwire Company, P. O. Box 1000, Carrollton, GA 30119
49. A. P. Malozemoff, American Superconductor Corporation, Two Technology Dr., Westborough MA 01581
50. K. R. Marken, Jr., Oxford Superconducting Technology, P.O. Box 429, Carteret, NJ 07008-0429
51. S. P. Mehta, Waukesha Electric Systems, 400 S. Prairie Ave., Waukesha, WI 53186-5937
52. C. E. Oberly, WL/POOX-2, Aerospace Power Div., Wright Laboratory, 2645 Fifth St., WPAFB OH 45433-6563
53. P. N. Overholt, EE-2D, U.S. Department of Energy, 1000 Independence Avenue, S.W., Washington, DC 20585
54. S. M. Parker, Oxford Superconducting Technology, P.O. Box 429, Carteret, NJ 07008- 0429
55. W. P. Parks, Jr., EE-2D, U.S. Department of Energy, 1000 Independence Avenue, S.W., Washington, DC 20585
56. D. E. Peterson, Los Alamos National Laboratory, Superconductivity Technology Center, P.O. Box 1663, MS K763, Los Alamos, NM 87545
57. E. Pleva, Waukesha Electric Systems, 400 S. Prairie Ave., Waukesha, WI 53186-5937
58. M. J. Reed, EE-2D, U.S. Department of Energy, 1000 Independence Avenue, S.W., Washington, DC 20585
59. M. W. Rupich, American Superconductor Corporation, Two Technology Drive, Westborough, MA 01581
60. J. Scudiere, American Superconductor Corporation, Two Technology Drive, Westborough, MA 01581
61. V. Selvamanickam, SuperPower, Inc., 450 Duane Avenue, Schenectady, NY 12305
62. S. S. Shoup, MicroCoating Technologies, 3901 Green Industrial Way, Chamblee, GA 30341
63. M. Suenaga, Brookhaven National Laboratory, Bldg. 480, P. O. Box 5000, Upton,NY 11973-5000
64. S. Thorn, Southwire Company, P.O. Box 1000, Carrollton, GA 30119
65. D. T. Verebelyi, American Superconductor Corporation, Two Technology Drive, Westborough, MA 01581
66. Charles Weber, SuperPower, Inc., 450 Duane Avenue, Schenectady, NY 12305
67. D. O. Welch, Brookhaven National Laboratory, Materials Science Division, Upton, Long Island, NY 11973
68. W. Wong-Ng, National Institute of Standards and Technology, Ceramics Division, Building 223, A-256 Materials, Gaithersburg, MD 20899
69. G. J. Yurek, American Superconductor Corporation, Two Technology Drive, Westborough, MA 01581